Chamber Studies of Glyoxal Yields from the Oxidation of Selected Biogenic VOCs

William James Warman

Submitted in accordance with the requirements for the degree of Doctor of Philosophy

The University of Leeds

School of Chemistry

January 2024

The candidate confirms that the work submitted is his own, except where work which has formed part of jointly-authored publications has been included. The contribution of the candidate and the other authors to this work has been explicitly indicated below. The candidate confirms that appropriate credit has been given within the thesis where reference has been made to the work of others.

The temperature dependent calibration of the Fluorescence Assay by Gas Expansion (FAGE) instrument is detailed in Chapter 4 of this work, and is included in part of the jointly-authored publication detailed below:

Winiberg, F.A.F., Warman, W.J., Brumby, C.A., Boustead, G., Bejan, I.G., Speak, T.H., Heard, D.E., Stone, D., Seakins P.W. 2023. Comparison of temperature-dependent calibration methods of an instrument to measure OH and HO_2 radicals using laser-induced fluorescence spectroscopy. *Atmospheric Measurement Techniques*. **16**(19), pp.4375-4390.

Within the above publication, the current author (Warman, W.J.) contributed the experimental method of hydrocarbon decay outlined in section 3.2 alongside the corresponding Figure 3; and the experimental results displayed in section 4.2.1 alongside the corresponding Figure 7a. The remainder of the manuscript is attributable to the co-authors.

Acknowledgements

Well… this is it. We've reached the end of a very long road. There are so many people I need to mention, and I'm not sure I'll fit everyone in, but we'll see how we get on.

To my supervisors, Paul and Dan, thank you for the tremendous amount of support you've given me over the last few years. There are times where I would've been tempted to give up on me, so I can't imagine what it must have been like for the two of you. I definitely wouldn't have made it to the end without the occasional push I needed from you both. It's been a rollercoaster, but I've made it!

To the basement lot. Graham, you're a legend, and I'm pretty sure the lab would stop running without you around. Thank you for being a seemingly endless fount of knowledge, it's helped me grow in confidence in the lab, and I've become a somewhat competent researcher thanks to your help. Danny, it's been a pleasure working with you in my last year at Leeds. We've had good times with getting that glyoxal laser to run. Best of luck with the rest of your PhD. Abi, Rae, Sam, thanks for the occasional chats and coffee breaks, they made me feel less guilty for not working.

To the Dainton lot. Mark, you've definitely helped with lasers sometimes, not to mention helping with trying to fix the HIRAC glass delivery line (which I somehow managed to break twice). Your input and advice has been useful over the years. Rachel, Niamh, Kate, Ffion, we've always had entertaining chats and good times, it's just a shame you lived three flights up! Granted there's more sunlight up there, but still… You've been a real boost to my morale at times, and I hope the rest of your PhDs all go well.

My housemates for the duration of this marathon deserve a special mention. Vincent, I could not have done this without your support. Of all of them, you stuck with me through to the end (or at least until you got married anyway, but close enough). Ben (and Rosie), your lockdown support was a real encouragement to me. Lyds and Beth, your compassion is truly appreciated. It hasn't always been easy, and you've been there for me through that. Henry, we didn't have much time together, but we're making up for that in Sheffield, so you're included too! Lara and Sasha, it goes without saying that my final year of the PhD was so much more bearable thanks to you guys. Lara, let's be honest, we weren't great for each other's work ethic, but hey, it was nice to have a fellow PhDer in the house for solidarity, and you did encourage me in writing. I have so many memories with you all and I'm incredibly thankful.

Of course, I have to thank my family too. You've mostly stayed out of my hair (which I inevitably lost along the way, but we've mourned and moved on), but you've also encouraged me to keep going despite my exasperation at points. Particular thanks to dad for your heroism in moving my mountain of stuff from house to house over the years. Especially the piano. And the TV. And… well, you get the picture. Thank you all for supporting me in my choices, no matter how much concern they've caused you.

And finally, a massive thanks to my church family. To everyone who has been at Mosaic alongside me over the last few years (of which there are too many people to name so I won't name anyone for fear of missing someone out), thank you! You've been by my side through this journey week in week out, and you've helped me to grow and develop, encouraging me just as I hope I've also encouraged you in return. I hope the PhD hasn't made me too grumpy all the time, but some of you have definitely borne the brunt of my dissatisfaction with failed experiments or misaligned lasers. Your kindness, wisdom and advice has helped me see the best in my circumstances, and even when things have been rough, you've stood by my side faithfully. I'm no longer the same person I was when I started this endeavour, and that is, in part, definitely thanks to you guys.

Let me finish by saying I definitely won't have mentioned everyone that has been a part of this journey with me. If I've forgotten you, then I'm sorry. There are too many people to remember, but all of you have had an impact, and all of you have formed a meaningful part of my life in some way or another. Wherever you are now, whatever you're doing, I wish you the best, and maybe one day our paths will cross again.

Abstract

Knowledge of volatile organic compounds (VOCs) and their mixing ratios present in air on a regional and global scale is critical for understanding of air quality and climate. Measurement of individual non-methane hydrocarbons (NMHCs) present in ambient air presents a significant challenge, and the separation of hydrocarbon structures from measurement techniques such as infrared spectroscopy is rendered impossible by the number of species of NMHCs, on the order of 10^4 - 10^5, directly emitted or produced by oxidative chemistry in the atmosphere. Whilst a majority of NMHCs cannot be directly measured, the oxidation products, oxygenated VOCs (OVOCs), are more accessible to detection techniques. The qualification and quantification of VOC species within the troposphere may be resolved through the increased mechanistic understanding of glyoxal (CHOCHO) and formaldehyde (HCHO) production from a range of precursor VOCs. The ratio of glyoxal to formaldehyde (R_{GF}) produced through oxidation varies dependent on the VOC precursor, and yield measurements of these products are therefore paramount to deciphering global tropospheric R_{GF} measurements and the nature of their origin.

This thesis has a focus on chamber studies of glyoxal yields from the OH-initiated oxidation of biogenic VOCs (BVOCs), specifically acetaldehyde and isoprene, in the Highly Instrumented Reactor for Atmospheric Chemistry (HIRAC). HIRAC is equipped with several selective detection techniques, including a Proton Transfer Reaction-Time of Flight-Mass Spectrometer (PTR-ToF-MS), a glyoxal laser-induced-phosphorescence (GLYOX-LIP) instrument, and a Fluorescence Assay by Gas Expansion (FAGE) instrument. Simultaneous measurement with these instruments during oxidation reactions allowed detection of hydroxyl (OH) radicals, glyoxal, and BVOCs of interest, including acetaldehyde and isoprene, for the direct measurement of glyoxal yields.

Sources of OH were investigated and compared for chamber studies involving glyoxal, with a focus on GLYOX-LIP interference and first-order loss rates of glyoxal. Photolysis of either hydrogen peroxide or ozone were determined to be the most effective methods of OH generation in NO_x-free reactions (NO_x = NO and NO_2), whilst methyl nitrite (CH_3ONO) was distinguished as an effective OH precursor for studies involving NO_x. FAGE measurements of OH were investigated through the comparison of two FAGE calibration techniques; water vapour photolysis, calculating [OH] from water vapour concentrations in a flow of air; and VOC decay, calculating [OH] from PTR-ToF-MS detection of cyclohexane removal in HIRAC. Upon adjustment of the relative sampling

positions for FAGE and PTR-ToF-MS, both calibration techniques showed excellent agreement in the OH calibration factor (C_{OH}) for FAGE (to within 4 %). However, further investigation of C_{OH} measured through isoprene decay revealed a large discrepancy in measured C_{OH} between both calibration techniques. C_{OH} determined through water vapour photolysis was at least 7 times higher, however consistent ratios between measurements could not be determined. FAGE detection of OH during isoprene oxidation therefore relied upon C_{OH} determined through the isoprene decay.

Yields of glyoxal (Y_{GLY}) were measured both from the oxidation of acetaldehyde (Y_{GLY} = 0.12 ± 0.03 %) and isoprene (Y_{GLY} = 0.52 ± 0.06 %). The low glyoxal yield through acetaldehyde oxidation has implications for readdressing a missing source of glyoxal in the marine boundary layer (MBL), and discrepancies between observed and modelled glyoxal mixing ratios in the MBL remain unaccounted for. Meanwhile, to the author's knowledge, this work represents the first direct measurement of glyoxal yields from isoprene oxidation in the absence of NO_x through selective GLYOX-LIP detection. Measurements in this study combined with future work considering the dependence of glyoxal yield on NO_x mixing ratios will help reduce uncertainties in the global budget of glyoxal production through isoprene emissions in the troposphere.

Table of Contents

Table of Figures

Table of Tables

List of Abbreviations

BVOC	Biogenic Volatile Organic Compound
CH_3CHO	Acetaldehyde
CH_3OH	Methanol
CH_3ONO	Methyl Nitrite
CHOCHO	Glyoxal
CI_{MGLY}	Methylglyoxal Criegee Intermediate
CIMS	Chemical Ionisation Mass Spectrometry
CPM	Channeltron Photomultiplier Tube
DOAS	Differential Optical Absorption Spectroscopy
DOM	Dissolved Organic Matter
EUPHORE	European Photoreactor
FAGE	Fluorescence Assay by Gas Expansion
FFR	Field-Free Region
FTIR	Fourier Transform Infrared Spectroscopy
GC-FID	Gas Chromatography-Flame Ionisation Detector
GC-MS	Gas Chromatography-Mass Spectrometry
GD	Glow Discharge
GEOS	Global Earth Observing System
GLY	Glyoxal
GLYOX-LIP	Glyoxal Laser-Induced Phosphorescence
GOME-2	Global Ozone Monitoring Experiment-2
HCHO	Formaldehyde
HIRAC	Highly Instrumented Reactor for Atmospheric Chemistry
$HMVKAO_2$	Methyl Vinyl Ketone Peroxy Radical A
$HMVKBO_2$	Methyl Vinyl Ketone Peroxy Radical B
HO_2	Hydroperoxy Radical
HONO	Nitrous Acid
HORUS	Hydroxyl Radical Measurement Unit Based on Fluorescence Spectroscopy
HO_x	Hydroxyl and Hydroperoxy Radicals

HPLC	High Performance Liquid Chromatography
IEPOX	Isoprene Epoxydiol
IPI	Inlet Pre-Injector
IR	Infrared
ISC	Intersystem Crossing
IUPAC	International Union of Pure and Applied Chemistry
LIF	Laser-Induced Fluorescence
LIP	Laser-Induced Phosphorescence
MACR	Methacrolein
MAX-DOAS	Multi Axis-Differential Optical Absorption Spectroscopy
MBL	Marine Boundary Layer
MCM	Master Chemical Mechanism
MCP	Microchannel Plate Detector
MCT	Mercury Cadmium Telluride
MESMER	Master Equation Solver for Multi-Energy Well Reactions
MFC	Mass Flow Controller
MIR	Mid-Infrared
MMS	Multipass Matrix System
MVK	Methyl Vinyl Ketone
Nd: YAG	Neodymium-Doped Yttryium Aluminium Garnet
NMHC	Non-Methane Hydrocarbon
NMVOC	Non-Methane Volatile Organic Compound
NO	Nitrogen Oxide
NO_2	Nitrogen Dioxide
NO_3	Nitrate Radical
NO_x	Nitrogen Oxides
OH	Hydroxyl Radical
OMI	Ozone Monitoring Instrument
OVOC	Oxygenated Volatile Organic Compound
PM	Particulate Matter
PMT	Photomultiplier Tube
PRD	Pearl River Delta

PRF	Pulse Repetition Frequency
PS_{GLY}	Glyoxal Phosphorescence Signal
PS_{MGLY}	Methylglyoxal Phosphorescence Signal
PTFE	Polytetrafluoroethylene
PTR	Proton Transfer Reactor
PTR-MS	Proton Transfer Reaction-Mass Spectrometer
PTR-ToF-MS	Proton Transfer Reaction-Time of Flight-Mass Spectrometer
R_{GF}	The Ratio of Glyoxal to Formaldehyde
RH	Relative Humidity
RO	Organic Alkoxy Radicals
RO_2	Organic Peroxy Radicals
ROC	Radius of Curvature
RONO	Organic Nitrites
$RONO_2$	Organic Nitrates
ROOOH	Organic Trioxide
SAPHIR	Simulation of Atmospheric Photochemistry In a Large Reaction Chamber
SCIAMACHY	Scanning Imaging Absorption Spectrometer for Atmospheric Cartography
SD	Source Drift
SENEX	Southeast Nexus Campaign
SNR	Signal to Noise Ratio
SOA	Secondary Organic Aerosol
TME	Tetramethylethylene
TROPOMI	Tropospheric Monitoring Instrument
UNFOGS	Understanding Formaldehyde and Glyoxal Chemistry for New Satellite Measurements
UV	Ultraviolet
VOC	Volatile Organic Compound
VUV	Vacuum Ultraviolet

Chapter 1 The Role of Tropospheric VOC Emissions

1.1 Study Motivations and Outline

The chemistry in the troposphere is complex. Thousands of volatile organic compound (VOC) species are released into the atmosphere with varying emission rates, atmospheric lifetimes, capacities for water uptake and aerosol formation, negative health impacts, and global warming effects leading to climate change. The global impact of VOC emissions is difficult to assess, and the fate of VOCs in the atmosphere, briefly outlined in section 1.3, can only be predicted through models that are able to accurately simulate chemical transport processes, reaction rates, and mechanistic routes leading to product formation. An analysis of common oxidative products originating from a majority of important VOC precursors, including such oxygenated VOCs (OVOCs) as glyoxal (CHOCHO) and formaldehyde (HCHO), may be the solution to providing additional insight into the impacts of these VOC emissions, as detailed in section 1.4.

Field studies in this instance are useful in providing an indication of ambient concentrations for VOCs of interest, as well as their oxidation products, to assess the accuracy of currently understood atmospheric mechanisms in model simulations. Field studies in distinct environments can be useful in observing the impact of local conditions, including temperature, humidity, remoteness, emission sources, and NO_x (= NO + NO_2) mixing ratios, on concentrations of species of interest. However, chamber studies offer the advantage of a controlled environment in which a single reaction may be observed under known and variable conditions to measure oxidation product yields, reaction rates, and analyse mechanism routes. Chambers also offer the advantage of studying reactions at higher concentrations over longer time periods than typically observed in ambient air samples, overcoming any issues whereby instrument detection limits may reduce species monitoring capacity. Both field and chamber studies are complementary to one another in filling any gaps in the mechanistic understanding of atmospheric VOC oxidation processes and their subsequent impacts on air quality and climate change.

Biogenic VOCs (BVOCs) in particular are an unavoidable source of emissions through natural processes, and comprise an integral category of atmospheric oxidation and secondary organic aerosol (SOA) formation. Oxidation products from BVOCs, including glyoxal and formaldehyde, have significant overlap with those from anthropogenic emissions. Measurement of these oxidation products will provide valuable insight only with an accurate knowledge of their yields from both anthropogenic and biogenic precursors. An introduction to significant glyoxal precursors and their atmospheric contexts relevant for this study is outlined in section 1.5.

This thesis highlights the apparatus used for chamber studies of BVOC oxidation reactions, namely the Highly Instrumented Reactor for Atmospheric Chemistry (HIRAC) at the University of Leeds, in Chapter 2, with a focus on the instrumentation employed for specific detection of atmospherically relevant VOCs and radical species. Included is the selective detection of HO_x (= OH and HO_2) *via* the Fluorescence Assay by Gas Expansion (FAGE) instrument, where, in the majority of reactions studied, OH forms the primary oxidant for the initiation of BVOC oxidation. Available methods of OH generation for chamber studies are investigated and discussed in Chapter 3, with a focus on usefulness for the study of glyoxal yields from oxidation processes. Two alternative methods of calibration for the FAGE instrument are discussed and compared in Chapter 4 to assess the reliability of OH measurements for applications in chamber studies. The primary focus of this study addresses the yields of glyoxal from acetaldehyde, of particular significance in the marine boundary layer (MBL), and isoprene, the largest contributor to VOC emissions globally. The glyoxal yields were examined to investigate the current mechanistic understanding of the oxidation processes based on the Leeds Master Chemical Mechanism (MCMv3.3.1). The oxidation reactions of acetaldehyde and isoprene are discussed in Chapters 5 & 6 respectively.

1.2 Introduction

The importance of VOC oxidation in the atmosphere has led to an increasing number of studies into the effects of anthropogenic emissions on air quality and human health, as a result of initial findings following episodes of smog formation in the early 1950s (Haagen-Smit, 1952; Haagen-Smit and Fox, 1954). There are various ways in which VOCs and their oxidative products can impact air quality, particularly in urban areas. The production of NO_x (= NO + NO_2) through high temperature combustion processes, alongside VOC emissions, acts as a catalyst for tropospheric O_3 formation, a key species associated with the formation of photochemical smog (reactions R1.1-5).

$$RH + OH \rightarrow R + H_2O \quad \text{(R1.1)}$$

$$R + O_2 (+M) \rightarrow RO_2 (+M) \quad \text{(R1.2)}$$

$$RO_2 + NO \rightarrow RO + NO_2 \quad \text{(R1.3)}$$

$$NO_2 + h\nu \xrightarrow{\lambda < 400\ nm} NO + O(^3P) \quad \text{(R1.4)}$$

$$O_2 + O(^3P) (+ M) \rightarrow O_3 (+ M) \quad \text{(R1.5)}$$

In this typical oxidation scheme, where R represents a generic VOC substituent with at least one bonded hydrogen atom, NO and NO_2 are cycled over one another through reaction with peroxy (RO_2) radicals (R1.3) and subsequent NO_2 photolysis (R1.4). This produces the atomic oxygen needed to form ozone. The recombination reactions (R1.2 & R1.5) require the presence and subsequent collision of a bath gas, M, typically either molecular nitrogen (N_2) or oxygen (O_2), to absorb any excess vibrational energy resulting from the formation of a chemical bond where there is no previous bond cleavage. Failing vibrational relaxation of the recombined molecule, in this case RO_2 or O_3, it will simply revert back into its former constituents through spatial dissociation.

It is worth noting that, in general, the hydroxyl radical, OH, acts as the primary daytime oxidant for VOCs, being produced through the photolysis of ozone during daylight hours (R1.6, 1.7).

$$O_3 + h\nu \rightarrow O_2 + O(^1D) \quad \text{(R1.6)}$$

$$H_2O + O(^1D) \rightarrow 2OH \quad \text{(R1.7)}$$

This is recognised in the general diurnal cycle for HO_x (= OH + HO_2), which reaches a peak around midday to early afternoon, where influx of solar radiation, alongside consequent processes such as ozone photolysis, is at its highest. An example of this can be seen in the measured and modelled data taken by Ren et al. (2003) in July and August, 2001, at Queens College in New York City (Figure 1.1). The yield of OH through ozone photolysis is not unity, owing to relaxation of the electronically excited atomic oxygen state ($O(^1D)$) down to its ground state ($O(^3P)$) being on a similar timescale to reaction with water, and this ultimately results in the reformation of ozone (R1.5). However, this is effectively a cycle of ozone destruction and formation, where producing OH simply serves as a termination of the cycle, therefore in this process, the rate of formation of OH is primarily impacted by photolysis rates of ozone. Concentrations of OH present in ambient air are determined by the ratio of formation to removal rates, where removal of OH is primarily categorised by the reaction with VOCs emitted into the troposphere.

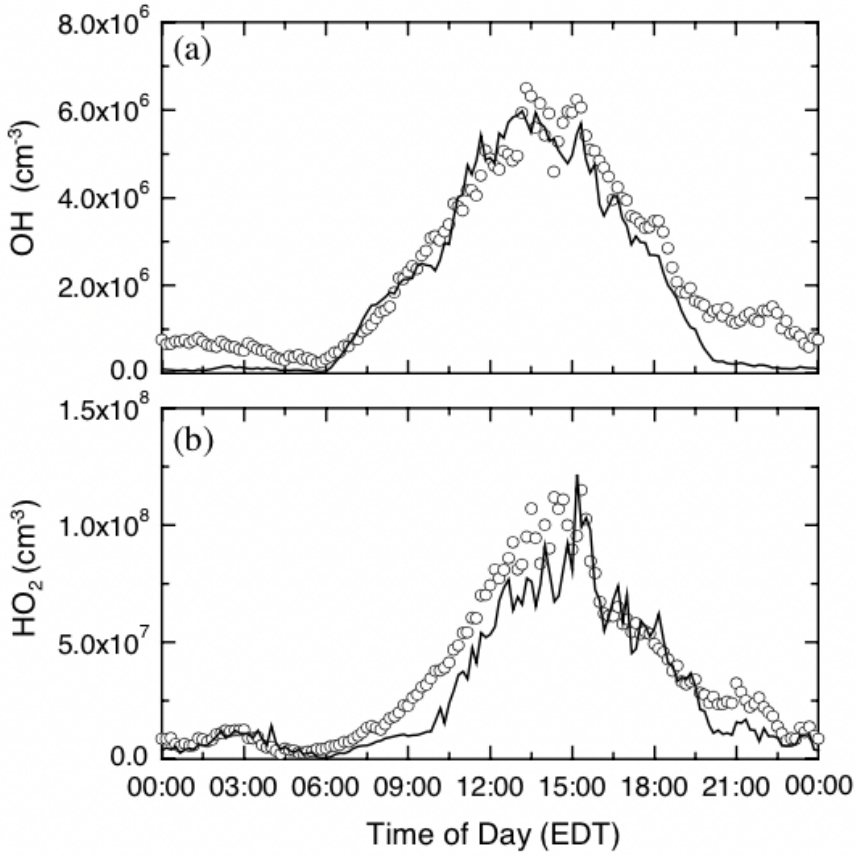

Figure 1.1 The median diurnal variations for a) OH and b) HO_2 averaged over the period of 10th July to 2nd August 2001. Measurements conducted at Queens College in New York City. Figure shows comparison of field measurements (open circles) and modelled concentrations (solid line) which shows relatively good understanding of OH production and reactivity. Taken from Ren *et al*. (2003).

From this foundation, we can recognise the importance of a quantitative knowledge of OH reaction rates with relevant VOCs emitted through biogenic and anthropogenic means. The reactivity of the hydroxyl radical will have a significant impact on O_3 concentrations present in the boundary layer, yet despite this acknowledgement, mitigating tropospheric ozone pollution is not as simple as merely reducing NO_x or VOC emissions. The relationship between O_3, VOCs and NO_x is not trivial, as demonstrated by localised ozone isopleth plots (Figure 1.2), examples of which have been mapped by Roselle and Schere (1995) in their investigations on the response of modelled O_3 mixing ratios across the eastern United States through the variation of VOC and NO_x emissions. The nature of this relationship requires that each scenario of urban air pollution must have different strategies for controlling and reducing ozone concentrations, dependent on the ratio between NO_x and VOC concentrations in each emissions scenario, as well as the reactivity of VOCs present (Sillman, 1999). This emphasises that quantitative knowledge

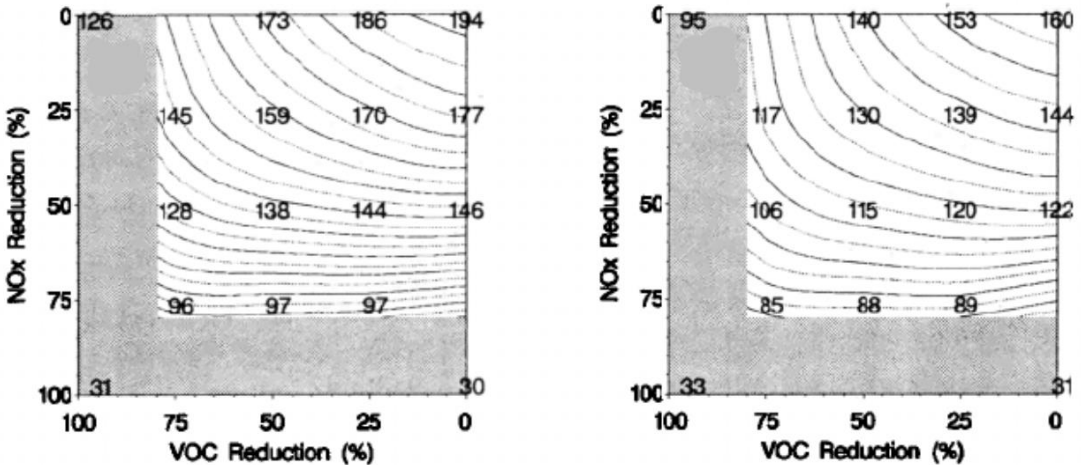

Figure 1.2 Two examples of modelled scenarios of ozone production over portions of the eastern United States in which the reduction in emissions of NO_x or VOCs results in a varied response of ozone mixing ratios. The specific locations differ in initial concentrations of NO_x and VOCs, which alters the effect of ozone pollution mitigation through emissions reductions. Plot lines represent isopleths for ozone mixing ratios in ppbv, labelled in a grid format as a clear demonstration of the impact on ozone levels through solely reducing either VOC or NO_x emissions. Adapted from Roselle and Schere (1995).

of both total VOC mixing ratios and categories of VOCs based on their reactivity are needed to approach reasonable strategies for reduction of air pollution on a specific scenario basis.

Air pollution has long been associated with respiratory health issues and mortality with both short-term and long-term effects (Jerrett et al., 2009; Bell et al., 2005; Ito et al., 2005). Lelieveld et al. (2015) have estimated an increase in projected mortality rates attributable to chronic obstructive pulmonary disease linked with elevated ozone and $PM_{2.5}$ (Particulate Matter, ≤2.5 μm in size) levels from 3.3 million in 2010 to 6.6 million by 2050, an increase of 100 %. They base their estimations on a combination of the global burden of disease for 2010 (Lim et al., 2012); a model for simulating atmospheric chemistry and transport; regional population data; and health statistics on a country basis. An assumption of continuation in current global emissions trends, under a 'business-as-usual' model scheme, leads to predict an increase from 142,000 deaths attributable to ozone pollution alone for 2010 to 358,000 deaths for 2050. Despite accounting for the estimated increase in population by 2050, this still represents a predicted increase of 88% in the premature mortality rate from ozone-associated respiratory disease over the 40 years.

It is evident then that tropospheric ozone pollution has significant respiratory health impacts, and monitoring both NO_x and VOC concentrations within urban environments

is crucial in limiting the detrimental effects of poor air quality. However, this chemistry is not limited to the boundary layer in which we live. Oxygenated VOCs (OVOCs) that reach the upper troposphere due to longer chemical lifetimes may undergo photolysis, which promotes ozone formation through the generation of OH and HO_2 radicals (McKeen et al., 1997; Wennberg et al., 1998; Jaeglé et al., 2001). Unlike within the stratosphere, ozone in this region will absorb and re-radiate outgoing infra-red (IR) radiation from the Earth more than any incoming solar radiation, and is therefore a contributor to the "greenhouse" effect. Whilst the effects of planetary warming are not as immediate as air quality, they will dictate serious consequences on a longer term, with a delayed impact of greenhouse gas emissions on subsequent warming, therefore preventative measures are necessarily urgent.

This highlights the need for conducting experiments not only at surface temperatures and pressures, but also at conditions relevant for upper tropospheric chemistry (i.e. down to ~200 K and 100 mbar), achievable through the use of the HIRAC (Highly Instrumented Reactor for Atmospheric Chemistry) apparatus (see Chapter 2). Investigating the temperature and pressure dependence of reaction rates and product yields will assist in providing better predictions for the formation and accumulation of ozone, greenhouse gases and OVOCs at higher altitudes. However, it should be noted that these issues will require more widespread solutions, due to chemical transport in the free troposphere typically being on a more hemispherical scale. This is the result of a combination of the 'convective cells' that provide the major mode of transport for material in the free troposphere as well as lower temperatures and pressures dictating fewer successful collisions and subsequently increasing the lifetimes of species.

Other conditions that have an impact on product yields and chemical transport include relative humidity and mixing ratios of NO_x. Relative humidity will play a large role in the quantity of VOCs that undergo heterogeneous uptake, removing organic reactants from the gaseous phase into the aqueous phase and forming aerosol. Aerosol formation naturally affects both the chemistry of VOCs, and subsequently, their atmospheric lifetime, altering their impact on air quality. Higher mixing ratios of NO_x, typically observed in urban environments, also impact the mechanistic routes to oxidation products, both through faster conversion of RO_2 to RO species (R1.3), and through the formation of organic nitrates ($RONO_2$) and nitrites (RONO). The quantities of NO_x present will therefore affect the rate of formation of oxidation products, and may also impact the ratio at which oxidation products are formed in a singular reaction. Studies of

product yields for glyoxal and formaldehyde from BVOCs must therefore take into consideration the impact of NO_x for a complete understanding and assessment of product formation relevant for both urban and rural environments.

1.3 Atmospheric Fate of VOCs

Organic compounds released into the atmosphere may be oxidised in different ways, and the pathways taken in these oxidation mechanisms is largely pivotal upon the chemistry of the alkoxy radical (RO) produced; a general mechanism of which is shown in Figure 1.3 (Orlando et al., 2003). This VOC oxidation mechanism details the favoured pathways in most cases, and enables a fair prediction of products that will be generated, even in the absence of any empirical data (Atkinson, 1990; Atkinson and Carter, 1991; Atkinson, 1994; Atkinson, 1997). More recent studies have indicated the importance of reaction between RO_2 and OH radicals as a competing sink for RO_2 in oxidation mechanisms, both through simple conversion to RO and HO_2 and through formation of a trioxide species (ROOOH) (Fittschen et al., 2014; Yan et al., 2016; Yan and Krasnoperov, 2019), both of which has been neglected in the mechanism outlined by Orlando et al. (2003). These reactions should be given consideration in model studies as alternative mechanistic

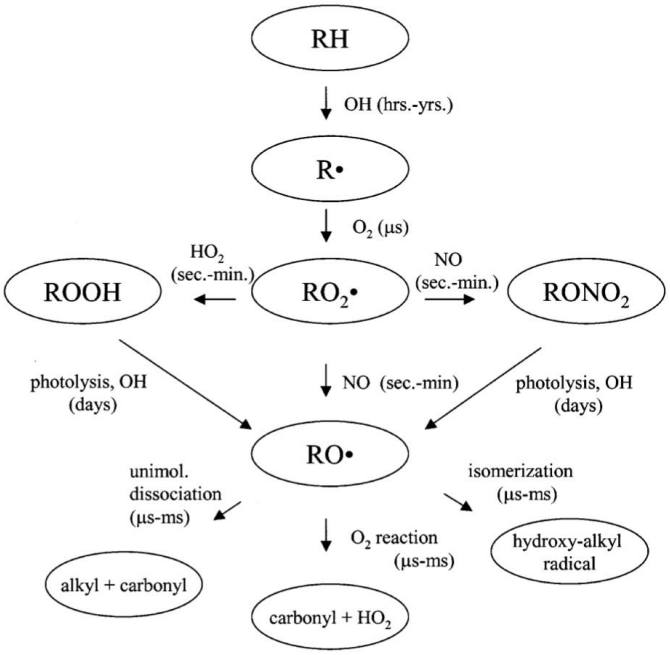

Figure 1.3 A general schematic illustrating the OH-initiated oxidation pathways of hydrocarbons released into the atmosphere, alongside the magnitudes of timescales typical for each process to occur. Taken from Orlando *et al*. (2003).

pathways in oxidation schemes where it is possible to measure or estimate reaction rate coefficients. Measuring the branching ratios of the alkoxy radical pathways, combined with initial abstraction or addition mechanisms, provides a better understanding of the average concentrations of species present in the atmosphere, an essential ingredient for matching global models with field observations. Difficulties arise here in the inability to measure specific alkoxy concentrations, as a result of their very short atmospheric lifetimes due to rapid reaction or dissociation. However, one can attempt to identify proposed products for the predicted fate of an alkoxy radical.

A key example of this is the oxidation of isoprene (2-methyl-1,3-butadiene, $CH_2=C(CH_3)CH=CH_2$, see section 1.5.3 & Chapter 6), constituting the most abundant BVOC emission and the largest contributor to glyoxal formation on a global scale (Guenther et al., 2006; Fu, T.-M. et al., 2008; Guenther et al., 2012). The OH-initiated oxidation of isoprene predominantly proceeds through the addition of OH to either side of the two C=C double bonds, forming six major peroxy radicals consisting of the cis and trans stereoisomers at both the secondary and tertiary sites as well as the two primary addition sites (Campuzano-Jost et al., 2000; Paulson and Seinfeld, 1992; Paulson et al., 1992). These peroxy radicals will subsequently form alkoxy radicals as depicted in the general scheme of Figure 1.3. To take one of these alkoxy intermediates,

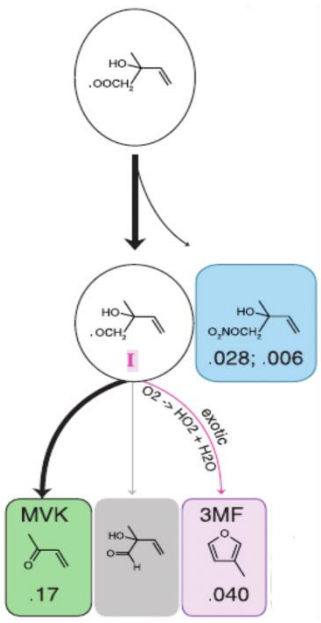

Figure 1.4 A mechanism demonstrating the various reaction pathways available to one of the initial peroxy and subsequent alkoxy radicals formed upon the OH-initiated oxidation of isoprene (2-methyl-1,3-butadiene) through addition at the methyl-substituted double bond site. Decimal figures below each stable species represent fractional yields taken from Paulson and Seinfeld (1992), where, of the displayed species, only methyl vinyl ketone (MVK) was measured directly. Adapted from Sprengnether *et al*. (2002).

CH_2=CHC(CH_3)(OH)CH_2O·, this may then follow any one of three pathways, illustrated by Sprengnether et al. (2002). It may dissociate, producing methyl vinyl ketone ($CH_3C(O)CH=CH_2$, MVK) and formaldehyde; simply be oxidised by oxygen to form the resulting aldehydic species CH_2=CHC(CH_3)(OH)CHO, considered negligible in this case; or undergo a cyclisation rearrangement upon reaction with oxygen, where dehydration of the molecule results in loss of the hydroxyl group and formation of 3-methyl furan (Figure 1.4). Expanding this consideration to all of the initial alkoxy radicals produced by isoprene oxidation, prediction of the ratios of second- and third-generation oxidation products will lack accuracy without further empirical evidence to determine the branching ratios for each reaction pathway.

1.4 The UNFOGS Project

1.4.1 Understanding Formaldehyde and Glyoxal Chemistry for New Satellite Measurements (UNFOGS)

In the quest for global coverage of emissions inventories and their oxidative products, a difficulty arises in that a high majority of non-methane hydrocarbon (NMHC) emissions are very difficult to observe directly through satellite detection techniques. The majority of NMHCs are indistinguishable in the infrared region as a result of large overlaps in absorption cross-sections, particularly regarding C-H stretches (2800-3000 cm^{-1}), and a lack of unique absorption features in a complex mixture of species makes separation difficult in IR analysis. Similarly, UV measurements do not provide any more of a solution, owing to most NMHCs absorbing solely in the vacuum ultraviolet (VUV) region (10-200 nm), where strong absorbance due to ozone and molecular oxygen dominates.

Whilst these primary emissions prove difficult to measure, more recent studies have brought to light a link between the product ratio of glyoxal (CHOCHO) to formaldehyde (HCHO), denoted as R_{GF}, observed from atmospheric oxidation compared with the respective NMHC emissions (Vrekoussis et al., 2010; Chan Miller et al., 2016). This relationship may be exploited due to the observability of glyoxal and formaldehyde from long path differential optical absorption spectroscopy (DOAS) measurements (Volkamer et al., 2005a; Volkamer et al., 2006), and the potential for satellite observations utilising this technique which have been previously performed with the satellite instruments GOME-2 (Global Ozone Monitoring Experiment-2) and SCIAMACHY (SCanning

Imaging Absorption spectroMeter for Atmospheric CartograpHY) (Wittrock et al., 2006; Vrekoussis et al., 2009; Lerot et al., 2010), as well as more recently with TROPOMI (TROPOspheric Monitoring Instrument) on board the Sentinel-5 Precursor satellite, launched initially in 2017 (Alvarado et al., 2020; Chen et al., 2022), and the Sentinel-4 satellite launch.

The UNFOGS Project (UNderstanding FOrmaldehyde and Glyoxal chemistry for new Satellite measurements) aims to make use of the improved measurements of formaldehyde and glyoxal from these satellites to determine the concentrations and compositions of a greater number of NMHC emissions on a global scale. However, in order to maximise the usefulness of these observations, a wider understanding of the chemistry involved in reaction mechanisms and branching pathways from both known and further potential glyoxal precursors is necessary in developing and improving models.

This thesis aims to contribute to the work of UNFOGS through the direct measurement of glyoxal yields from isolated systems in chamber experiments as a means for updating BVOC oxidation mechanisms in atmospheric chemistry models. Whilst UNFOGS relies on the measurement of R_{GF} from the initiated photo-oxidation (see section 1.4.3), formaldehyde yields were not a focus of this work due to a lack of specific instrumentation for formaldehyde detection (see Chapter 2). Glyoxal yields measured here therefore seek to provide the foundations for further work in which the mechanisms are better characterised for simultaneous detection of glyoxal and formaldehyde. These mechanisms, improved through isolated reaction systems, can then be coupled with global simulations to increase the understanding of observed R_{GF} measurements through satellite detection.

1.4.2 Glyoxal as a VOC Indicator

Glyoxal, the simplest α-dicarbonyl species, is significant in that it is relatively short-lived in ambient air, but not so short-lived as to be undetectable in the atmosphere. Its typical lifetime is within a timescale of 2-3 hours, dependent primarily on photolysis rates, displaying seasonal and diurnal variation; OH concentrations, and similarly nitrate radical (NO_3) concentrations more prevalent at night; and relative humidity (RH) levels, due to a high solubility in water (effective $K_H = 4.2 \times 10^5$ mol dm^{-3} atm^{-1}) resulting in rapid heterogeneous uptake into organic aerosol matter (Coburn et al., 2014). This relatively

short lifetime is a convenient property for glyoxal to act as an indicator for VOC emissions within a small radius using local knowledge of a region and its typical emissions and weather patterns. An understanding of the oxidative routes that lead to glyoxal formation from its precursors, alongside empirical measurements of R_{GF}, should assist the identification of primary emissions and their secondary oxidative products.

There are some primary emissions of glyoxal that are important to characterise for model inputs as a result of biofuel and biomass burning, which produce a higher percentage of oxygenated VOCs than their fossil fuel counterparts (Hays et al., 2002). However, glyoxal as a primary VOC indicator is of greater interest to this work, where yield measurements from BVOCs become more important in the determination of R_{GF}. More recently, direct observations of isoprene concentrations have been obtained from satellite measurements conducted in September 2014 using cross-track infrared sounder instrumentation on-board the Suomi-NPP satellite (Fu, D. et al., 2019). These observations will be especially useful in tandem with future glyoxal and formaldehyde monitoring equipment, particularly with the purpose of resolving isoprene-sourced production of these compounds and differentiating from anthropogenic or pyrogenic sources.

The primary objectives for this project therefore were the accurate determination of glyoxal yields from relevant atmospheric precursors, including isoprene, for use in model studies, and an analysis of the key branching ratios in VOC oxidation schemes relevant for glyoxal production, with a particular focus here on biogenic VOCs (BVOCs). A range of measurement techniques (see Chapter 2) were employed to investigate reaction rates, branching ratios, and product yields of BVOCs in the HIRAC facility, including the use of a glyoxal-specific phosphorescence instrument based on the design by Henry et al. (2012) and described in detail in Chapter 2. Developing models through the analysis of reaction kinetics and product yields from this project aims to improve the quantification of emissions inventories to a greater degree of accuracy using satellite measurements of glyoxal and formaldehyde concentrations.

1.4.3 A Case Study on R_{GF}

The significance of R_{GF} becomes apparent in its variable dependence on the precursor VOC, where similar R_{GF} values may typically be found within particular categories of VOCs, demonstrated in Figure 1.5 by Chan Miller et al. (2016) through use of the annual emissions inventory over the Pearl River Delta (PRD) in 2006 (Zheng et al., 2009) and

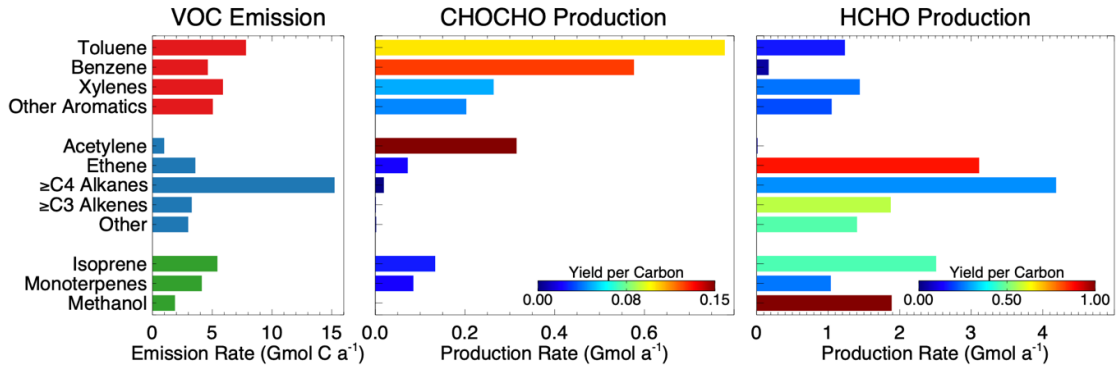

Figure 1.5 Annual emission rates of a selection of VOCs from the 2006 emissions inventory over the Pearl River Delta (PRD) (Zheng *et al*., 2009), and their corresponding glyoxal and formaldehyde yields per carbon, calculated using the Master Chemical Mechanism (Jenkin *et al*., 1997; Jenkin *et al*., 2003). Data demonstrates the variable R_{GF} values presented, particularly in view of specific categories of VOC emissions present over the PRD. Taken from Chan Miller *et al*. (2016).

their respective glyoxal and formaldehyde yields, calculated with version 3.2 of the Master Chemical Mechanism (MCM) (Jenkin et al., 1997; Jenkin et al., 2003). Although there has been significant research investigating this area, including the estimations of glyoxal global budgets through analysis of production rates and known sinks (Fu, T.-M. et al., 2008; Myriokefalitakis et al., 2008), there is a further need for evaluating these global budgets on a smaller scale and gaining insight into more local glyoxal and formaldehyde concentrations to identify emission rates for a greater range of VOCs with more certainty. This is emphasised by the observation that although the majority contributor to glyoxal global budget stems from biogenic emissions, including isoprene, ethylene, monoterpenes and methylbutenols approximating ~54 % of glyoxal production (Fu, T.-M. et al., 2008), anthropogenically produced aromatic compounds have a much greater impact on glyoxal levels on a regional scale over the PRD, rather than simple aliphatic hydrocarbons or biogenic terpenes (Chan Miller et al., 2016).

Computationally derived R_{GF} values over the PRD reveal an underestimation of modelled glyoxal concentrations in this region with the MCM database when compared with direct observations from OMI satellite data (Chan Miller et al., 2014), and has been to some extent attributed to either a lack of understanding in glyoxal formation from the oxidation mechanisms of aromatic VOCs or an incomplete aromatic emissions inventory. Large quantities of aromatic compounds such as toluene and xylene are emitted from anthropogenic sources at industrial sites around the PRD region due to a rapid increase in industrial growth in recent decades (Zhong et al., 2013), however there are other aromatics either directly emitted or produced from biogenic sources, such as in the case

of furans formed through the oxidation of isoprene and monoterpenes (Volkamer et al., 2001; Sprengnether et al., 2002), which may be unaccounted for in modelled simulations. Figure 1.5 demonstrates the strong variation in produced glyoxal and R_{GF} values even between aromatic compounds, the presence of other species notwithstanding, and incomplete emissions inventories or inaccurate yield data may have a large impact on R_{GF} results.

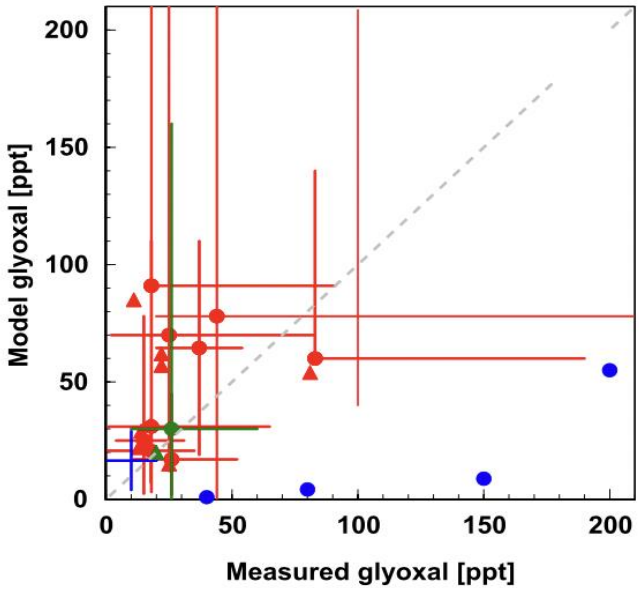

Figure 1.6 A set of comparisons between modelled glyoxal concentrations using the MCM dataset and observed satellite measurements in locations around the globe including east and west coast United States, Portugal, Germany and Japan, showing the lack of correlation and understanding of the chemistry. Data points represent rural continental region (red), marine boundary layer (blue) and the free troposphere (green) measurements. Data includes both mean (circles) and median (triangles) values. Solid lines indicate concentration ranges detected, and the grey dashed line indicates 1:1 agreement between models and observations. Adapted from Fu *et al.*, (2008).

Previous attempts to establish an agreement between measured and modelled glyoxal concentrations has likewise been of limited success, owing perhaps to the difficult nature of measuring α-dicarbonyls at such low mixing ratios (10 – 100 pptv) in ambient air. Fu, T.-M. et al. (2008) compared previously collected glyoxal measurement data, observed through a variety of techniques including HPLC (High Performance Liquid Chromatograohy), GC-FID (Gas Chromatography-Flame Ionisation Detector), GC-MS (Gas Chromatography-Mass Spectrometry) and MAX-DOAS (Multi Axis-Differential Optical Absorption Spectroscopy). Modelled predictions typically show an overestimation of glyoxal mixing ratios in rural continental areas and a large underestimation of glyoxal in the marine boundary layer (MBL), shown in Figure 1.6. Whilst localised isoprene emissions are a possible cause for the discrepancies observed

in continental air, there is clearly a large missing source of glyoxal in the MBL (discussed further in Chapter 5).

It is evident that measured R_{GF} values, determined from data recorded by the OMI (Ozone Monitoring Instrument) satellite via measurements of backscattered solar radiation (Chan Miller et al., 2014; Chan Miller et al., 2016; González Abad et al., 2015; Bucsela et al., 2013), differ dependent on location as a result of local emissions (Figure 1.7). Of particular remark is the elevated glyoxal concentration in the PRD region, compared with more evenly distributed formaldehyde. Awareness of this accentuated chemistry over the PRD naturally provides scope for investigating the oxidative routes of precursors leading to glyoxal formation, with the objective of qualitatively and quantitatively describing

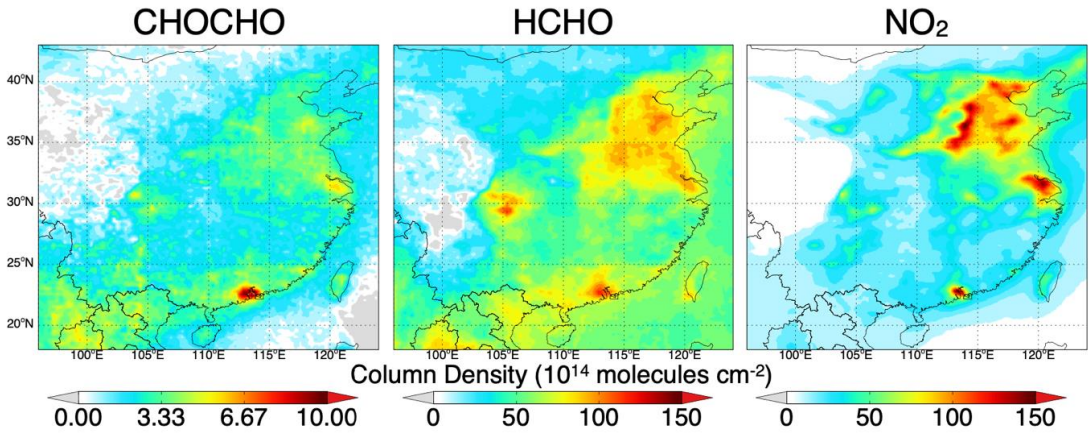

Figure 1.7 A display of the mean column densities from analysed satellite observations of glyoxal (Chan Miller *et al*., 2014), formaldehyde (González Abad *et al*., 2015), and NO_2 (Bucsela *et al*., 2013) over China from 2006-2007 measured with the OMI satellite instrument. Observed are the localised disparities between glyoxal and formaldehyde mixing ratios, with a particular hotspot of glyoxal over the PRD. Taken from Chan Miller *et al*., (2016).

local emissions inventories to improve the disparity between satellite measurements and model simulations.

1.5 Glyoxal Precursors

1.5.1 Acetylene

Acetylene (HC≡CH) is the largest anthropogenic contributor to global concentrations of glyoxal, despite its relatively low emissions, which are estimated at a total of 6.6 Tg a^{-1} through a combination of fossil fuel, biofuel and biomass combustion primarily in vehicular and wildfire emissions (Xiao et al., 2007). The oxidation mechanism of

acetylene has been studied in detail previously both with and without NO_x present (Yeung et al., 2005; Hatakeyama et al., 1986; Galano et al., 2008; Bohn et al., 1996; Bohn and Zetzsch, 1998), and is currently understood to involve two dominant channels.

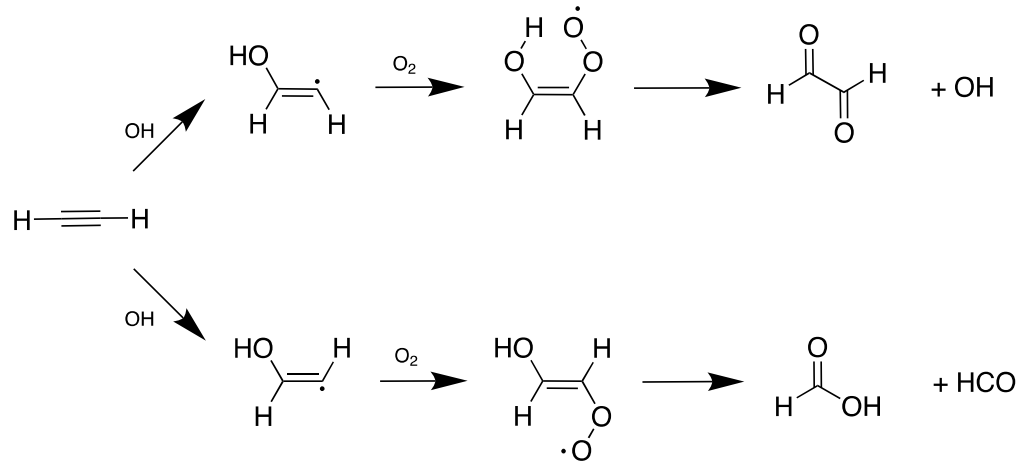

Figure 1.8 A schematic demonstrating the mechanistic routes for the formation of glyoxal and formic acid following the oxidation of acetylene initiated by an addition reaction with OH.

Initial reaction of acetylene with OH proceeds via formation of an acetylene-OH adduct (C_2H_2-OH), which is rapidly oxidised by O_2 under atmospheric conditions. However, as the resulting adduct has fixed geometry with an unsaturated double bond, both cis and trans isomers will form, dictating the reaction products generated further down the mechanism (Figure 1.8). Reaction of the cis adduct with O_2 produces glyoxal through the elimination of OH in a six-membered cyclic unimolecular decomposition process (R1.8a). The trans adduct peroxy radical similarly proceeds through formation of a four-membered cyclic intermediate, as postulated by Hatakeyama et al. (1986), which then rapidly decomposes into formic acid and HCO through cleavage of the peroxy O-O and C-C bonds (R1.8b).

$$HO - C_2H_2 + O_2 \rightarrow CHOCHO + OH \quad \text{(R1.8a)}$$

$$HO - C_2H_2 + O_2 \rightarrow HCOOH + HCO \quad \text{(R1.8b)}$$

The substantial glyoxal yield, which is significantly higher than most other anthropogenic or biogenic glyoxal precursors, has been quantified by Hatakeyama et al. (1986) as 0.7 ± 0.3. Bohn et al. (1996) report excellent agreement with this value through measurement of an OH regeneration yield (0.70 ± 0.04). Lockhart et al. (2013) likewise assert a good agreement of the glyoxal and OH regeneration yield from acetylene oxidation, calculated

as 0.71 through the use of the MESMER (Master Equation Solver for Multi-Energy Well Reactions) package (Glowacki et al., 2012). Although acetylene is predominantly of anthropogenic origin, the large and reasonably well established glyoxal yield does make acetylene an ideal candidate as a method of calibration for the laser-induced phosphorescence (LIP) glyoxal instrument (see Chapter 2) employed as part of the HIRAC instrumentation for selective detection of glyoxal in chamber studies, and is therefore of some relevance to this study.

1.5.2 Acetaldehyde

The oxidation of acetaldehyde in the troposphere may contribute an unlikely source of glyoxal for consideration in model simulations (see Chapter 5). Whilst acetaldehyde has not been previously reported as a significant source of glyoxal, there has recently been investigation into a link between acetaldehyde and glyoxal within the MBL (Zhu, Y. and Kieber, 2019; Walker et al., 2022), represented by Figure 1.9 in a demonstration of suggested marine sources for both compounds, including ocean-air fluxes, photolysis of dissolved organic matter (DOM) and marine biological activity such as gas release through microbial metabolic processes. Both acetaldehyde and glyoxal have been observed in measurable quantities in the MBL previously (Lary and Shallcross, 2000; Lawson et al., 2015; Carpenter and Nightingale, 2015), however, based simply on the chemistry and processes already known above the oceans, models have consistently and significantly underpredicted levels of glyoxal compared to *in situ* measurements (Lawson et al., 2015; Sinreich et al., 2010; Walker et al., 2022).

Through estimates of glyoxal and methylglyoxal production based on constrained measurements of known precursors such as isoprene at Chatham Rise and Cape Grim, Lawson et al. (2015) predict yields of glyoxal and methylglyoxal that are only 10 – 30 % of the observed concentrations detected using High Performance Liquid Chromatography (HPLC) analysis of ambient marine air samples from both sites. This presents an interesting enigma on the missing source of glyoxal in the MBL which may have wider implications for global glyoxal concentrations. One possible explanation for this, as suggested by (Lawson et al., 2015), is the direct release of biogenic emissions from biologically active oceans, though neither biological production nor consumption of glyoxal in seawater have been observed to date from any studies, as indicated in Figure

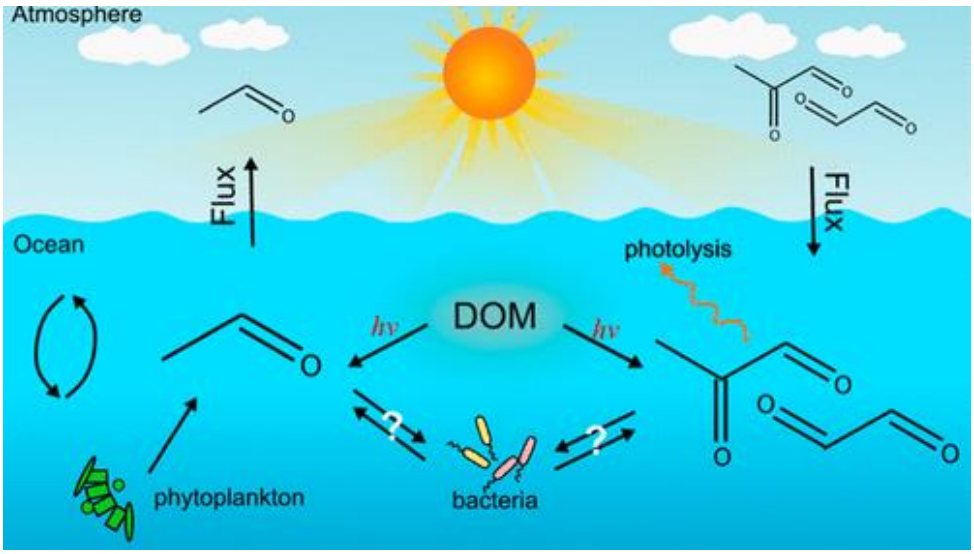

Figure 1.9 A simplified diagram showing observations and flux between ocean surface and marine air of acetaldehyde, glyoxal and methylglyoxal within the MBL. Diagram suggests a marine source of acetaldehyde in the MBL through biological activity at the surface layer of the ocean, as well as sources of both acetaldehyde and glyoxal through photolysis of dissolved organic matter (DOM) and proposed gas release from microbial metabolic processes. Taken from Zhu and Kieber (2019).

1.9 (Fu, T.-M. et al., 2008; Myriokefalitakis et al., 2008; Takeda et al., 2014; Zhu, Y. and Kieber, 2019). It is therefore likely that an alternative source of glyoxal in the MBL exists instead.

The production of glyoxal from acetaldehyde may occur through a minor channel of abstraction at the methyl group via production of the vinoxy (CH_2CHO) radical (R1.9a), either by OH or by atomic chlorine, Cl, which plays an important role in the oxidative capacity of the atmosphere in the MBL (Wingenter et al., 1996).

$$\mathbf{CH_3}CHO + X \rightarrow CH_2CHO + XH \qquad (X{=}OH/Cl;\ XH = H_2O/HCl) \qquad \text{(R1.9a)}$$

This channel purportedly accounts for a mere 5 – 7 % of total abstraction (Butkovskaya et al., 2004; Bartels et al., 1989) dependent on the radical initiator. As this is a very minor channel, detection of glyoxal and the quantification of glyoxal yields in chamber experiments are likely to be difficult.

The major product from acetaldehyde oxidation is formaldehyde, formed through abstraction at the aldehydic site (R9b), producing the acetyl peroxy ($CH_3C(O)OO$) radical.

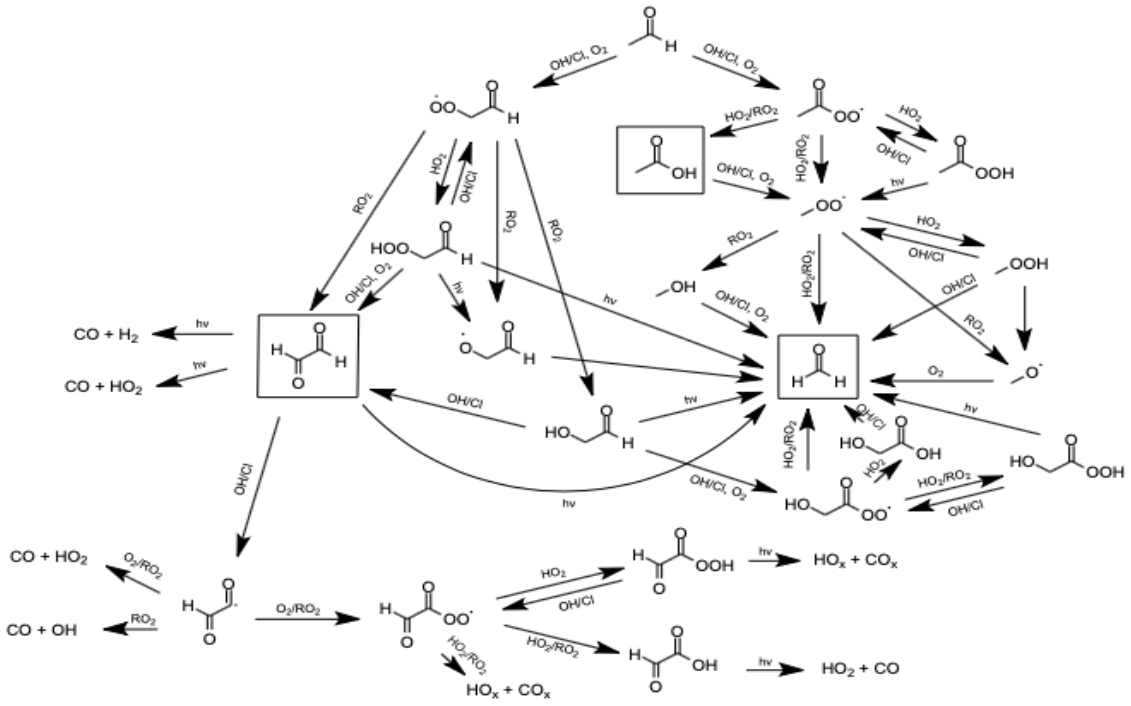

Figure 1.10 A schematic detailing the reaction mechanism listed in the MCM (Saunders *et al.*, 2003) for the OH- or Cl-initiated oxidation of acetaldehyde. Formaldehyde, acetic acid and glyoxal are outlined as products of interest in the analysis of R_{GF} and other product ratios relevant for an accurate model of acetaldehyde oxidation.

$$CH_3C\mathbf{H}O + X \rightarrow CH_3CO + XH \qquad (X{=}OH/Cl;\ XH = H_2O/HCl) \qquad \text{(R1.9b)}$$

Formaldehyde is then generated by the release of CO_2 from the acetyl alkoxy radical ($CH_3C(O)O$) in the presence of oxygen, where the resultant methoxy (CH_3O) radical can then be oxidised to formaldehyde. Growth of CO_2 during the course of a reaction in chamber experiments can be seen clearly through Fourier Transform Infrared (FTIR) spectroscopy, providing additional evidence for the proposed mechanism (Figure 1.10). However, for the purposes of R_{GF} analysis, CO_2 detection is a purely qualitative measure that will not indicate formaldehyde yields due to fluctuations in background CO_2 and alternative sources of CO_2 through VOC oxidation, therefore more direct detection techniques are preferred for formaldehyde measurement (see Chapter 7 for discussion of future work).

Another avenue of interest is a potential difference in R_{GF} in the presence of NO_x. In the remote MBL, NO_x mixing ratios are typically quite low, and alkoxy radicals are predominantly produced through either peroxy radical self-reaction (R1.10) or reaction with HO_2 (R1.11a, b).

$$RO_2 + RO_2 \rightarrow RO + RO + O_2 \quad \text{(R1.10)}$$

$$RO_2 + HO_2 \rightarrow ROOH + O_2 \quad \text{(R1.11a)}$$

$$ROOH + h\nu \rightarrow RO + OH \quad \text{(R1.11b)}$$

However, acetaldehyde is also released as a result of biomass burning (McDonald et al., 2000), and high NO_x concentrations through combustion in this environment may affect product ratios through enhancing alkoxy formation in the mechanism. This is caused by the catalytic NO_x cycling scheme detailed in section 1.2, shown again here for convenience, which rapidly converts peroxy radicals to their equivalent alkoxy species (R1.3, 1.4).

$$RO_2 + NO \rightarrow RO + NO_2 \quad \text{(R1.3)}$$

$$NO_2 + h\nu \xrightarrow{\lambda < 400\ \text{nm}} NO + O(^3P) \quad \text{(R1.4)}$$

This is true of all VOC oxidation routes, but particularly important in those that are relatively abundant in both low- and high-NO_x regions. In the specific case of acetaldehyde, formation of glyoxal from the $CHOCH_2O$ alkoxy radical through reaction with O_2 is not listed in the MCM, despite being a typical alkoxy reaction route. Enhancement of this alkoxy radical should therefore diminish glyoxal yields whilst enhancing formaldehyde yields, altering R_{GF} measurements drastically. To this end, a detailed analysis of the OH- and Cl-initiated oxidation of acetaldehyde is investigated in Chapter 5.

1.5.3 Isoprene

As isoprene is the largest contributing source of glyoxal (Fu, T.-M. et al., 2008), it seems prudent to study glyoxal yields and R_{GF} values from the OH-initiated oxidation of isoprene (see Chapter 6). Glyoxal can be produced through several routes from secondary chemistry of isoprene oxidation products (Figure 1.11), and mapping out these routes and their respective contributions to glyoxal yield, which are sensitive to temperature, HO_x (= OH and HO_2), O_3, and NO_x concentrations, is not straightforward. Previous chamber studies indicate a glyoxal yield from isoprene oxidation in high NO_x conditions between

2-3 % (Volkamer et al., 2006; Galloway et al., 2011), although the uncertainties are considerable and yields may be elevated due to a poor reflection of isoprene peroxy radical distributions in ambient conditions (Peeters et al., 2014; Li et al., 2016).

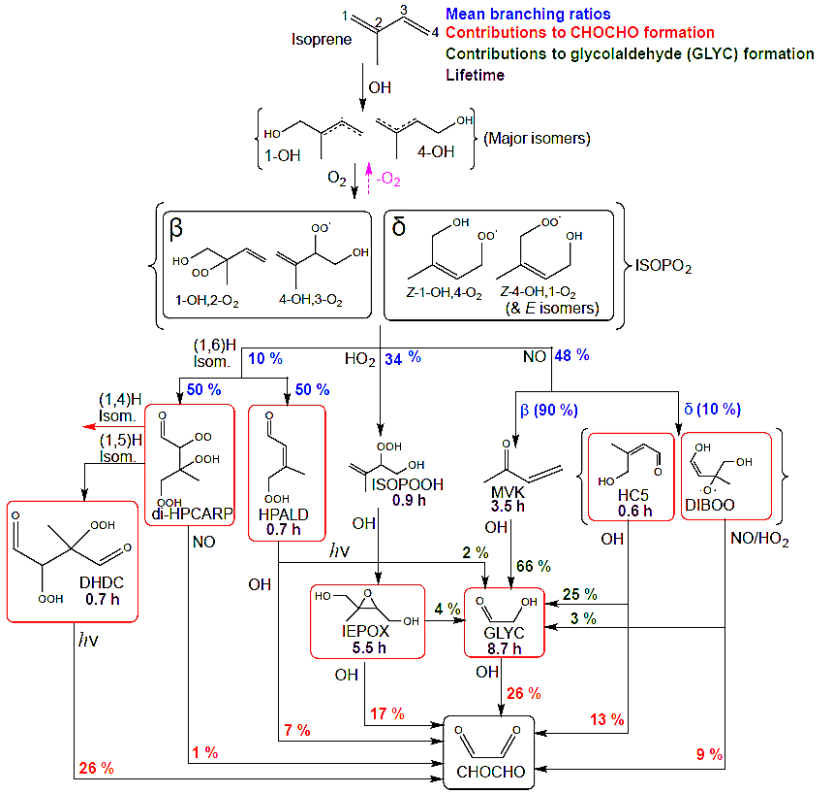

Figure 1.11 Mechanistic routes to glyoxal through the OH-initiated oxidation of isoprene as presented by the Goddard Earth Observing System chemical transport model (GEOS-Chem). Representative branching ratios, species atmospheric lifetimes, and percentage contributions to glycolaldehyde (GLYC) or glyoxal (CHOCHO) are taken from mean quantities measured over the south eastern United States during the Southeast Nexus (SENEX) campaign in the summer of 2013. Taken from Chan Miller *et al*. (2017).

The Southeast Nexus (SENEX) campaign, launched in the summer of 2013, sought to improve mechanistic understanding of the formation of glyoxal and formaldehyde from isoprene, using aircraft data taken over the southeast United States including measurements of NO_x, isoprene, monoterpenes, O_3, glyoxal and formaldehyde (Warneke et al., 2016; Li et al., 2016; Chan Miller et al., 2017). Using measured isoprene data as constraints in model comparisons of glyoxal yields, Li et al. (2016) report significant discrepancies in predicted glyoxal concentrations between the AM3ST (the standard AM3 model based on the Geophysical Fluid Dynamics chemistry-climate model), AM3B (the beta version of the AM3 model with updated isoprene chemistry), and MCMv3.3.1 models, and show a much closer agreement with observed R_{GF} values using the AM3B oxidation mechanism. In contrast, the MCMv3.3.1 model appears to underestimate the

production of glyoxal through isoprene epoxydiol (IEPOX) routes, and mechanism adjustment for modelled IEPOX chemistry in isoprene oxidation may improve predictions of R_{GF} compared with global observations. However, it should be noted that IEPOX chemistry is difficult to investigate experimentally through chamber studies, therefore did not comprise a primary aim of this work.

Whilst isoprene is a biogenic VOC and primarily considered in rural or forested regions, contributions of urban isoprene emissions to glyoxal concentrations are also relevant, both due to urban tree plants (Taha, 1996; Benjamin and Winer, 1998) and possible anthropogenic sources including vehicular emission (Christensen et al., 1999; Reimann et al., 2000; Borbon et al., 2001) and human exhalation (Kinoyama et al., 2008; Kushch et al., 2008). As the biogenic emission rate of isoprene has a strong positive dependence sunlight and temperature conditions (Guenther et al., 1991; Guenther et al., 1993), emissions will vary with geographic location and season, and anthropogenic isoprene sources can become more significant in colder or cloudier environments, particularly during winter months (Hellén et al., 2012).

Investigations are conducted with the HIRAC apparatus to establish a glyoxal yield through the OH-initiated oxidation of isoprene at room temperature and pressure (see Chapter 6). With the aid of experimental observation constraints, this study aims to reduce the disparities between measured and modelled glyoxal comparisons using the MCMv3.3.1 for isoprene atmospheric oxidation, alongside the recommended mechanism improvements previously characterised by Li et al. (2016) and Chan Miller et al. (2017) following evaluation of data from the SENEX aircraft campaign.

Chapter 2 The Highly Instrumented Reactor for Atmospheric Chemistry

2.1 Reaction Chamber

All laboratory studies and experiments throughout this project were conducted using the Highly Instrumented Reactor for Atmospheric Chemistry (HIRAC) (Glowacki et al., 2007a). The main body of the chamber consists of a stainless steel cylinder with dimensions of 2.0 m in length and 1.2 m in diameter. The corresponding volume of the cylinder is therefore approximately 2.25 m^3, with an internal wall surface area of ~9.8 m^2. Internal fittings, including the lamp tubing (see section 2.2) and mixing fans, add an extra ~3 m^2 to the surface area, and HIRAC therefore contains a surface/volume ratio of ~5.7 m^{-1}. This has implications for surface adsorption rates of species in the chamber. As the size of a chamber increases, the surface/volume ratio will decrease, and larger chambers advantageously lower surface loss rates relative to the rate of reactions under study. Whilst a decreased surface/volume ratio undoubtedly provides an environment that more closely simulates that of the open atmosphere, it also consequently induces a financial and time cost in chamber fills for each experiment. Gas quantities required are much larger, concerning both gas mixtures and the appropriate concentration of reactant species required for instrument detection. Conversely, the accelerated surface loss observed in a smaller chamber such as HIRAC can be measured and accounted for in kinetics analysis, and species more susceptible to surface adsorption can be delivered into HIRAC in higher concentrations with ease to extend the duration of oxidation reactions.

The exterior of the chamber is fitted with stainless steel square tubing welded to the sides with maximum surface contact, equipping HIRAC with the ability to adjust the internal temperature within the range of ~253 – 363 K through circulation of a thermofluid (DW-Therm) connected to a dynamic temperature control unit (Huber Unistat 690W). Both the thermofluid tubing and the chamber exterior were covered in a layer of neoprene for insulation against external room temperature. HIRAC temperature capabilities therefore cover a large proportion of the range of temperatures over the troposphere (Seakins, P.W., 2010), which typically span between ~200 – 320 K, dependent on altitude, latitude, and seasonal flux. This is an appropriate prerequisite for the needs of this study, owing to the primary interest of VOC oxidation being within the boundary layer and, with some slightly longer-lived compounds, the free troposphere. Temperatures within the boundary layer may reach as low as 240 – 250 K, excluding extreme conditions in the polar regions, where anthropogenic activity is scarce, and the emissions of VOCs are minimal. It is

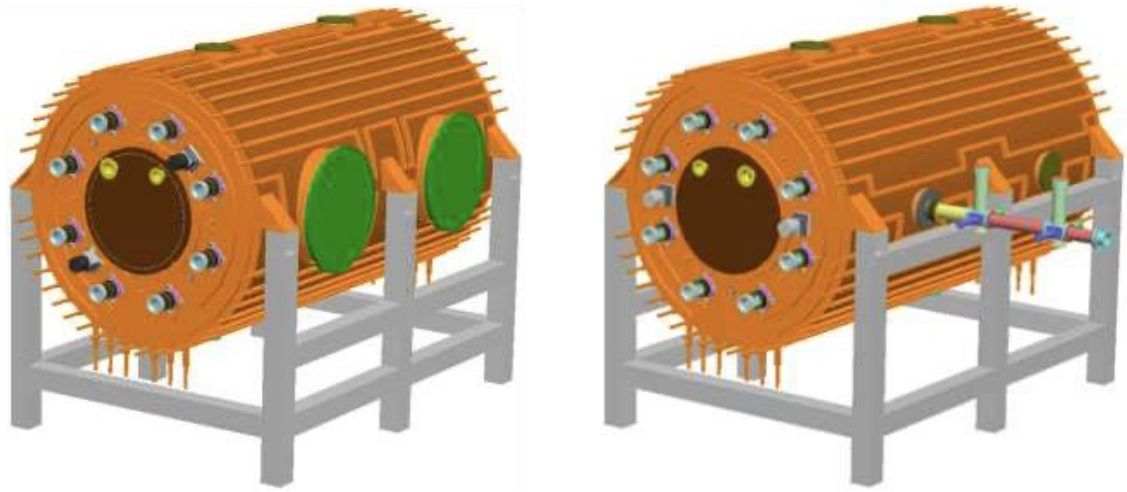

Figure 2.1 A schematic depicting the exterior of the HIRAC facility with external flange access ports to the sides, top, bottom, front, and rear; mixing fans positioned to front and rear on opposite sides of the access flanges; and quartz lamp tubing distributed evenly in a circle around the central line of the cylinder. Also depicted is the Fluorescence Assay by Gas Expansion (FAGE) OH monitoring instrument (right), attached to an ISO-K160 flange on one side of the chamber. Taken from Glowacki *et al*. (2007a).

within the capabilities of HIRAC to reproduce conditions appropriate for the purposes of this study, and experiments herein did not exceed beyond the range of 273 – 348 K.

Access ports are located all around the chamber for relative ease of attaching and exchanging instrument sampling points; gas delivery inlets; liquid injection stream; vacuum line; thermocouples; and a pressure gauge (Leybold Thermovac TTR 91) (Figure 2.1). These ports consist of four larger ISO-K500 flanges arranged with one at each end of the cylinder and two along one side of the cylinder. Six smaller ISO-K160 flanges are arranged with two ports each on the underside, ceiling, and the side of the cylinder opposite the K500 flanges. Additionally, four ISO-KF16 flanges are located on each end plate of the cylinder, allowing for further gas delivery ports, slots for pressure gauges and thermocouples, and windows for Fourier-Transform Infrared (FTIR) detection (see section 2.3.3). A powerful rotary pump (Leybold Trivac D40B) with backed roots blower (Leybold Ruvac WAU251) and charcoal catchpot trap (BOC Edwards, ITC300) is connected to HIRAC through one of the underside flanges, enabling evacuation of the chamber from atmospheric pressure to <1 mbar in ~30 minutes. HIRAC can be refilled with a bath gas of nitrogen or air in ~10 minutes at a delivery rate of ~225 slm.

Four aluminium circulation fans are positioned at either end of the cylinder to ensure efficient mixing of gases introduced into HIRAC in an even spatial distribution. Typical

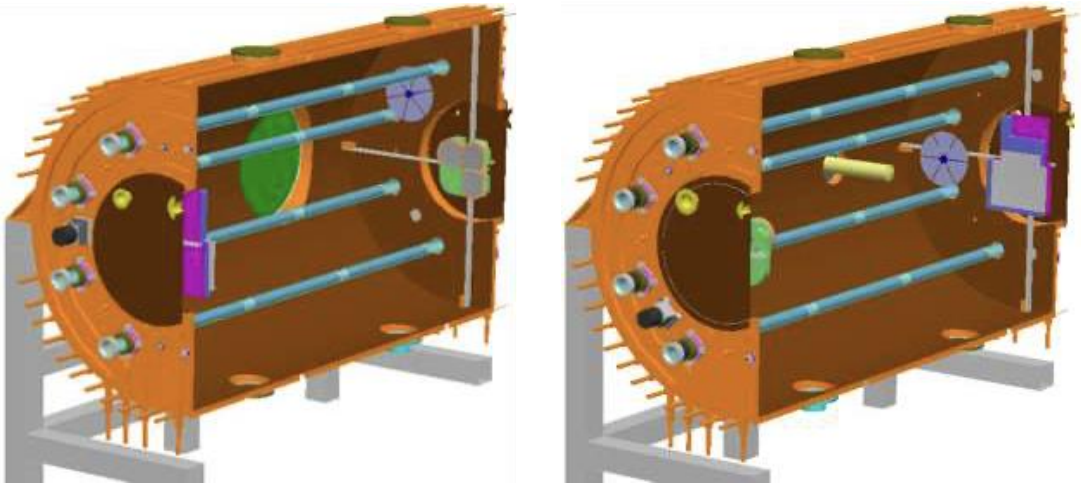

Figure 2.2 A schematic depicting the interior of the HIRAC facility, displaying the eight quartz tubes spanning the length of the chamber; two of the four fans fixed between lamp tubing at either end of the chamber; the inlet tube of the FAGE instrument sampling inside HIRAC through one of the ISO-K160 access flanges (right); and the Fourier-Transform Infrared (FTIR) reflective mirrors positioned on internal steel cross-beams away from the chamber walls. Also depicted is the vacuum line connecting one of the underside ISO-K160 ports to the rotary pump for chamber evacuation. Taken from Glowacki *et al*., (2007a).

mixing times in HIRAC are short, on a timescale of ~20 – 30 seconds, dependent on fan rotation speed, and can be observed through the stability of instrumental signal corresponding to species detection upon delivery into the chamber. The fans are attached to motors externally mounted on the two end plates of HIRAC, and rotation speed can be varied between 0 – 3000 rpm. Where current studies show a primary interest in the photooxidation of biogenic volatile organic compounds (BVOCs), the mixing time for reagents is only required to be a shorter length of time than between reactant or precursor delivery and reaction initiation through manual activation of the ultra-violet lamps (described below).

2.2 Lamps

Eight quartz tubes are situated through the inside length of the chamber in an even spatial distribution (Figure 2.2), with each containing a ~90 cm lamp mounted on a plastic collar to avoid contact with the quartz, allow air flow past the lamps to avoid ozone build-up, and allow placement of power supply wiring and thermocouples alongside the lamps within the quartz tubing. The housing of the lamps alternates between occupying the front or rear half of the chamber to achieve approximately even radiation distribution throughout. The lamps can also be exchanged selectively to generate alternative

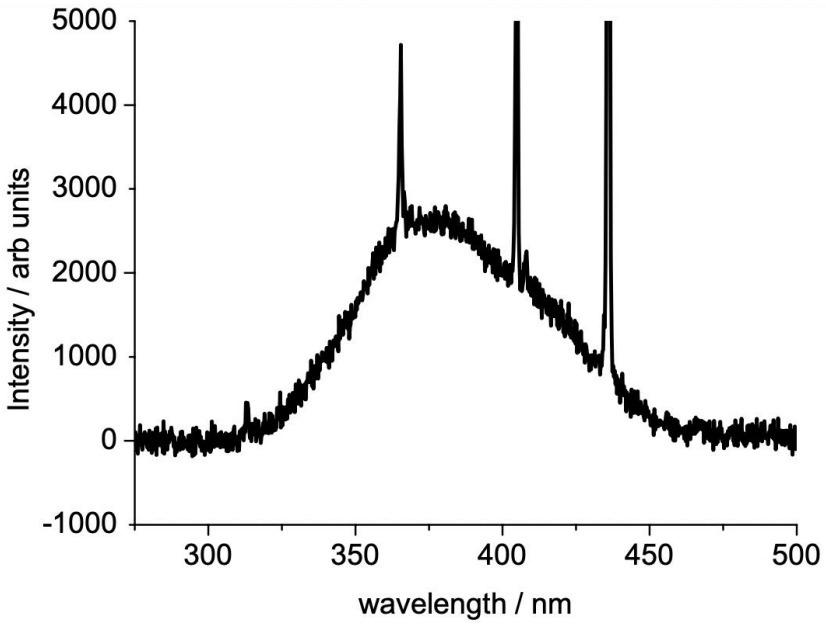

Figure 2.3 The emission spectrum for the Philips TLK40W/05 blacklamps used in HIRAC for the photolysis of molecular chlorine or nitrite (RONO) species, generating Cl and OH radicals respectively. Taken from Glowacki *et al*., (2007a).

photolysis wavelengths. The two primary lamp types used in this work were the GE Optica GE55T8/HO lamps emitting photons at 254 nm and the Philips TLK40W/05 blacklamps which have an emission spectrum with a broad peak in the range of 325 – 450 nm (Figure 2.3).

OH radicals may be generated through a variety of methods, some of which are explored in this work (see Chapter 3), however the primary methods of OH generation were through photolysis of peroxides, namely hydrogen peroxide, and ozone. Photolysis of these species was typically induced at 254 nm, towards the upper limit of hydrogen peroxide photolysis due to its absorption cross-section (Molina et al., 1977; Lin et al., 1978; Molina and Molina, 1981), using the GE Optica lamps. The absorption cross-section of ozone has a maximum ($\sigma \approx 1.2 \times 10^{-17}$ cm^2 molecule^{-1}) centred around 255 nm (Molina and Molina, 1986; Brion et al., 1993; Malicet et al., 1995), therefore photolysis at 254 nm is highly effective.

An alternative method of OH generation is through the photolysis of nitrites (RONO) at longer wavelengths. Whilst nitrites (e.g. methyl nitrite, CH_3ONO) can undergo photolysis at shorter wavelengths, the absorption cross-section allows for photolysis in the region of ~320 – 380 nm due to the presence of smaller structured absorption bands in this region (Taylor et al., 1980; Maricq and Wallington, 1992). This can be advantageous in reducing the photolysis of other species within the chamber, and therefore the Philips blacklamps

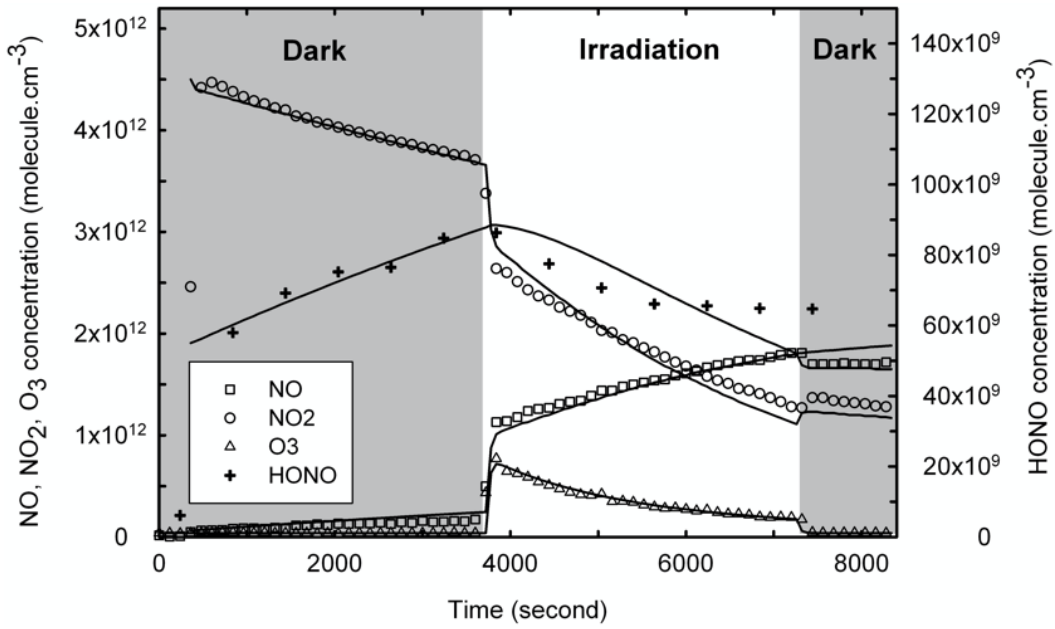

Figure 2.4 Measurements performed during an actinometry in the Experimental Multiphasic Atmospheric Simulation Chamber (CESAM) using NO_2 photolysis to determine the lamp photon flux. Species measured include NO (squares), NO_2 (circles), O_3 (triangles) and HONO (crosses). Solid lines indicate modelled concentration profiles over time alongside their respective empirical measurements. Shaded regions indicate dark periods in which chamber lamps are not activated and no photolysis is occurring. Taken from Wang *et al*., (2011).

were more appropriately used for methyl nitrite photolysis. Similarly, the absorption spectrum for molecular chlorine contains a broad band in the region of 280-400 nm (Atkinson et al., 2004; Sander et al., 2011), and consequently a much longer wavelength can likewise be used for photolysis and oxidation initiation *via* the generation of Cl atoms.

The lamp photon flux can be determined through actinometry with NO_2 photolysis, a characterisation technique employed by several other indoor simulation chambers (O'Brien, R.J., 1974; Carter et al., 1979; Doussin et al., 1997; Hynes et al., 2005; Metzger et al., 2008; Wang et al., 2011). This is achieved by monitoring NO_x and O_3 concentrations over time using commercial NO_x and O_3 analysers (see section 2.3.5) upon lamp activation (Figure 2.4), and fitting the consequent NO_2 decay to calculate a photolysis rate constant, j_{NO2}. The lamp photon flux may then be calculated using equation E2.1:

$$j_{\mathrm{NO_2}} = F_\lambda \phi_{\mathrm{NO_2},\lambda} \sigma_{\mathrm{NO_2},\lambda} \qquad \text{(E2.1)}$$

where F_λ is the photon flux of the lamps, $\phi_{NO2,\lambda}$ is the quantum yield of NO_2 photolysis, and $\sigma_{NO2,\lambda}$ is the absorption cross-section of NO_2, all dependent on wavelength. As the absorption cross-section and quantum yield are well known from previous works (Mérienne et al., 1995; Bohn et al., 2005; Hofzumahaus et al., 1999; Troe, 2000), the photon flux can be calculated as the singular remaining unknown quantity following determination of the NO_2 photolysis rate.

2.3 Instrumentation

HIRAC is equipped with a suite of instrumentation that enable detection of a range of VOCs, radicals and inorganic compounds relevant for kinetics studies within this work. The instruments employed for species detection in HIRAC here include the Fluorescence Assay by Gas Expansion (FAGE) instrument, enabling specific detection of HO_x (= OH and HO_2) through laser-induced fluorescence (section 2.3.1); a Proton Transfer Reaction-Time of Flight-Mass Spectrometer (PTR-ToF-MS), which has the capability to detect primarily unsaturated VOCs and oxygenated VOCs (OVOCs) appropriate for these studies through high resolution mass separation (section 2.3.2); the Fourier-Transform Infra-Red spectrometer (FTIR), allowing the *in situ* detection of species in the reaction chamber through their unique ro-vibrational absorption structure in the mid-infrared region (section 2.3.3); a glyoxal laser-induced phosphorescence (GLYOX-LIP) instrument designed for the specific detection of glyoxal (Section 2.3.4); and commercial NO_x and O_3 analysers for detection of NO, NO_2 and O_3 formation at ppbv mixing ratios (Section 2.3.5). These techniques were typically used simultaneously to maximise species concentration data obtained for kinetics analysis. A brief description of each instrument employed is provided below.

2.3.1 FAGE

2.3.1.1 Principles

The HO_x instrumentation design for HIRAC has been detailed elsewhere (Glowacki et al., 2007a; Malkin, 2010; Winiberg, 2014), but a brief description is provided here. The FAGE apparatus, widely used for the detection of HO_x (= OH and HO_2) (Wood and Cohen, 2006; Stone et al., 2012), utilised a laser-induced fluorescence (LIF) technique in

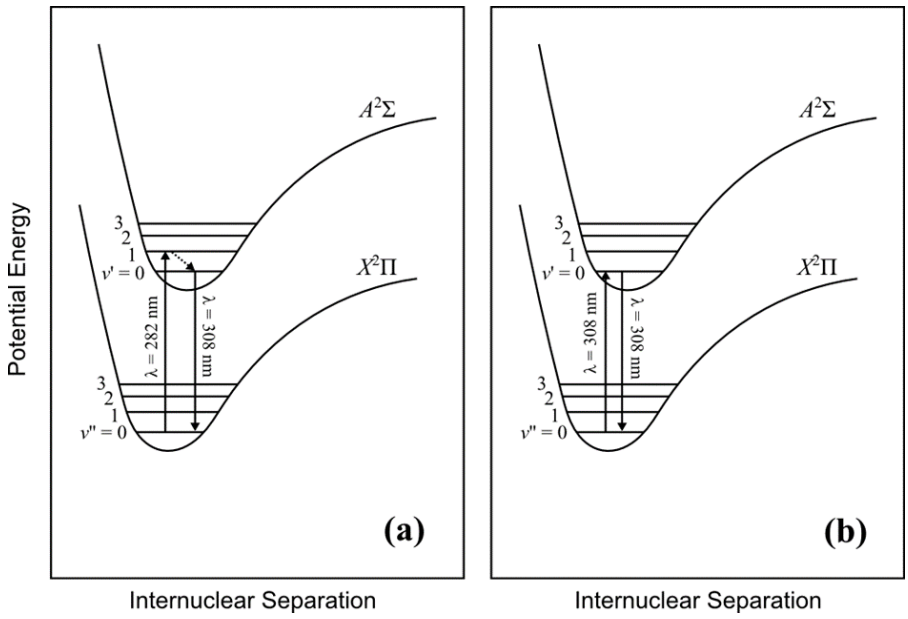

Figure 2.5 Diagrams for the energy transitions involved in the laser-induced fluorescence of OH radicals. Depicted are the transitions for (a) off-resonant fluorescence, with a laser excitation pulse at 282 nm ($A^2\Sigma^+$ ($v' = 1$) ← $X^2\Pi_i$ ($v'' = 0$)) followed by vibrational relaxation (dotted arrow) and fluorescence at 308 nm, and (b) resonant fluorescence, with a laser excitation pulse at 308 nm ($A^2\Sigma^+$ ($v' = 0$) ← $X^2\Pi_i$ ($v'' = 0$)) followed by fluorescence at 308 nm. Taken from Winiberg (2014).

which a laser pulse at 308 nm was used to electronically excite OH radicals ($A^2\Sigma^+$ ($v' = 0$) ← $X^2\Pi_i$ ($v'' = 0$), Figure 2.5b) in a low-pressure (~2 – 3 Torr) sample flow. The excited OH subsequently releases the energy through photon emission, and the resulting fluorescence is detected at the resonant wavelength of 308 nm.

Initial FAGE designs opted for an off-resonant fluorescence technique, exciting OH to a higher vibrational level with a laser pulse at 282 nm ($A^2\Sigma^+$ ($v' = 1$) ← $X^2\Pi_i$ ($v'' = 0$), Figure 2.5a) before subsequent vibrational relaxation and fluorescence observed at 308 nm (Davis et al., 1976). The off-resonant fluorescence technique was designed for negating any impacts of laser backscatter on fluorescence signal interference. However, complications arise in chamber studies, whereby 282 nm light is energetic enough to induce ozone photolysis (R2.1) and consequently produce excessive quantities of OH (R2.2).

$$O_3 + h\nu \xrightarrow{\lambda = 282\ \text{nm}} O_2 + O(^1D) \quad \text{(R2.1)}$$

$$O(^1D) + H_2O \longrightarrow OH + OH \quad \text{(R2.2)}$$

The additional fluorescence signal detected as a result of this phenomenon is unsatisfactory, and the data are therefore no longer usable (Winiberg et al., 2015).

2.3.1.2 Operation in HIRAC

To address the issue of laser backscatter interference using the resonant fluorescence technique, gated detection was employed, in which the detector was switched off for the duration of the laser pulse (~12 ns) by a delay generator and then triggered again to begin counting photons again immediately after the laser pulse expired, allowing fluorescence detection (Figure 2.6). The FAGE detection cells were evacuated down to a low pressure (~2 – 3 Torr) to reduce collisional quenching and increase the fluorescence lifetime, maximising the detected signal. Photons were detected by a Channeltron PhotoMultiplier tube (CPM) through generation of an electron pulse, and the resultant signal collected by photon counting cards (Becker and Hickl PMS-400A). The collected photon counts were deposited into 'bins' of 1 µs width for a total period of 30 µs. The 'A bin' constitutes the total photon counts during the fluorescence period immediately after the laser pulse.

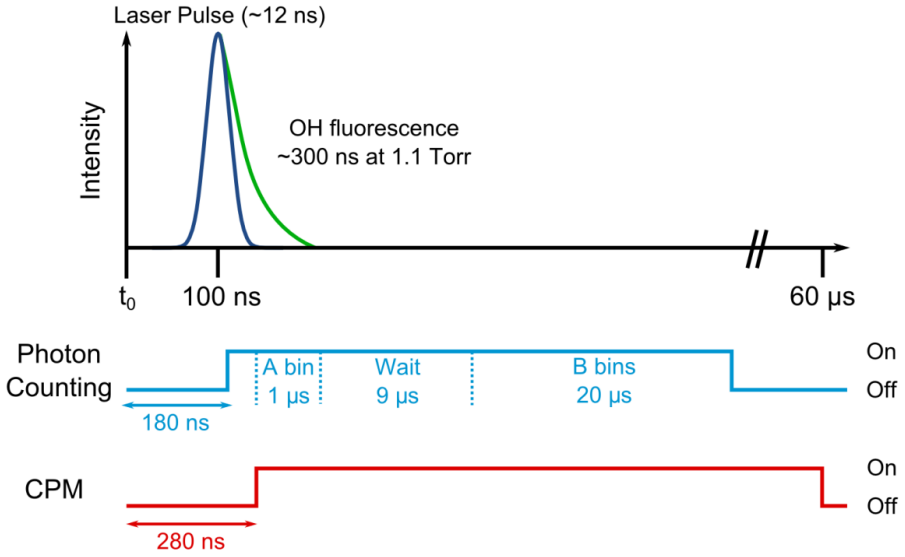

Figure 2.6 Schematic demonstrating the electronic gating system employed for fluorescence detection of OH in FAGE using a master clock to denote time t_0 as the trigger for the cycled laser pulse, Channeltron PhotoMultiplier tube (CPM) gain and photon counting card data collection. Each cycle has a duration of 60 µs. Photon counts are deposited into bins of 1 µs detection time, where the 'A bin' constitutes all photon counts including fluorescence, and the 'B bins' constitute photon counts from laser scatter, providing an averaged background subtraction signal. Schematic not to scale. Taken from Winiberg (2014).

Directly following the ‘A bin’ counts was a wait period of 9 µs, followed by collection into the ‘B bins’ for 20 µs, which constitute photon counts detected as a result of scattered light or dark counts, providing a background subtraction signal which was averaged across each ‘B bin’. The OH fluorescence signal was then calculated through equation E2.2:

$$\text{Signal} = Sig_{\text{A}} - \frac{Sig_{\text{B}}}{x} \qquad \text{(E2.2)}$$

where Sig_{A} and Sig_{B} are the cumulative photon counts in the ‘A bin’ and ‘B bins’ respectively, and x denotes the quantity of ‘B bins’, which in this case is 20. Each cycle had a total duration of 60 µs.

The FAGE apparatus designed for HIRAC (Figure 2.7) was constructed from black anodised aluminium with an internal tubing diameter of 50 mm. Gas was sampled at a rate of ~6 slm through a pinhole of 1.0 mm diameter at the end of a conical nozzle, and passed through two fluorescence detection cells prior to being evacuated by the HIRAC rotary pump (see section 2.1). The cell pressure was maintained at ~2.7 Torr during sampling. The first detection cell was positioned at a distance of ~280 mm from the inlet pinhole. Whilst a longer inlet tube inevitably increases radical losses to the FAGE interior walls between sampling and detection (Faloona et al., 2004), radical losses are also

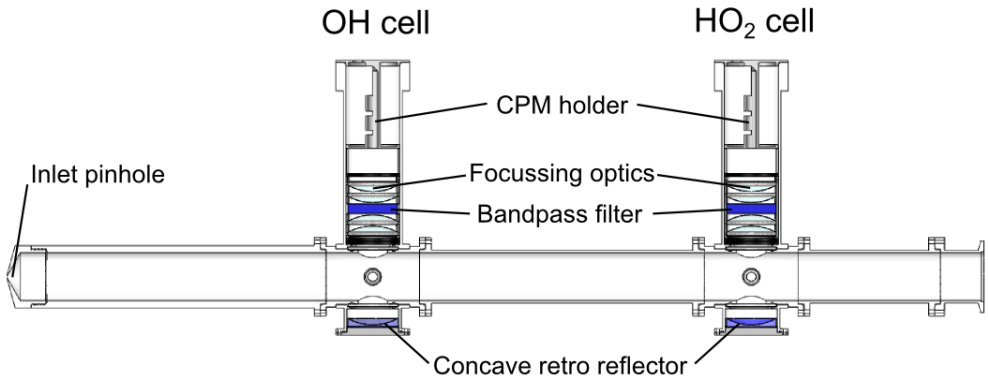

Figure 2.7 A vertical cross-section of the HIRAC FAGE apparatus demonstrating the distance between the inlet pinhole and the first (OH) fluorescence detection cell (~280 mm), and the subsequent distance to the second (HO_2) fluorescence detection cell (~300 mm). Also displayed are the optics within each cell for maximising signal gain. Taken from Winiberg (2014).

enhanced within the vicinity of the chamber walls (Malkin, 2010), therefore a longer inlet tube was utilised to balance and minimise OH losses both before and after sampling.

The second detection cell was positioned a further ~300 mm along from the first cell to allow the simultaneous indirect detection of HO_2 radicals. This involved flowing a steady continuous stream of NO injected between the OH and HO_2 detection cells to rapidly convert HO_2 into OH (Bardwell et al., 2003; Bohn and Zetzsch, 1997) and observe the resultant OH fluorescence. An appropriate distance was therefore given to allow time for reaction of NO with HO_2 (R2.3).

$$NO + HO_2 \longrightarrow NO_2 + OH \qquad \text{(R2.3)}$$

The total concentration of OH and HO_2 was then detected through LIF measurement of OH in a second chamber, and the calibrated OH signal (see Chapter 4 on instrument calibration) for the first detection cell is subtracted from the equivalent calibrated signal in the second cell to leave the remainder as signal solely attributable to HO_2. The majority of oxidation reactions in this study were performed in an air mixture, resulting in significant concentrations of HO_2. Quantifying HO_2 levels within a reaction can be an important model constraint in characterising potential branching pathways within oxidation mechanisms involving HO_2 reactions.

Laser pulses at 308 nm wavelength were passed through each detection cell *via* two distinct fibre-optic cables screwed into one end of an arm running perpendicular to the gas flow (Figure 2.8). The laser light was split between partially reflective (~85 %) beamsplitter mirrors to direct the beam into both fibre-optic cables. The laser power was monitored at the opposite end of the detection cell arms through use of a photodiode to account for laser power fluctuations in the normalisation of measured fluorescence signal. Inside the detection cells, fluorescence was detected on the vertical axis, perpendicular to both the gas flow and laser beam. The fluorescence photons passed through two collimating lenses to direct the light, then subsequently travelled through a bandpass filter centred around 308.75 nm with a 5.0 nm bandwidth for selective wavelength detection. Two focusing lenses were used to refocus the photons back onto the CPM where the electrical signal generated could be multiplied, ready for collection by a photon counting card. A concave retroreflector was installed on the underside of the detection cell to increase the collected fluorescence signal by twofold.

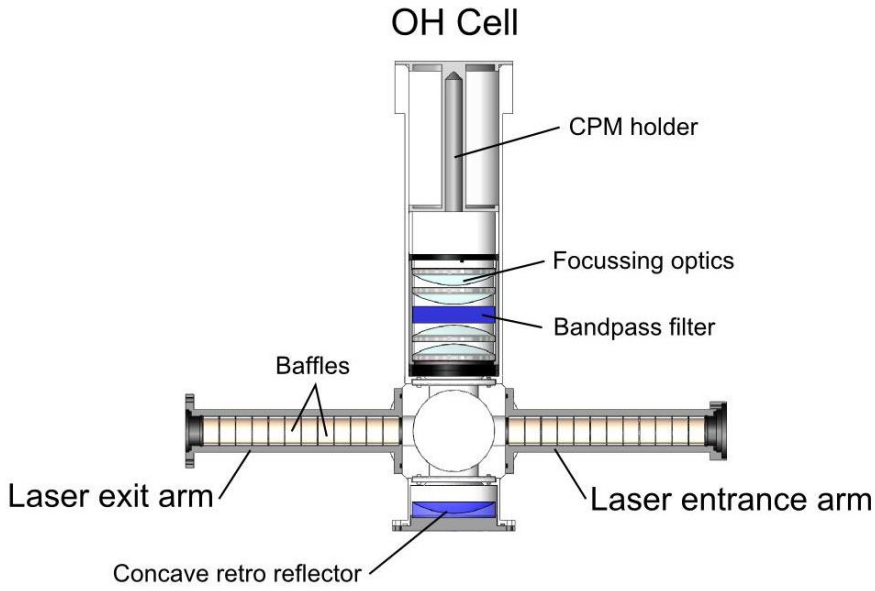

Figure 2.8 A vertical cross-section of one of the fluorescence detection cells in the HIRAC FAGE apparatus, displaying the optics and laser pathway within each cell. The laser beam passes through the detection cell perpendicular to both the gas flow and detection axis, and laser power fluctuations are monitored at the exit arm by a photodiode. Fluorescence photons are passed through two collimating lenses, a bandpass filter centred at 308.75 nm with a 5.0 nm bandwidth, and two focusing lenses before the signal is detected by the CPM. A concave retro reflector on the underside of the detection cell increases the detected fluorescence signal by twofold. Taken from Winiberg (2014).

The laser light was generated using a Q-switched Nd:YAG (neodymium-doped yttrium aluminium garnet) diode pumped laser (JDSU Q201-HD) at 1064 nm with 5 kHz pulse repetition frequency (PRF). The beam was passed through a frequency doubling crystal (lithium triborate) to achieve a wavelength of 532 nm. The 532 nm beam then pumped a tunable dye laser (SIRAH Lasertechnik CobraStretch) with a dye mixture of 0.2 g L^{-1} Rhodamine B and 0.05 g L^{-1} Rhodamine 101 in methanol to generate red-shifted light centred around a maxima at ~616 nm. The 616 nm beam was passed through a second frequency doubling crystal (potassium dihydrogen phosphate) to generate light at 308 nm wavelength. The laser light was further fine-tuned to within 98 % of the absorption maxima for the OH $Q_1(2)$ rotational transition line by splitting some of the laser light off into a reference cell. OH radicals were produced in the reference cell at low pressure (<4 mbar) with a hot wire filament in air saturated with water vapour through use of a water bubbler. Fluorescence in the reference cell was detected over wavelength range (~0.050 nm) around the OH $Q_1(2)$ line with a wavelength resolution of 0.001 nm to determine the optimum wavelength for maximum fluorescence signal.

2.3.1.3 Calibration

Fluorescence spectroscopy is not an absolute detection technique, with observed fluorescence signal being dependent on a number of factors including the laser power, electronic gating time, fluorescence quantum yield, and fluorescence quenching. Instrument calibration is therefore required to convert observed signal into concentrations of OH and HO_2. Two methods of FAGE calibration used in HIRAC are discussed and compared in detail in Chapter 4.

2.3.2 PTR-ToF-MS

Specifications and hardware for the Kore Series 1 custom PTR-ToF-MS instrument used in the context of HIRAC oxidation experiments for this work have been listed elsewhere (KoreTechnology, 2015) and described previously (Speak, 2019). Therefore primarily the general principles of PTR-ToF-MS (shortened to PTR-MS) operation are discussed here.

2.3.2.1 Principles

PTR-MS is a useful ion detection tool for differentiating species by mass within a gas sample. There are several methods of species ionisation available, however the PTR-MS opts for chemical ionisation primarily through proton transfer from the hydronium ion, H_3O^+, to a species, R, in the sample flow (R2.4):

$$R + H_3O^+ \rightleftharpoons RH^+ + H_2O \qquad \text{(R2.4)}$$

Protonation increases the mass of an ion by ~1 atomic mass unit, and species are therefore typically detected with a mass-to-charge ratio of m/z = n + 1, where n is the parent molecular mass of the detected species (g mol^{-1}). There is an advantage to be had in hydronium protonation being a comparatively 'soft' form of ionisation, that is, ion fragmentation reduced upon impact with the sample species. In contrast, techniques such as electron ionisation and electrospray ionisation cause significant amounts of fragmentation which, in the detection of a mixture of species present within chamber oxidation reactions, is an undesirable outcome due to the complexity of the resultant mass spectra.

However, protonation ionisation has considerable dependence on the proton affinity of a species. If the proton affinity for a species within the gas sample is considerably lower than that of water (686 ± 17 kJ mol^{-1} (Long and Munson, 1970)), the equilibrium for R2.4 will lie too far to the left hand side, and the species becomes undetectable due to a lack of ionisation. Conversely, proton affinities considerably higher than that of water demonstrate an appropriate detection sensitivity for monitoring *via* PTR-MS. Where the proton affinities for water and the target species are similar in value, the equilibrium position, and hence ionisation efficiency, is more dependent on their relative concentrations instead. This is accentuated by the increased humidity at higher water concentrations leading to clustering into dimer and trimer forms. The proton affinity for water dimer has been determined to be significantly higher (808 ± 6 kJ mol^{-1}) than that of the monomer (Goebbert and Wenthold, 2004), and higher cluster forms, such as trimers, tetramers, etc., serve to increase the proton affinity even further (Cheng, H.-P., 1998; Kawai et al., 2003; Wròblewski et al., 2004). Any ionisation of VOCs occurring *via* reaction with protonated water clusters (R2.5) will therefore inevitably be less effective the larger the oligomer.

$$R + (H_2O)_nH_3O^+ \rightleftharpoons RH^+ + (H_2O)_{n+1} \quad \text{(R2.5)}$$

2.3.2.2 Operation in HIRAC

The PTR-MS contained a water reservoir maintained at approximately two thirds full with deionised water (Thermo Fisher, HPLC Grade) surrounded by an aluminium heating jacket. The reservoir was maintained at 308.0 ± 0.2 K, monitored using a K-type thermocouple, to avoid pressure fluctuations due to changes in ambient temperature. The tubing and water vapour valves were threaded with heated wiring to maintain the temperature of the valves and pipework above that of the reservoir, preventing condensation of water vapour which would block the valves. The PTR-MS was equipped with a water adjust valve for fine control over the humidity, and consequently the ratio of water monomer to dimer, in the reagent gas flow line. Once an optimum position on the water adjust valve was chosen, the position remained unchanged for the duration of a series of experiments to ensure the consistency of acquired data.

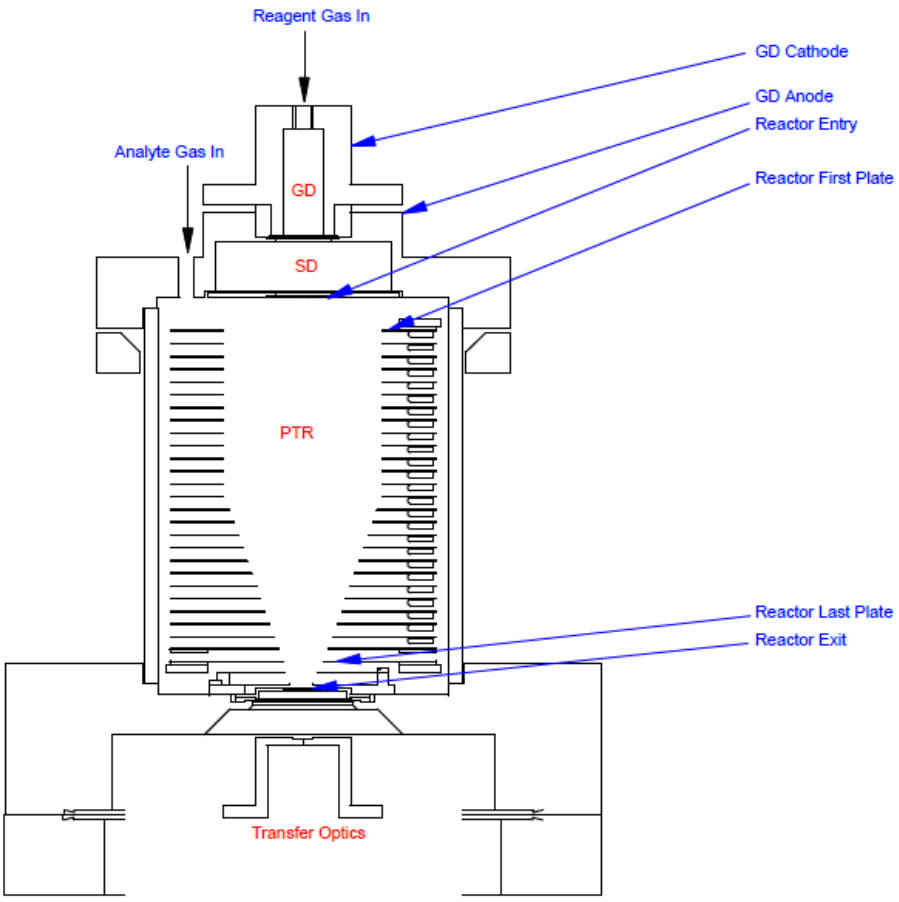

Figure 2.9 A schematic of the hardware contained within the PTR-MS reactor oven. Depicted is the flow of the reagent gas through the glow discharge (GD) source and the source drift (SD) region before merging with the analyte gas flow in the proton transfer reactor cell (PTR) and finally reaching the transfer optics at the end of the cell. Taken from the Kore PTR-ToF-MS hardware reference manual (KoreTechnology (2015)).

Water vapour was then introduced into a hollow cathode glow discharge (GD) region (Figure 2.9), contained within an insulated oven maintained at a higher temperature of 378.0 ± 0.5 K, to be ionised into a beam of H_3O^+ ions. The GD source was typically operated at an internal pressure of 1.80 ± 0.02 mbar and a voltage of 400 ± 2 V. The H_3O^+ ion beam was passed through a source drift (SD) region to remove unwanted ions (e.g. O^+, H^+, N^+, etc.) by transferring charge to remaining H_2O molecules through subsequent collision after the GD source, purifying the resulting H_3O^+ ion beam to ~99.5 %. Following purification in the source drift region, the ion beam was then introduced to the proton transfer reactor (PTR) cell, where collisions with species in the analyte gas flow occur to ionise affinitive species through protonation. The resultant ions were propelled towards the reactor exit through a series of electrostatic plates that provided a voltage gradient, alongside a radio frequency ion funnel generated by internally mounted

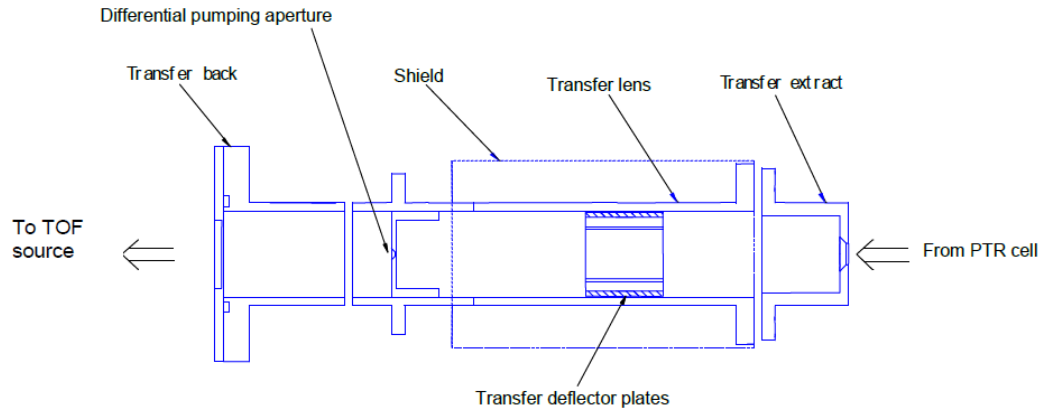

Figure 2.10 The transfer optics at the end of the proton transfer reactor cell designed to focus the analyte ions onto the ToF source. Ions are passed through a transfer lens and deflector plates to direct the ions towards the exit, and then pass through two pumping apertures to reduce the pressure sequentially down from reactor pressure (~1.8 mbar) to an intermediate vacuum system (~10^{-4} mbar), and finally down to a high vacuum system (~10^{-7} mbar) in the ToF source. Taken from the Kore PTR-ToF-MS hardware reference manual (KoreTechnology (2015)).

electronics designed to minimise the loss of ions hitting the detector due to pressure gradient gas expansion. At the end of the reactor cell, the analyte ions were passed through the transfer optics (Figure 2.10) to focus the ions through the exit towards the ToF source. The transfer optics were operated at an intermediate vacuum (~10^{-4} mbar) by pumping through a 1 mm aperture, and included a transfer lens and deflector plates to direct the ions and discriminate against neutral species in the ion beam. The ions were directed through a second slit aperture (~1×4 mm) to achieve a high vacuum system in the ToF source (~10^{-7} mbar).

Upon entry into the ToF source, the analyte ions were pulsed in a direction perpendicular to the flow of the ion beam from the transfer optics (Figure 2.11). The ToF source consists of a backplate, a pulsed extraction plate, an intermediate electrode, and a final acceleration electrode, where the flight energy of the ions was achieved. Each pulse dictated the start of the flight time for the analyte ions. Beyond the acceleration electrode, the ions passed through X and Y deflector plates consisting each of a fixed-voltage and variable voltage plate. The voltage in the variable plates for the X and Y deflectors can be adjusted to optimise the flight path towards the detector. The ions traversed a field-free region (FFR), where they were free of any external electromagnetic fields, before being reflected back onto the detector by a reflectron with a tuneable central electrode.

The ions were detected by a dual microchannel-plate detector (MCP) with a large active area (25 mm) diameter which gives a high sensitivity and good time resolution. Each ion impact generated an electron emission which was amplified with an excitation voltage to

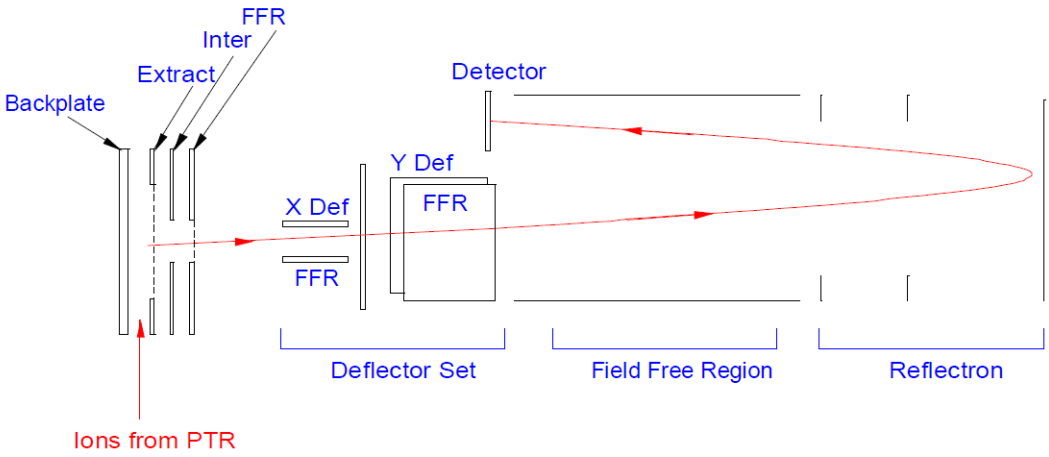

Figure 2.11 A schematic of the time-of-flight (ToF) source depicting the flight path of the ions upon exiting the proton transfer reactor (PTR) through the transfer optics. Ions are pulsed perpendicular to the flow from the PTR through a series of plates including a backplate, pulsed extraction plate, intermediate electrode, and acceleration electrode. Ions are then directed through X and Y deflectors, and fly through a field-free region (FFR) before being reflected back through the FFR and onto the detector by the reflectron. Taken from the Kore PTR-ToF-MS hardware reference manual (KoreTechnology (2015)).

produce a detectable electrical signal corresponding to an ion count. The signal was accumulated over a series of pulses, where the typical ToF cycle was 40 µs, and each spectrum displayed the cumulative signal from a set experiment time. For most experiments within this study, the experiment time was set to 9 s, and spectra were recorded every 10 s. The time-of-flight is directly proportional to the square root of the ion mass, and the ToF data were therefore converted into ion masses using equation E2.3:

$$m = \left(\frac{t - t_0}{Cb}\right)^2 \qquad \text{(E2.3)}$$

where m is the ion mass, t is the time-of-flight, t_0 is the initial pulse time, and Cb is the linear calibration gradient for mass-time conversion. Both t_0 and Cb parameters are calculated from the arrival times of known peaks (e.g. H_3O^+ and $(H_2O)H_3O^+$), and can be determined using the calibration software supplied by KoreTechnology. Kore software also provided the ability to select a 'region of interest' within a mass spectrum, where the integrated signal count between two selected masses could be traced over time by monitoring an individual peak area across mass spectra during oxidation reactions. Unless the CPM becomes oversaturated at high concentrations, the peak area is linearly proportional to species concentration, and this method was used to trace the concentration

of reactants from a known initial concentration and, where previously calibrated, the concentration of oxidation products generated upon reaction initiation.

A final note added that due to instrumental bulk, the PTR-MS was positioned in an adjacent room a short distance from the simulation chamber. It was considered that the analyte gas was sampled from HIRAC through a length (~8 m) of PTFE tubing (1/8") at a sample rate of ~0.2 slm. Despite the long sampling distance, at this flow rate it took ~19 s for the analyte gas to reach the PTR cell. This slight time difference was accounted for when comparing timestamped data from different sampling instruments connected to HIRAC. However, the longer sampling distance, whilst unavoidable, may also reduce the sensitivity for certain species that are more prone to surface adsorption. Sufficiently high initial concentrations (~10^{13} – 10^{14} molecule cm^{-3}) were delivered into HIRAC in an attempt to overcome this issue.

2.3.2.3 Calibration

The PTR-MS was typically calibrated for individual species concentrations by delivering a known concentration of the species into HIRAC for instrument sampling. The observed integrated peak counts, taking the parent ion *m*/*z* peak unless stated otherwise, were averaged over a time period of ~5 – 10 minutes, with data points taken every 10 s, and the standard deviation of the measured counts calculated over the time period at each concentration. Concentrations were diluted by repeatedly evacuating the chamber to a fraction of the total pressure (e.g. 70 %), then refilling the chamber to atmospheric pressure with bath gas. Averaged counts were taken at each concentration, and the observed signal was plotted against the known concentrations to ascertain the linear proportionality of signal to concentration achieve a calibration factor specific to that species.

2.3.3 FTIR Spectrometer and Optics

HIRAC incorporates an FTIR system comprised of a Bruker IFS 66/S spectrometer, several optics mirrors contained within a box flushed with nitrogen, and a multipass instalment of two field mirrors and three objective mirrors inside the chamber. More detailed descriptions of this instrumentation are found elsewhere (Glowacki et al., 2007a; Glowacki et al., 2007b), but the basic workings will be described here.

2.3.3.1 Principles and Operation

The Bruker IFS 66/S spectrometer comes equipped with a glowbar mid-infrared (MIR) light source which was passed through a rotatable aperture wheel selected at a 2.5 mm aperture. The light beam was then introduced into a Michelson interferometer using a KBr beamsplitter to direct the light between a fixed mirror and a movable mirror. The light was reflected back towards the beamsplitter from both mirrors, and the resultant wave interference resulted in a selected wavelength beam scan exiting the interferometer. The distance of the movable mirror from the beamsplitter was then adjusted through motorised control to alter the wave interference and the consequent wavelength output. This procedure was repeated over a number of scans (typically ~60 – 100) to achieve a full wavelength output (700 – 4000 cm^{-1}) for each spectrum, with a spectral resolution of ~0.48 cm^{-1}.

Upon exiting the interferometer, the beam passed through a nitrogen-flushed box *via* a series of transfer optics mirrors (Figure 2.12). The beam was reflected first off two plane mirrors (P1 & P2) with 75 mm diameter and ~7.5 mm thickness, and then reflected towards the chamber multipass system *via* a concave mirror (S1) with 101.6 mm diameter, ~7.5 mm centre thickness, and 2400 ± 12 mm radius of curvature (ROC). After leaving the multipass system, the beam path was reversed, reflected first off a second concave mirror with equivalent dimensions, then off a final two planar mirrors before

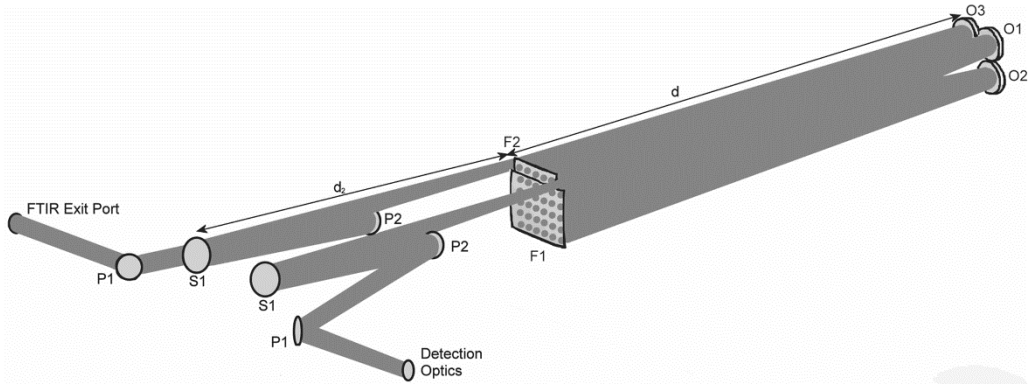

Figure 2.12 A schematic of the FTIR optics and beam path from the infrared spectrometer exit port to the detection optics. The beam is reflected off two planar mirrors (P1 & P2) and a concave mirror (S1) with 2400 ± 12 mm radius of curvature before passing through a multipass system inside HIRAC. The multipass system includes three objective mirrors (O1, O2 & O3) and two field mirrors (F1 & F2), and typically achieves 72 passes inside HIRAC to extend the path length and increase detection sensitivity. The beam path is reversed upon exiting HIRAC to reflect first off a concave mirror and then off the two planar mirrors before hitting the detection optics. Taken from Glowacki *et al*. (2007a).

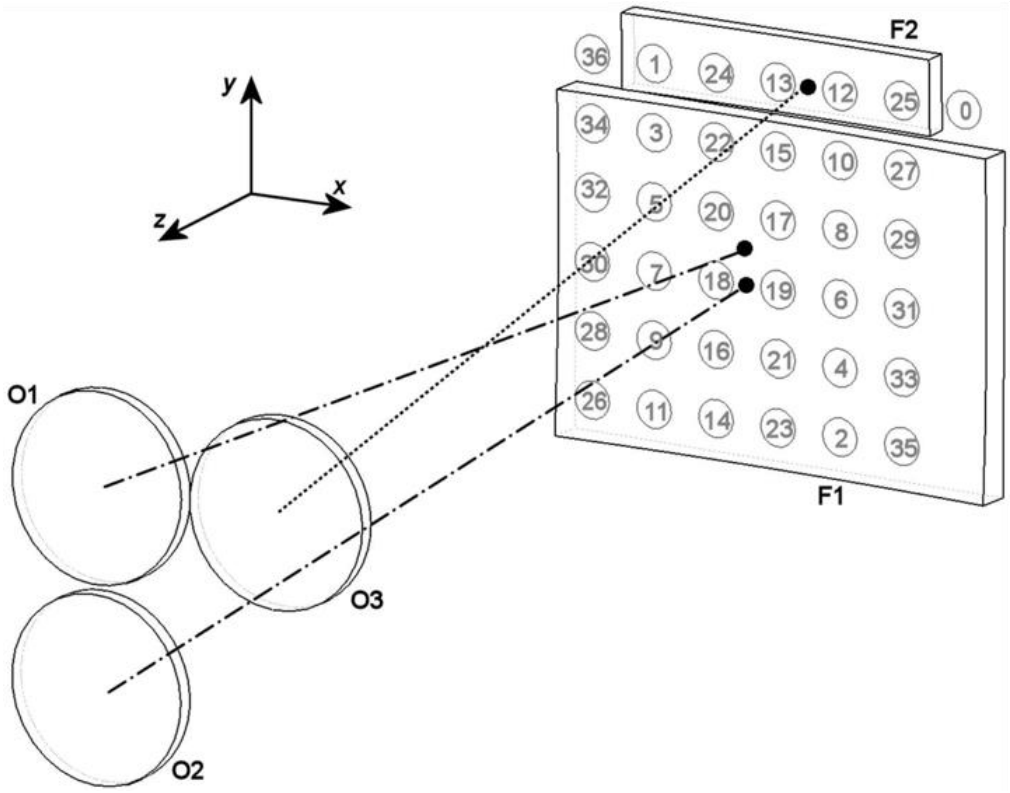

Figure 2.13 A schematic of the beam path between the field and objective FTIR mirrors within HIRAC. The beam enters HIRAC at position 0 and traces the path shown in numerical order from 1 to 35 on the field mirrors (F1 & F2) to create a matrix of images before exiting HIRAC at position 36. A total of 72 passes are therefore attained, with a resultant path length of ~128.5 m. Taken from Glowacki *et al*., (2007a).

hitting a mercury-cadmium-telluride (MCT) detector with a sufficient measurement range of 12,000 – 600 cm^{-1}. The beam entered and exited HIRAC through two windows (8.7 millirad wedged, KBr, 75 mm diameter, 5 mm thick) inserted in one of the end K500 flanges.

Once inside the chamber, the beam entered a multipass matrix system (MMS), reflecting back and forth between three objective mirrors (O1, O2 & O3), with equivalent dimensions of 100 mm diameter and ~7.5 mm centre thickness, and two field mirrors (F1 & F2) displaying a matrix of light images (Figure 2.13). The larger F1 mirror had dimensions of 180×255 mm with ~12 mm centre thickness, and the smaller F2 mirror had dimensions of 45×180 mm with ~9 mm centre thickness. All field and objective mirrors were designed with an ROC of 1785 ± 1 mm to match the length of a single beam pass in HIRAC. Rather than being attached to the end flanges themselves, the interior mirrors were instead mounted on aluminium cross beams positioned 10 mm away from either end of the chamber on the cylindrical frame itself. This was intended to prevent misalignment

of the mirrors due to minor yet non-negligible bow of the flanges as a result of pressure variations during experiments. Consequently, removal and alignment of the objective mirrors was also easier due to the flexibility in removing the K500 flange on the objective end to access the rear screw adjustment panel.

The MMS takes advantage of increasing the path length of light within HIRAC to lower the limit of detection down to ppbv mixing ratios. This relationship has been described by the Beer-Lambert law, denoted in equation E2.4:

$$\ln \frac{I_0}{I} = \sigma c l \qquad \text{(E2.4)}$$

where $\ln(I_0/I)$ is the species absorbance, σ is the species absorption cross-section, c is the species concentration, and l is the path length of light. The multipass system was achieved more easily through the ROC of the field mirrors optimised to the length of one pass (~1.785 m), and 72 passes are typically attained (36 in each direction) before exiting the chamber, so as to achieve a total path length in the chamber of ~128.5 m. Where the absorption cross-section of a species shows distinctive characteristic peaks, measured spectra provide a good metric for measuring the concentrations of reactants and products formed over time during oxidation, with a detection limit of ~10 – 100 ppbv dependent on the species.

2.3.3.2 Calibration

Calibration of species for the FTIR system involved measuring the absorption spectrum of a known concentration of species into HIRAC which could then be used as a reference spectrum to be fitted against more complex spectra recorded during oxidation reactions. As the Beer-Lambert law is an absolute method for determining the concentration, measurement of reference spectra served primarily to confirm the path length of light inside the MMS with the current optics alignment. Reference spectra were used as a normalisation factor for calculating species concentrations based on the ratio of fitted spectra peak areas to reference spectra peak areas with a known concentration.

2.3.4 GLYOX-LIP

Laser-induced phosphorescence (LIP) has been employed as a selective detection technique for glyoxal over the last 15 years with increasing success through improved detection limits (Huisman et al., 2008; Huisman et al., 2011; DiGangi et al., 2012; Ahlm et al., 2012; Pusede et al., 2014; Walker et al., 2022). The GLYOX-LIP instrument used in this work has been described recently for use in field measurements of glyoxal (Walker et al., 2022), and a brief description of the instrument setup and principles of LIP will therefore be given here.

2.3.4.1 Principles

Glyoxal LIP detection involves the precise electronic excitation of glyoxal molecules at λ = 440.141 nm (Figure 2.14), involving the ^1A_u ($\nu'_8 = 1$) ← ^1A_g ($\nu''_0 = 0$) transition ($S_1 \leftarrow S_0$) corresponding to the ground (S_0) and first excited (S_1) singlet states. The excited glyoxal molecule then undergoes inter-system crossing (ISC) to the first excited triplet state, T_1 (^3A_u), where any occupied excited vibrational levels subsequently relax down to the T_1 vibrational ground ($\nu' = 0$) level (Anderson et al., 1973). Radiative relaxation back

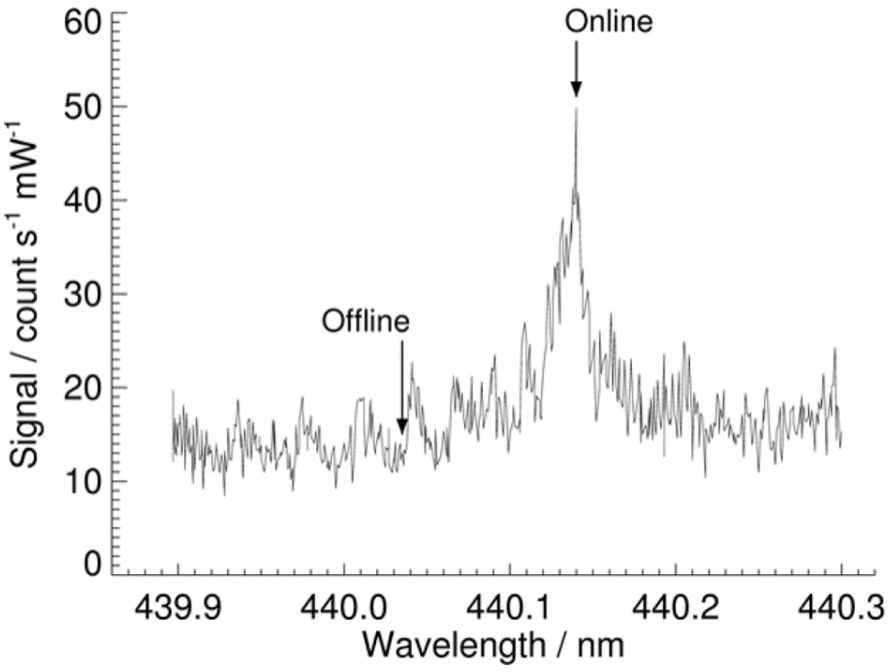

Figure 2.14 The fine-structure laser-induced phosphorescence spectrum of glyoxal centred around the optimal wavelength for electronic excitation at λ = 440.141 nm, with the offline wavelength also displayed (λ = 440.034 nm). The spectrum was measured with a wavelength resolution of 0.0008 nm. Taken from Walker *et al.* (2022).

down to the singlet S_0 state then involves phosphorescence, which can be observed most intensely through the ^3A_u ($\nu'_8 = 0$) $\rightarrow$ ^1A_g ($\nu''_0 = 0$) transition corresponding to phosphorescence wavelength λ = 520.8 nm (Holzer and Ramsay, 1970). Glyoxal phosphorescence signal was therefore detected around 520 nm to increase the instrument sensitivity.

2.3.4.2 Operation in HIRAC

Laser light was generated by a diode-pumped Nd:YAG laser (Photonics Industries DS-532-10), which was used to pump a Ti:Sapphire laser (Photonics Industries TU-UV-308) tunable between $\lambda \approx 700 – 960$ nm. The wavelength was tuned to λ = 880 nm by adjusting the angle of a diffraction grating inside the Ti:Sapphire cavity through motorised rotation of the grating. Upon exiting the cavity, the infrared beam was passed through a lithium borate frequency doubling crystal to produce 440 nm blue light, which was then introduced into the phosphorescence detection cell through an adjustable iris to focus the beam and reduce laser scatter inside the cell (Figure 2.15). A small percentage of the blue laser light was directed towards a wavemeter (Coherent WaveMaster) with a wavelength resolution of ± 0.001 nm to precisely tune the wavelength to online (λ = 440.141 nm) and offline (λ = 440.034 nm) wavelengths, as well as to monitor the wavelength for the duration of any online measurements.

As with the FAGE apparatus (section 2.3.1), the phosphorescence detection cell cylinder (50 mm internal diameter) and arms (each 210 mm length) for entrance and exit of the laser light were constructed from black anodised aluminium. Laser light was introduced

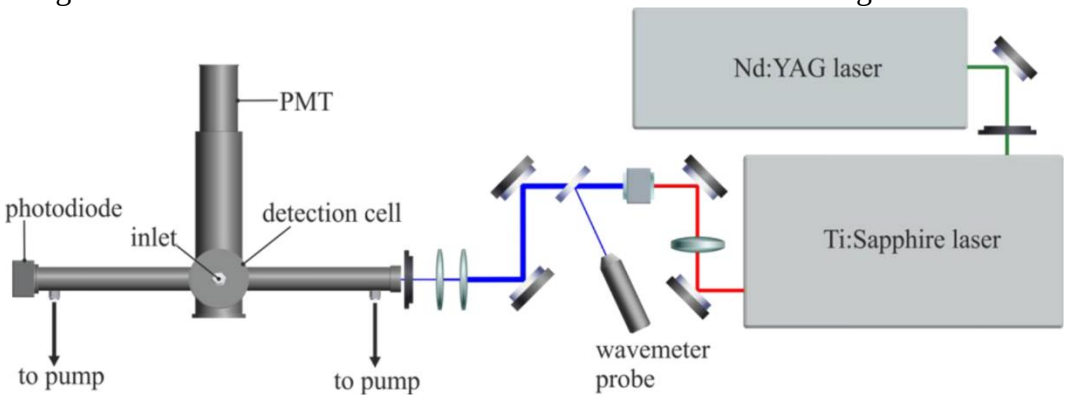

Figure 2.15 A schematic of the GLYOX-LIP instrument setup as shown from above. Depicted is the laser system including 532 nm green light produced by the diode-pumped Nd:YAG laser, 880 nm infrared light produced by the tunable Ti:Sapphire laser, and the frequency-doubled 440 nm blue light after passing through the lithium borate doubling crystal. Also shown is a schematic of the phosphorescence detection cell, where the sample flow through the inlet is on the plane directed out of the page, however the detection optics prior to the photomultiplying tube (PMT) are excluded. Taken from Walker *et al*. (2022).

at the entrance arm through an iris and fluctuations in laser power were measured by positioning a photodiode over the window at the end of the exit arm to account for laser power normalisation of phosphorescence signal. Gas was sampled from HIRAC into the detection cell perpendicular to the direction of the laser beam through a length (~4 m) of PTFE tubing (1/4") connected above the cell and drawn through by a dry scroll pump (Agilent IDP-3). The sample flow rate was controlled to ~5 L min^{-1} by a quarter-turn plug valve inserted into the vacuum line so that an internal cell pressure of ~100 Torr was achieved to optimise phosphorescence signal where a broad maximum has been previously observed in air as a result of variations in phosphorescence quenching (Walker et al., 2022).

The detection optics were similar to those described for the FAGE apparatus (section 2.3.1). Photons were detected perpendicular to both the gas flow and laser beam directions, passed first through a bandpass filter centred around 520 nm (Semrock FF02-520/28, ± 14 nm bandwidth) and subsequently through two focusing lenses before detection *via* a photomultiplier tube (PMT). A retroreflector was also installed on the opposite side of the phosphorescence cell to maximise photon detection. A photon counting card (Becker and Hickl, PMS 400) was used to receive the electronic signal from the PMT.

Phosphorescence signal was collected using a delay generator (Berkeley Nucleonics Corporation, Model 555) to trigger the laser pulse and collection bin windows to differentiate phosphorescence from background signal (Figure 2.16). After the cycle had been triggered by the delay generator, the Ti:Sapphire laser pulse (35 ns) occurred 5 μs later, and a further delay of 3 μs was given to allow for the decay of any short-lived fluorescence in the system from the cell walls or any species in the sample flow. As phosphorescence decay occurs on a much longer timescale, a collection bin of 35 μs was used to obtain any phosphorescence signal after complete fluorescence decay. Phosphorescence detection was then followed by a delay of 50 μs and subsequently a collection bin of 105 μs to determine any background counts. The total trigger cycle time spanned ~200 μs, and the laser was pulsed with a 5 kHz PRF, integrating the signal from each pulse over a 1 s time period to acquire the data points. The background-subtracted phosphorescence signal could then be calculated as in equation E2.2 (see section 2.3.1), where the number of B bins in this instance was 3. The resultant background-subtracted signal is linearly proportional to the concentration of glyoxal in the system, however calibration is required to determine the conversion of signal to concentration. Details of the GLYOX-LIP instrument calibration are discussed in Chapter 5.

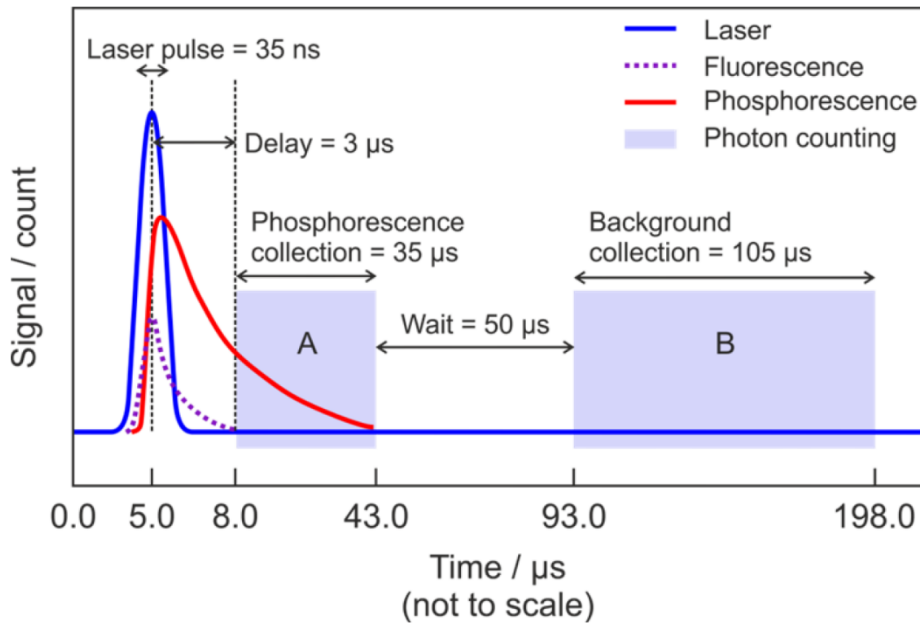

Figure 2.16 A diagram of the trigger cycle for data acquisition of phosphorescence signal controlled by a delay generator. The Ti:Sapphire laser pulse (blue) is triggered 5 µs after the cycle start followed by a 3 µs delay to allow for the complete decay of any fluorescence (dashed purple) due to the anodised cell walls or other species in the gas sample. Phosphorescence (red) signal is collected in the A bin and any background signal is collected in the B bins. Taken from Walker *et al*. (2022).

2.3.5 Commercial Analysers

In monitoring O_3 and NO_x (= NO + NO_2) concentrations in HIRAC during oxidation reactions, two commercial analysers were employed for the selective detection of O_3 (Thermo Electron Corporation Model 49C) and NO_x (Thermo Environmental Instruments Model 42C) respectively. Both analysers sampled from HIRAC *via* lengths of 1/4" PTFE tubing (~3 – 4 m) connected to a port on one of the ceiling K160 flanges. The principles of operation for both analysers will be described briefly here.

2.3.5.1 NO_x Analyser

The NO_x analyser measures NO concentrations through chemiluminescence occurring *via* reaction R2.6:

$$NO + O_3 \longrightarrow NO_2 + O_2 + h\nu \qquad \text{(R2.6)}$$

The intensity of the light produced by chemiluminescence of electronically excited NO_2 is linearly proportional to the concentration of NO within the sample chamber inside the NO_x analyser. NO_2 concentrations were likewise measured through conversion of NO_2 to NO prior to chemiluminescence by passing the sample over a molybdenum catalytic converter heated to ~598 K. A solenoid valve controlled the flow of gas to switch between the catalytic converter and flow straight through to the reaction chamber, enabling alternated detection of total NO_x concentration and NO concentration specifically. The NO_2 concentration in the gas sample was therefore calculated by subtracting the measured NO concentration from the total NO_x concentration during the two phases (E2.5):

$$[NO_2] = [NO_x] - [NO] \quad \text{(E2.5)}$$

A second prereactor solenoid valve controlled the sample flow either to the reaction chamber, where chemiluminescent reaction with O_3 occurred to give an NO concentration, or to a prereactor chamber, where NO was depleted *via* reaction with O_3 prior to the reaction chamber to give a zero reading. Samples containing <200 ppbv NO were depleted to a degree of >99 % in the prereactor. Ozone was produced in sufficient quantities within the apparatus by passing a flow of dry air through a silent discharge ozonator before entering the reaction chamber and mixing with NO. Chemiluminescence of NO_2 was detected *via* a PMT contained within a thermoelectric cooler. The typical detection limit for NO_x was ~0.4 ppbv over a 15 s averaged measurement period at a sample rate of ~0.6 L min^{-1}, which was sufficient for measuring concentrations of NO_x used in current chamber experiments (~10 – 100 ppbv).

2.3.5.2 O_3 Analyser

Detection of O_3 *via* the O_3 analyser was achieved through UV photometry at 254 nm. Using the Beer-Lambert law (E2.4, see section 2.3.3), the ratio of light intensities between a cell containing ozone and a reference cell 'scrubbed' of ozone allowed calculation of the ozone concentration through knowledge of the path length (38 cm) and molar absorption cross-section at 254 nm.

The sample flow was split so that half of the sample gas proceeded *via* an ozone scrubber and the other half proceeded unfiltered. Two solenoid valves then controlled the

alternation of the gas flow between two absorption cells, where one cell contains the sample gas and the other contains reference gas scrubbed of ozone. The solenoid valves periodically switched the cells containing sample gas and reference gas, and the averaged measurement was recorded, so as to minimise any error from either cell having slightly different absorption properties to the other. After each solenoid valve switch, a delay in recorded light intensity measurements for several seconds allowed for cell flushing.

Similarly to the NO_x analyser, the ozone analyser had a detection limit of ~1.0 ppb for measurements averaged over 15 s, with a slightly higher volumetric flow rate of 2 L min^{-1}. For chamber oxidation applications, ozonolysis reactions and ozone photolysis were examined as methods of OH generation in HIRAC (see Chapter 3), and ozone mixing ratios were therefore typically in the region of ~50 – 150 ppbv. The comparatively low detection limit was sufficient for all O_3 monitoring requirements within this work.

Chapter 3 OH Generation Methods for Chamber Studies Involving Glyoxal

3.1 Introduction

A key process in the investigation of atmospheric reactions within a laboratory environment is the generation of hydroxyl (OH) radicals (see Chapter 1 on the background of OH-initiated oxidation chemistry of VOCs). In outdoor chamber experiments, such as those performed at the EUPHORE (EUropean PHOtoREactor) facility in Valencia (Zádor et al., 2006) and SAPHIR (Simulation of Atmospheric PHotochemistry In a large Reaction chamber) in Jülich (Karl et al., 2004; Rohrer et al., 2005), sunlight is typically used in photolytic radical production, often with nitrous acid (HONO) and methyl nitrite (CH_3ONO) as important sources of OH, introducing NO_x to the chamber. This method of OH generation in outdoor chambers provides a good approach for monitoring reactions under ambient conditions of photolysis and radical concentration as a more direct comparison with field measurements. However, despite the advantages of studying reactions at ambient conditions, there are also limitations in which those conditions are relevant primarily to mid-latitude boundary layer chemistry. Due to the nature of outdoor chambers, being comprised mainly of a Teflon film, achieving a wider range of conditions that cover the changing conditions across all latitudes and altitudes within the troposphere, through variation of temperatures (~200-320 K) and pressures (1000-100 mbar), is not feasible. It is also difficult to work under NO_x-free conditions when using HONO as an OH source due to an inability to clean the chamber walls regularly or evacuate the chamber to encourage desorption off the walls, limiting relevance of mechanistic studies and yield measurements to urban environments where NO_x is significantly more prevalent as a result of high temperature combustion activity, particularly from vehicular emissions.

With an interest in biogenic emissions and their mechanistic routes to glyoxal, analysis of chemistry initiated in the absence of NO_x becomes important, and it is therefore prudent to investigate these reactions with the versatility of an indoor chamber in addition to outdoor chamber studies. The Highly Instrumented Reactor for Atmospheric Chemistry (HIRAC; see Chapter 2) offers a number of ports across ten external flanges surrounding the chamber, which are used for sampling, gas delivery, liquid injection and chamber evacuation, as well as fittings for exchangeable UV lamps housed within quartz tubes along the length of the chamber. This provides an ideal framework for investigating the merits and drawbacks of alternative methods of OH generation in an indoor chamber environment, with a focus on biogenic studies and glyoxal yield analysis. All experiments conducted within the scope of this chapter were performed in HIRAC under the base

conditions of a synthetic air mixture consisting of 80 % nitrogen (N_2, BOC, O.F.N., 99.998 %) and 20 % oxygen (O_2, BOC, Industrial Grade, 99.5%) at 1000 ± 3 mbar pressure and 293 ± 2 K.

This chapter aims to review the effectiveness, advantages and disadvantages of several methods of OH generation available for chamber experiments, including photolysis of nitrites for NO_x studies, photolysis of hydrogen peroxide and ozone as NO_x-free precursors, and ozonolysis reactions for dark chemistry OH production. As any study with a desired outcome favours a certain set of conditions, this review is an attempt to optimise such conditions with the goal of ensuring the best opportunity for measuring a definitive glyoxal yield from the OH-initiated oxidation of its biogenic precursors.

3.2 NO_x Study Precursors

Whilst biogenic volatile organic compounds (BVOCs) are usually associated with more remote environments, where average NO_x mixing ratios constitute much smaller quantities (~1 – 5 ppbv) than their urban counterparts (~20 – 100 ppbv), recent studies have highlighted the importance of considering biogenic emissions within urban areas, in addition to identifying anthropogenic sources of isoprene and monoterpenes, which will impact BVOC oxidation routes, secondary organic aerosol (SOA) formation and increase pollution of tropospheric ozone (Hsieh et al., 2017; Khan et al., 2018; Cheng, X. et al., 2018; Mishra and Sinha, 2020; Panopoulou et al., 2020; Bryant et al., 2023). This consideration merits a study of nitrites as an indirect source of OH in chamber experiments, whilst also introducing NO_x to the chamber and promoting NO_x-driven alkoxy chemistry (see Chapter 1) relevant for urban environments, where typically the alkoxy is oxidised to the subsequent carbonyl, occasionally in competition with dissociation or isomerisation processes (Orlando et al., 2003).

3.2.1 Methyl Nitrite

Methyl nitrite (CH_3ONO) has been widely used as a precursor to OH in a combination of chamber experiments, SOA studies and relative rate measurements (Atkinson et al., 1981b; Picquet et al., 1998; Volkamer et al., 2009; Nguyen et al., 2015), a testament to its usefulness in a range of applications. Methyl nitrite indirectly produces OH through the photolytically induced reaction scheme shown in reactions R3.1-R3.3:

$$CH_3ONO + h\nu \longrightarrow CH_3O + NO \quad \text{(R3.1)}$$

$$CH_3O + O_2 \longrightarrow HCHO + HO_2 \quad \text{(R3.2)}$$

$$HO_2 + NO \longrightarrow OH + NO_2 \quad \text{(R3.3)}$$

Whilst the NO required to convert HO_2 into OH is produced in the initial photolysis (R3.1), additional NO is typically introduced into the chamber or reaction cell to accelerate this process. This also helps to mitigate the effect of NO being used up in reaction with peroxy radicals produced upon the initial oxidation of hydrocarbons *via* OH (R3.4-R3.6):

$$RH + OH \longrightarrow R + HO_2 \quad \text{(R3.4)}$$

$$R + O_2\,(+M) \longrightarrow RO_2\,(+M) \quad \text{(R3.5)}$$

$$RO_2 + NO \longrightarrow RO + NO_2 \quad \text{(R3.6)}$$

Synthesis of methyl nitrite has been described previously in the literature (Taylor et al., 1980; Atkinson et al., 1981b), consisting of the dropwise addition of a concentrated solution of sulfuric acid (H_2SO_4, Sigma-Aldrich, ACS Reagent, 98%) into methanol (CH_3OH, Sigma-Aldrich, Laboratory Reagent, ≥ 99.6%) saturated with sodium nitrite ($NaNO_2$, Sigma-Aldrich, ACS Reagent, ≥ 97 %) at 273 K. A flow of nitrogen (BOC, O.F.N., 99.998%) is passed through the reaction mixture as a bubbler to encourage vapour flow through the system. The methyl nitrite vapour was then passed through a solution of sodium hydroxide (NaOH, Sigma-Aldrich, 50% in H_2O) to neutralise the acid and subsequently through anhydrous calcium chloride ($CaCl_2$, Supelco, granules, Reag. Ph Eur) as a drying agent before depositing the remaining product in a cold trap under liquid nitrogen at 77 K. The product was thawed into a glass bulb and the gaseous methyl nitrite diluted to 31% in nitrogen. The infrared spectrum of methyl nitrite (~1.5×10^{14} molecule cm^{-3}) was measured using a Fourier Transform Infrared spectrometer (FTIR, see Chapter 2 for details), and compared against the known absorption cross-section (Sharpe et al., 2004) to analyse for impurities (Figure 3.1). The overlapped spectra reveal only background levels of water, methane and carbon dioxide alongside methyl nitrite, which

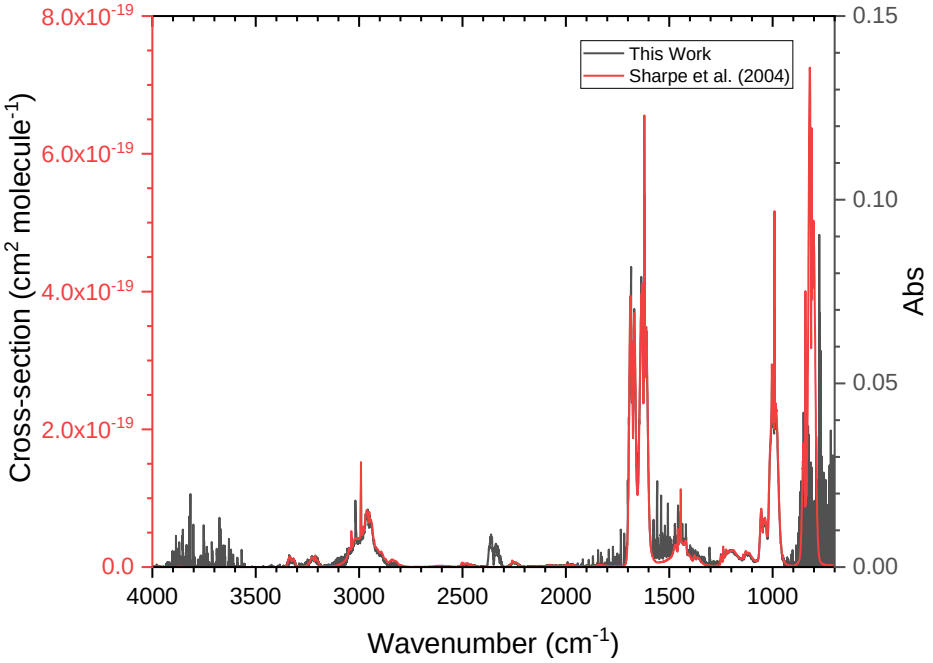

Figure 3.1 A comparison of the FTIR spectrum of synthesised gaseous methyl nitrite (~1.5 × 10^{14} molecule cm^{-3}) measured in HIRAC at 293 K with the absorption cross-section of methyl nitrite measured by Sharpe *et al*. (2004). Comparison shows good agreement between spectra, revealing only background levels of water, carbon dioxide and methane in the chamber, which are known impurities in the nitrogen bath gas used in HIRAC experiments.

are known impurities in the nitrogen bath gas, and no traces of methanol or other species present, suggesting an appropriate purity (estimate ≥95 %) for the reagent.

Owing to the structure of the UV absorption cross-section of methyl nitrite around 310-360 nm (Taylor et al., 1980; Maricq and Wallington, 1992) (Figure 3.2), the blacklamps (Philips TLK40W/05) were used rather than the 254 nm lamps (GE Optica GE55T8/HO), having a longer wavelength output centred around 300-450 nm (see Chapter 2). This is advantageous in lowering the average photon energy and minimising photolysis of other species within the chamber, including reaction products. In particular, there is less potential for glyoxal loss throughout the reaction, making smaller yields easier to measure. In considering photo-oxidation mechanisms of BVOCs initiated at longer wavelengths (λ > 300 nm) , photolysis rates start to become insignificant, and the reaction becomes simpler to simulate in model runs as a method of reproducing experimental yields. As an example, the photolysis rate of acetaldehyde was measured under the output of both lamp sets, determined as j_{CH3CHO} = (1.01 ± 0.14) × 10^{-4} s^{-1} under the 254 nm lamps, whereas negligible acetaldehyde photolysis was observed under the blacklamps (see Chapter 5).

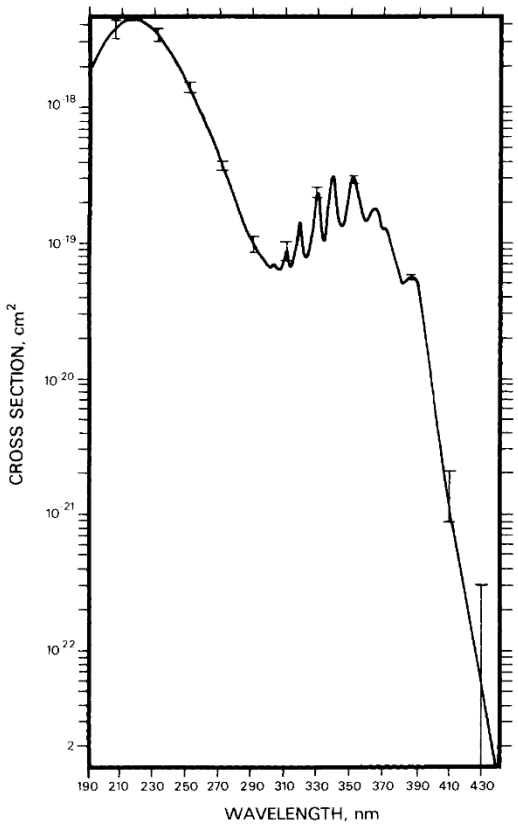

Figure 3.2 The UV absorption cross-section of gaseous methyl nitrite at 298 K between 190 – 435 nm. The structure and quantity of cross-section values between 300 – 400 nm promotes photolysis in this wavelength region, allowing use of the blacklamps with wavelength output centred around 300 – 450 nm. Taken from Taylor *et al*. (1980).

As the quantities of OH generated throughout a reaction depend on the rate of NO recycling *via* the photolysis of NO_2 (R3.7), these wavelengths are likewise ideal for optimising the NO_2 photolysis rate, j_{NO2}, in considering the absorption cross-section and photodissociation efficiency (Bogumil et al., 2003; Volz-Thomas et al., 1996).

$$NO_2 + h\nu \xrightarrow{\lambda \leq 400\ nm} NO + O \qquad \text{(R3.7)}$$

Methyl nitrite was tested as an OH source in HIRAC through studying the oxidation of acetaldehyde (CH_3CHO, Sigma-Aldrich, ACS reagent, ≥ 99.5%). Acetaldehyde is a

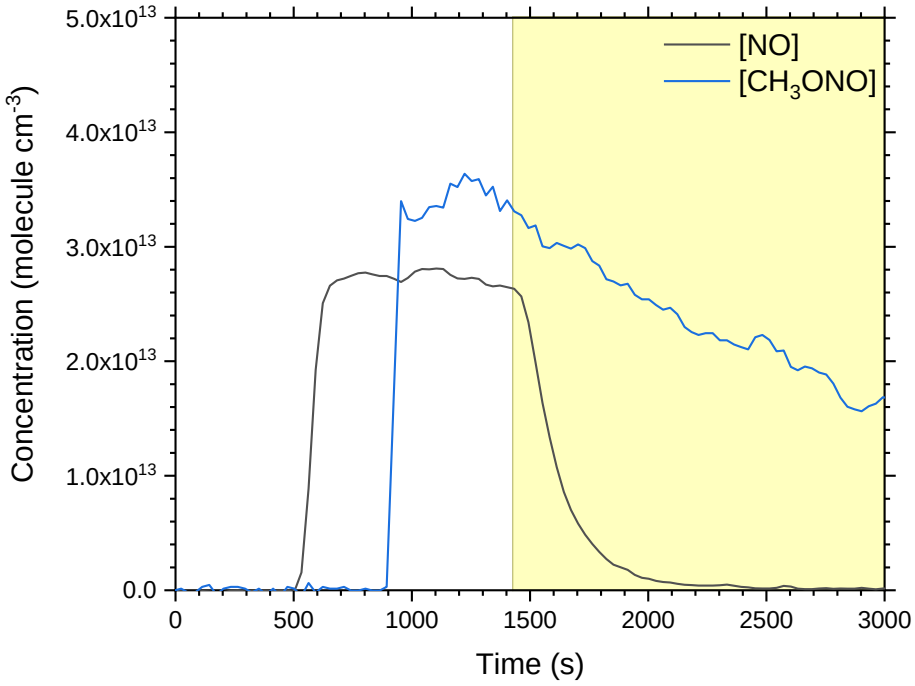

Figure 3.3 Depletion of excess NO (black) during the photolysis of methyl nitrite (blue) upon activation of UV blacklamps (shaded yellow region). UV photolysis of methyl nitrite triggers formation of HO_2 radicals, which react with NO to produce OH and NO_2. OH then oxidises VOCs in HIRAC, subsequently forming RO_2 radicals, and the RO_2 then similarly reacts with and depletes NO. Photolysis of NO_2 is too slow to replenish NO concentrations above that of the NO_x Analyser detection limit (~0.5 ppbv) once depleted. Complementary data shown in Figures 3.4 & 3.5.

relatively simple oxygenated VOC (OVOC) of interest to this work as a potential biogenic precursor to glyoxal in the marine boundary layer (MBL) (Zhu, Y. and Kieber, 2019), and constitutes an appropriate compound for study in this instance (see Chapter 5 for further details). Additional NO (BOC, Nitric Oxide, N2.8 Grade) was introduced to the chamber to assist in the generation of OH through conversion of HO_2 (R3.3). However, despite the supplementary NO in the chamber, any excess was typically depleted within 10 minutes of reaction initiation (Figure 3.3), falling below the detection limit (~0.5 ppbv) of the commercial NO_x analyser (see Chapter 2). It is clear that NO is still being produced through both NO_2 and methyl nitrite photolysis from the continued generation of OH measured by the FAGE (Fluorescence Assay by Gas Expansion, see Chapter 2) instrument (Figure 3.4), as well as the ongoing oxidation of acetaldehyde throughout the experiment, however OH production is limited by the rate of NO_2 photolysis achieved by the output of the blacklamps, as evidenced by the drop in OH levels upon depletion of the excess NO. At longer experiment times, a natural increase in average OH concentrations

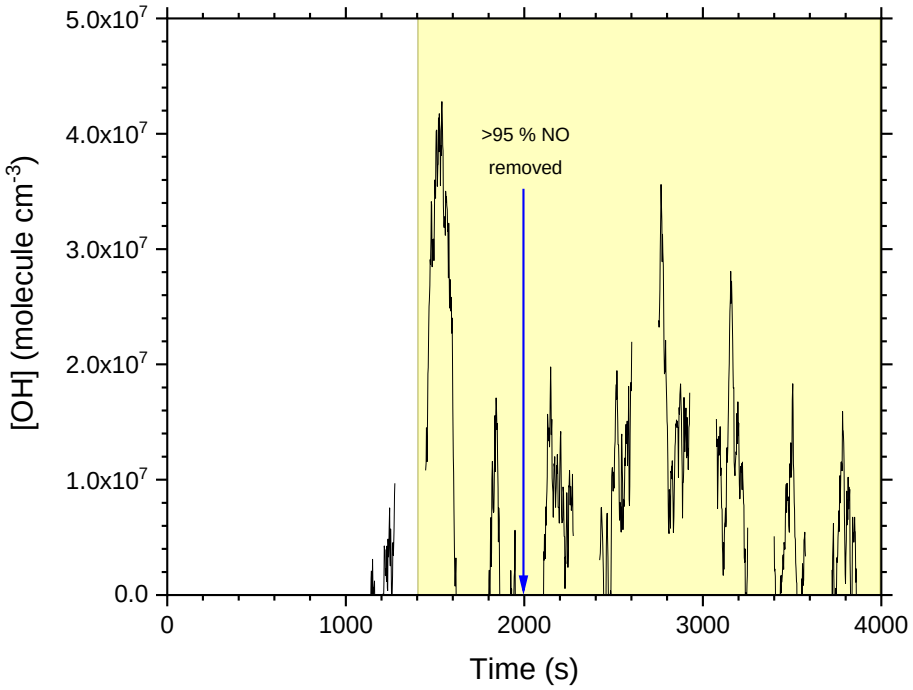

Figure 3.4 OH concentrations measured by the HIRAC FAGE instrument upon photolysis of methyl nitrite. The yellow shaded region indicates activation of UV blacklamps initiating photolysis, followed by a clear increase in OH molecules. Despite depletion of excess NO in the system, OH continues to be produced, however lower concentrations indicate a slower rate of production for the remainder of the experiment time. Complementary data shown in Figures 3.3 & 3.5.

is seen due to a decrease in the quantity of acetaldehyde remaining in the chamber, however this is also balanced with decreasing methylnitrite concentrations consequently reducing OH generation. Variations in average OH concentration are primarily a result of these fluctuating production and removal rates.

Due to the reduced concentrations of OH produced through methyl nitrite photolysis, as well as through other methods discussed in this chapter, the FAGE data (fluorescence signal accumulated over 1 s, see Chapter 2) were averaged over a number of points, typically between 10 – 20, to improve the instrument limit of detection. Data averaging gave a more clear structure to the time profile through an improved signal-to-noise ratio (SNR). However, due to the method of averaging used, which was indiscriminate of the time gaps present from the offline cycling measurement phase, data at the beginning or end of an online cycle included an averaging from the adjacent online cycle. This 'cross-averaging' often resulted in a slight oscillation of the averaged online data points, as

observed in Figure 3.4. This phenomenon was accentuated as the averaging window was increased to account for changes in the SNR and consequently the limit of detection.

Another concern with reduced OH concentrations in chamber studies was the slower production of glyoxal competing against various loss processes impacting the feasibility of glyoxal yield measurements. These losses include removal *via* reaction with OH; photolysis; adsorption onto wall surfaces; heterogeneous uptake by water molecules and aerosol components; and dilution through instrument sampling. It should be noted, however, that despite the reduced production rate of glyoxal, several of these loss processes will also be lowered due to the OH generation method used. Lower OH concentrations naturally result in a reduced loss of glyoxal *via* OH, and the longer wavelength blacklamps will slightly lower the photolysis rate of glyoxal from the 254 nm GE Optica lamps (see Chapter 2) throughout the reaction, with the absorption cross-section at a minimum between ~325 – 375 nm (Orlando and Tyndall, 2001). The use of methyl nitrite as an OH precursor also assists in reducing the relative humidity, and consequently the amount of heterogeneous uptake by water, an otherwise significant loss process in HIRAC due to the high solubility of glyoxal in water (effective Henry's law constant, $K_H = 4.2 \times 10^5$ mol dm^{-3} atm^{-1}) (Matsumoto et al., 2005; Coburn et al., 2014). Wall surface and dilution losses will remain unchanged, although these are typically relatively small quantities in comparison. Whilst lower OH concentrations inevitably extend the total reaction time in chamber oxidation studies due to slower VOC decay and product accumulation, reasonable glyoxal quantities were nonetheless observed through the specific glyoxal laser-induced phosphorescence (GLYOX-LIP, see Chapter 2) technique, following the OH-initiated oxidation of acetaldehyde *via* methyl nitrite photolysis (Figure 3.5). Indeed, decreased loss rates both through lower OH concentrations and drier conditions assisted in the calculation of glyoxal yields with the benefit of a larger dataset to increase the confidence in a linear yield plot (see Chapter 5).

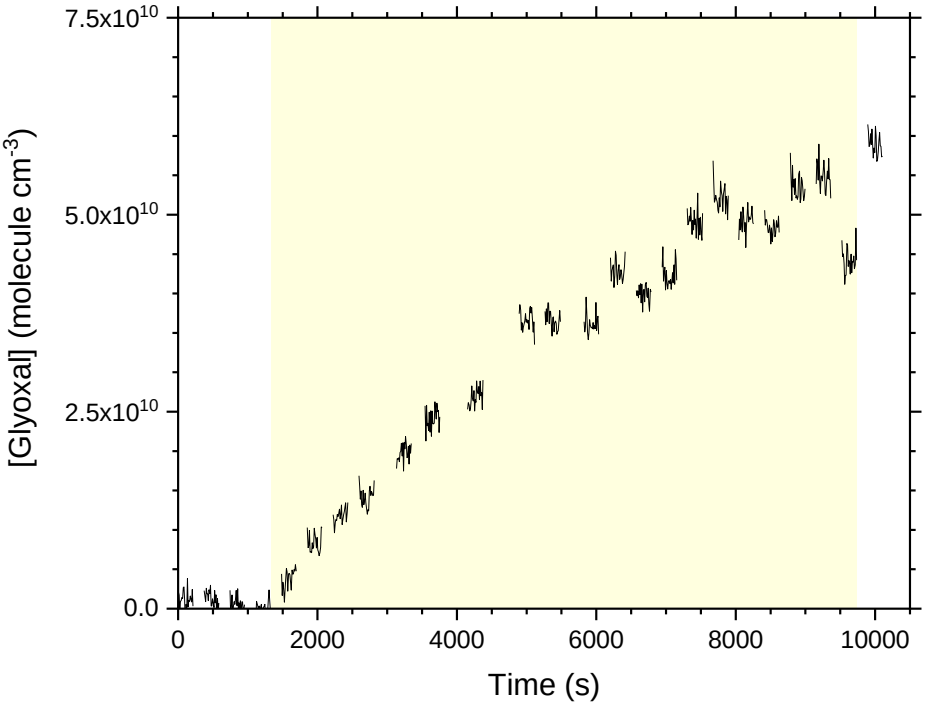

Figure 3.5 Growth in glyoxal concentration, measured using a laser-induced phosphorescence technique upon photolysis of methyl nitrite, producing OH radicals in the presence of acetaldehyde. Yellow shaded region indicates period with UV blacklamps on, initiating production of OH and instigating oxidation of acetaldehyde with clear glyoxal production over a period of ~2 hours. Complementary data shown in Figures 3.3 & 3.4.

Another element to the study of BVOC oxidation is the measurement of formaldehyde yields, with the aim of establishing a ratio of glyoxal to formaldehyde production (R_{GF}) from a particular precursor (see Chapter 1). However, photolysis of methyl nitrite produces formaldehyde as a byproduct itself (R3.2), and this makes it difficult to distinguish the quantity of formaldehyde produced directly from methyl nitrite photolysis compared with the product of secondary chemistry from its BVOC precursors. Attempts were made to quantify a formaldehyde yield directly from methyl nitrite photolysis, however this yield is also dependent on the OH concentrations present in the chamber which primarily determine the loss rate of formaldehyde during the reaction period. As OH concentrations are subject to the total quantity and second order rate coefficients of all VOCs in the reaction mixture determining OH loss, this complicates the ability to reproduce a separately determined formaldehyde yield from methyl nitrite photolysis during BVOC oxidation, relying on models to reproduce any measured total yields. Concentration profiles of photolysis initiated chemistry, such as that of methyl nitrite, are

difficult to replicate, so models in this work rely simply on constraints of experimentally determined OH data instead, and the distinction of formaldehyde sources is lost.

3.2.1.1 Summary

Methyl nitrite remains a useful precursor to OH when investigating reactions in the presence of NO_x. Despite the typical recommendation of additional NO and the slow generation of OH as a result of NO_2 photolysis rates in indoor chamber studies, evidence suggests steady OH production for a period of at least 2 hours, and a measurable glyoxal yield over the course of a reaction as a result of reduced glyoxal loss processes. The primary limitation within the UNFOGS project (see Chapter 1) lies in the loss of formaldehyde yield data from VOC oxidation as a result of photolytic production, a critical parameter in the determination of R_{GF}. Whilst establishing a glyoxal yield and reaffirming the associated mechanistic routes are important to ascertain, this method of OH generation should be paired with other sources, both with and without NO_x, to complement data sets with formaldehyde yields and analyse R_{GF} values relevant for both urban and remote environments.

3.2.2 Isopropyl Nitrite

Isopropyl nitrite ($(CH_3)_2CHONO$) has more recently been used as an alternative source of OH to methyl nitrite in the study of atmospheric reactions under NO_x conditions (O'Brien, J.M. et al., 1998; Berndt et al., 2019; Berndt, 2021). This photolysis method is very similar to methyl nitrite, instead producing acetone ($CH_3C(O)CH_3$) as a byproduct (R3.9) rather than formaldehyde. As before, longer wavelength lamps may be used, limiting photolysis of both glyoxal and its biogenic precursors.

$$(CH_3)_2CHONO + h\nu \longrightarrow (CH_3)_2CHO + NO \quad \text{(R3.8)}$$

$$(CH_3)_2CHO + O_2 \longrightarrow CH_3C(O)CH_3 + HO_2 \quad \text{(R3.9)}$$

$$HO_2 + NO \longrightarrow OH + NO_2 \quad \text{(R3.3)}$$

Although OH generation here still relies on NO recycling through photolysis of NO_2, the yield of OH from isopropyl nitrite photolysis has been found to be independent of any additional NO included in the reaction mixture (Raff and Finlayson-Pitts, 2010), reported as an average of $\Phi_{OH} = 0.54 \pm 0.07$. It is therefore easier to study the NO_x dependence of a reaction mechanism and product yield whilst maintaining OH concentrations relatively consistently between experiments. Experiments with isopropyl nitrite photolysis were performed in HIRAC to investigate the efficiency and viability of this OH generation method for applications in chamber studies of biogenic glyoxal precursors.

Isopropyl nitrite was prepared through the dropwise addition of a mixture of isopropanol ($(CH_3)_2CHOH$, Sigma-Aldrich, Laboratory Reagent, ≥ 99.5%, 40 mL) and concentrated hydrochloric acid (HCl, Sigma-Aldrich, ACS Reagent, 37%, 68 mL) into a solution of sodium nitrite ($NaNO_2$, Sigma-Aldrich, ACS Reagent, ≥ 97 %, 30.67 g) in water (45 mL) at 273 K. Once addition of the acid-alcohol mixture was complete, the reaction was left stirring for 10 minutes and the resultant mixture separated out into aqueous and organic phases. Discarding the aqueous phase, the organic mixture was washed first with saturated sodium bicarbonate solution ($NaHCO_3$, Sigma-Aldrich, ACS Reagent, ≥ 99.7%) to neutralise any excess acid, discarding the washings, and then subsequently washed with saturated sodium chloride solution (NaCl, Sigma-Aldrich, ACS Reagent, ≥ 99.0%) to dry the product. The liquid isopropyl nitrite was stored in a chemical freezer at 255 K. Although it is difficult to distinguish any impurities – of which the most anticipated were HCl, isopropanol and acetone – in the sample under FTIR spectroscopy due to significant overlap in the absorption spectra, there was little evidence to suggest these species may be present in any measurable quantities in HIRAC upon addition of isopropyl nitrite (~5.2×10^{14} molecule cm^{-3}). However, analysis of mass spectra from Proton Transfer Reaction-Time of Flight-Mass Spectrometer (PTR-ToF-MS, shortened

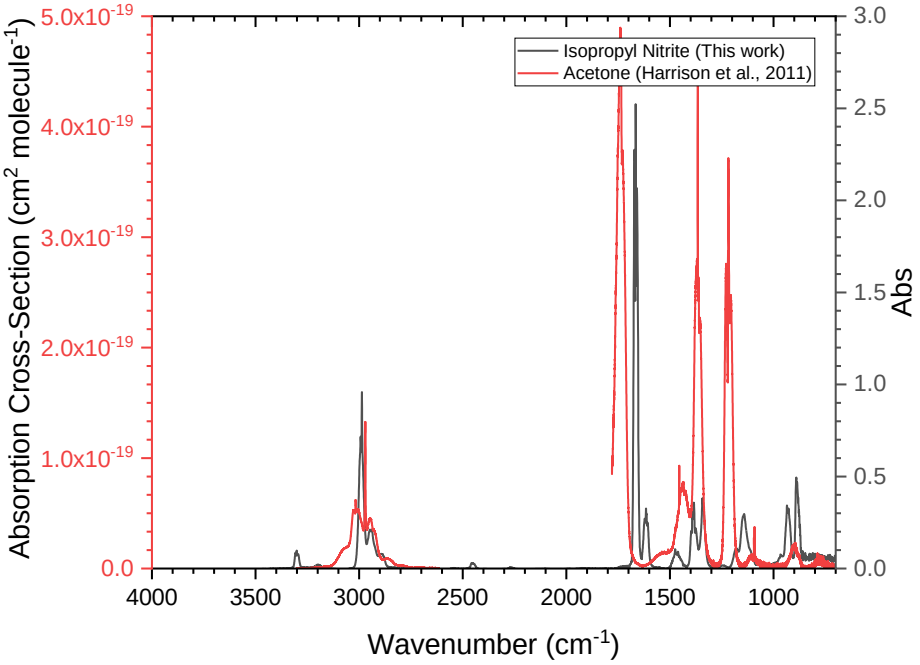

Figure 3.6 Comparison of the measured absorption of isopropyl nitrite (black, ~5.2 × 10^{14} molecule cm^{-3}) with the FTIR spectrometer against the absorption cross-section of acetone (red) (Harrison *et al.*, 2011a, b), the dominant product of isopropyl nitrite decomposition. The measured spectrum shows very little evidence of acetone present in the isopropyl nitrite sample.

to PTR-MS, see Chapter 2) measurements indicated the presence of acetone from an increase in counts at *m*/*z* 59.09, consistent across two equivalent additions of isopropyl nitrite (100 µL) injected as a liquid. It is uncertain whether this signal corresponds to an acetone impurity or merely a fragment ion of isopropyl nitrite, yet as the presence of acetone alters the chemistry of interest very little due to its stability and slow oxidation through reaction with OH, it was considered unimportant for the sake of these tests. Very little, if any, acetone could be observed with the FTIR from comparison of the absorption cross-section of acetone (Harrison et al., 2011a; Harrison et al., 2011b) with the isopropyl nitrite spectrum (Figure 3.6).

Upon initial injection of the liquid isopropyl nitrite into the chamber through a flow of nitrogen, the isopropyl nitrite loss rate was measured over a period of 15 minutes to assess the stability of the precursor in HIRAC. A first order loss rate of (1.04 ± 0.24) × 10^{-4} s^{-1} was measured, and was comparable with a typical loss rate (0.5 – 1.0 × 10^{-4}) for the majority of VOCs in HIRAC, dependent primarily on wall surface adsorption and instrument sampling rates. The blacklamps were then switched on, and OH concentrations monitored with FAGE, initially reaching (6.0 ± 1.8) × 10^{8} molecule cm^{-3}

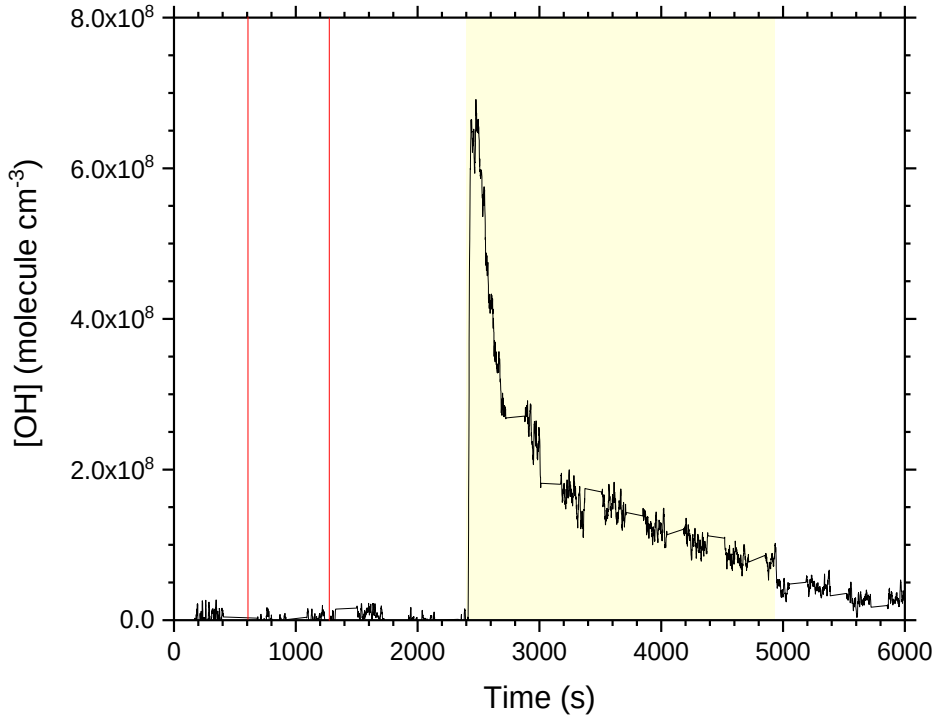

Figure 3.7 Production of OH from isopropyl nitrite photolysis in HIRAC without the addition of any other VOCs, measured by the HIRAC FAGE instrument. Red lines indicate liquid injections of isopropyl nitrite (100 µL) into the chamber, and shaded yellow area denotes activation of UV blacklamps. Data complementary to Figures 3.8 & 3.9.

prior to the addition of any other VOCs into HIRAC (Figure 3.7) before slowly decreasing over the duration of an hour as the isopropyl nitrite was gradually used up. These elevated OH levels in comparison with methyl nitrite photolysis should be expected, as the primary losses for OH in this system will be reaction with isopropyl nitrite and acetone, neither of which are especially fast. The bimolecular rate coefficient for reaction of acetone with OH is recommended to be $(2.3 \pm 0.2) \times 10^{-13}$ cm^3 molecule^{-1} s^{-1} at 298 K (Atkinson et al., 1989), and that for isopropyl nitrite, whilst not directly measured, has been estimated as 7.2×10^{-13} cm^3 molecule^{-1} s^{-1} (Raff and Finlayson-Pitts, 2010) through extrapolation of previously studied rate coefficients with alkyl nitrites.

Accounting for loss of isopropyl nitrite through surface adsorption, dilution and reaction with OH, the photolysis rate with the HIRAC blacklamps was measured throughout the decay as $(2.00 \pm 0.12) \times 10^{-4}$ s^{-1}. With the reported OH quantum yield of $\Phi_{OH} = 0.54 \pm 0.07$ from isopropyl nitrite photolysis (Raff and Finlayson-Pitts, 2010), and initial concentrations of isopropyl nitrite around 5×10^{14} molecule cm^{-3}, the average production of OH can be calculated using equation E3.1, reaching approximately ~5.4×10^{10} molecule cm^{-3} s^{-1}.

$$\frac{+\mathrm{d[OH]}}{\mathrm{d}t} = j_{(\mathrm{CH_3})_2\mathrm{CHONO}}[(\mathrm{CH_3})_2\mathrm{CHONO}]_t \Phi_{\mathrm{OH}} \quad \text{(E3.1)}$$

With relevance to biogenic glyoxal precursors (see Chapters 5 & 6), acetaldehyde present in the chamber at 1×10^{14} molecule cm^{-3}, using a bimolecular rate coefficient of k_{OH} = $(1.58 \pm 0.17) \times 10^{-11}$ cm^3 molecule^{-1} s^{-1} (Niki et al., 1978), a steady state concentration of OH, $[OH]_{SS}$, can be calculated using equation E3.2, where OH loss rate is equivalent to OH production and assuming acetaldehyde is the dominant sink of OH. Under these conditions, a steady state $[OH]_{SS} \approx 3.4 \times 10^7$ molecule cm^{-3} would be achieved, reaching ~5 times higher than steady state concentrations using methyl nitrite as a precursor.

$$[\mathrm{OH}]_{\mathrm{SS}} = \frac{\frac{+\mathrm{d[OH]}}{\mathrm{d}t}}{k_{\mathrm{OH}}[\mathrm{CH_3CHO}]_t} \quad \text{(E3.2)}$$

However, despite the benefit of increased OH concentrations over methyl nitrite, it was found that photolysis of isopropyl nitrite resulted in a growth in signal on the GLYOX-LIP instrument (Figure 3.8). It is unclear how glyoxal might be produced in this system, and the only possible route appears to be decomposition of the isopropoxy radical ($(CH_3)_2CHO$), forming acetaldehyde and the methyl radical (CH_3) (Devolder et al., 1999), with the resultant acetaldehyde subsequently oxidising to glyoxal *via* reaction with OH at the methyl abstraction site (see Chapter 5). This potential glyoxal source does not hold much merit here, as reaction of the isopropoxy radical with oxygen at tropospheric oxygen concentrations (~5×10^{18} molecule cm^{-3}) will outcompete unimolecular dissociation enough for acetaldehyde to be a very minor product. Some acetaldehyde was observed in PTR-MS spectra at *m*/*z* 45.06, however [CH_3CHO] did not climb above concentrations of ~8×10^{12} molecule cm^{-3}. With a recommended methyl branching abstraction of 5.1 ± 2.4 % from acetaldehyde oxidation by OH (Butkovskaya et al., 2004), it is unlikely that this would contribute enough to glyoxal concentrations to account for the observed phosphorescence signal.

Another possibility lies in the production of methylglyoxal ($CH_3C(O)CHO$), a prominent product from acetone oxidation (R3.10-13) (Rosado-Reyes and Francisco, 2007), which has an increased, fine-structured absorption cross-section in the region around 440 nm

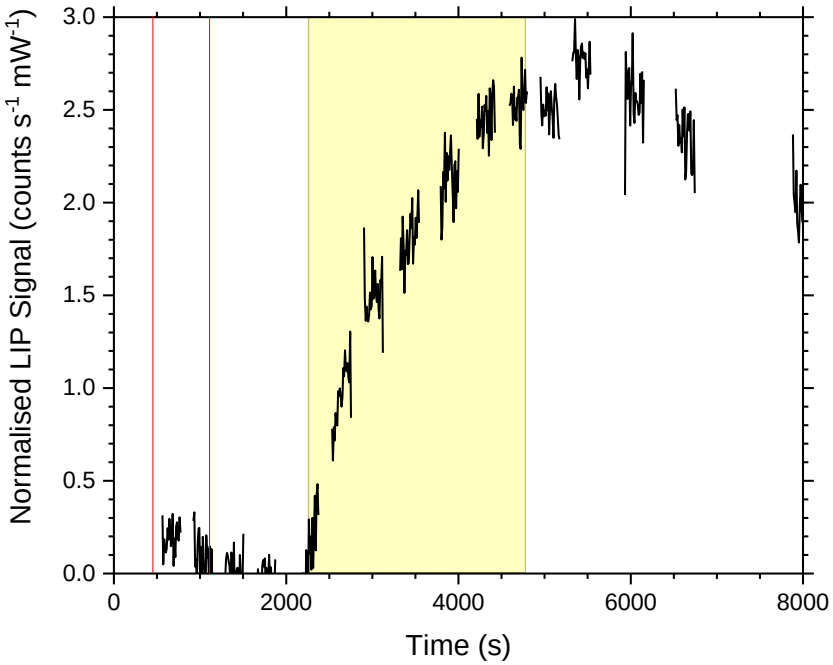

Figure 3.8 Growth of phosphorescence counts normalised for laser power with GLYOX-LIP measurements upon photolysis of isopropyl nitrite. Red lines indicate liquid injections of isopropyl nitrite (100 µL, ~2.6 × 10^{14} molecule cm^{-3}) into HIRAC, and yellow shaded area indicates activation of UV blacklamps initiating photolysis. A lack of suitable glyoxal sources from isopropyl nitrite photolysis suggests methylglyoxal as the source of LIP signal growth. Data complementary to Figures 3.7 & 3.9.

(Meller et al., 1991), the chosen wavelength to induce phosphorescence, and phosphoresces in a similar manner to glyoxal. Phosphorescence of methylglyoxal is a known issue in glyoxal LIP detection, and these two species can be distinguished in a LIP setup through analysis of their differing phosphorescence decay lifetimes (Henry et al., 2012), however for these experiments the decay data were not recorded, therefore signal separation in this manner was not possible.

$$CH_3C(O)CH_3 + OH \longrightarrow CH_3C(O)CH_2 + H_2O \quad \text{(R3.10)}$$

$$CH_3C(O)CH_2 + O_2\,(+M) \longrightarrow CH_3C(O)CH_2O_2\,(+M) \quad \text{(R3.11)}$$

$$CH_3C(O)CH_2O_2 + NO \longrightarrow CH_3C(O)CH_2O + NO_2 \quad \text{(R3.12)}$$

$$CH_3C(O)CH_2O + O_2 \longrightarrow CH_3C(O)CHO + HO_2 \quad \text{(R3.13)}$$

Whilst, as stated previously, acetone oxidation is a relatively slow process, it may nevertheless be a plausible explanation for the signal observed on the GLYOX-LIP instrument. Steady growth of a peak at *m/z* 73.07 was observed in PTR-MS spectra, attributed to methylglyoxal, after photolysis initiation of isopropyl nitrite. The change in signal over time was compared with that of the growth in GLYOX-LIP signal to analyse whether their profiles coincided (Figure 3.9), and although there are slight discrepancies in the initial production rate, these may be partially attributed to noise in the PTR-MS data as a result of the very low counts measured. Further investigations on the correlation between PTR-MS data for methylglyoxal concentrations and the corresponding GLYOX-LIP signal observed are discussed in Chapter 6.

3.2.2.1 Summary

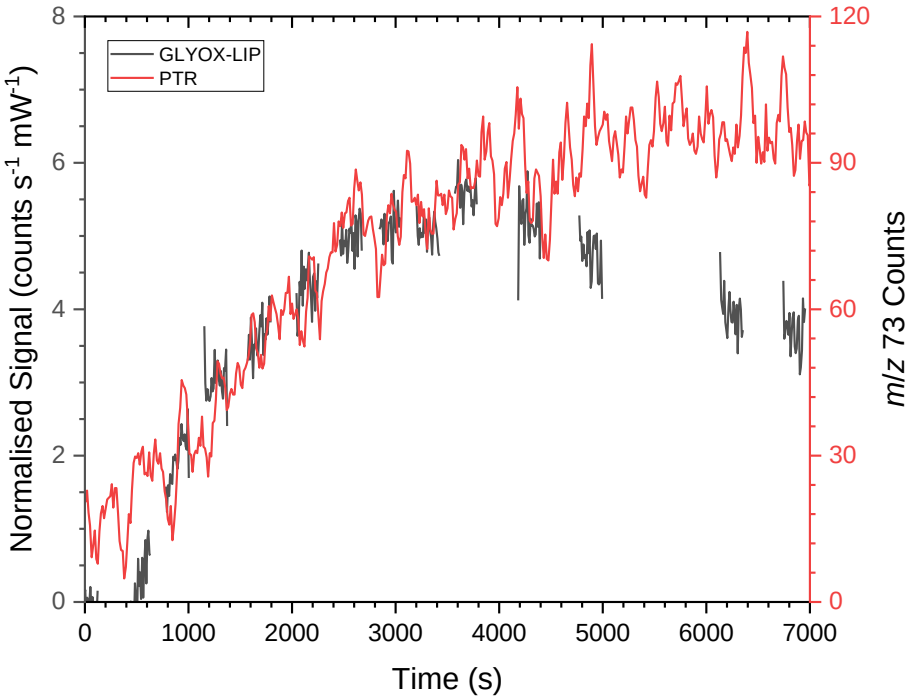

Figure 3.9 A comparison between the change in observed signal over time during isopropyl nitrite photolysis from phosphorescence detected with the GLYOX-LIP instrument (black) and counts measured at *m/z* 73.07 on the PTR-MS (red). Both instrument signals show a similar growth profile, indicating the potential interference from methylglyoxal in the phosphorescence signal, however there is a discrepancy at longer time scales that is unaccounted for by this hypothesis. Data complementary to Figures 3.7 & 3.8.

Isopropyl nitrite is a useful OH precursor for NO_x studies, producing at least ~5 times more OH than methyl nitrite in equivalent conditions, a particularly useful characteristic in studying faster BVOC oxidation reactions. Contrary to methyl nitrite photolysis, additional NO does not seem to be necessary in maintaining OH production, however it may still be beneficial where faster oxidation reactions increase RO_2 concentrations and deplete excess NO more quickly. Despite an increase in OH generation, isopropyl nitrite was disregarded as an OH source due to the issue of interference with GLYOX-LIP signal. With an inability to diagnose the cause of the interference accurately coupled with the lack of phosphorescence decay data required to distinguish contributions to signal from glyoxal and methylglyoxal, analysing glyoxal yields from BVOC oxidation through isopropyl nitrite photolysis becomes unnecessarily difficult. This method of OH generation may be more viable with the measured phosphorescence decays throughout an experiment, however more investigations would still be needed to ascertain that the resultant GLYOX-LIP signal from isopropyl nitrite photolysis is caused solely by methylglyoxal.

3.3 Dark Reaction Studies

Dark reaction studies have a particular atmospheric relevance for the oxidation of VOCs *via* night-time chemistry or during winter months, where photo-oxidation processes are much slower due to a lack of sunlight. Although generation of OH during daylight hours is typically dominated by the photolysis of ozone, there remain alternative sources of OH that do not rely upon UV light, including ozonolysis reactions. These OH sources, alongside nitrate radical chemistry, contribute considerably more to the oxidation and removal of VOCs in the absence of sunlight.

In chamber study contexts, the generation of OH radicals in the absence of UV light can be a useful study in monitoring reactions and product formation without the additional complication of photolysis processes. Whilst photolysis is an important factor particularly in the initiation of atmospheric oxidation mechanisms, the lack of photolysis in laboratory studies eliminates these processes from mechanism models, reducing their complexity and improving the ability to reproduce rate coefficients and branching ratios observed in experiment through VOC decays and product growth. The ozonolysis of alkenes is well known to indirectly produce OH through the formation and unimolecular dissociation of carbonyl oxides (Kroll et al., 2002), otherwise termed Criegee intermediates (Criegee and

Wenner, 1949). It has only relatively recently been discovered that Criegee intermediates that are energetically stabilised through collision with bath gas molecules can undergo reactions with several other species present in the atmosphere, including H_2O, NO, NO_2, SO_2 and other VOCs, dictating a more complex fate of these intermediates in the atmosphere than previously imagined (Vereecken, 2013; Taatjes et al., 2012; Taatjes et al., 2013). These reactions have since been studied in more detail, particularly with respect to the smallest Criegee intermediate, formaldehyde oxide (CH_2OO) (Welz et al., 2012; Stone et al., 2014; Berndt et al., 2015; Lewis et al., 2015; Howes et al., 2018; Onel et al., 2020), however, the yield of OH radicals through the competitive unimolecular dissociation process is still reasonably high at atmospheric pressure for Criegee intermediates produced in significant ratios of the syn-conformer, where the terminal oxygen faces an α-hydrogen to form an energetically favourable cyclic transition state (Drozd et al., 2017). This is especially prominent in the acetone oxide Criegee intermediate ($(CH_3)_2COO$) formed through ozonolysis of 2,3-dimethylbut-2-ene (tetramethylethylene, TME), where the terminal oxygen has access to an α-hydrogen on both sides of the carbonyl bond, increasing the yield of OH seen through Criegee unimolecular dissociation. Ozonolysis of TME was therefore investigated first as a source of OH in dark reactions.

3.3.1 TME Ozonolysis

Ozonolysis of TME proceeds through reaction at the double bond to form an ozonide ring product ($(CH_3)_2C(OOO)C(CH_3)_2$), which then subsequently decomposes into a Criegee intermediate and carbonyl species. In this instance, as TME is a symmetrical alkene, this should be unity yield of the C_3 Criegee species ($(CH_3)_2COO$) and acetone as a byproduct. The C_3 Criegee intermediate can then undergo further unimolecular decomposition, generating OH molecules and resulting in acetonyl radicals ($CH_3C(O)CH_2$) that will oxidise to a mixture of hydroxyacetone ($CH_3C(O)CH_2OH$), formaldehyde, and methylglyoxal (Figure 3.10).

Initial tests were performed in the absence of any other VOCs to assess the OH production capability and product formation involved in ozonolysis reaction. Ozone was introduced

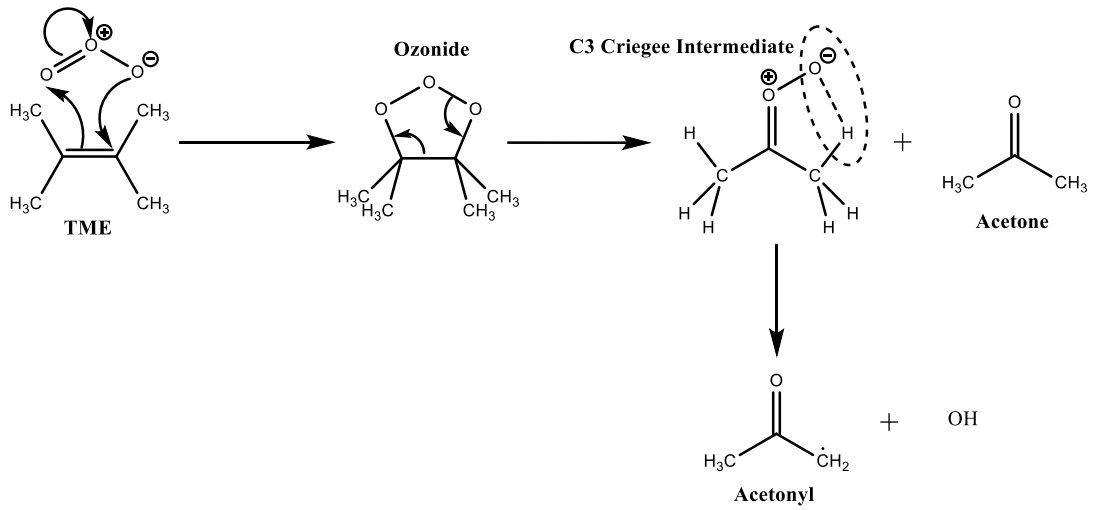

Figure 3.10 Oxidation mechanism for the generation of OH from TME (tetramethylethylene, 2,3-dimethylbut-2-ene) ozonolysis through production of the C_3 Criegee intermediate. Reaction proceeds through formation of a primary ozonide before dissociating into the Criegee intermediate and acetone. The Criegee intermediate can then undergo further dissociation through a 1,4-H shift to produce OH, whilst the resulting acetonyl radical is rapidly oxidised into other products.

to the chamber *via* a flow of oxygen through an ozone generator (Fischer Technology, OZ 500 MM Series), photolysing molecular oxygen into two oxygen atoms, which will then recombine with O_2 in the gas flow to produce ozone (R3.14, 3.15).

$$O_2 + h\nu \longrightarrow O + O \quad \text{(R3.14)}$$

$$O + O_2\,(+M) \longrightarrow O_3\,(+M) \quad \text{(R3.15)}$$

Large amounts (~10 ppmv) of ozone were delivered into HIRAC in order to promote ozonolysis, rather than reaction of TME with OH, however it is inevitable that OH removal of TME will occur alongside the chemistry of interest, complicating product analysis. TME reacts rapidly with both O_3 and OH, with recommended rate coefficients of $k_{O3} = (1.10 \pm 0.08) \times 10^{-15}$ cm^3 molecule^{-1} s^{-1} (Cox et al., 2020) and $k_{OH} = (1.13 \pm 0.08) \times 10^{-10}$ cm^3 molecule^{-1} s^{-1} (Atkinson, 1986), therefore O_3 concentrations at least 5 orders of magnitude higher than OH are desired for effective OH generation and reduced OH-initiated oxidation chemistry. However, assuming oxidation *via* OH proceeds ubiquitously through the addition channel at the double bond, the dominant oxidation product is likely to be acetone, which, as discussed previously, should not overly affect other chemistry occurring in the chamber. Ideally, O_3 concentration should be kept high

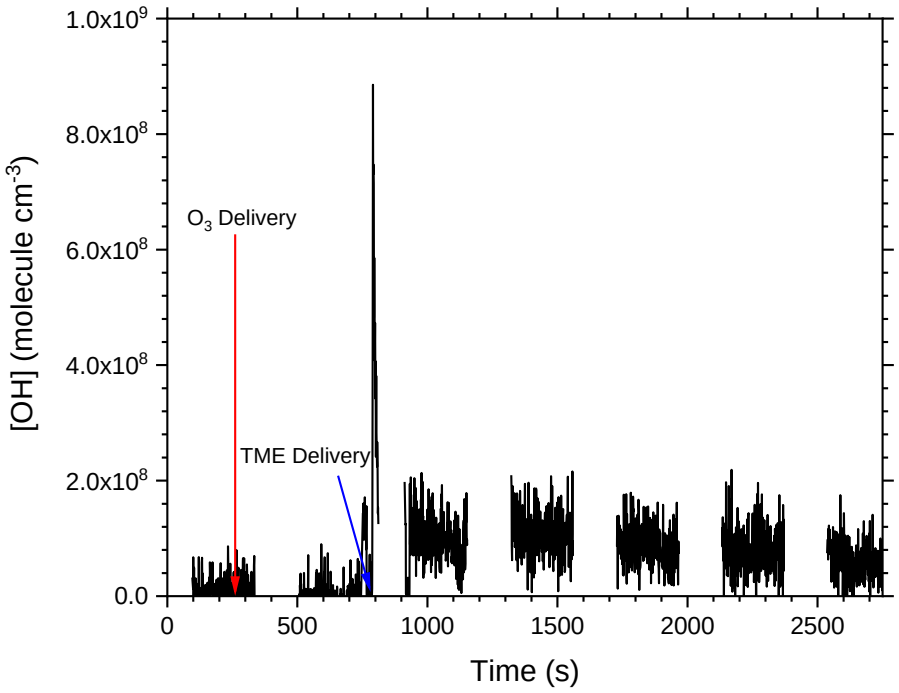

Figure 3.11 FAGE detection of OH concentrations produced through the ozonolysis of TME in HIRAC. OH generation begins immediately as the second precursor (in this instance TME, ~2.4 × 10^{14} molecule cm^{-3}) is delivered into the chamber. Initial concentration of O_3 delivered was ~2.5 × 10^{14} molecule cm^{-3}. After an initial spike in OH concentration, a steady state is reached at ~1 × 10^8 molecule cm^{-3} for a period of at least 30 minutes. Data complementary to Figure 3.12.

whilst simultaneously maintaining lower TME concentrations, maximising OH production and favouring subsequent reaction of OH with the VOC of interest rather than with TME.

In these experiments, both TME and O_3 were delivered into HIRAC in singular additions, rather than delivering a constant flow, yet following an initial spike in OH concentration, an approximate steady state was soon reached, maintaining $[OH]_{SS} \approx 1 \times 10^8$ molecule cm^{-3} for ~30 minutes (Figure 3.11), where the primary sink for OH was reaction with TME, with [TME] = 5.3 × 10^{13} molecule cm^{-3} after the initial instantaneous depletion through ozonolysis. Whilst this ozonolysis reaction does produce sufficient amounts of OH at these TME concentrations, lower TME concentrations are required to avoid competition of OH reaction. [TME], and consequently $[OH]_{SS}$, should be an order of magnitude lower for feasibility of this method.

Although the ozonolysis reaction produced relatively high quantities of OH, addition of TME into the chamber after O_3, initiating the ozonolysis, produced instantaneous phosphorescence signal on the GLYOX-LIP instrument (Figure 3.12). This result

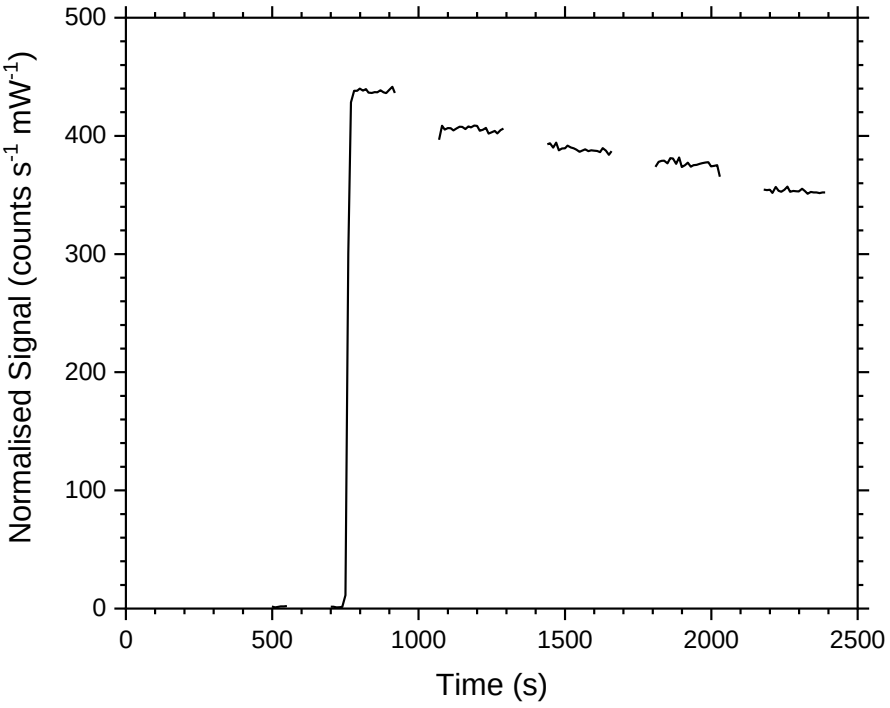

Figure 3.12 Normalised phosphorescence signal measured with the GLYOX-LIP instrument immediately after introduction of TME to HIRAC following ozone delivery, initiating the ozonolysis reaction. Phosphorescence detection is likely a result of methylglyoxal production from oxidation of the acetonyl radical produced during OH generation. Data complementary to Figure 3.11.

highlighted three possibilities; a phosphorescence interference from TME itself; phosphorescence interference from an oxidation product, most likely methylglyoxal, having been a potential culprit from previous investigations with isopropyl nitrite photolysis (see section 3.2.2); or production of glyoxal in the oxidation mechanism. It is unclear how glyoxal might be produced from TME oxidation, where products mostly consist of C_3 species through cleavage of the central carbon-carbon bond after formation of the primary ozonide. Further oxidation of acetone, the dominant product, leads to hydroxyacetone and methylglyoxal, and will eventually be broken down further through release of CO or CO_2 forming the acetyl peroxy radical ($CH_3C(O)OO$), which does not produce glyoxal (see Chapter 5 for details on acetaldehyde oxidation mechanism).

In order to examine the possibility of phosphorescence interference from TME, the delivery into the chamber was made prior to addition of ozone, so that any phosphorescence signal corresponding to TME could be established before the formation of any oxidation products. Delivery of TME into HIRAC in this order, detected by the PTR-MS at *m*/*z* 85.17, did not produce a phosphorescence signal on the GLYOX-LIP

instrument, and was ruled out as a source of interference. The most likely cause is therefore methylglyoxal, produced through the acetonyl peroxy radical from Criegee intermediate dissociation. Temporal signal profiles measured from PTR-MS data at *m*/*z* 73.07 loosely match with those from GLYOX-LIP data, further reinforcing evidence that methylglyoxal is the primary source of interference here, and complementing the data found during isopropyl nitrite photolysis experiments.

3.3.1.1 Summary

Ozonolysis of TME is an effective source of OH for studying simple, saturated VOCs. Due to the rapid nature of the ozonolysis reaction, OH is produced in quantities of (5 – 10) × 10^7 molecule cm^{-3} for periods of at least 30 minutes, dependent on O_3 and TME concentrations. Consistent, relatively high OH concentrations are ideal for chamber studies where VOCs are present in higher concentrations (~10^{13} – 10^{14} molecule cm^{-3}) than typically found in ambient air, and allows for detecting a smooth VOC decay curve as well as measuring product yields throughout a reaction. The VOC of interest should be kept in excess of TME due to rapid reaction of TME with OH, where k_{OH} = (1.13 ± 0.08) × 10^{-10} molecule cm^{-3}. Study of unsaturated VOCs will result in competition of ozonolysis with that of OH-initiated oxidation, and should therefore be treated with caution, particularly where ozonolysis rate coefficients are large relative to the bimolecular rate coefficient for reaction with OH.

A key disadvantage to generation of OH with this method is the additional complexity of Criegee intermediate chemistry. As this chemistry is not yet fully understood, measurement of product yields from VOC oxidation can be difficult to distinguish from those produced through the Criegee intermediate, either from unimolecular dissociation or reaction with other species in the chamber. In particular, dissociation of the C_3 Criegee, acetone oxide, oxidises into methylglyoxal as a byproduct, which evidence suggests is a significant source of interference for phosphorescence signal measured by the GLYOX-LIP instrument. This will cause difficulties in measurements of glyoxal yields from BVOCs, especially as the interference with this method is so large, and is hence considered a less appropriate source of OH for this work.

3.3.2 Ethylene Ozonolysis

Ethylene ($H_2C=CH_2$), the simplest alkene, presents an alternative for the generation of OH through ozonolysis. The mechanism for OH production is of the same vein as TME ozonolysis, producing the formaldehyde oxide C_1 Criegee intermediate (H_2COO) from unimolecular dissociation of the primary ozonide ($H_2C(OOO)CH_2$) formed. Further decomposition produces the HCO radical alongside OH, which is then oxidised into carbon monoxide and HO_2 (R3.16 – 3.19).

$$H_2C = CH_2 + O_3 \longrightarrow H_2C(OOO)CH_2 \quad \text{(R3.16)}$$

$$H_2C(OOO)CH_2 \longrightarrow HCHO + H_2COO \quad \text{(R3.17)}$$

$$H_2COO \longrightarrow HCO + OH \quad \text{(R3.18)}$$

$$HCO + O_2 \longrightarrow CO + HO_2 \quad \text{(R3.19)}$$

Similarly to TME ozonolysis, the symmetry of ethylene ensures reduced complexity in formation of both the Criegee intermediate and the byproducts in the reaction mechanism, which are primarily formaldehyde and CO. However, despite this distinct advantage in ozonolysis reactions, the OH yield for ethylene ozonolysis has been reported as four times lower than that of TME ozonolysis (Rickard et al., 1999), and several other studies seem to confirm an average OH yield of 0.17 ± 0.04 using a variety of experimental methods including VOC tracers, a cyclohexane scavenger method, and a low pressure LIF-based (Laser-Induced Fluorescence) system (Paulson et al., 1999; Kroll et al., 2001; Mihelcic et al., 1999; Atkinson et al., 1992; Fenske et al., 2000; Alam et al., 2011). The bimolecular rate coefficient for ethylene ozonolysis is also three orders of magnitude lower than that of TME ozonolysis, reported as $k_{O3} = (1.45 \pm 0.25) \times 10^{-18}$ cm^3 molecule^{-1} s^{-1} (Alam et al., 2011), and OH concentrations are therefore expected to be greatly reduced in chamber experiments.

Ethylene ozonolysis was initiated in HIRAC using high ozone mixing ratios (>1 ppmv) to facilitate OH generation, with ethylene concentrations similar to those used in TME ozonolysis experiments (~$5 – 10 \times 10^{13}$ molecule cm^{-3}). As expected, OH was produced at average concentrations around ~$0.5 – 1.0 \times 10^7$ molecule cm^{-3}, measured by the FAGE instrument prior to the addition of any other VOCs (Figure 3.13), at least an order of

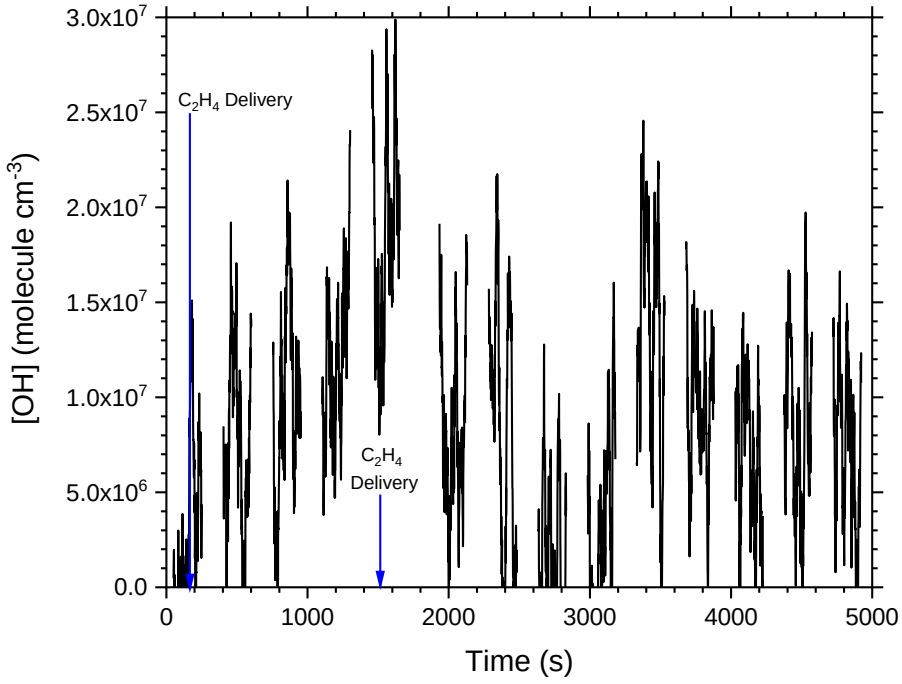

Figure 3.13 FAGE measurements of OH generated through the ozonolysis of ethylene in HIRAC. Ozone (~4 × 10^{13} molecule cm^{-3}) was delivered into the chamber prior to ethylene, and an initial addition of ethylene (~3 × 10^{13} molecule cm^{-3}) followed at ~200 s. A second addition of ethylene (~1 × 10^{14} molecule cm^{-3}) was made at ~1500 s to boost OH concentrations, however after an initial increase, [OH] quickly falls to a steady state approximating $[OH]_{SS} \approx 7 \times 10^6$ molecule cm^{-3}. Data complementary to Figure 3.14.

magnitude lower than the equivalent TME ozonolysis method. Concentrations much lower than this would cause issues with being close to the detection limit of FAGE, which may vary anywhere upwards of 10^6 molecule cm^{-3}, dependent primarily upon the laser power, pressure, temperature and bath gas substituents (see Chapter 4). OH concentrations are further hindered, as with TME ozonolysis, by the reaction of OH with ethylene. Using a previously reported bimolecular rate coefficient of k_{OH} = (8.23 ± 0.33) × 10^{-12} cm^3 $molecule^{-1}$ s^{-1} at 298 K (Cleary et al., 2006), the ratio of k_{O3}/k_{OH} for ethylene oxidation is assumed to be 1.76 × 10^{-7}, compared with ~1 × 10^{-5} for TME oxidation. OH-initiated oxidation will therefore constitute a significant source of removal for ethylene within this ozonolysis system, limiting the maximum OH concentration that may be attained. An approximation of $[OH]_{SS}$ may be made using equation E3.3:

$$[\mathrm{OH}]_{\mathrm{SS}} = \frac{k_{\mathrm{O_3}}}{k_{\mathrm{OH}}}[\mathrm{O_3}]_t Y_{\mathrm{OH}} \qquad \text{(E3.3)}$$

where $[O_3]_t$ is the ozone concentration at time t, and Y_{OH} is the yield of OH from ozonolysis of ethylene, taken to be 0.17. To achieve a steady state OH concentration above 1×10^7 molecule cm^{-3}, ozone mixing ratios should be maintained at ~10 ppmv, however due to such elevated ozone levels, ethylene ozonolysis cannot be considered an appropriate method of OH generation for study of unsaturated VOCs, such as isoprene, that will readily react with ozone. As $[OH]_{SS}$ is largely independent of the concentration of ethylene in this system, this can be kept at lower mixing ratios, as long as a constant flow into the chamber is maintained, thereby helping to reduce removal of OH *via* ethylene when introducing a VOC of interest. A secondary source of OH may contribute to $[OH]_{SS}$ through the reaction of ozone with HO_2 (R3.20):

$$O_3 + HO_2 \longrightarrow OH + 2O_2 \qquad \text{(R3.20)}$$

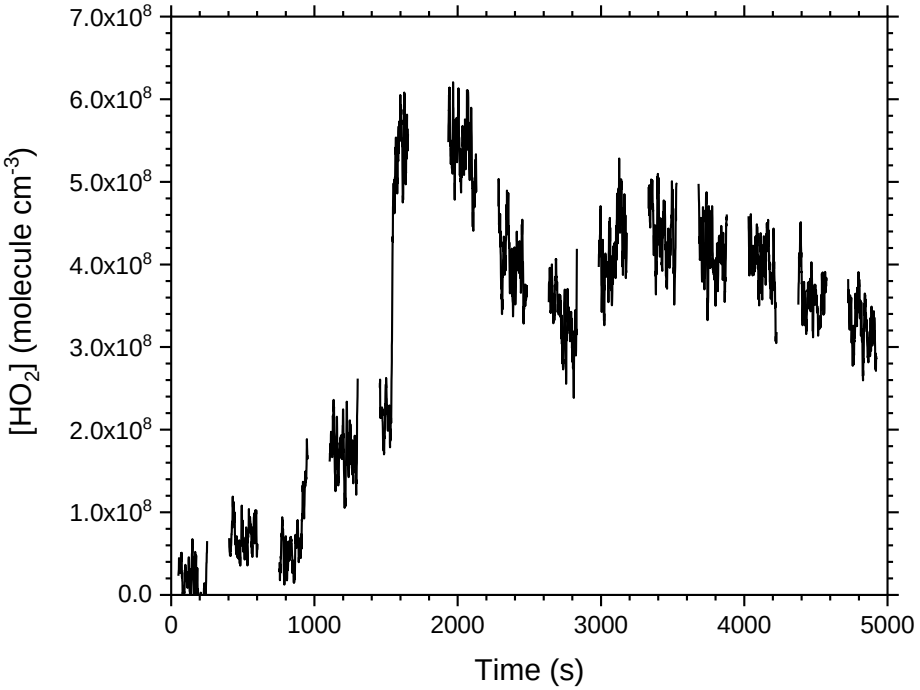

Figure 3.14 FAGE measurements of HO_2 concentrations during ozonolysis of ethylene in HIRAC. Data complementary to Figure 3.13, where the large increase in $[HO_2]$ seen at ~1500 s results from a second addition of ethylene into the chamber, temporarily increasing HO_2 production. $[HO_2]$ does not rise above ~6×10^8 molecule cm^{-3} throughout ozonolysis reaction, limiting capacity for additional OH generation through reaction of HO_2 with O_3.

The recommended bimolecular rate coefficient for this reaction, k_{O3+HO2} = (2.0 ± 0.2) × 10^{-15} cm^3 $molecule^{-1}$ s^{-1} (Atkinson et al., 2004), is three orders of magnitude larger than that for ethylene ozonolysis, however HO_2 concentrations were measured between (1 – 5) × 10^8 molecule cm^{-3} in this system with the FAGE instrument (Figure 3.14), lying between five and six orders of magnitude lower than ethylene throughout an experiment. Under these experimental conditions, only a very small quantity (<1 %) of OH will come from reaction of O_3 with HO_2, however this may become a more important source of OH for this system at lower ethylene mixing ratios (10 – 100 ppbv).

The OH-initiated oxidation of ethylene is a known source of glyoxal in the atmosphere (Fu, T.-M. et al., 2008), and even prior to inclusion of any BVOC oxidation reactions, glyoxal observation through reaction of ozonolysis-generated OH with ethylene is expected. Glyoxal formation was indeed observed with the GLYOX-LIP instrument (Figure 3.15), producing a glyoxal yield, Y_{GLYOX}, of 0.84 ± 0.02 % (Figure 3.16), calculated simply using equation E3.4:

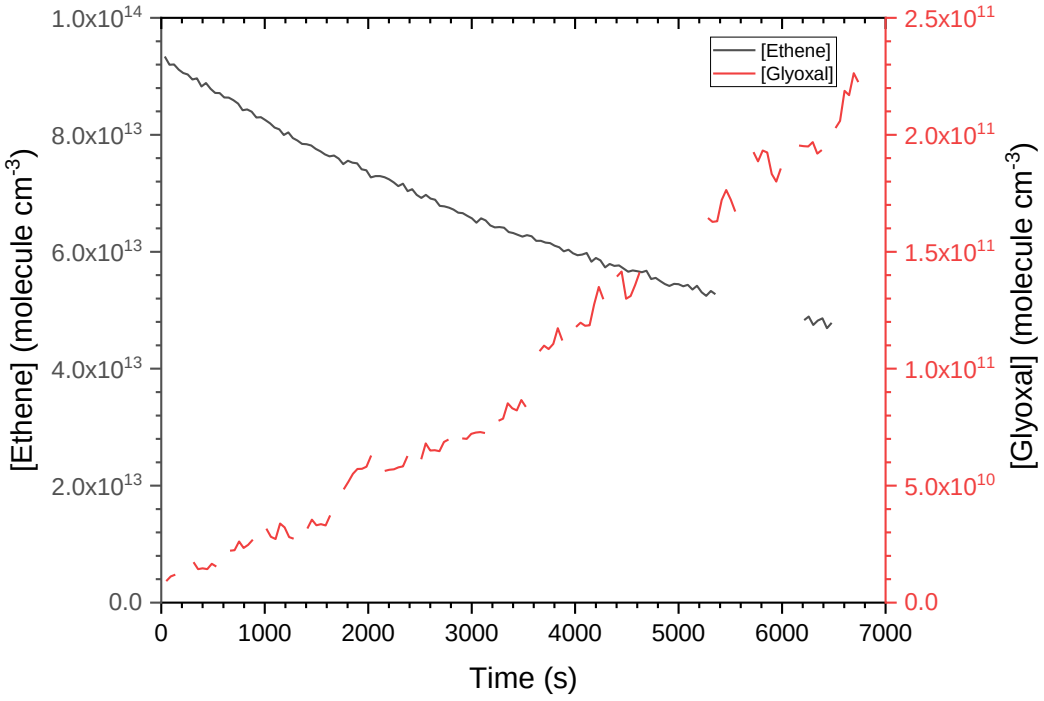

Figure 3.15 Production of glyoxal (red) measured by the GLYOX-LIP instrument during the ozonolysis of ethylene (black) through the reaction of ethylene with OH. Ethylene decay was measured with the FTIR spectrometer, and spectra have a temporal resolution of 44 s. The gap in FTIR data indicates where the spectrometer has paused measurements before restarting scans. Data complementary to Figure 3.16.

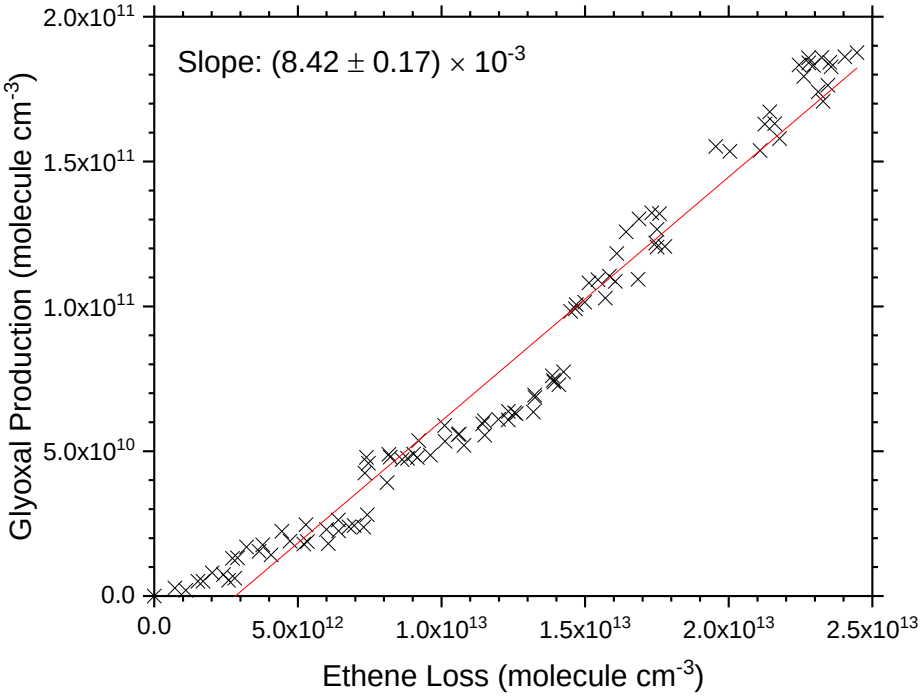

Figure 3.16 Calculated glyoxal yield (0.84 ± 0.02 %) from the OH-initiated oxidation of ethylene. Yield was calculated as the concentration of glyoxal produced against the fraction of ethylene removed as a result of reaction with OH. The fraction of ethylene removed due to ozonolysis was accounted for using measured ozone concentrations throughout the experiment and the predetermined bimolecular rate coefficient, k_{O3} (Alam et al., 2011). Increasing curvature in the yield plot indicates a growth in glyocolaldehyde throughout the reaction as direct glyoxal precursor. Data complementary to Figure 3.15.

$$Y_{\mathrm{GLYOX}} = \frac{\Delta[\mathrm{CHOCHO}]}{-\Delta f[\mathrm{C_2H_4}]_{\mathrm{OH}}} \qquad \text{(E3.4)}$$

where Δ[CHOCHO] is the positive change in concentration of glyoxal, and $\Delta f[C_2H_4]_{OH}$ is the fraction of the negative change in concentration of ethylene as a result of removal *via* OH. Removal of ethylene through reaction with O_3 was accounted for by measuring ozone mixing ratios using a commercial analyser (see Chapter 2) and determining the fraction of ozone removal through equation E3.5:

$$\left(\frac{-\mathrm{d}[\mathrm{C_2H_4}]}{\mathrm{d}t}\right)_{f_{\mathrm{O_3}}} = k_{\mathrm{O_3}}[\mathrm{O_3}][\mathrm{C_2H_4}] \qquad \text{(E3.5)}$$

where k_{O3} is the bimolecular rate coefficient for reaction of ethylene with ozone, taken to be 1.45×10^{-18} cm^3 $molecule^{-1}$ s^{-1} (Alam et al., 2011). Whilst this yield is not large, it will still cause difficulties in apportioning the source of glyoxal in BVOC oxidation studies through ethylene ozonolysis. However, if ethylene is maintained at a much lower (one or two orders of magnitude) concentration than the VOC of interest, the low yield from ethylene oxidation should have very little impact on the total measured production of glyoxal throughout an experiment. A correction can be applied if O_3 and OH concentrations are known, assuming a consistent glyoxal yield from OH-initiated oxidation of ethylene.

3.3.2.1 Summary

Although the OH yield for ethylene ozonolysis is smaller than that for TME ozonolysis (Rickard et al., 1999), measurable quantities of OH were produced in HIRAC, detected with the FAGE instrument in a range between ~$0.5 – 1.0 \times 10^7$ molecule cm^{-3}. In order to keep OH concentrations above the FAGE detection limit, an ozone mixing ratio of ~10 ppmv should be maintained, however such high ozone concentrations make this method of OH generation inappropriate for study of VOCs with C=C double bonds, such as isoprene, susceptible to ozonolysis themselves. As with TME ozonolysis, ethylene concentrations should be kept at least an order of magnitude lower than the VOC of interest, both to reduce removal rates of OH through reaction with ethylene and consequently to limit production of glyoxal through ethylene oxidation. At lower ethylene concentrations, production of OH through the reaction of ozone with HO_2 will become more significant, and should assist in offsetting the decrease in OH production rates at a lower ethylene concentration. Whilst glyoxal production from OH-initiated oxidation of ethylene is a concern, the yield of glyoxal is low (0.84 ± 0.02 %), and can be accounted for if ozone and OH concentrations are known, apportioning the contribution of ethylene oxidation to the overall glyoxal yield from BVOC chamber studies. However, further studies should be performed on the reaction of ethylene with OH in the absence of O_3 to establish a glyoxal yield when OH constitutes the dominant source of removal for ethylene.

3.4 NO_x-Free Photolysis

The generation of OH molecules in chamber studies from NO_x-free precursors is particularly important in the reaction and yield measurement of BVOCs. Rural environments where BVOC oxidation dominates formaldehyde and glyoxal production will typically contain lower NO_x mixing ratios (~1 – 10 ppbv), most likely emitted through a combination of agricultural soil emissions and wildfires. In these conditions, reactions of peroxy radicals with HO_2 can become more favourable, altering the mechanistic routes to the formation of oxidation products (see Chapter 1).

Whilst alkene ozonolysis achieves the goal of a NO_x-free environment, there is an advantage in producing OH through the photolysis of precursors that are not organic in nature. Additional VOCs in chamber studies can complicate product yield measurements, as demonstrated by the alkene ozonolysis experiments in Section 3.3, and generating OH without additional VOCs removes this factor. This can be achieved through the photolysis of peroxides (RO-OH), which in the case of hydrogen peroxide (H_2O_2), will produce two OH molecules upon cleavage of the peroxide bond (Section 3.4.1). Another method is the photolysis of ozone in the presence of water vapour, coincidentally the primary method by which OH is produced in the troposphere and stratosphere through solar radiation (Section 3.4.2). For these methods, shorter wavelength lamps (254 nm) than those used for alkyl nitrite photolysis were used to increase OH formation rates, and as a result, photolysis rates were increased in a greater number of compounds studied in the chamber, including glyoxal and formaldehyde, therefore this additional source of removal must be taken into account when determining product yields. However, whilst this artificial light source does not perfectly emulate sunlight, it can provide a good indication of realistic product yield ratios where photolysis processes are not negligible under ambient atmospheric conditions. Hydrogen peroxide and ozone are therefore reviewed as photolytic precursors for OH in BVOC oxidation chamber studies.

3.4.1 Hydrogen Peroxide

The photolysis of hydrogen peroxide is an intuitive method of producing OH in VOC oxidation studies. Whilst almost all other sources of OH inevitably involve the generation of byproducts from the precursor compound, hydrogen peroxide photolysis involves only

the production of OH molecules in double the quantity of hydrogen peroxide removed (R3.21):

$$H_2O_2 + h\nu \longrightarrow OH + OH \qquad \text{(R3.21)}$$

This is a distinct advantage in providing the ability to examine the products within one reaction mechanism without the interference from other byproducts causing uncertainty in the measured yields. The UV absorption cross-section for hydrogen peroxide between 190 and 350 nm is well established (Lin et al., 1978; Molina and Molina, 1981; Nicovich and Wine, 1988; Vaghjiani and Ravishankara, 1989), becoming very small ($<10^{20}$ cm^2 molecule^{-1}) above 300 nm (Figure 3.17). Lower wavelength lamps (GE Optica GE55T8/HO) centred around 254 nm (see Chapter 2) must therefore be used, where the cross-section measured by Molina and Molina (1981) at 255 nm is 6.23×10^{-19} cm^2 molecule^{-1}, at least an order of magnitude higher than the cross-section at the wavelengths

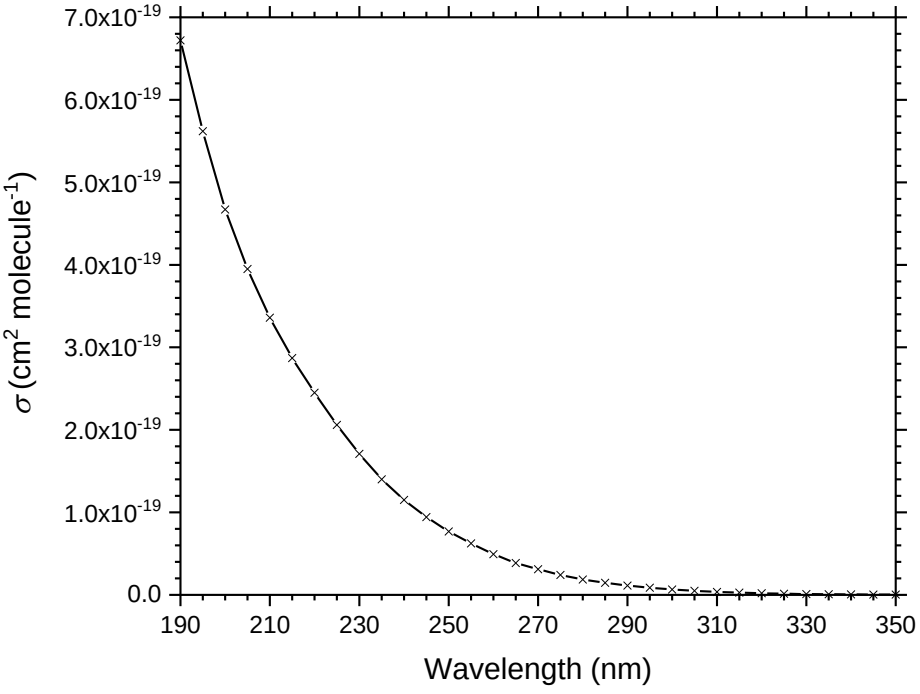

Figure 3.17 The absorption cross-section of hydrogen peroxide between 190 – 350 nm reproduced from data taken by Molina and Molina (1981). The wavelength resolution is 5 nm, and the absorption cross-section at 255 nm, close to the wavelength output for the GE Optica UV lamps (254 nm) measured here is 6.23×10^{-20} cm^2 molecule^{-1}, at least an order of magnitude higher than cross-sections between 300 – 350 nm ($0.3 – 6.6 \times 10^{-21}$ cm^2 molecule^{-1}).

of the blacklamp output. As mentioned previously, this can be disadvantageous by way of promoting photolysis in other species, one such example being acetaldehyde (see Chapter 5), and must therefore be measured separately to determine the loss rate of each species due to photodissociation in HIRAC.

Solutions of hydrogen peroxide (Sigma-Aldrich, 50 wt. % in H_2O, stabilised) were delivered into HIRAC through liquid injection in a stream of nitrogen gas, typically in 1 mL quantities. Liquid injection was chosen over gas delivery partially due to the low vapour pressure of hydrogen peroxide solutions (Giguère and Maass, 1940), and partially due to the volatile nature of peroxide species, decomposing over time at room temperature, particularly in the presence of UV light (Baxendale and Wilson, 1957). A liquid delivery system allows the sample to be stored in the dark at freezer temperatures (~ 255 K) to inhibit decomposition rates. Experiments were performed primarily with acetaldehyde (Sigma-Aldrich, ACS reagent, ≥ 99.5 %) present in concentrations between $5 – 10 \times 10^{13}$ molecule cm^{-3}, to examine the quantity of OH generated in the presence of

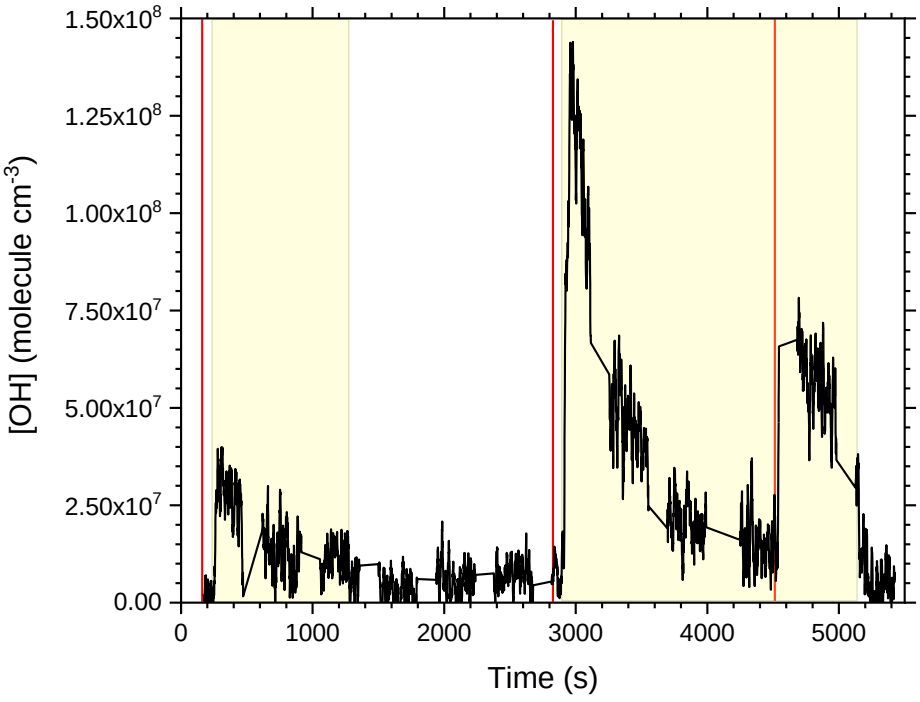

Figure 3.18 FAGE detection of OH generated in HIRAC through the photolysis of hydrogen peroxide using 254 nm UV lamps. Activation period of the lamps is shown in the yellow shaded area. Red lines indicate injections of hydrogen peroxide (1 mL) into the chamber. After a second hydrogen peroxide addition, [OH] reaches as high as 1.4×10^8 molecule cm^{-3}. Data are complementary to Figure 3.19.

a VOC of interest (see Chapter 5), initiating oxidation of acetaldehyde through activation of the UV lamps cleaving the peroxide bond.

Activation of the lamps after a single injection of hydrogen peroxide saw OH concentrations initially peaking at 3×10^7 molecule cm^{-3}, whilst a second injection during the middle of a reaction yielded as much as four times higher OH concentration before gradually decaying to a lower steady state (~$1 – 2 \times 10^7$ molecule cm^{-3}) as the hydrogen peroxide was depleted (Figure 3.18). Significantly higher peak OH concentrations are expected with the second injection of hydrogen peroxide, noting that the acetaldehyde present in the chamber will be oxidised relatively quickly due to its high bimolecular rate coefficient (see Section 3.2.2 & Chapter 5). Typically, at least one third of the total acetaldehyde is depleted upon a second addition of hydrogen peroxide (Figure 3.19), lowering the removal rate of OH enough to increase the average concentrations.

Although hydrogen peroxide may produce among the highest OH concentrations of any precursors investigated here, evidence has shown that the presence of hydrogen peroxide in HIRAC increases the removal rate of glyoxal, even with UV lamps deactivated and all

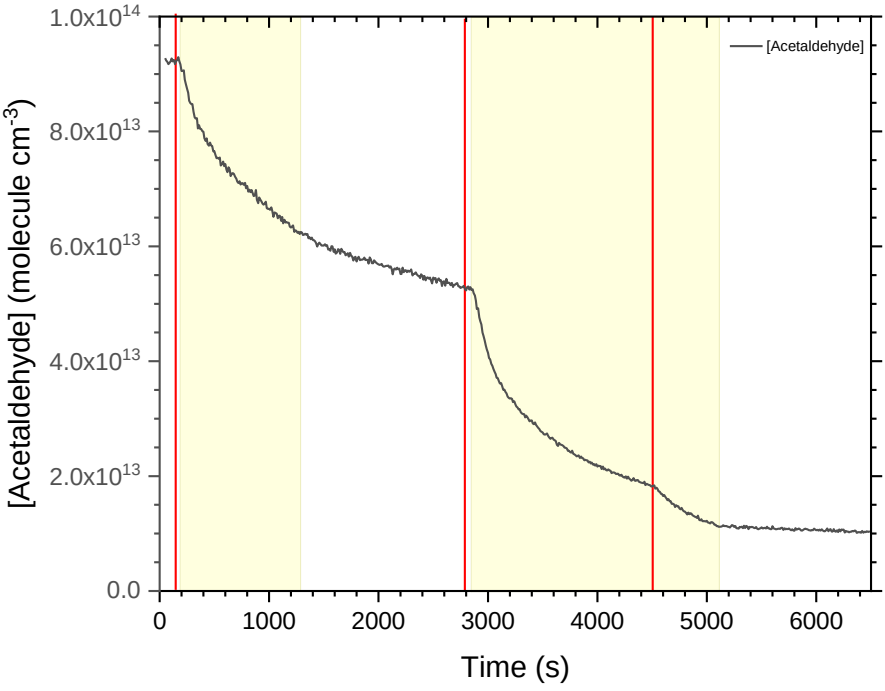

Figure 3.19 A typical VOC decay profile, measured through PTR-MS spectra with a time resolution of 10 s, for the OH-initiated oxidation of acetaldehyde through hydrogen peroxide photolysis. Red lines indicate injection of hydrogen peroxide (1 mL) into HIRAC, and yellow shaded areas indicate activation of 254 nm UV lamps, generating OH. Data are complementary to Figure 3.18.

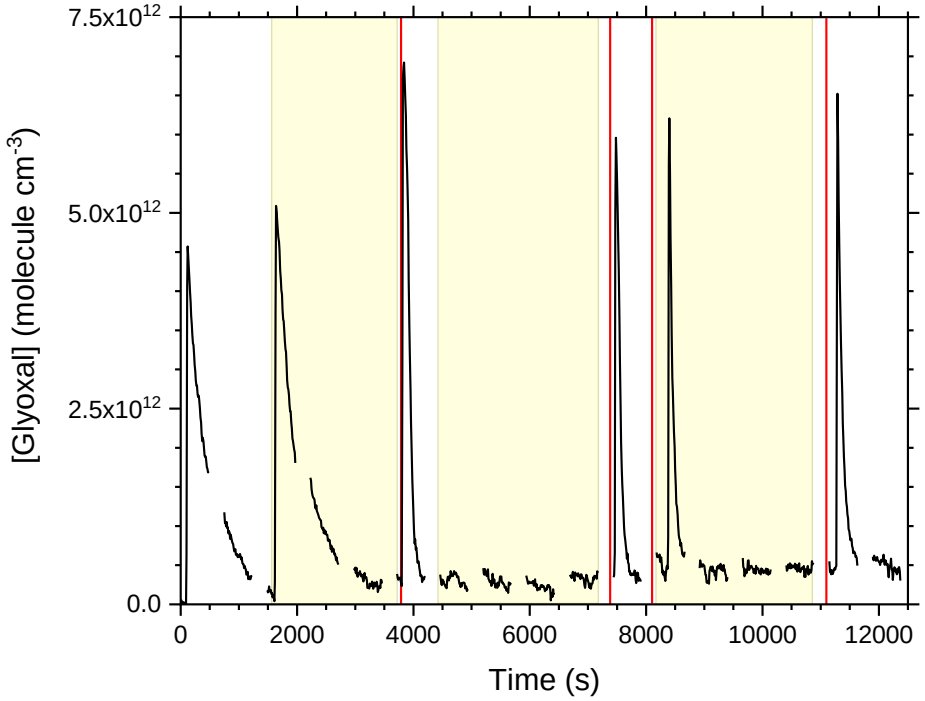

Figure 3.20 Measurements of glyoxal additions into HIRAC, detected using the GLYOX-LIP instrument. Chamber contained only an air mixture at 1000 mbar pressure prior to addition of glyoxal. Red lines indicate injections of hydrogen peroxide solution (50 wt. % in H_2O), and yellow shaded areas indicate activation of 254 nm lamps. The plot demonstrates rapid removal of glyoxal as a result of wall loss, dilution, photolysis and heterogeneous uptake into the aqueous phase. Removal rates are amplified by the presence of hydrogen peroxide solution, even without OH generation, giving strong evidence for the swift uptake of glyoxal into aqueous solution due to hydrogen peroxide injections into the chamber.

OH eliminated from the chamber (Figure 3.20). Although there have been no studies of any direct interactions between glyoxal and hydrogen peroxide, it is known that glyoxal in the gas phase will readily undergo heterogeneous uptake by water molecules and aerosols (Schweitzer et al., 1998; Volkamer et al., 2007; Corrigan et al., 2008). It is therefore likely that the volume of water added into HIRAC through the hydrogen peroxide solution exacerbates the removal of glyoxal in the chamber through uptake into the aqueous phase.

Glyoxal loss in HIRAC experiments is rapid compared with other VOCs, and a first order loss rate coefficient was measured after the introduction of glyoxal to the chamber filled only with an air mixture, where k_{loss} = (2.28 ± 0.03) × 10^{-3} s^{-1}. This loss rate is a combination of instrument sampling dilution, heterogeneous uptake and adsorption onto the chamber wall surfaces, and whilst wall surface loss may be altered slightly across the duration of an experiment due to surface saturation, sampling dilution is consistent at all

times. Introduction of the hydrogen peroxide solution, with lamps deactivated, saw a significant increase of this first order loss rate, averaging $k_{loss} = (1.30 \pm 0.35) \times 10^{-2}$ s^{-1}, and is likely be attributable to the increase in water content in the chamber resulting in heterogeneous uptake of glyoxal into the aqueous phase. From results obtained here, it is unclear how glyoxal uptake is dependent on water concentration, and may therefore be difficult to predict during BVOC oxidation studies when generating OH through the photolysis of hydrogen peroxide. Removal of glyoxal in HIRAC experiments at this magnitude may also begin to cause issues when attempting to measure smaller glyoxal yields from BVOCs where the rate of removal of glyoxal nears that of the rate of production, so that little-to-no glyoxal signal is observed.

3.4.1.1 Summary

Hydrogen peroxide photolysis produces among the highest OH concentrations of the reviewed methods covered in this chapter, reaching above 10^8 molecule cm^{-3} immediately following UV lamp activation. This is advantageous for FAGE detection of OH, falling well within detection limits and providing reliable data for use in model constraints. A further advantage lies in the ability to generate OH without the requirement of additional VOCs present, simplifying oxidation mechanisms in the chamber and allowing the measurement of glyoxal yields from BVOC oxidation without interference from other reactions occurring simultaneously. However, introduction of hydrogen peroxide solution to the chamber has been found to inhibit the growth of glyoxal signal through significantly increased loss rates due to heterogeneous uptake into the aqueous phase. The uptake rate coefficient is difficult to establish, and no dependence on water content was identified here, therefore glyoxal yields may prove challenging to accurately quantify without knowledge of the overall loss rate during a BVOC oxidation reaction. Hydrogen peroxide photolysis remains an effective method of OH generation, however glyoxal yields measured through this method should be treated with caution.

3.4.2 Ozone

The photochemistry of ozone is an important source of OH in the troposphere and stratosphere, initiated through solar irradiation at wavelengths below 411 nm (Wayne, 1987; Malicet et al., 1995; Matsumi and Kawasaki, 2003), the mechanism of which

contributes greatly toward the global oxidative capacity of the lower atmosphere. In the UV region, photons have enough energy to produce an excited state singlet atomic oxygen which is capable of reaction with water to produce two OH molecules (R3.22, 3.23) in a similar manner to that of hydrogen peroxide photolysis:

$$O_3 + h\nu \xrightarrow{\lambda < 411\ nm} O_2 + O(^1D) \quad \text{(R3.22)}$$

$$O(^1D) + H_2O \longrightarrow OH + OH \quad \text{(R3.23)}$$

Due to a maximum in the absorption cross-section of O_3 centred around 254 nm (Malicet et al., 1995), O_3 makes an ideal candidate for the generation of OH in HIRAC using 254 nm UV lamps. Ozone photolysis produces singlet atomic oxygen with a quantum yield of ~0.9 at wavelengths below 300 nm (Junkermann et al., 1989; Sander et al., 2000; Takahashi et al., 2002), and any triplet atomic oxygen produced will recombine with molecular oxygen instantaneously at atmospheric pressure (R3.24), reproducing ozone before undergoing photolysis again.

$$O(^3P) + O_2\ (+M) \longrightarrow O_3\ (+M) \quad \text{(R3.24)}$$

As with hydrogen peroxide photolysis, the photolysis of O_3 has the advantage of generating no byproducts in the process of OH formation, simplifying the analysis of VOC species generated during an oxidation reaction. However, unlike with hydrogen peroxide, care must be taken in the study of alkene oxidation reactions using this OH generation method, as there will inevitably be removal of the alkene and subsequent formation of products through ozonolysis in tandem with OH removal. This will likely alter the ratio of products formed as the reaction proceeds through differing mechanistic routes. As with the ozonolysis methods (section 3.3), these two removal rates can be quantified if both OH and O_3 concentrations are known (see Chapter 6).

Ozone was introduced into HIRAC by passing a flow of air mixture over a mercury pen-ray lamp at 184.9 nm, initiating the photolysis of molecular oxygen and generating two triplet oxygen atoms (Okabe, 1978) *via* reaction R3.25:

$$O_2 + h\nu \xrightarrow{\lambda = 184.9\ nm} O(^3P) + O(^3P) \quad \text{(R3.25)}$$

The atomic oxygen can then recombine with molecular oxygen not photolysed in the gas flow to produce ozone as in reaction R3.24. The delivery of ozone into HIRAC was controlled both through setting the air flow rate with a mass flow controller (Brooks Instruments) with Labview software designed to replenish the gas lost in the chamber through sampling dilution, and through varying the mercury pen-ray lamp current. A set flow rate at ~8 slm ensured a steady, consistent delivery of ozone into HIRAC throughout an entire experiment, whilst the lamp current was altered to determine the rate of production of ozone in the gas flow. A lamp current of ~12 mA at the set flow rate was typically sufficient to maintain ozone concentrations in the range of ~2.0 – 2.5 × 10^{12} molecule cm^{-3} such that a steady state condition was achieved, where the removal of ozone through photolysis and dilution was balanced by generation of ozone (Figure 3.21). This is particularly advantageous for experiments involving alkenes, which will be prone

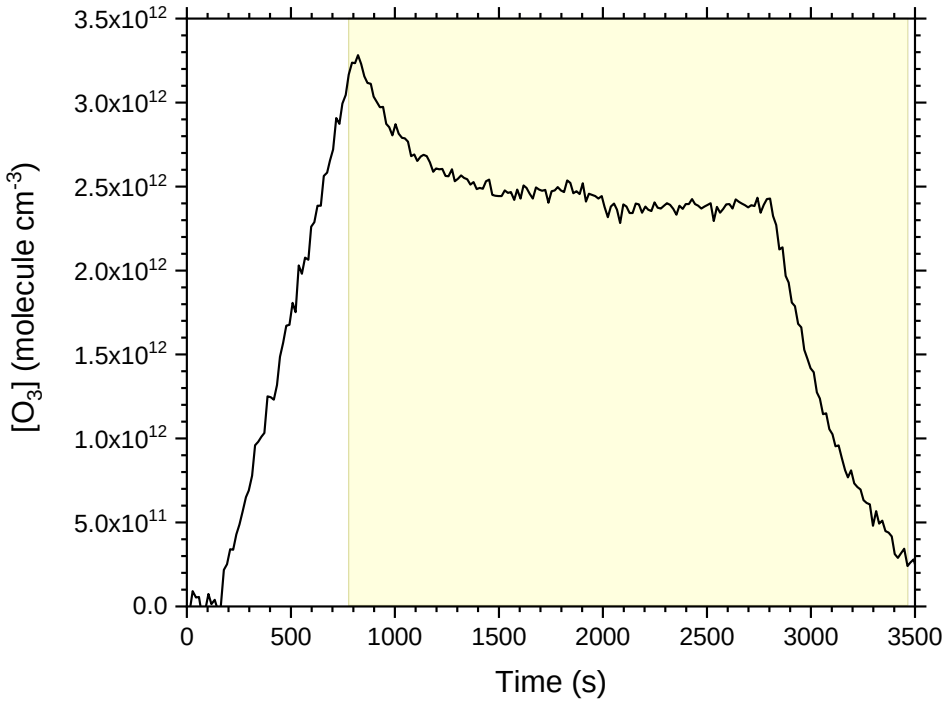

Figure 3.21 Ozone concentrations in HIRAC measured using a commercial O_3 Analyser for generation of OH through photolysis of ozone. Yellow shaded area indicates activation of 254 nm lamps in HIRAC. Ozone was introduced into the chamber through activation of a 184.9 nm mercury pen-ray lamp, resulting in photolysis of O_2 in a flow of air mixture. Production rate of O_3 was varied by altering the current output of the mercury pen-ray lamp, adjusted to achieve an approximate steady state during O_3 photolysis. Data are complementary to Figure 3.22.

to ozonolysis chemistry, where the loss rate for the unsaturated VOC due to ozonolysis may be treated as a pseudo-first order loss for the duration of the reaction, as highlighted in equation E3.6:

$$\frac{-\mathrm{d[VOC]}}{\mathrm{d}t} = [\mathrm{VOC}](k_{\mathrm{OH}}[\mathrm{OH}] + k' + k_{\mathrm{d}}) \qquad \text{(E3.6)}$$

where k_{OH} is the bimolecular rate coefficient for reaction with OH, k' (= $k_{O3}[O_3]$) is the pseudo-first-order rate coefficient for reaction with ozone and k_d is the collective first order rate coefficient for removal of the VOC *via* all other loss processes. Even without knowledge of the exact O_3 concentration, so long as it is known to be constant, k' can be measured easily through analysis of the loss in VOC concentration.

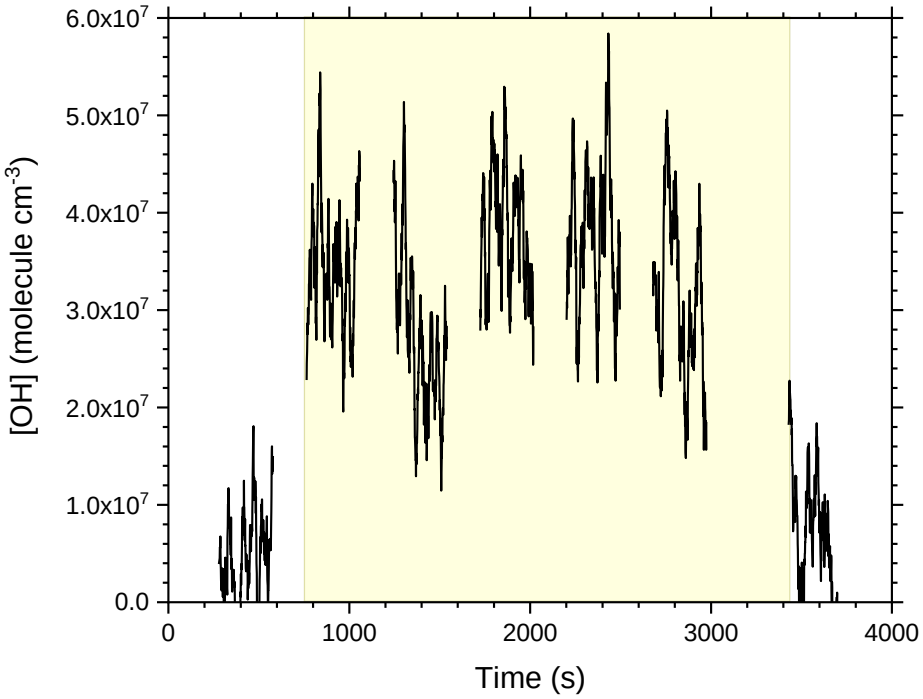

Figure 3.22 OH concentrations generated through photolysis of ozone and measured with the FAGE instrument. Yellow shaded area indicates activation of 254 nm UV lamps, initiating photolysis. OH quickly reaches a steady state approximating $[OH]_{SS} \approx 3.5 \times 10^7$ molecule cm^{-3} for a period of at least 30 minutes. Initial acetaldehyde concentration in HIRAC was $[CH_3CHO]_0 \approx 5.0 \times 10^{13}$ molecule cm^{-3}. Data are complementary to Figure 3.21.

For all ozone photolysis experiments, deionised water (20 mL, ~2.3×10^{17} molecule cm^{-3}) was injected into the chamber through a stream of nitrogen during chamber fills. Injecting the water whilst at low pressure (< 300 mbar) assisted in drawing as much water as possible into the gaseous phase, reducing the clustering of water droplets in the mixing process. Ozone was delivered into HIRAC once filled with an air mixture to atmospheric pressure, building up to concentrations between 2.5 – 3.0 × 10^{12} molecule cm^{-3} before activation of the UV lamps for OH generation. With acetaldehyde present in the system, OH concentrations swiftly reach a steady state around 3.0 – 4.0 × 10^{7} molecule cm^{-3}, maintained for at least 30 minutes (Figure 3.22). Although hydrogen peroxide photolysis is able to reach higher concentrations than this initially, a steady state cannot be maintained for the same period of time, and depletes far more quickly than the duration of a reaction in HIRAC (typically ~1 hour). The ability to easily deliver a steady stream

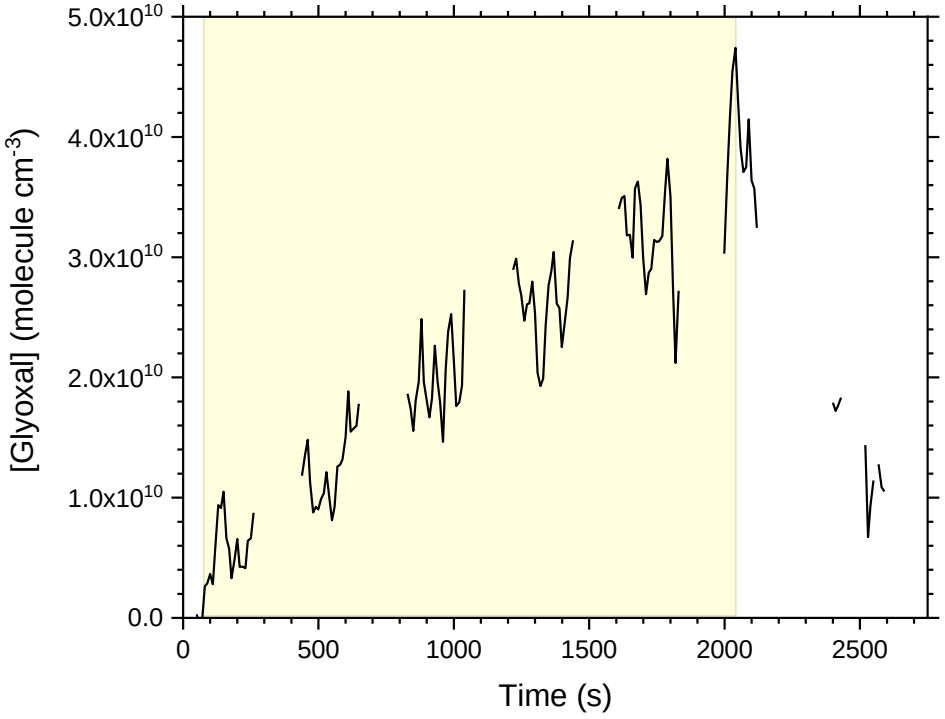

Figure 3.23 Glyoxal concentrations detected by the GLYOX-LIP instrument following the OH-initiated oxidation of isoprene (2-methyl-1,3-butadiene, $CH_2=C(CH_3)CH=CH_2$). OH was generated through UV photolysis of ozone, and yellow shaded area indicates activation of 254 nm lamps. Deactivation of lamps demonstrates rapid loss of glyoxal through wall loss, dilution and heterogeneous uptake by water. First order removal rate coefficient for glyoxal under these conditions, k_{loss} = (1.7 ± 0.2) × 10^{-3} s^{-1}, indicates that the impact of heterogeneous uptake is not as severe as with hydrogen peroxide solution present.

of ozone into the chamber throughout the experiment is therefore a big advantage in OH generation methods.

With the addition of water into HIRAC for OH generation *via* reaction with $O(^1D)$ (R3.23), there was a concern that the increased glyoxal depletion seen with the hydrogen peroxide system would likewise occur during ozone photolysis. To investigate this issue, glyoxal was generated through the OH-initiated oxidation of isoprene (2-methyl-1,3-butadiene, $CH_2=C(CH_3)CH=CH_2$, see Chapter 6) before subsequently deactivating the UV lamps to terminate OH generation and prevent further formation of glyoxal (Figure 3.23). The loss of glyoxal was then observed as a first order process over a 10 minute period, measured as $k_{loss} = (1.7 \pm 0.2) \times 10^{-3}$ s^{-1}. The loss rate measured here is similar to that observed in HIRAC prior to the addition of any hydrogen peroxide, suggesting that the addition of water in the ozone photolysis system contributes very little to the total removal of glyoxal, contrary to the hypothesised heterogeneous uptake seen in the presence of hydrogen peroxide solution. It is possible that the injection of water at lower pressures causes enough dispersion of the water molecules in the chamber that any heterogeneous uptake of glyoxal is less impacted due to decreased clustering of water molecules. Consistent water concentrations across all ozone photolysis experiments may also assist in quantifying glyoxal loss more reliably for input into model simulations. Without the need for any further injections of water once atmospheric pressure is reached, ozone photolysis can be considered a very effective method of OH generation for observations of glyoxal formation from BVOCs. However, in both hydrogen peroxide photolysis and ozone photolysis, simultaneous measurements of the relative humidity in HIRAC alongside glyoxal, O_3 and OH data may be beneficial in characterising loss rates for glyoxal in further chamber studies, crucial to the model simulation of glyoxal yields from BVOC oxidation.

3.4.2.1 Summary

The photolysis of ozone is a simple method of OH generation for chamber studies that, similarly to hydrogen peroxide photolysis, does not create any byproducts that would complicate analysis of the products formed through BVOC oxidation. This method is very effective at producing large quantities of OH, capable of maintaining steady state concentrations between $3.0 – 4.0 \times 10^7$ molecule cm^{-3} over long periods of time relevant for chamber experiments. A controlled flow of O_3 into HIRAC throughout the duration

of a reaction allows a steady state to be achieved with respect to O_3 concentrations, and any ozonolysis rates can be quantified as a pseudo-first-order process through measuring the decay of unsaturated VOCs. Despite the requirement for considerable quantities of water for OH generation through reaction with $O(^1D)$, glyoxal loss rates, particularly due to heterogeneous uptake by water, do not appear to be impacted to the same extent as with the addition of hydrogen peroxide solution. Although loss rates for glyoxal remain unavoidably high compared with other VOCs in HIRAC, this reduced impact from the presence of water makes ozone photolysis an effective method of OH generation for observations of glyoxal from BVOC oxidation.

3.5 Conclusions

The availability of several methods for the generation of OH in VOC oxidation studies is an advantage of simulation chambers that cannot be understated. Selection of OH precursors can be critical in inducing controlled experimental parameters including relative humidity, NO_x concentrations, $[OH]_{SS}$, and photolysis rates. A particular concern of this study is the detection of glyoxal for quantification of glyoxal yields from the OH-initiated oxidation of BVOCs.

The detection of glyoxal *via* laser-induced phosphorescence is highly advantageous in pursuit of this goal, however observational evidence suggests interference of phosphorescence signal due to the production of methylglyoxal, supported by previous evidence and characterisation in the literature (Henry et al., 2012). OH generation methods involving the production of methylglyoxal, namely isopropyl nitrite photolysis and TME ozonolysis, are therefore problematic without the ability to assign methylglyoxal contributions to the normalised LIP signal. Isopropyl nitrite photolysis produces small quantities of methylglyoxal that generate comparative phosphorescence signal counts to those observed in glyoxal detection from BVOC oxidation, and may therefore be distinguishable with further calibration experiments. However, TME ozonolysis generates normalised phosphorescence signal two orders of magnitude higher than those observed in glyoxal yield measurements. Any glyoxal measurements would therefore be unreliable even with subtraction of methylglyoxal data, and TME ozonolysis should be avoided as a method of OH generation.

Ethylene ozonolysis indirectly produces glyoxal through the OH-initiated oxidation of ethylene. Similarly to isopropyl nitrite photolysis, glyoxal yields from ethylene oxidation

should be well established before any attempts are made at measuring glyoxal yields from the OH-initiated oxidation of other BVOCs using ethylene ozonolysis as a source of OH. With experimental measurements of O_3 and OH alongside glyoxal yields, the contributions of ethylene oxidation to glyoxal production can be simulated in model runs, however further work is needed to demonstrate the understanding of current ethylene oxidation models and their accurate simulation of glyoxal yields compared with chamber experiment data. Ethylene ozonolysis may be a valuable comparative method of OH generation for future studies, however was not used further in this work.

Photolysis of hydrogen peroxide, ozone, and methyl nitrite all demonstrate promising measurements of glyoxal from the oxidation of acetaldehyde and isoprene (see Chapters 5 & 6 respectively). Methyl nitrite is recommended as a suitable choice for OH generation with the study of glyoxal yields in the presence of NO_x. Appropriate quantities of OH (~1 – 2 × 10^7 molecule cm^{-3}) were generated in HIRAC, and detectable quantities of glyoxal were observed. However, future work may examine the possibility of investigations into NO_x-dependence studies through greater control of the NO concentration in HIRAC, which may require smaller quantities of both methyl nitrite and VOCs. Further studies should also characterise the yield of formaldehyde from methyl nitrite photolysis in HIRAC under the blacklamps to establish R_{GF} values through the simultaneous measurement of both glyoxal and formaldehyde yields from BVOC oxidation.

All further NO_x-free OH-initiated oxidation studies in this work utilise either ozone or hydrogen peroxide photolysis as OH precursors. The primary disadvantage to either of these methods is the increased loss rate of glyoxal. It is anticipated that due to the high solubility of glyoxal in water (effective K_H = 4.2 × 10^5 mol dm^{-3} atm^{-1}), the increased water content in HIRAC demanded by both of these methods increases the rate of heterogeneous uptake of glyoxal into aqueous solution. Further studies should therefore consider the simultaneous detection of relative humidity alongside glyoxal loss to assess any correlation between water content and increased glyoxal loss rates. However, both ozone and hydrogen peroxide photolysis produce sufficient quantities of OH (~2 – 5 × 10^7 molecule cm^{-3}), and direct measurement of glyoxal loss rates for each of the experimental conditions should be suitable for the model simulation of glyoxal yields.

Chapter 4 A Comparison of FAGE Calibration Methods for OH Detection

4.1 Introduction

Measurements of the hydroxyl radical (OH) provide key information on the chemistry occurring within the lower atmosphere. As the primary oxidant during daylight hours for the extensive range of volatile organic compounds (VOCs) released into the atmosphere (see Chapter 1), OH concentrations contain valuable information on the atmospheric lifetimes for these VOCs (R4.1, R4.2).

$$RH + OH \rightarrow R + H_2O \quad \text{(R4.1)}$$

$$R + O_2 \ (+M) \rightarrow RO_2 \ (+M) \quad \text{(R4.2)}$$

A key element to the measurement of OH, particularly in a laboratory setting, is the reliability and reproducibility of chamber studies monitoring OH concentrations throughout the oxidation of a VOC of interest. The ability to apportion the contributions of VOC removal to OH or any other loss during chamber experiments is paramount to both accurately determining product yields and constraining chamber models in order to predict and emulate any relevant chemistry measured within a particular reaction. The majority of bimolecular rate coefficients for reactions between OH and VOCs relevant for this study are well established (D'Anna et al., 2001; Atkinson and Pitts Jr., 1978; Stief et al., 1980; Yetter et al., 1989; Tyndall et al., 1995; Plum et al., 1983; Feierabend et al., 2008; Dillon et al., 2017; Kleindienst et al., 1982), therefore the contribution to removal of these species by reaction with OH can be determined through concurrent measurements of OH and the desired VOCs prevalent in a reaction. Equation E4.1 demonstrates the two dominant competing methods for the removal of a VOC, denoted over time by -d[VOC]/dt (molecule cm^{-3} s^{-1}):

$$\frac{-\mathrm{d[VOC]}}{\mathrm{d}t} = k_{\mathrm{OH}}[\mathrm{OH}][\mathrm{VOC}] + k_{\mathrm{d}}[\mathrm{VOC}] \quad \text{(E4.1)}$$

where k_{OH} is a generic bimolecular rate coefficient for reaction between OH and any VOC (cm^3 molecule^{-1} s^{-1}), and k_d represents the first order rate coefficient for any other unimolecular loss processes (s^{-1}), typically consisting of surface adsorption, dilution through instrument sampling lines, and photolysis, combined into one parameter. The

assumption that there are no other bimolecular reactions depleting a particular VOC may be tested through comparison of two methods, detailed below, used to determine OH concentration throughout a reaction.

This chapter will investigate the use of the FAGE (Fluorescence Assay by Gas Expansion) technique, a low pressure laser-induced fluorescence (LIF) instrument (Hard et al., 1979) (see chapter 2 for instrument description), in detecting OH radicals, detailing typical FAGE calibration methods through water vapour photolysis (section 4.2.1) and analysing the accuracy of these measurements through comparison with the VOC decay method (section 4.2.2), a means of calculating OH concentrations indirectly through equation E4.1. Whilst historically water vapour photolysis has been successfully employed as the primary method of calibration for FAGE (Creasey et al., 1997a; Faloona et al., 2004), this chapter argues some of the additional benefits to multiple calibration methods and the replication of experimental conditions for chamber reaction studies within the VOC decay calibration technique, as well as discussing the potential for the temperature dependent calibration of FAGE through the intercomparison of two calibration methods (section 4.3).

4.2 FAGE Calibration Methods

As a laser-induced fluorescence (LIF) technique, calculated OH concentrations from a measured fluorescence signal, S_{OH} (counts s^{-1} mW^{-1}), require a pre-determined calibration factor, C_{OH} (counts cm^3 $molecule^{-1}$ s^{-1} mW^{-1}), shown in equation E4.2.

$$S_{OH} = C_{OH}[OH] \quad \text{(E4.2)}$$

This calibration factor is dependent on a number of parameters, including the intensity of the laser light source, owing to the quantity of OH excited from each pulse as a result of laser power, beam width and wavelength line width; the electronic gating time dictating how much of the fluorescence decays is detected; the fluorescence quantum yield of OH as a function of cell pressure and sample gas composition influencing fluorescence quenching; the quality and alignment of optics within the cell; and the quantum yield of the channeltron photomultiplier (CPM) converting collected photons into electrical current (Faloona et al., 2004; Creasey et al., 1997a; Creasey et al., 1997b).

Calibration is therefore a crucial aspect of LIF measurements as it is a non-absolute detection technique, and calibration factors will vary both between FAGE instruments and within the same instrument over time, accounting for any shifts in laser power, CPM efficiency, and any deposit build up on surfaces within the FAGE cell which may affect either OH adsorption or fluorescence detection.

4.2.1 Water Vapour Photolysis

Water vapour photolysis is a method of calibration for LIF-based OH and HO_2 measurements that has been established and since employed over the last three decades, for both chamber and field observations (Aschmutat et al., 1994; Schultz et al., 1995; Heard and Pilling, 2003; Stone et al., 2012; Tan et al., 2017). Water is photolysed at 184.9 nm using a mercury pen-ray lamp to produce an equal ratio of OH and HO_2 (R4.3, 4.4) (Schultz et al., 1995; Fuchs et al., 2011).

$$H_2O + h\nu \xrightarrow{\lambda = 184.9\ nm} OH + H \quad \text{(R4.3)}$$

$$H + O_2\ (+M) \rightarrow HO_2\ (+M) \quad \text{(R4.4)}$$

OH radicals can then be probed directly at 308 nm once sampled by the FAGE instrument, and the resulting resonant fluorescence is measured to give a signal (counts s^{-1}) corresponding to a particular HO_x concentration. HO_2 radicals are converted to OH through reaction with NO (R4.5), which is injected directly into the inlet tube.

$$HO_2 + NO \rightarrow OH + NO_2 \quad \text{(R4.5)}$$

The HO_2 signal is calculated as the difference between signals when NO flow is on or off, accounting for any signal present as a result of the initial OH concentration prior to HO_2 conversion. The raw HO_x (= OH or HO_2) signal is subsequently normalised for the laser power to account for any fluctuations during measurement, giving the normalised signal $S_{OH/HO2}$ (counts s^{-1} mW^{-1}) used in determining $C_{OH/HO2}$ (counts cm^3 $molecule^{-1}$ s^{-1} mW^{-1}).

The OH and HO_2 concentrations must then be calculated for each corresponding signal to provide the calibration data points using the following equation:

$$[OH] = [HO_2] = [H_2O]\phi_{OH}\sigma_{H_2O,184.9\ nm}F_{184.9\ nm}\Delta t \quad \text{(E4.3)}$$

where $[H_2O]$ is the concentration of water vapour present; ϕ_{OH} is the photodissociation quantum yield of OH (molecule photon^{-1}) , taken to be 1 (Fuchs et al., 2011); $\sigma_{H2O,184.9\ nm}$ is the absorption cross-section of water at 184.9 nm, reported as (7.22 ± 0.22) × 10^{-20} cm^2 $molecule^{-1}$ by Creasey et al. (2000) and (7.14 ± 0.20) × 10^{-20} cm^2 $molecule^{-1}$ by Cantrell et al. (1997) at 298 K; $F_{184.9\ nm}$ is the photon flux of light from the mercury lamp at 184.9 nm (photon cm^{-2} s^{-1}) ; and Δt is the exposure time of the gas sample to the lamp output dictated by the flow velocity (s). Within this study, the photon flux and exposure time parameters are obtained simultaneously as a product of one another through actinometric methods, described in more detail in section 4.2.1.3. Concentrations of water vapour are measured using a hygrometer (CR4, Buck Research Instruments), so only the actinometry data are required to calculate OH and HO_2 concentrations at a particular lamp output.

A schematic of the calibration apparatus used is displayed in Figure 4.1 (Winiberg, 2014), and described briefly herein. Water vapour was produced in the apparatus by passing a flow of oxygen free nitrogen (BOC, 99.998%) or synthetic air (BOC, industrial grade, 21 ± 0.5 % O_2) through a bubbler of deionised water. The humidified flow was then passed through a flow tube at 20-40 slm, controlled using mass flow controllers (MFCs), with the mercury pen-ray lamp positioned towards the end of the flow tube. The lamp was attached outside the flow tube with a transparent window introducing the photolysis light source whilst minimising surface interactions and flow disruption for OH and HO_2 produced. The end of the flow tube was positioned immediately before the FAGE inlet to prevent loss of HO_x to the surroundings before sampling. A small flow (10 sccm) of nitrogen was flushed through the lamp casing to avoid any build-up of O_3 around the lamp *via* reactions R4.6 and R4.7.

$$O_2 + h\nu \xrightarrow{\lambda = 184.9\ nm} O + O \quad \text{(R4.6)}$$

$$O_2 + O\,(+M) \rightarrow O_3\,(+M) \quad \text{(R4.7)}$$

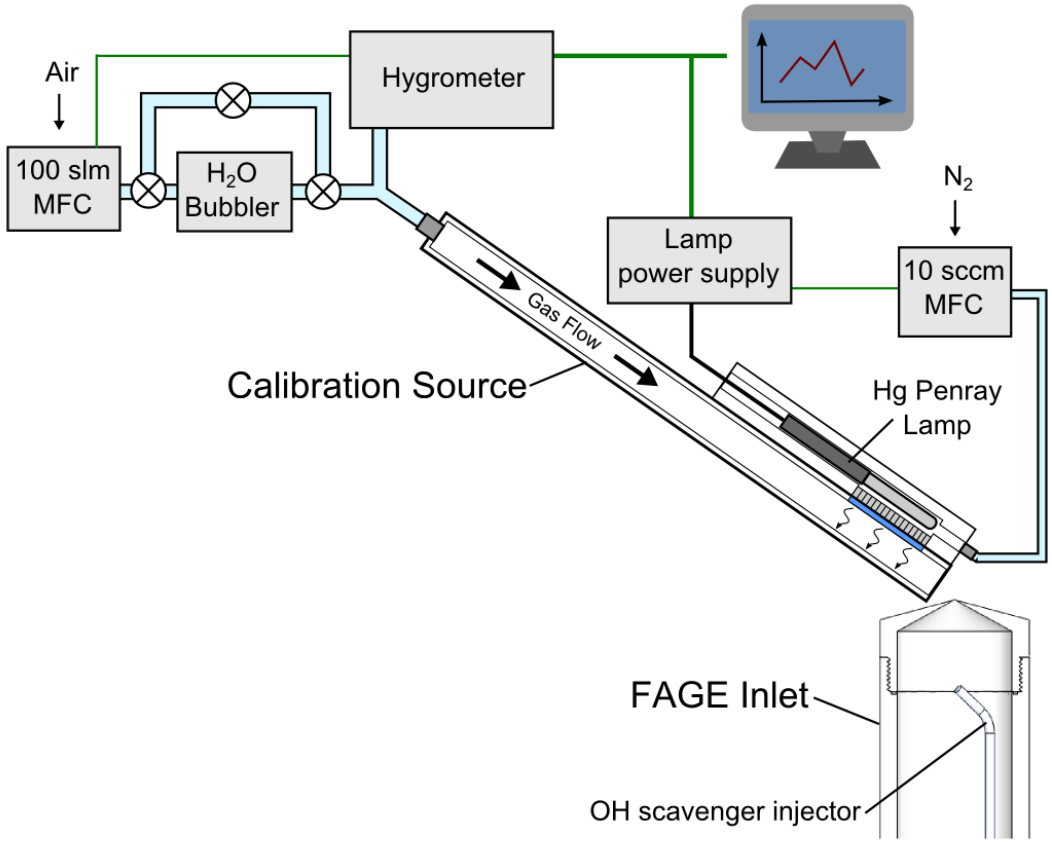

Figure 4.1 A schematic of the apparatus for the water photolysis HO_x calibration of the FAGE instrument. The gas flow used was either air or oxygen free nitrogen. Green lines indicate connections from mass flow controllers, hygrometer and power supply to the PC to control flow rates and record data for lamp current output, water vapour concentrations and flow rates. Crossed circles indicate taps to control proportion of flow through the water bubbler. The OH scavenger injector was not used in this calibration technique, but is discussed in section 4.3.3. Taken from Winiberg, 2014.

The FAGE instrument was then calibrated with a range of HO_x concentrations in both nitrogen and air to obtain $C_{OH/HO2}$ for both sets of conditions used in chamber studies, as a result of the differing quenching efficiencies between oxygen and nitrogen. The HO_x concentrations were altered by adjusting the current in the power supply for the lamp, consequently changing the photon flux of the lamp and hence HO_x production. Each current setting was applied for 1-2 minutes and the resulting FAGE data points (taken every second) averaged over this time period. Data from the MFCs, hygrometer and lamp power supply were collected and recorded on a computer to obtain gas flow rates, water concentrations and lamp current, enabling calculation of HO_x concentrations each second, which could then be averaged.

4.2.1.1 HO_x Calibration Results

Initial calibrations covered a range of HO_x concentrations between (0.18 - 1.00) × 10^{10} molecule cm^{-3} produced through adjusting the lamp current at a set gas flow of 40 slm N_2. Zero lamp output is assumed to produce no HO_x, and performs as a baseline signal for calibrations. Using nitrogen as a bath gas limits reliable measurements to OH only, as it cannot be guaranteed that any O_2 impurities in the bath gas are enough to produce an equivalent proportion of HO_2 (R4.4), however there is an advantage of increased OH sensitivity due to reduced quenching from the lack of oxygen. The normalised and averaged FAGE signal (counts s^{-1} mW^{-1}) at each lamp current was plotted against the respective calculated OH concentrations (molecule cm^{-3}) to produce a linear correlation with slope C_{OH} = (2.33 ± 0.25) × 10^{-8} counts cm^3 $molecule^{-1}$ s^{-1} mW^{-1}. The uncertainty in C_{OH} is calculated from the linear regression of the fit, weighted to uncertainties in both normalised FAGE signals and OH concentrations, which are taken as the standard deviation of each group of measurements to 1σ.

The sensitivity reported here is considerably lower than previous calibrations, with Winiberg (2014) demonstrating FAGE capabilities producing a calibration factor of (4.64 ± 1.68) × 10^{-8} counts cm^3 $molecule^{-1}$ s^{-1} mW^{-1}, performed in a flow of synthetic air, and thus also subject to additional OH quenching due to oxygen content. A decreased sensitivity inevitably leads to a worse signal to noise ratio (SNR) at lower concentrations, and ultimately raises the limit of detection, calculated here as ranging between (7.6 – 10.4) × 10^6 molecule cm^{-3}, when relying on this calibration factor. The limit of detection, $[OH]_{min}$, was calculated using equation E4.4:

$$[OH]_{min} = \frac{SNR}{C_{OH} \times P} \sigma_{offline} \sqrt{\frac{1}{m} + \frac{1}{n}} \quad \text{(E4.4)}$$

where SNR was set to a value of 2, C_{OH} is the determined calibration factor as stated previously, P is the online laser power, $\sigma_{offline}$ is the standard deviation of the unnormalised offline signal, m is the number of online data points, and n is the number of offline data points. The OH concentrations present in typical HIRAC (Highly Instrumented Reactor for Atmospheric Chemistry, see chapter 2) experiments (~10^7 – 10^8 molecule cm^{-3}) are generated in significantly smaller quantities than those measured in water photolysis calibrations (see Chapter 3), and consequently elevate this particular

concern of reduced sensitivity. Further calibrations must therefore be performed to determine the cause of any loss in sensitivity.

The water vapour photolysis calibration method has its limitations in obtaining accurate data. Calibration of the FAGE instrument itself depends on the photon flux of the mercury lamp, which must be determined through actinometry. Performing an N_2O actinometry to determine the photon flux relies on accurate NO_x (= NO + NO_2) concentrations (see section 4.2.1.2) (Edwards et al., 2003; Heard and Pilling, 2003; Faloona et al., 2004; Glowacki et al., 2007a), so calibration of a commercial NO_x analyser (Thermo Environmental Instruments Model 42C Chemiluminescence NO-NO_2-NO_x Analyser, see Chapter 2) must also be undertaken. The subsequent calibrations involved in this method introduce a ~34 % total uncertainty in C_{OH}, calculated from the sum in quadrature of the uncertainties for each parameter in equation E4.3. This total uncertainty is heavily weighted by dependence on several experimentally determined rate coefficients for the actinometric method and measurements of NO concentrations from N_2O photolysis, yielding a photon flux uncertainty of ~32 %, and each calibration stage relies on the validity of all prior calibration results.

4.2.1.2 N_2O Actinometry

N_2O actinometry is a method of measuring the product of photon flux, F, and sample exposure time, Δt, through photolysis of a known concentration of N_2O at the desired wavelength to produce NO, which can then be detected using a commercial NO_x analyser. Initial photolysis of N_2O will produce an excited oxygen atom (R4.8), $O(^1D)$, which subsequently reacts with a another N_2O molecule resulting in formation of two NO molecules (R4.9) (Glowacki et al., 2007a; Edwards et al., 2003; Heard and Pilling, 2003; Faloona et al., 2004).

$$N_2O + h\nu \xrightarrow{\lambda = 184.9\ nm} N_2 + O(^1D) \quad \text{(R4.8)}$$

$$O(^1D) + N_2O \rightarrow 2NO \quad \text{(R4.9)}$$

$$O(^1D) + N_2 \rightarrow O(^3P) + N_2 \quad \text{(R4.10)}$$

$$O(^1D) + O_2 \rightarrow O(^3P) + O_2 \quad \text{(R4.11)}$$

$$O(^1D) + N_2O \rightarrow O(^3P) + N_2O \quad \text{(R4.12)}$$

$$O(^3P) + O_2 (+M) \rightarrow O_3 (+M) \quad \text{(R4.13)}$$

$$O(^1D) + N_2O \rightarrow N_2 + O_2 \quad \text{(R4.14)}$$

The temperature dependent rate coefficients for reactions R4.9 – 4.12 were all taken from Burkholder et al. (2020) and, at 293 K, were considered to be $k_{4.9}$ = (7.76 ± 0.79) × 10^{-11} cm^3 $molecule^{-1}$ s^{-1}; $k_{4.10}$ = (3.13 ± 0.33) × 10^{-11} cm^3 $molecule^{-1}$ s^{-1}; $k_{4.11}$ = (3.98 ± 0.41) × 10^{-11} cm^3 $molecule^{-1}$ s^{-1}; $k_{4.12}$ = (4.96 ± 0.50) × 10^{-11} cm^3 $molecule^{-1}$ s^{-1}; and $k_{4.14}$ = (4.96 ± 0.50) × 10^{-11} cm^3 $molecule^{-1}$ s^{-1}. Although the ratio of NO production to N_2O concentrations depends primarily on the N_2O absorption cross-section, $\sigma_{N2O,184.9\,nm}$, $O(^1D)$ photodissociation quantum yield, Φ_{O1D}, photon flux, and gas sample exposure time, as well as the subsequent reaction of $O(^1D)$ with N_2O (R4.9), a simplified equation of which is stated in equation E4.5, additional complexity arises due to the highly reactive and unstable nature of $O(^1D)$. Upon collision with another molecule, $O(^1D)$ can be rapidly relaxed to the triplet ground state, as in reactions R4.10 – R4.12. Ground state atomic oxygen, $O(^3P)$, will react primarily with molecule oxygen, producing ozone (R4.13). Formation of molecular nitrogen and oxygen will also compete with NO production from the reaction of $O(^1D)$ and N_2O (R4.14). Accounting for these competing removal rates of $O(^1D)$ results in an adjusted fraction of NO produced, displayed in equation E4.6, where the denominator consists of the sum of all removal rates for $O(^1D)$, excepting reaction R4.12, which contributes little to removal *via* N_2O (Nishida et al., 2004):

$$[NO] = 2k_{4.9}[N_2O]^2 \sigma_{N_2O,184.9\,nm} \Phi_{O^1D} F_{184.9\,nm} \Delta t \quad \text{(E4.5)}$$

$$[NO] = \frac{2k_{4.9}[N_2O]^2 \sigma_{N_2O,184.9\,nm} \Phi_{O^1D} F_{184.9\,nm} \Delta t}{k_{4.10}[N_2] + k_{4.11}[O_2] + (k_{4.9} + k_{4.14})[N_2O]} \quad \text{(E4.6)}$$

The N_2O absorption cross-section at 184.9 nm was taken from Creasey et al. (2000), reported as σ_{N2O} = (1.43 ± 0.02) × 10^{-19} cm^2 $molecule^{-1}$ at 298 K, and photodissociation quantum yield of $O(^1D)$, Φ_{O1D}, is taken to be unity (Dusanter et al., 2008). Low NO mixing ratios (~1 – 5 ppb) produced through N_2O photolysis, close to the limit of detection for the NO_x Analyser, make NO detection difficult, and hence increase the uncertainties involved in actinometry data.

The gas sample irradiation time, Δt, was calculated using equation E4.7 in order to determine the average photon flux at each lamp current:

$$\Delta t = \frac{\text{lamp length (cm)} \times \text{lamp cross section (cm}^2\text{)}}{\text{total gas flow (cm}^3\ \text{s}^{-1}\text{)}} \qquad \text{(E4.7)}$$

Typical gas flows within these actinometries constituted synthetic air (BOC, industrial grade, 21 ± 0.5 % O_2) at 40 slm mixed with ~1500 sccm N_2O (BOC, medical grade). Similarly to the water photolysis calibration, data from MFCs and the lamp power supply were logged electronically to determine total gas flow and lamp current. The flow sample was then passed by a mercury pen-ray lamp to initiate photolysis and subsequently through a commercial analyser to detect NO produced from the reaction scheme. The photon flux between an old lamp and a new lamp were compared to determine the change

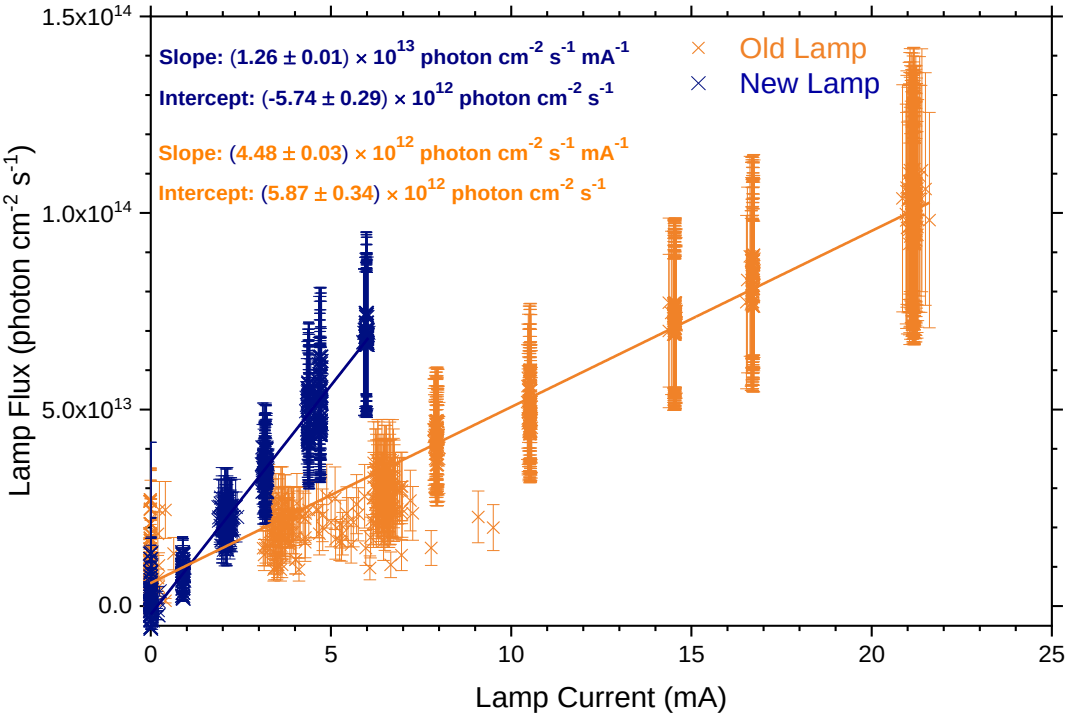

Figure 4.2 A plot of the actinometry data measuring photon flux of mercury pen-ray lamps used in HO_x calibrations as a function of lamp current. Orange data points show the actinometry plot from an old lamp; blue data points show the plot for a replacement lamp. New lamp data demonstrates the increased sensitivity with lamp current input, enabling a wider range of HO_x concentrations to be achieved during calibration of the FAGE instrument.

in sensitivity to lamp current input, demonstrating increased sensitivity with the new lamp (Figure 4.2). The non-zero intercepts observed are partially a symptom of the difficulties

in recording an accurate lamp current at low power inputs, however the large uncertainties involved in calculation of the photon flux (~32 %) due to dependence on the rate coefficients for reactions R4.9-4.14 also have a significant impact on the intercept from linear regression fits. This may be accounted for by an appropriate inclusion of the measurement uncertainties.

The photon flux was calculated over a range of lamp currents between 0 – 10 mA, and a linear regression of the data gave the photon flux of the new lamp as a function of supply current ((1.26 ± 0.40) × 10^{13} photon cm^{-2} s^{-1} mA^{-1}, 32 % measurement uncertainty applied). In increasing the sensitivity of the mercury lamp to the current input, and thus achieving an increased range of HO_x concentrations in water photolysis calibration, a slight increase in sensitivity of C_{OH} through subsequent HO_x calibration was also obtained (1.45 × 10^{-8} counts cm^3 $molecule^{-1}$ s^{-1} mW^{-1} in air), more readily allowing determination of OH concentrations relevant for chamber studies (Figure 4.3).

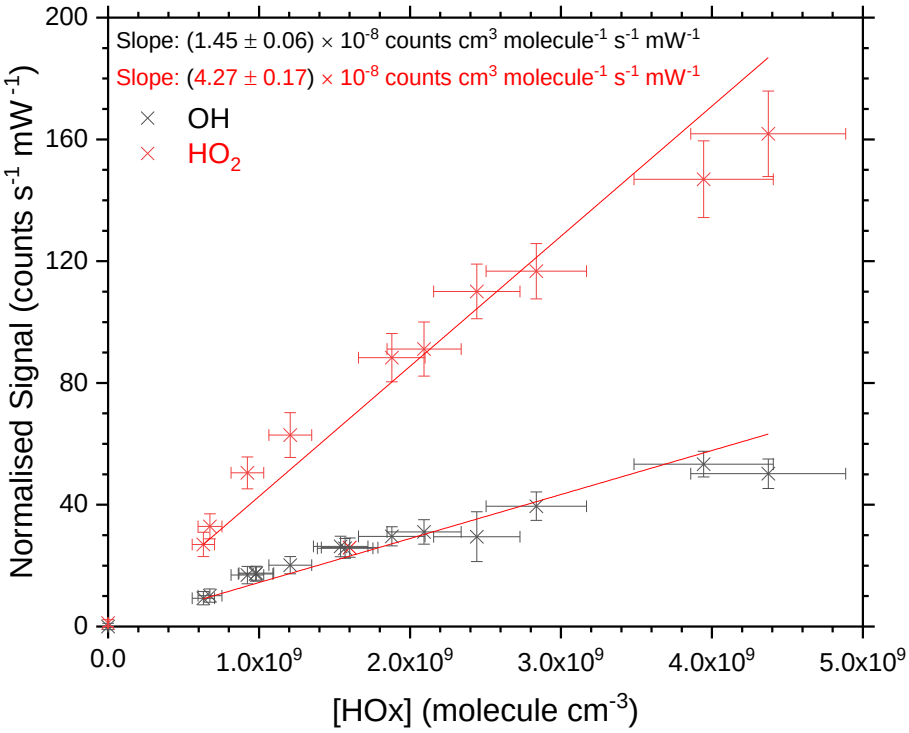

Figure 4.3 Calibration of the FAGE instrument for both OH (black) and HO_2 (red) using the water vapour photolysis method in air. OH and HO_2 were measured within the same FAGE detection cell by alternating a flow of NO on or off. Calibration was performed after replacing the mercury pen-ray lamp as the photon source for water photolysis.

4.2.2 VOC Decay Method

The VOC decay calibration method is a technique that relies on calculation of OH concentrations based on the rate of removal of a VOC *via* reaction with OH, demonstrated previously in equation E4.1. This method is dependent on previous knowledge of the bimolecular rate coefficient for reaction of OH with a VOC, and assumes that this is the predominant removal process involved in the decay. Concentrations of OH can be calculated at any given time point, *t*, through equation E4.1, rearranged to:

$$[\mathrm{OH}]_t = \left(\frac{\frac{-\mathrm{d}[\mathrm{VOC}]}{\mathrm{d}t}}{[\mathrm{VOC}]_t} - k_\mathrm{d} \right) / k_\mathrm{OH} \qquad \text{(E4.8)}$$

where $[\mathrm{OH}]_t$ and $[\mathrm{VOC}]_t$ correspond to the respective concentrations at time *t* (molecule cm^{-3}), -d[VOC]/d*t* is the variable gradient of the VOC concentration over time (molecule cm^{-3} s^{-1}), k_{OH} is the bimolecular rate coefficient for reaction of the VOC with OH (cm^3 $molecule^{-1}$ s^{-1}), and k_d is the unimolecular combined rate coefficient for any other physical loss processes of the VOC (s^{-1}). The gradient values of the VOC decay were calculated using the Savitzky-Golay smoothing method (Savitzky and Golay, 1964) within Origin software, fitting a second order polynomial across 10 – 15 data points either side of a central datum point with a least squares procedure in calculation of the first derivative to improve the SNR. The number of data points used in the smoothing window was dependent on the rate of change of –d[VOC]/d*t*, where a sharper gradient necessitated a smaller smoothing window to avoid overcompensating the data averaging and affecting the OH concentration output.

This calibration method was initially developed for field measurements of OH (Hard et al., 1995), however presents difficulties in generating a VOC decay that can be reliably used to calculate OH concentrations from, and is considered a less practical approach to calibration in the field compared with that of the water vapour photolysis method (Dusanter et al., 2008). The technique has since been employed with EUPHORE (the European Photoreactor Facility) in Valencia, comparing calculated OH concentrations from a number of aromatic hydrocarbon decays detected through Fourier-Transform Infrared spectroscopy (FTIR), displaying reasonable agreement of calculated OH concentrations to within 15 % for the majority of VOCs studied (Bloss, W.J. et al., 2004). Whilst water vapour photolysis remains a more feasible method of calibration for field

studies, the VOC decay technique offers a method of calibrating the FAGE instrument within a range of OH concentrations and experimental conditions relevant for chamber studies of OH-initiated oxidation processes, where calibration is achieved through direct sampling from HIRAC into the FAGE system.

4.2.2.1 Instrumentation

Within these calibrations, VOCs were detected using Proton Transfer Reaction Mass Spectrometry (PTR-MS, see Chapter 2), utilising the ability to measure a range of VOCs with good mass resolution (full width half max m/z = ~0.02 – 0.05) and achieve a good SNR at a measurement time resolution of 10 s for mixing ratios down to ~50 ppb. The PTR-MS sampled gas from HIRAC through a ~10 m length of 1/8" PTFE (polytetrafluoroethylene) tubing with residence time ~22 s throughout the entire course of reactions. The standard ionisation source for PTR-MS involves protonation of the detected species *via* the hydronium ion, H_3O^+ (R4.15), however calibrations here primarily utilised a small flow of nitrogen, promoting N_2^+ as the ionising reagent through a simple electron transfer (R4.16) and consequently avoiding the issue of low proton affinities typical for alkanes; simple compounds that have well-documented bimolecular rate coefficients.

$$RH + H_3O^+ \rightarrow RH_2^+ + H_2O \quad \text{(R4.15)}$$

$$RH + N_2^+ \rightarrow RH^+ + N_2 \quad \text{(R4.16)}$$

The alternative reagent for ionisation enabled detection of simple alkanes as VOC indicators, a desirable outcome for monitoring hydrocarbon decays whilst also reducing any complex chemistry in the system that might interfere with the measured signal for PTR-MS m/z peaks. The glow discharge (GD) ionisation source was set at a reduced voltage of 240 V (compared with a 400 V GD source voltage employing the H_3O^+ ionising reagent) with an internal reactor pressure of 1.50 mbar to minimise fragmentation of molecules upon collision in the reactor and optimise signal of the parent mass peak for the VOCs being monitored.

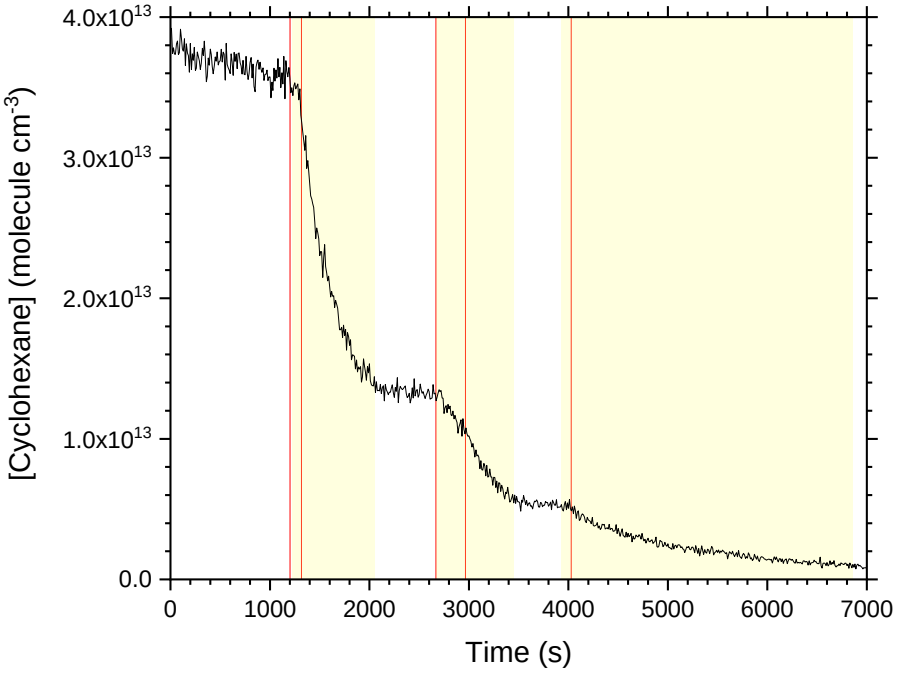

Figure 4.4 An example of a typical cyclohexane decay in HIRAC. Reaction is initiated through UV photolysis of H_2O_2 at 254 nm to produce OH radicals. Red lines indicate points where H_2O_2 is injected into HIRAC in 1 mL quantities. Yellow boxes indicate time periods where UV lamps are switched on.

Production of OH in all VOC decay calibrations was achieved by photolysis of hydrogen peroxide (Thermo Scientific, 50 wt. % in water) at 254 nm (R4.17) *via* eight lamps (GE Optica, GE55T8/HO) positioned equidistantly around the inside of the chamber (see chapter 2 for lamp details).

$$H_2O_2 + h\nu \xrightarrow{\lambda = 254\ nm} 2\ OH \qquad \text{(R4.17)}$$

Four fans positioned at either end of HIRAC allowed constant mixing in the chamber to establish an even distribution of species throughout the reaction. Initial calibrations primarily studied cyclohexane decays at room temperature as the VOC indicator for OH concentrations in HIRAC (Figure 4.4), and all calibration reactions conducted in HIRAC were performed at 1000 ± 3 mbar pressure. Any further investigations and considerations will be discussed in section 4.3 as comparisons with the water vapour photolysis calibration method.

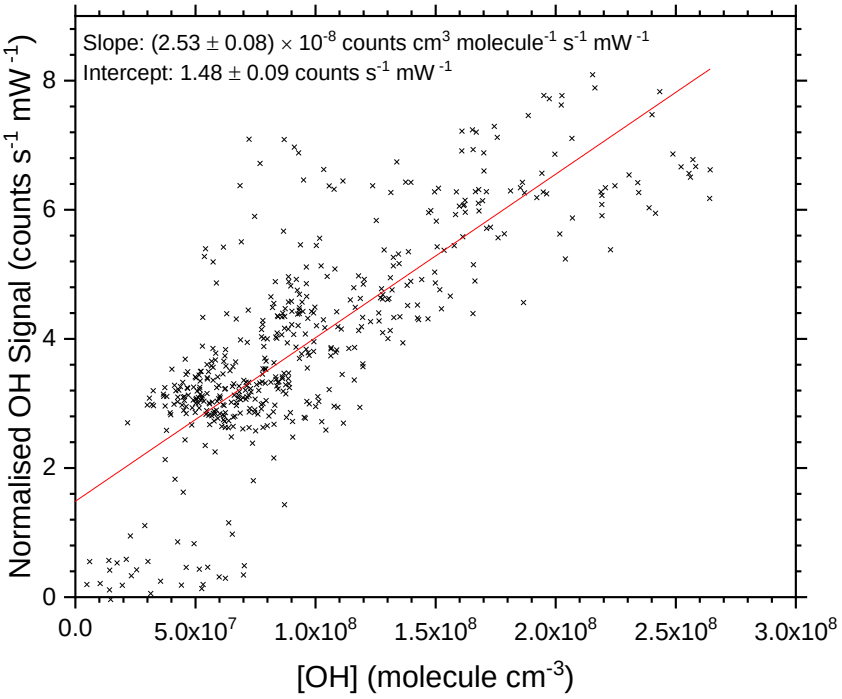

Figure 4.5 An OH calibration plot of the FAGE instrument conducted *via* OH-initiated oxidation and decay of cyclohexane in N_2 at 1000 mbar pressure and 293 K. OH is assumed to be the dominant source of removal for cyclohexane, and any other unimolecular loss rates are accounted for through subtraction from the cyclohexane decay in calculation of OH concentrations (as in E4.8). FAGE signal is normalised for the laser power, accounting for fluctuations measured by a photodiode.

4.2.2.2 Results

Initial calibration factors for the FAGE instrument through cyclohexane decays were determined in the same manner as with the water vapour photolysis method in section 1.2.1.1. Normalised OH signal measured by FAGE sampling from HIRAC was plotted against calculated OH concentrations during the course of cyclohexane depletion. Calibration factors from reactions performed in nitrogen (BOC, 99.998 %) were averaged, calculating a mean C_{OH} = (2.47 ± 0.28) × 10^{-8} counts cm^3 $molecule^{-1}$ s^{-1} mW^{-1}, with the uncertainty, σ_{COH}, propagated from the linear regression of each calibration plot *via* the general equation E4.9:

$$\sigma_{C_{OH}} = \frac{\sqrt{\sum_i^n m_i^2 \sigma_i^2}}{n} \qquad \text{(E4.9)}$$

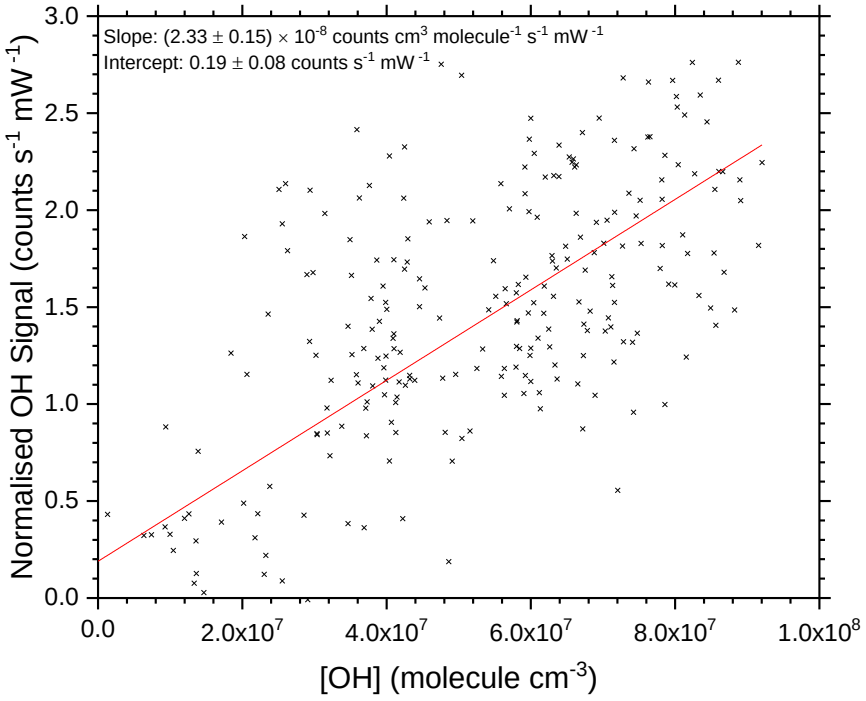

Figure 4.6 An OH calibration of the FAGE instrument conducted *via* OH-initiated oxidation and decay of cyclohexane in synthetic air at 1000 mbar pressure and 293 K. OH is assumed to be the dominant source of removal for cyclohexane, and any other unimolecular loss rates are accounted for through subtraction from the cyclohexane decay in calculation of OH (as in E4.8). FAGE signal is normalised for the laser power, accounting for fluctuations measured by a photodiode.

where m_i and σ_i are the slope and uncertainty of the i-th linear regression fit respectively, and n denotes the number of calibrations considered in the average. An example of a plot determining C_{OH} in nitrogen from a cyclohexane decay is shown in Figure 4.5. Calibrations in air (BOC, industrial grade, 21 ± 0.5 % O_2) were conducted in an equivalent manner, producing a mean C_{OH} = (2.24 ± 0.22) × 10^{-8} counts cm^3 $molecule^{-1}$ s^{-1} mW^{-1}, perhaps surprisingly within error of calibrations performed in nitrogen. A considerably less sensitive calibration factor might be expected as a result of the greater quenching efficiency of oxygen, and comparatively, the wand calibration in air yielded a lower calibration factor of C_{OH} = (1.37 ± 0.07) × 10^{-8} counts cm^3 $molecule^{-1}$ s^{-1} mW^{-1} (see section 4.2.1.2), with a sensitivity approximately 2 times lower than that of the calibration in N_2.

This similarity in signal sensitivities from VOC decay measurements may be caused in part by the level of scatter observed in calibration plots (Figures 4.5, 4.6). Whilst water vapour photolysis calibrations provide an advantage of averaging each HO_x concentration and corresponding normalised FAGE signal over 60 – 120 data points, the nature of

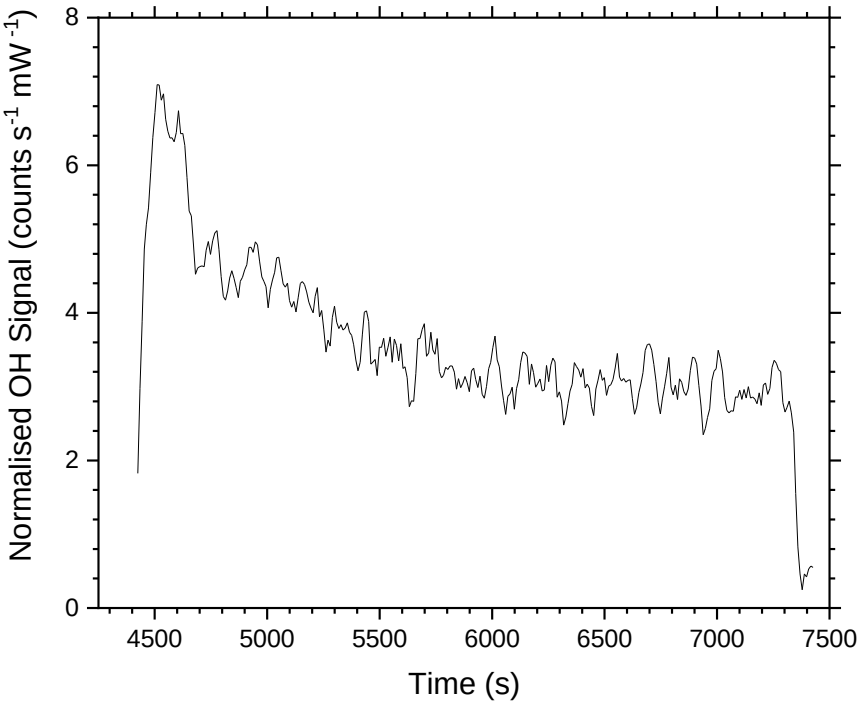

Figure 4.7 A typical time profile for detection of OH sampled from HIRAC *via* the FAGE instrument during reaction with one or more VOCs. FAGE signal is averaged over 10 s to reduce noise in the data. Lamp activation immediately produces a peak in OH concentrations through photolysis of hydrogen peroxide, and during reaction swiftly plateaus to a steady state concentration.

reactions within HIRAC demand much shorter averaging periods due to the variability of OH concentrations as the reaction proceeds. The noise associated with both FAGE and PTR-MS signals then inevitably leads to a much greater level of scatter in VOC decay calibrations.

This similarly has an impact on the resultant positive intercepts observed, particularly at lower OH concentrations which begin to approach the FAGE limit of detection. At concentrations below ~2 – 3 × 10^7 molecule cm^{-3}, the SNR becomes increasingly poor, and the normalised fluorescence signal will therefore be more varied. Another consideration that may impact the non-zero intercepts fitted is any variation in first order loss rates during the VOC decay. It is not possible to distinctly measure the first order loss rate of VOCs due to photolysis, dilution and surface adsorption during reaction with OH, therefore any changes throughout the experiment may cause small inaccuracies in the calculated OH concentration, particularly where, at lower concentrations, first order loss constitutes a larger proportion of all VOC loss.

An additional factor, compounded with greater scatter, is the reduced range of concentrations recorded within chamber reactions. There is a considerable benefit of providing a calibration factor that directly translates onto OH concentrations typical of HIRAC oxidation reactions, however data falling within a small range of concentrations can cause skewing of the linear regression as a result of increased scatter. This would be improved by increasing the range of OH concentrations with a more even distribution, though this would rely on more regulated H_2O_2 additions to control OH concentrations more closely. Calibrating for a longer time period to achieve a larger quantity of data over an increased range would help refine the calibration plots, however this is usually difficult to achieve due to limitations in total lamp actinic flux and quantity of VOC required resulting in a maximum OH concentration available during a reaction, with limited decay times.

Typical OH time profiles upon addition of hydrogen peroxide and lamp activation demonstrate an immediate peak in concentration before subsequent plateauing to an

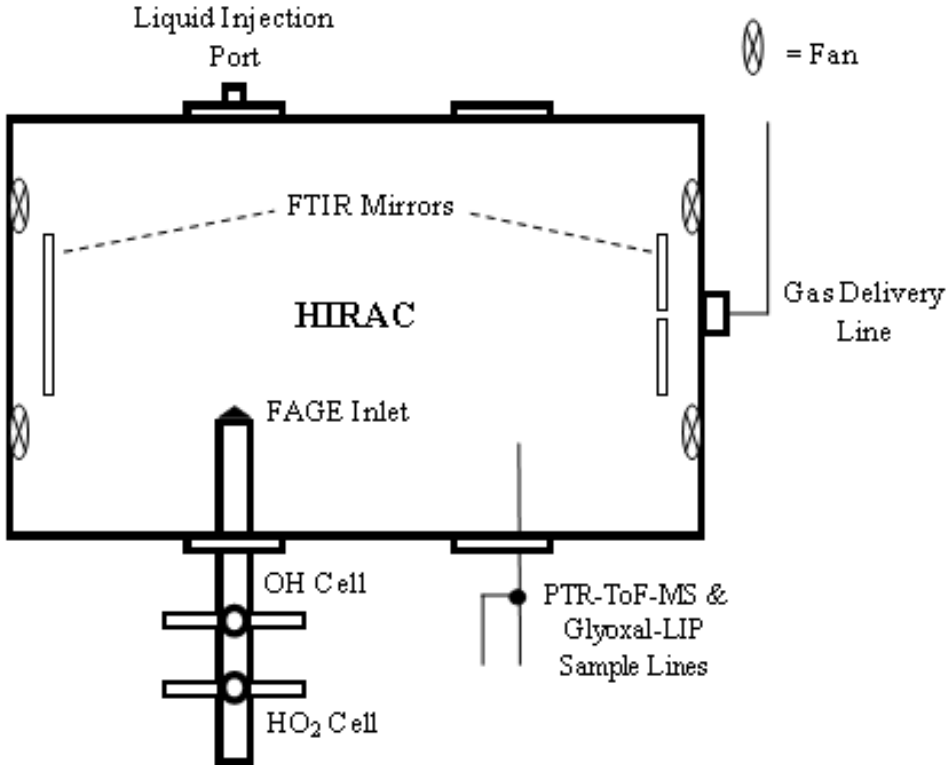

Figure 4.8 A cross-section of the Leeds HIRAC facility as viewed from above. The schematic shows positioning of the instrument sample lines, FAGE inlet, gas delivery line and liquid injection port on separate flanges around the chamber. Fans positioned at either end of the chamber provide a uniform distribution of constituents during the reaction. FTIR mirrors are placed at either end of the chamber to maximise path length of infra-red light and lower limit of detection for spectroscopic measurements, although are not used for the majority of these calibration comparisons. Additional sample lines attached to a port on the chamber ceiling are not shown here.

approximate steady state, where production and removal of OH are near equivalent (Figure 4.7). Whilst this plateauing nature inhibits the sole calibration of FAGE by VOC decay due to lack of concentration range, it does provide an easy means of comparing OH measurements from water vapour photolysis calibration with OH concentrations calculated through cyclohexane decays. Therefore, in an attempt to further validate these calibration methods, an emphasis was placed on the simultaneous comparison of these techniques employed within HIRAC experiments, designed to optimise calibration and reduce uncertainties associated with each individual technique.

4.3 Comparison of OH Calibration Methods

The majority of intercomparison studies focused on reaction of cyclohexane with OH, as in section 4.2.2. The FAGE inlet was positioned inside HIRAC following determination of C_{OH} obtained through water vapour photolysis calibration and FAGE signal, S_{OH}, monitored during the reaction was subsequently converted to OH concentration through equation E4.2. The PTR-MS instrument was connected to a separate sample port adjacent

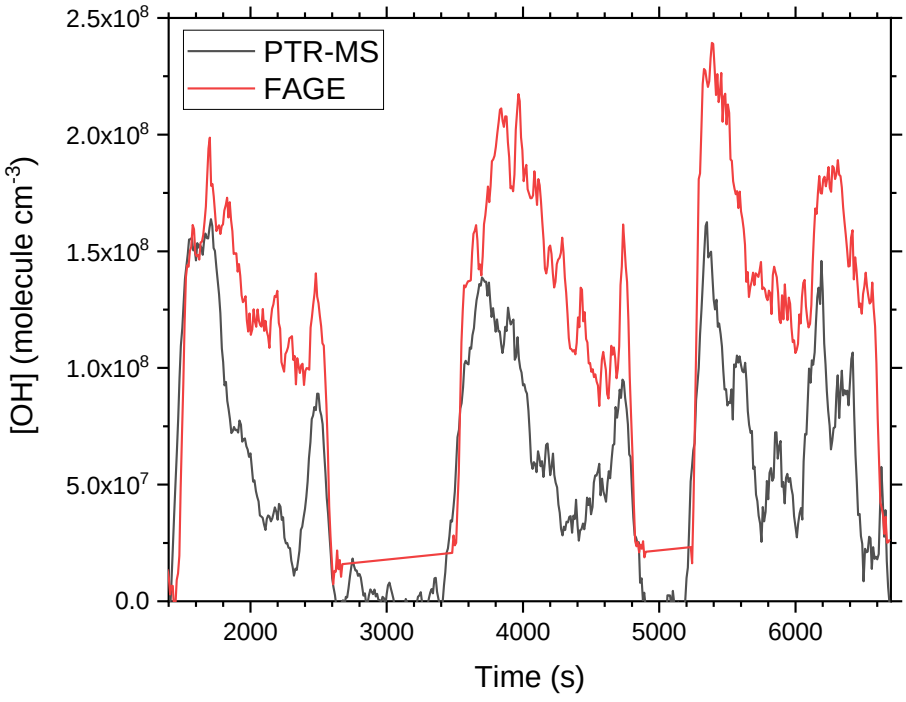

Figure 4.9 A comparison plot of the temporal profiles of OH concentrations throughout reaction with cyclohexane measured both directly through the FAGE instrument (red) and indirectly through calculation *via* determination of the cyclohexane decay rate measured with the PTR-MS instrument (black). Comparison highlights discrepancies in the two measurements, particularly noting an inconsistency in the ratio between both OH profiles throughout the reaction.

to the FAGE inlet (Figure 4.8) to detect cyclohexane *via* N_2^+ ionisation, and OH concentrations were simultaneously calculated from the cyclohexane decay, accounting for other unimolecular loss processes within each reaction. Fans were typically set to 600 rpm to ensure thorough mixing of constituents in the chamber. Hydrogen peroxide (Thermo Scientific, 50 wt. % in water) was introduced as an OH precursor through the liquid injection port opposite the FAGE inlet. OH concentrations determined from both methods were then compared and analysed to account for any discrepancies in the resulting data sets.

4.3.1 Sampling Position

Preliminary results highlight a discrepancy between the temporal OH profiles measured during reaction with cyclohexane (Figure 4.9). Whilst there is a general agreement in the patterns of concentration changes, the ratios between PTR-MS and FAGE based OH measurements are inconsistent, and FAGE measurements often appear to undergo

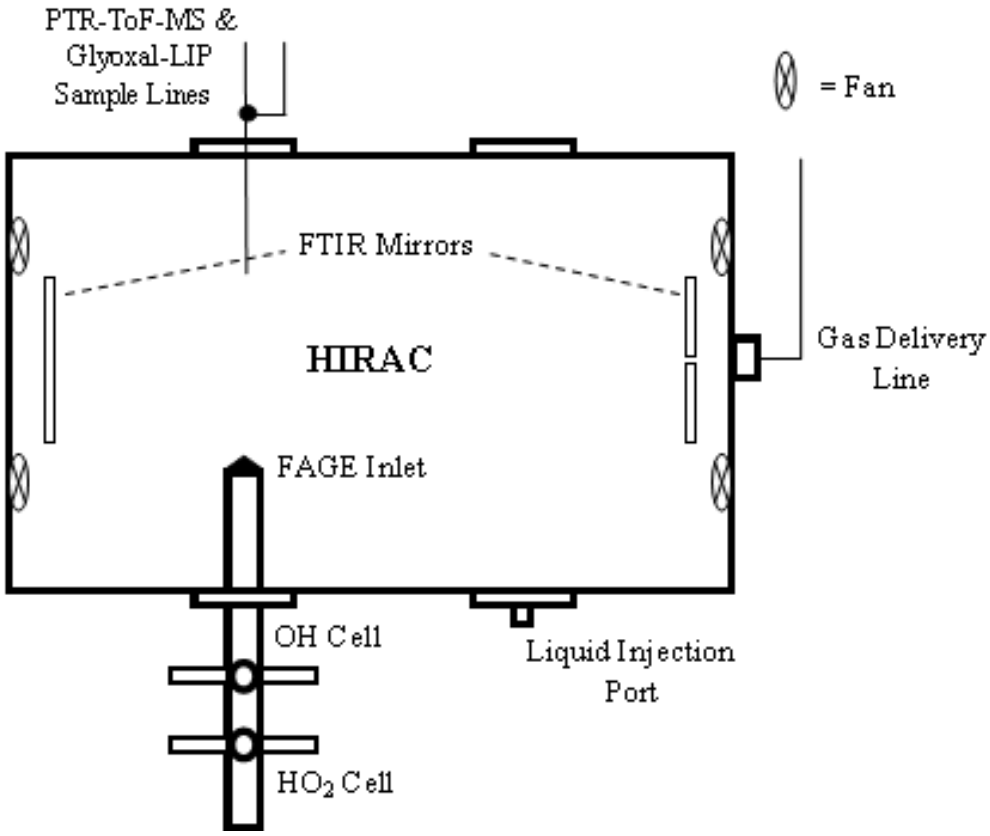

Figure 4.10 A schematic of HIRAC as seen from above. Liquid injection port flange is exchanged with PTR-MS sample line to prevent disproportionation of OH from hydrogen peroxide injections and surface adsorption directly opposite the FAGE inlet. This also ensures FAGE and PTR-MS sampling from within the same region of the chamber, minimising discrepancies in OH comparisons.

reduced decreases where plateauing behaviour is observed approaching steady state conditions. The timescales of these continued patterns suggest a cause alternative to mixing issues, where even distribution of OH should have been attained within ~30 s.

Investigation of the inside of the flange housing the liquid injection port revealed staining within the injection point vicinity. It was theorised that hydrogen peroxide adsorption concentrated around this surface was creating disproportionate quantities of OH closer to the FAGE inlet upon lamp activation prior to diffusion further down the chamber, at the PTR-MS sampling site. To circumvent this issue, flange positions containing the liquid injection port and PTR-MS sampling line were exchanged (Figure 4.10), preventing interference due to any non-uniform elevation of OH concentrations through sampling prior to subsequent diffusion across the chamber. This provided an additional benefit

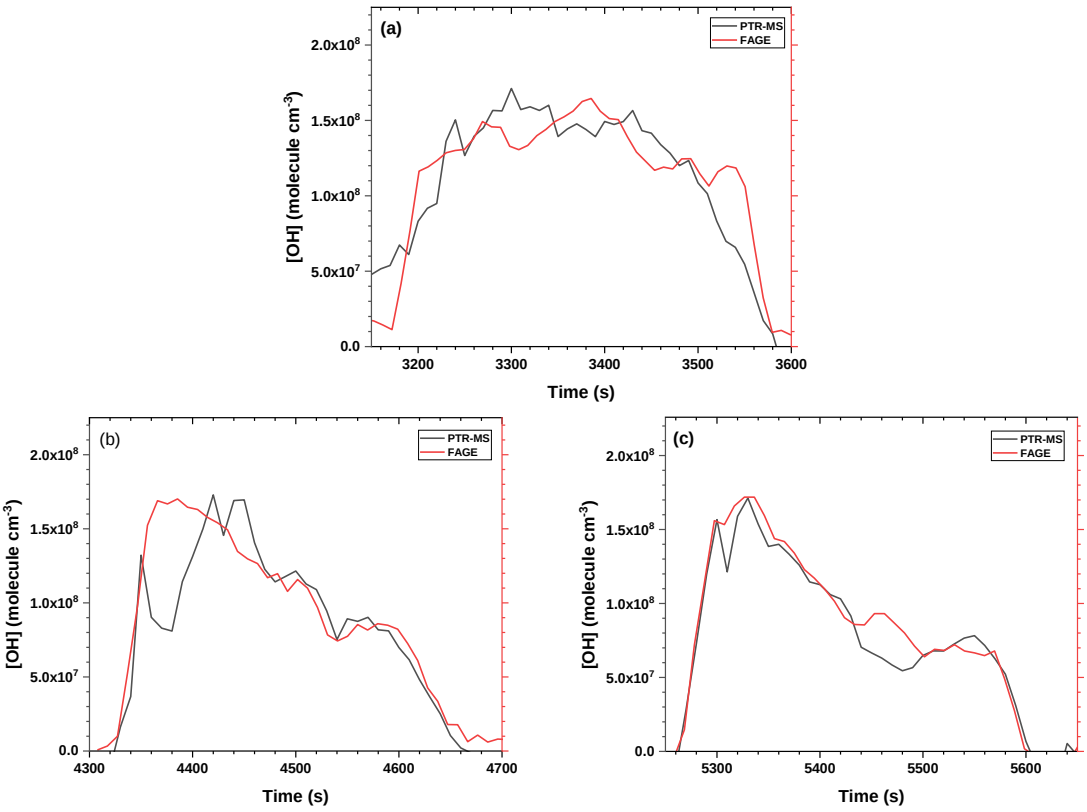

Figure 4.11 Multiple plots of comparison between OH measurements at room temperature during reaction with cyclohexane determined directly through FAGE detection (red) and indirectly through analysis of the cyclohexane decay monitored *via* the PTR-MS instrument (black). Comparisons were performed following exchange of the flanges containing the PTR-MS sample line and liquid injection port, and show excellent agreement between OH concentration profiles. Plots demonstrate three periods across a single cyclohexane oxidation where UV lamps are activated to produce OH through hydrogen peroxide photolysis. An addition of ~1 ml hydrogen peroxide was made before each period whilst lamps were deactivated to increase OH production.

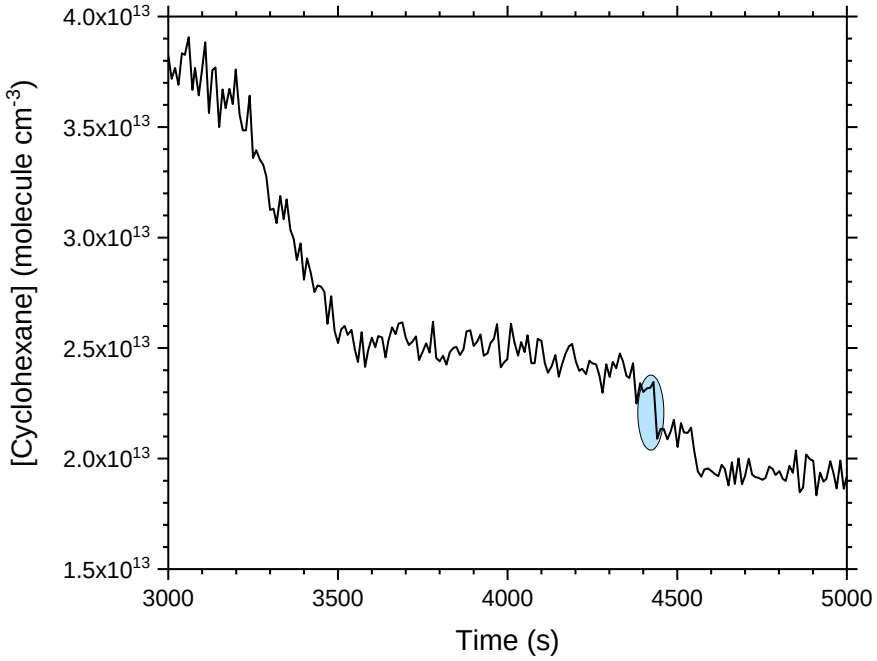

Figure 4.12 A selection of data from a cyclohexane decay at room temperature corresponding with OH measurements shown in Figures 4.11 (a) and (b). Data highlighted in the blue oval indicate a sharp decrease in cyclohexane concentrations caused by noise in the PTR-MS signal, influencing the calculated OH concentrations from the decay and resulting in the discrepancy observed in Figure 4.11(b).

from the FAGE and PTR-MS instruments sampling at points approximately only ~60 cm apart, minimising any discrepancies observed due to differences in sampling region.

Repetition of cyclohexane oxidations under the revised chamber setup following introduction of hydrogen peroxide at the new position yielded OH concentration profiles with much closer agreement between PTR-MS and FAGE measurements throughout entire reactions (Figure 4.11). Minor differences remain within small sections of the concentration comparisons, for example the initial increase in OH concentration observed in Figure 4.11(b). These discrepancies can largely be explained by noise in the PTR-MS cyclohexane data, particularly at lower concentrations further along the reaction time, where signal jumps interfere significantly with Savitzky-Golay smoothing analysis of the decay gradient polynomial fitting (Figure 4.12). This observation highlights the need for meticulous reference to the raw data collected when applying analytical treatment to a large portion of data. However, improved agreement between the two measurement sets provides confidence that OH concentrations determined during VOC oxidations should be accurate when observing the adjusted arrangement of flanges around HIRAC.

4.3.2 Temperature Dependence

Experimental details and data analysis in this section are included in elsewhere as part of a wider study on the temperature-dependent calibration of fluorescence instruments for the detection of OH and HO_2 (Winiberg et al., 2023).

Determining the effects of temperature on instrument sensitivity and therefore C_{OH} is important for investigating reactions appropriate for a multitude of environmental conditions. Measurement of product yields at typical laboratory ambient temperatures cannot necessarily be translated onto equivalent reactions at more extreme temperatures occurring within regional climates around the globe. Temperature impacts a number of parameters that will influence the amount of fluorescence observed at a given OH concentration inside the FAGE OH detection cell; number density; fluorescence quenching; Boltzmann distribution of OH rotational levels; and proportion of OH adsorbed onto FAGE surfaces prior to detection.

The number density, n (molecule m^{-3}), of the gas flow upon sampling through the FAGE inlet can be described, according to the ideal gas equation, by equation E4.10:

$$n = \frac{P}{k_B T} \tag{E4.10}$$

where P is the cell pressure (Pa) , T is the cell temperature (K), and k_B is the Boltzmann constant (1.38×10^{-23} J K^{-1} $molecule^{-1}$). As the FAGE instrument is constantly evacuated at ~2.7 Torr and assumed constant, any increase in temperature will therefore result in a decreased number density and OH fluorescence signal.

Fluorescence quenching is partly influenced by the collisional frequency, Z (m^3 s^{-1}) , defined through equation E4.11 under ideal gas conditions:

$$Z = N_A N_B \sigma_{AB} \sqrt{\frac{8 k_B T}{\pi \mu_{AB}}} \tag{E4.11}$$

where N_A and N_B are the number of molecules of A and B respectively in the sample, σ_{AB} is the collisional cross-section of the two molecules (m^2), and μ_{AB} is the reduced mass of molecules A and B (kg). As N_A and N_B are both dependent on number density and hence inversely proportional to temperature (as in equation E4.9), an increase in temperature will result in a net decrease in collisional frequency and consequently fluorescence quenching. The quenching rate coefficient, k_Q, of OH fluorescence *via* N_2 and O_2 has likewise been shown to decrease with increasing temperature between 204 – 310 K at a rate of ~1×10^{-13} cm^3 $molecule^{-1}$ s^{-1} K^{-1} (Bailey et al., 1997; Copeland and Crosley, 1986), further emphasising an increase in fluorescence signal at higher temperatures due to quenching contributions.

OH fluorescence is monitored at a specific wavelength (~308 nm) corresponding to the $Q_1(2)$ rotational transition of OH, and therefore dependent on the proportion of molecules within a particular rotational energy state. The Boltzmann distribution describes the ratio of probabilities, p_i/p_j, of a molecule occupying energy states i or j, as a function of temperature:

$$\frac{p_i}{p_j} = e^{(\varepsilon_j - \varepsilon_i)/k_B T} \quad \text{(E4.12)}$$

where ε_i and ε_j are the energies of two states, i and j. Considering i as the lower energy rotational state, an increase in temperature will therefore promote a higher proportion of OH molecules into higher rotational states, and consequently reduce detection of the $Q_1(2)$ transition and decrease instrument sensitivity.

As the three quantities discussed above can be calculated as a function of temperature, the primary unknown parameter of concern is the loss of OH molecules to the inside surfaces of the FAGE instrument prior to detection. Surface losses will be characterised predominantly by surface material and inlet tube length before the detection cell, therefore any variation in sensitivity with temperature will be specific to the instrument employed, however only one previous study has attempted to quantify a temperature dependence of C_{OH} for any FAGE instrument (Regelin et al., 2013). Regelin *et al*. demonstrate a slight increase in instrument sensitivity with decreasing temperature between ~268 – 293 K for the HORUS (HydrOxyl Radical measurement Unit based on fluorescence Spectroscopy) instrument, simulating lower temperature conditions by encasing the inlet tube in a

cooling coil, however no high temperature conditions which may be relevant for more tropical regions were explored.

In this study, cyclohexane oxidations were monitored with the PTR-MS instrument at chamber temperatures between 273 – 348 K, varied in HIRAC through thermofluid circulated around steel square tubing surrounding the chamber, controlled with the Huber thermostat unit (model 690W, see chapter 2 for details). OH concentrations were calculated at each temperature *via* the cyclohexane decay rate as in equation E4.8, using the temperature dependent rate coefficient recommended by Atkinson (Atkinson, 2003), and compared with the normalised OH fluorescence signal detected by FAGE. Normalised FAGE signal was converted to OH concentration with the calibration factor determined at room temperature, and ratios of OH concentrations between PTR-MS and FAGE measurements were compared to determine the variation in FAGE instrument sensitivity as a function of temperature.

Cyclohexane oxidations were monitored across four temperatures (273 K, 293 K, 323 K and 348 K) and the resulting ratios of OH concentrations measured plotted against temperature, yielding a minor positive dependence of FAGE instrument sensitivity on temperature with slope $(3.62 \pm 0.10) \times 10^{-3}$ K^{-1} (Figure 4.13). This is seemingly in contrast to the negative dependence observed by Regelin *et al*., however due to the long inlet tube (~280 mm) prior to the OH detection cell in the HIRAC FAGE instrument design (see chapter 2), compared with the 140 mm inlet on the HORUS instrument (Novelli et al., 2014), the positive dependence seen here may be a result of an increased emphasis on wall loss, typically reduced at higher temperatures.

Although any temperature dependence of OH detection will be instrument specific, with this study supplying calibration data solely for reactions studied in HIRAC, these investigations do highlight the opportunity for performing temperature dependent calibrations on other FAGE instruments employed in both chamber and field environments, with the purpose of improving OH data for use in reaction models. Whilst the temperature dependence of instrument sensitivity demonstrated here indicates only minor adjustments required for accurate OH measurements at varying temperatures with the FAGE instrument, this will provide data for model constraint that allows predictions of glyoxal yields from oxidation mechanisms relevant to this project that can be analysed on a temperature dependent basis.

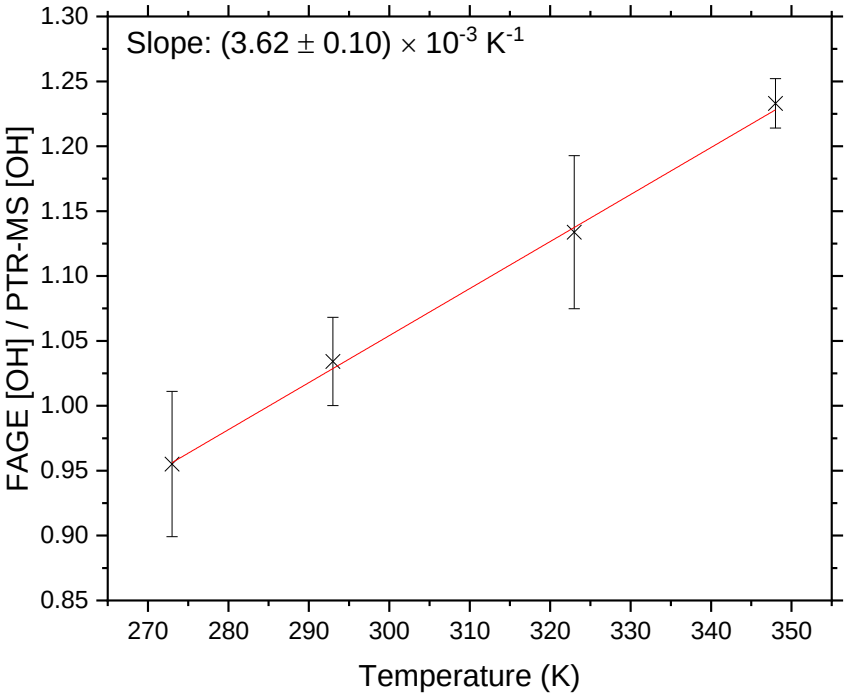

Figure 4.13 A plot showing the ratio of OH concentrations between FAGE and PTR-MS measurements as a function of temperature in HIRAC. Normalised FAGE signal was converted to an OH concentration using the water vapour photolysis calibration factor determined at room temperature. OH concentrations from PTR-MS measurements were determined *via* cyclohexane decay rates using a temperature dependent bimolecular rate coefficient recommended by Atkinson (2003). Concentration ratios were averaged over all measured values during individual experiments at each temperature. Plot demonstrates the increased FAGE instrument sensitivity with increasing temperature between 273 – 348 K.

4.3.3 Isoprene Decays

Final intercomparisons were conducted using isoprene as a VOC indicator for calculating OH concentrations through the hydrocarbon decay method. Isoprene is considered the most abundant biogenic VOC within the troposphere (Guenther et al., 2006), and represents the largest global contributor to glyoxal formation from both biogenic and anthropogenic emissions (Fu, T.-M. et al., 2008). With isoprene playing such a critical role in glyoxal production (see Chapter 6), reaction models constrained with measured OH concentrations are key in developing mechanistic understanding through investigating reaction pathways of isoprene oxidation.

A comparison of OH concentrations between PTR-MS and FAGE measurements was performed during isoprene oxidation at room temperature in HIRAC. As isoprene is more easily ionised through proton transfer and endures minimal fragmentation (Taucher et al.,

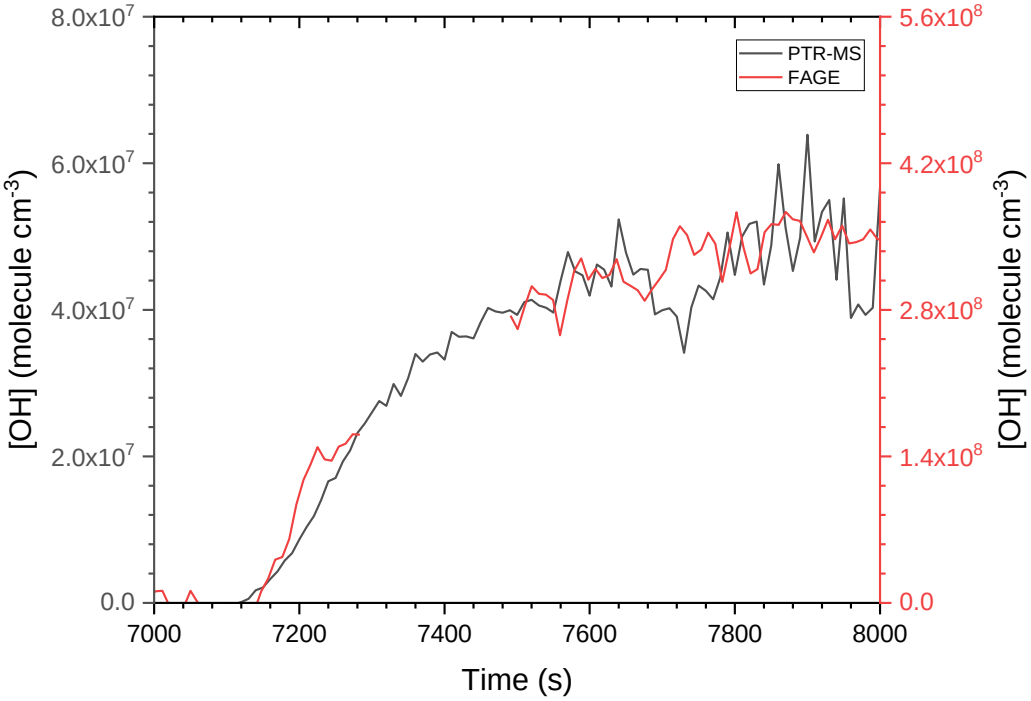

Figure 4.14 A comparison of OH concentrations measured through an isoprene decay *via* the PTR-MS instrument (black) and directly with the FAGE instrument (red). Time profiles follow the same outline, however the FAGE concentration scale (right) indicates OH concentrations a factor of seven higher than those inferred from the isoprene decay curve.

1997), the more traditional method of ionisation, utilising the H_3O^+ reagent, was chosen, as in reaction R4.15. Protonated isoprene ($C_5H_9^+$) was therefore monitored at m/z = 69.12. Reactions were typically conducted at 1000 mbar N_2 (BOC, 99.998%) with initial mixing ratios of isoprene (Sigma-Aldrich, 99%) between 1 – 4 ppm. FAGE measurements were normalised for laser power and converted to concentrations using C_{OH} obtained through water vapour photolysis calibration. Isoprene decays were analysed and converted to OH concentrations using a previously determined bimolecular rate coefficient at 298 K (k_{OH} = (1.04 ± 0.04) × 10^{-10} cm^3 $molecule^{-1}$ s^{-1}) (Medeiros et al., 2018).

Initial isoprene comparisons revealed a large discrepancy between FAGE and PTR-MS measurements, despite earlier agreements observed during cyclohexane oxidations. Although the general time profile follows a similar outline across both instruments, FAGE measurements based on prior water vapour photolysis calibrations indicate OH concentrations at least a factor of seven higher than those inferred from the isoprene decay (Figure 4.14). This behaviour was repeated across several isoprene oxidation reactions where conditions were repeated, however the data showed inconsistencies in the observed C_{OH} from isoprene decays, and hence the calculated OH concentrations. Investigations

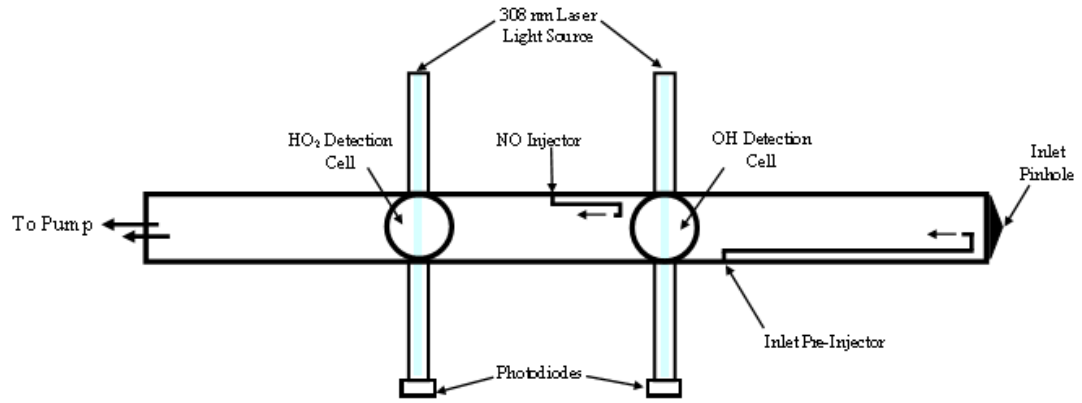

Figure 4.15 An overhead schematic of the FAGE instrument used in HIRAC experiments. Schematic shows positioning of the inlet pre-injector (IPI), comprised of 1/8" aluminium tubing, used to inject propane before the OH detection cell as a method of background measurement by scavenging any OH in the tube before reaching the detector. The tubing starts as close to the detection cell as possible to maximise the distance FAGE may be pushed into HIRAC, and finishes just after the inlet pinhole, slightly off-centre, to avoid disrupting the sample flow whilst making sure all OH molecules present can be scavenged effectively.

were therefore conducted to determine and counteract the source of interference in FAGE signal, in order to obtain an accurate calibration factor appropriate for isoprene studies.

Two methods can typically be employed to determine the background signal for FAGE measurements. The more traditional method shifts the laser wavelength slightly off the transition by ~0.02 nm, which is highly effective for distinguishing between any non-OH based interference in signal due to the narrow structure of the OH transition peaks; OH concentrations determined this way are termed OH_{WAVE}. A second method determines background signal chemically by injecting a scavenger compound into the FAGE tubing prior to the OH cell to facilitate removal of OH before detection using an inlet pre-injector (IPI); determined OH concentrations in this manner are denoted as OH_{CHEM} (Woodward-Massey et al., 2020). Analysis of OH_{WAVE} measurements in the presence of isoprene prior to OH generation demonstrated no difference in the normalised counts from both online and offline signals. This indicates that any interference of fluorescence signal in isoprene experiments occurs either as a result of additional OH chemically or photolytically produced within the FAGE inlet either, or due to a product or radical intermediate that is not observed prior to isoprene oxidation.

To investigate interference through OH_{CHEM} measurements, an IPI was installed into the FAGE tubing shortly after the inlet pinhole with 1/8" aluminium tubing (Figure 4.15). Care was taken in positioning the IPI slightly off-centre to avoid disrupting the sample flow too much upon entering the inlet. Propane (BOC, research grade, 99.95%) was used

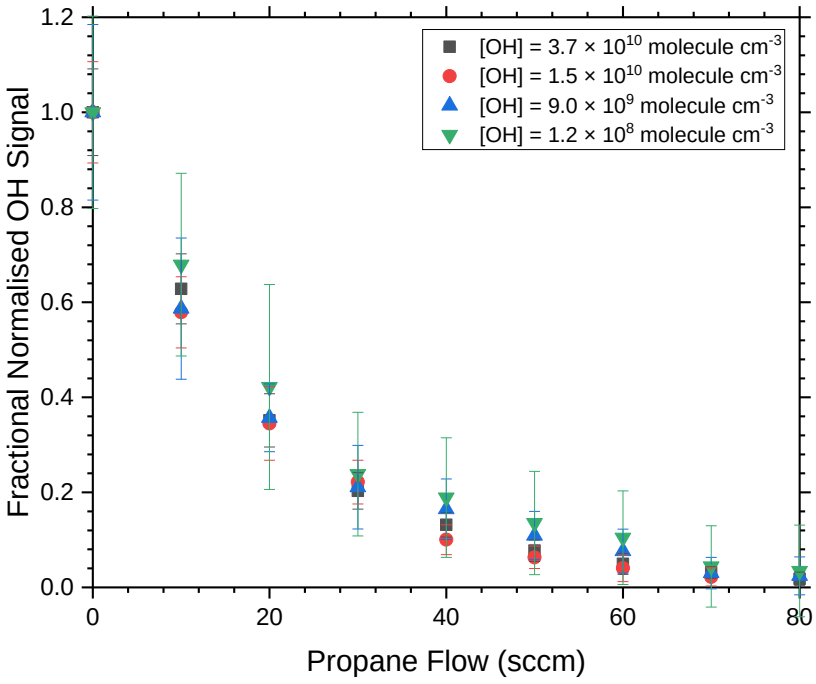

Figure 4.16 A plot demonstrating the fraction of OH removed in the FAGE cell at varying propane flow rates during water vapour photolysis calibration. Fraction of OH removed appears largely independent of OH concentrations, particularly at higher propane flows, and effectively complete removal occurs at 80 sccm propane across all OH concentrations.

as the OH scavenger, and flow rates were controlled *via* a 5 slm MFC (Brooks Instruments). To determine the flow rate required for complete removal of OH, the IPI was activated during water vapour photolysis over 0 – 80 sccm propane flow across a range of OH concentrations (1.2×10^8 – 3.7×10^{10} molecule cm^{-3}), and the fractional removal of OH recorded at each flow rate (Figure 4.16). Fractions of OH removed were found to be largely independent of OH concentration, displaying only minor differences at lower propane flows. Across all OH concentrations, a flow rate of at least 80 sccm was required to ensure complete removal of OH.

Further isoprene oxidations were monitored implementing the IPI to examine the impact on FAGE interference. OH concentrations inferred from normalised FAGE signals were compared during periods with no IPI flow and 80 sccm IPI flow (Figure 4.17). Although a portion of fluorescence signal remained with propane flows activated, OH_{CHEM} measured from this background subtraction remained in excess of concentrations calculated through analysis of the isoprene decay (OH_{ISOP}). Repetition of OH_{CHEM} measurements demonstrated an inconsistency in the ratio of OH_{CHEM} to OH_{ISOP} at varying initial isoprene concentrations, though there was no observable dependence on isoprene

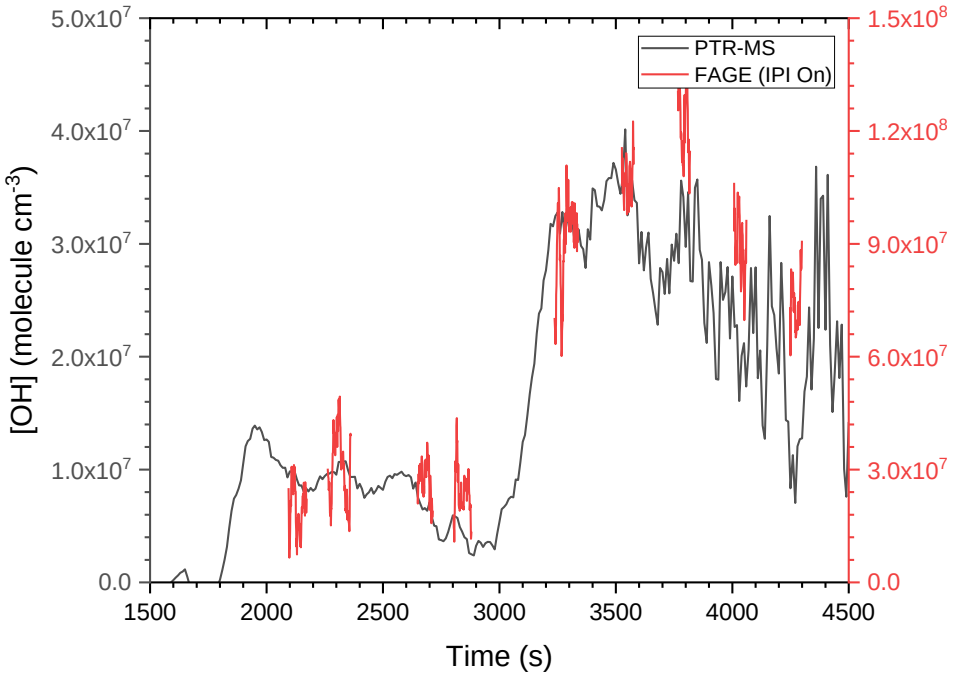

Figure 4.17 Plot shows OH_{CHEM} concentrations observed accounting for background subtraction determined with chemical removal of OH *via* a flow of propane at 80 sccm (red). OH_{CHEM} determinations do not fully mitigate interference observed in S_{OH} for FAGE measurements compared calculated OH concentrations from the analysed PTR-MS isoprene decay (black).

concentrations for the variation in this ratio, and it is unclear what else may be causing the inconsistency without further investigation.

Characterising the source of interference in observed S_{OH} due to isoprene oxidation chemistry has been unsuccessful in this study. FAGE measurements conducted within isoprene oxidations therefore remain unreliable despite efforts to mitigate observed interference using an IPI. Although OH_{ISOP} may still be calculated through PTR-MS measurements, this relies on knowledge of all other isoprene loss rates during reaction, and these should be determined at several timepoints throughout to ensure consistency. Of particular concern may be the generation of ozone within experiments, especially in reactions involving NO_x, which will deplete isoprene through ozonolysis reactions, however ozone concentrations can be measured to account for this loss source. Apportioning the contributions of OH and O_3 to isoprene depletion is crucial in determining the mechanistic routes for glyoxal yields, and are investigated more closely in Chapter 6.

4.4 Conclusions and Future Work

This study has attempted to emphasise the benefits of utilising multiple calibration methods for the FAGE technique in order to reinforce reliability of OH measurements particularly in chamber experiments. Whilst the calibration methods discussed here present both advantages and disadvantages performed separately, combining these methods contributes to minimising the effects of the disadvantages. Room temperature calibrations comparing the water vapour photolysis calibration factor with that calculated from cyclohexane oxidation decays demonstrate remarkable agreement (to within 5%) in comparison of the time profile of OH concentrations during chamber reactions.

Water vapour photolysis calibrations of FAGE were performed with a mercury pen-ray lamp at 184.9 nm. Data quality of calibration plots particularly at lower lamp currents highlight the necessity for regular assessment of the lamp flux through actinometry. Knowledge of the photon flux is critical in calculating HO_x concentrations produced in the photolysis region, and thus providing an accurate calibration factor for FAGE measurements. Results obtained in this study demonstrate the enhanced linearity in determination of C_{OH} upon replacement of the photon source and increase reliability of OH concentrations measured following calibration.

Cyclohexane reactions through OH-initiated oxidation in HIRAC yielded calibration factors for FAGE measurements of OH in both nitrogen ($(2.47 \pm 0.28) \times 10^{-8}$ counts cm^3 $molecule^{-1}$ s^{-1} mW^{-1}) and air ($(2.24 \pm 0.22) \times 10^{-8}$ counts cm^3 $molecule^{-1}$ s^{-1} mW^{-1}). Although C_{OH} values determined with this method are on the order of magnitude comparative to water vapour photolysis calibration ($(2.33 \pm 0.25) \times 10^{-8}$ counts cm^3 $molecule^{-1}$ s^{-1} mW^{-1}), only a minor difference was observed between calibration factors in nitrogen and air, and did not justify the additional quenching efficiency of oxygen compared with nitrogen. Comparison of OH concentrations calculated through C_{OH} factors from both calibration methods indicated disproportionate quantities of OH across the chamber, hypothesised as a result of hydrogen peroxide surface adsorption surrounding the liquid injection port to the chamber. Adjusting sampling positions of the FAGE and PTR-MS instruments relative to the hydrogen peroxide injection point improved similarities between both OH measurements, and emphasises the issues with hydrogen peroxide injections directly opposite or within the immediate vicinity of the FAGE inlet.

A temperature dependence was determined for the HIRAC-based FAGE instrument, reporting a minor positive dependence on instrument relative sensitivity with temperature between 273 – 348 K ($(3.62 \pm 0.10) \times 10^{-3}$ K^{-1}). Any temperature dependence of FAGE instruments will vary depending on the instrumental design, however that reported here allows accurate measurements of OH concentrations across a range of temperatures relevant to tropospheric chemistry appropriate for various climates. Future work should consider the applications of FAGE temperature dependence for investigations of VOC oxidation, product formation and mechanism analysis within HIRAC.

Investigations of OH measurements during isoprene oxidations were conducted, and comparisons found large discrepancies between VOC decay (OH_{ISOP}) and water vapour photolysis (OH_{WAVE}) methods. Installation of an IPI to remove OH after sampling through the FAGE inlet (OH_{CHEM}) did not completely nullify interferences produced within the OH detection cell, and the source of interference in FAGE measurements throughout isoprene reactions remains undiscovered. Further studies should monitor comparisons of OH_{ISOP} and OH_{CHEM} to investigate any dependencies on concentrations of isoprene or oxidation products in accounting for disparities in the ratio of determined OH concentrations from OH_{ISOP} and OH_{CHEM} across isoprene reactions. Further isoprene studies in this work will rely on the VOC decay method for determination of OH concentrations, taking account of ozonolysis reactions, and OH_{ISOP} profiles will be used in model constraints and mechanistic studies of glyoxal formation from isoprene.

Chapter 5 Direct Glyoxal Yields from Acetaldehyde Oxidation

5.1 Background

As mentioned in Chapter 1, the oxidation of acetaldehyde (CH_3CHO) is of interest within the UNFOGs project as a potential missing source of glyoxal in the marine boundary layer (MBL) through H-abstraction at the methyl site. There is a large discrepancy between measured and modelled glyoxal concentrations (displayed in Table 5.1) based on observational constraints (Sinreich et al., 2010; Lawson et al., 2015; Zhu, Y. and Kieber, 2019; Walker et al., 2022) which does not appear to be accounted for by the direct emission of glyoxal from the ocean surface through biological activity (Takeda et al., 2014). A recent attempt to characterise glyoxal sources in the MBL involved the Oceanic Reactive Carbon: Chemistry-Climate impacts (ORC^3) campaign at the Cape Verde Atmospheric Observatory, spanning two four-week segments in the summer of 2014. Glyoxal was detected using the laser-induced phosphorescence (LIP) instrument described previously (see Chapter 2), which was of similar design to that of the Madison LIP (MADLIP) instrument (Huisman et al., 2008). The ORC^3 campaign discovered average glyoxal mixing ratios ranging between 4 and 8 pptv throughout a typical 24 hour period. However, base models, which did not include constrained acetaldehyde concentrations, under-predicted glyoxal mixing ratios throughout both daytime and night-time measurements, achieving a maximum of ~2 pptv during the day and <1 pptv at night.

Location	Glyoxal Measurement Technique	Observed Glyoxal (pptv)	Model	Modelled Glyoxal (pptv)	Literature
Tropical Pacific	MAX-DOAS [a]	63 ± 21	TM4, GEOS-Chem	0	Sinreich *et al.* (2010)
Cape Grim, Chatham Rise	HPLC [b]	20 ± 7	- [d]	2 ± 1	Lawson *et al.* (2015)
Cape Verde	LIP [c]	5.6 ± 1.0	DSMACC [e]/ MCMv3.2 [f]	1.1 ± 0.8	Walker *et al.* (2022)

Table 5.1 Comparisons of previous averaged glyoxal observations in the marine boundary layer (MBL) compared with modelled simulations of glyoxal mixing ratios using observational constraints. Glyoxal is consistently underpredicted by models in the MBL, indicating a missing source of glyoxal in the MBL not currently accounted for in models. [a] Multi-Axis Differential Optical Absorption Spectroscopy. [b] High Performance Liquid Chromatography. [c] Laser-Induced Phosphorescence. [d] Glyoxal mixing ratios were calculated based on glyoxal yields reported by Fu, T.-M. et al. (2008) from measured concentrations of known glyoxal precursors. [e] The Dynamically Simple Model of Atmospheric Chemistry Complexity (Emmerson and Evans, 2009) using the Kinetic PreProcessor (Sandu and Sander, 2006). [f] The Master Chemical Mechanism version 3.2 (Saunders et al., 2003; Jenkin et al., 2003).

Walker et al. (2022) include a series of increasing concentrations of acetaldehyde in model constraints as an additional source of glyoxal, using the IUPAC recommended branching value of 0.05 for abstraction at the methyl site (Atkinson et al., 2006) based on room temperature measurements by Cameron et al. (2002), who show a yield of CH_3CO from abstraction at the aldehydic site to be 0.93 ± 0.18 through direct detection of CH_3CO with the pulsed laser photolysis transient absorption spectroscopy technique (described by Bauer et al. (1998)), and Butkovskaya et al. (2004), reporting a ratio of CH_2CHO yield of 0.05 ± 0.02 through direct detection with chemical ionisation mass spectrometry (CIMS) measurement in a turbulent flow reactor setup. With the addition of acetaldehyde oxidation in model simulations, there is a significantly reduced gap between daytime measured and modelled glyoxal mixing ratios (Figure 5.1), although there remains a sizeable disparity at night-time, where OH concentrations are much lower due to a lack of photolytic production. The result of this is a modelled diurnal profile that does not accurately represent current field observations with the current mechanistic understanding.

Despite the inclusion of a methyl abstraction branching ratio of 0.05 in the acetaldehyde oxidation mechanism (Figure 5.2) included in the Master Chemical Mechanism version 3.3.1 (MCMv3.3.1, see section 5.2.3 (Saunders et al., 2003; Jenkin et al., 2003)), there are still significant uncertainties around this ratio and the yield of glyoxal associated with it. Chamber studies in HIRAC with direct detection of glyoxal using a laser-induced

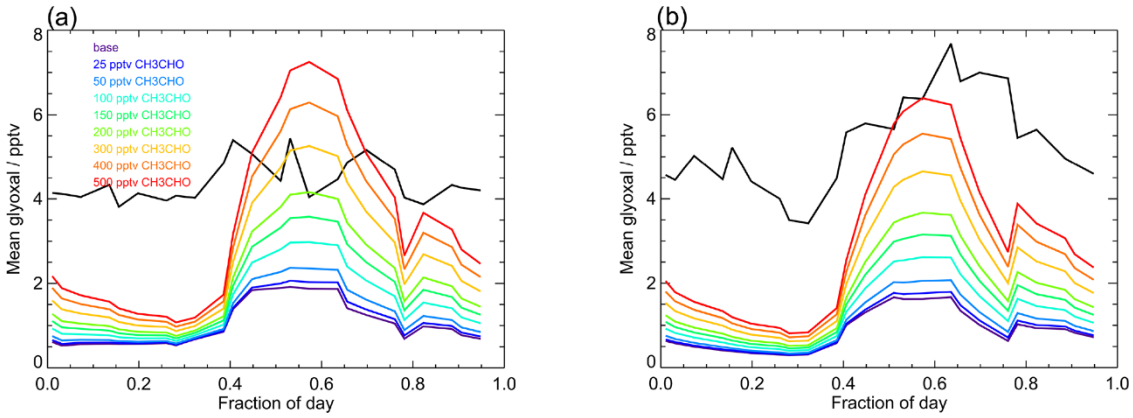

Figure 5.1 Comparisons of modelled glyoxal mixing ratios (coloured) with direct average observations (black) from the Cape Verde Atmospheric Observatory during the Oceanic Reactive Carbon: Chemistry-Climate impacts (ORC^3) campaign, showing data from (a) 22 June to 15 July, 2014, and (b) 18 August to 15 September, 2014. The base model, indicated in the legend, does not include any acetaldehyde constraints, showing large under-prediction of glyoxal mixing ratios during day and night. Further model runs, likewise indicated in the legend, used a fixed mixing ratio of acetaldehyde throughout each simulation, showing a decrease in the gap between measured and modelled glyoxal mixing ratios during daytime hours. Taken from Walker *et al*. (2022).

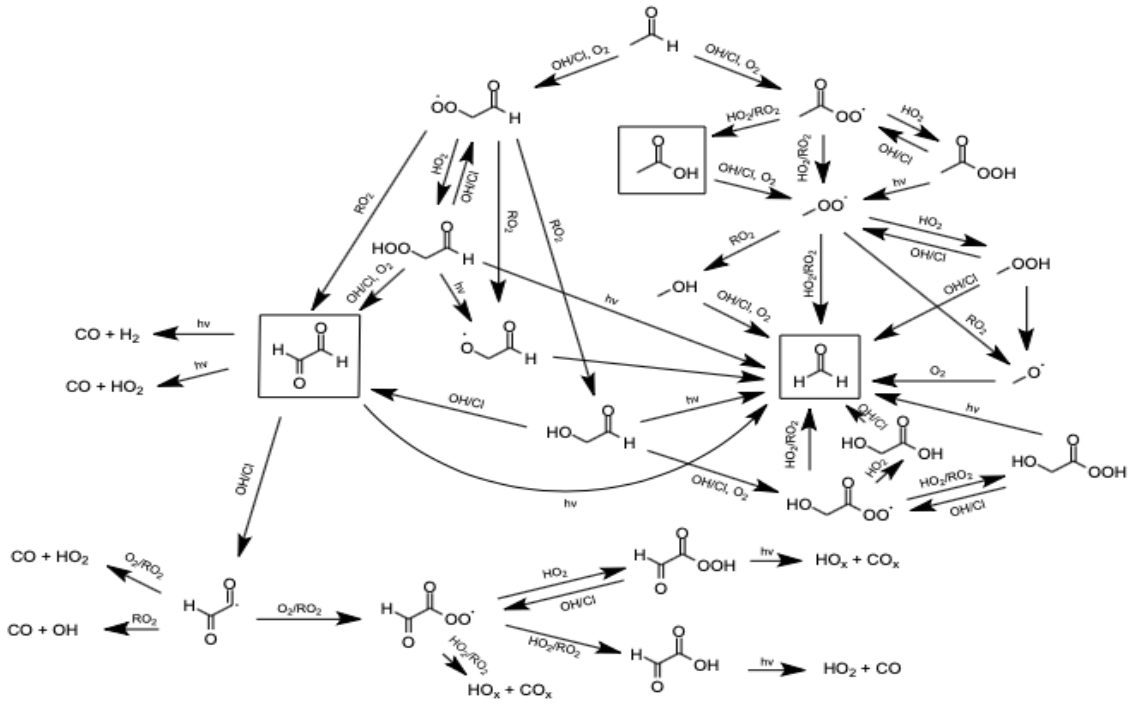

Figure 5.2 A schematic detailing the NO_x-free reaction mechanism listed in the MCMv3.3.1 (Saunders *et al*., 2003; Jenkins *et al*., 2003) for the OH- or Cl-initiated oxidation of acetaldehyde. Formaldehyde, acetic acid and glyoxal are outlined as products of interest in the analysis of R_{GF} and other product ratios relevant for an accurate model of acetaldehyde oxidation. The currently including branching ratio in the MCMv3.3.1 for generation of peroxy radicals $HC(O)CH_2OO$ and $CH_3C(O)OO$ through abstraction at the methyl and aldehydic hydrogen sites respectively is 5:95. Figure reproduced from Chapter 1.

phosphorescence (GLYOX-LIP) instrument (see Chapter 2) aim to clarify the yield of glyoxal from acetaldehyde oxidation. This chapter will investigate the reliability of glyoxal measurements using GLYOX-LIP detection; quantitative product yields from OH- and Cl-initiated oxidation of acetaldehyde in HIRAC; the impact of NO_x concentrations on glyoxal yields and key branching points in the oxidation mechanism; and the significance of glyoxal losses for chamber experiments and model simulations.

5.2 Experimental Methods

5.2.1 Chamber Studies of Acetaldehyde Oxidation

A series of experiments were conducted in HIRAC initiating the oxidation of acetaldehyde through the photolysis of OH or Cl precursors. In all experiments, unless stated otherwise, gaseous acetaldehyde (Sigma-Aldrich, ACS Reagent, ≥99.5%) and the radical precursor, including primarily hydrogen peroxide (H_2O_2, Sigma-Aldrich, 50 wt.

% in H_2O, stabilised), methyl nitrite (CH_3ONO), synthesised prior to oxidation experiments in the lab (see Chapter 3 for details), and chlorine gas (Cl_2, BOC, N2.5) were delivered into HIRAC, which was previously filled up to 1000 ± 3 mbar pressure with a synthetic air mixture of oxygen (O_2, BOC, Industrial Grade, 99.5%) and nitrogen (N_2, BOC, O.F.N., 99.998%) at 293 ± 2 K. The method of delivery typically used a vacuum line to introduce each reactant separately into a small stainless steel vessel (1 L) up to a known pressure measured through a pressure sensor connected to the system. The vessel was then isolated from the vacuum line and flushed into HIRAC through a flow of nitrogen, where the delivered concentration may be calculated from the ratio in volumes of the two chambers. In the case of hydrogen peroxide, a small volume (typically ~1 mL) was injected periodically with a syringe through a rubber seal in one of the side flanges of HIRAC (see Chapter 2 for chamber details), flushing the liquid through in a stream of nitrogen to encourage vaporisation of the hydrogen peroxide.

In all experiments, oxidative chemistry was initiated through activation of the UV lamps in HIRAC. Dependent on the radical precursor, either the GE Optica GE55T8/HO 254 nm lamps (H_2O_2) or the Philips TLK40W/05 black lamps (Cl_2 and CH_3ONO) were used. Reactions typically proceeded for 30 – 90 minutes, dictated by the amount of acetaldehyde removed. Loss rates, including wall loss, sampling dilution, and photolysis, were measured both before and after reaction periods. Concentrations of reactants and products were detected throughout each reaction using a combination of instruments, detailed in Chapter 2, including Proton Transfer Reaction-Mass Spectrometry (PTR-MS), Fourier-Transform Infrared (FTIR) spectroscopy, the Fluorescence Assay by Gas Expansion (FAGE) technique, a glyoxal Laser-Induced Phosphorescence (GLYOX-LIP) instrument, and commercial NO_x and O_3 analysers.

5.2.2 GLYOX-LIP Calibration

As the GLYOX-LIP instrument works through phosphorescence spectroscopy (see Chapter 2), a technique similar to that of the fluorescence spectroscopy employed in FAGE instruments (see Chapters 2 and 4), calibration is essential for the quantification of glyoxal concentrations from the detected signal during oxidation reactions. Whilst LIP instruments can be calibrated through the oxidation of acetylene, using actinometric methods to produce a known concentration of OH in the flow, such as that described by Walker et al. (2022), the simplest method of calibration involves a steady flow of glyoxal

in synthetic air (BOC, Industrial Grade, 21 ± 0.5% O_2), diluted to ppbv mixing ratios, through calibrated mass flow controllers (MFCs), allowing accurate determination of flow concentrations. The GLYOX-LIP instrument can then be calibrated through the linearly proportional equation E5.1:

$$S_{\mathrm{GLY}} = C_{\mathrm{GLY}}[\mathrm{GLY}] \quad \text{(E5.1)}$$

Where [GLY] is the glyoxal concentration (molecule cm^{-3}) flowing into the detection cell, S_{GLY} is the normalised phosphorescence signal (counts s^{-1} mW^{-1}) detected, and C_{GLY} is the established calibration factor (counts cm^3 $molecule^{-1}$ s^{-1} mW^{-1}) calculated through a linear plot of S_{GLY} against [GLY]. The concentration can be adjusted by altering the flow of glyoxal through the MFC to achieve a range of experimentally relevant concentrations required for a reliable calibration factor.

In order to conduct the calibration of GLYOX-LIP, glyoxal was first synthesised from a stable, commercially available glyoxal trimer dihydrate (Sigma-Aldrich, ≥97%), as detailed in several previous studies (Volkamer et al., 2005b; Feierabend et al., 2008; Washenfelder et al., 2008). The solid glyoxal trimer dihydrate was mixed with solid phosphorous pentoxide (P_2O_5, Sigma-Aldrich, ACS reagent, ≥98%) of equal mass (~5 g) and heated to ~433 K. A small flow of nitrogen was passed over the reaction mixture and the glyoxal vapours were collected into a glass bulb submerged in a dry ice trap at 195 K where the solid yellow glyoxal monomer formed. The glyoxal sample was subsequently warmed to room temperature without further purification and diluted in nitrogen, and the concentration in the bulb ([GLY] = (4.54 ± 0.11) × 10^{16} molecule cm^{-3}) was determined through UV/visible absorption spectroscopy *via* the Beer-Lambert law (E5.2):

$$\ln \frac{I_0}{I} = \sigma_{\mathrm{GLY}}[\mathrm{GLY}]l \quad \text{(E5.2)}$$

where $\ln(I_0/I)$ is the measured absorbance due to glyoxal, σ_{GLY} is the glyoxal absorption cross-section taken from measurements by Volkamer et al. (2005b), and l is the optical path length through the gas sample. With the known concentration, the diluted glyoxal sample was further diluted in nitrogen into an empty cylinder by a factor of ~30, measured

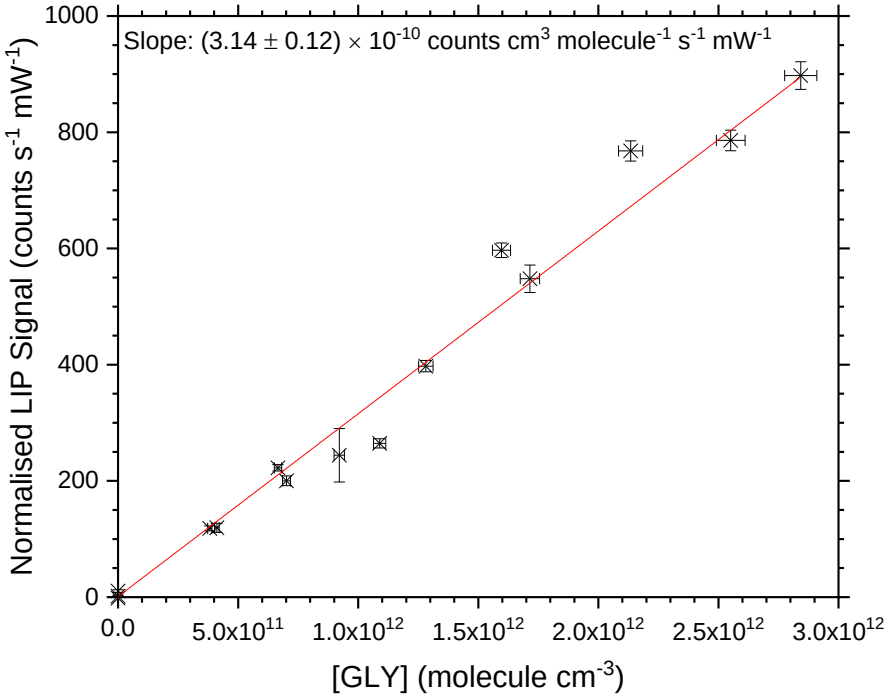

Figure 5.3 Calibration of the GLYOX-LIP instrument showing ppbv level sensitivity of the normalised phosphorescence signal and linearity up to at least 125 ppbv mixing ratios, suitable for glyoxal levels detected in chamber oxidation studies.

through pressure gauges on a vacuum line, to achieve a small enough concentration ([GLY] = (1.55 ± 0.04) × 10^{15} molecule cm^{-3}) fit for calibration at ppbv levels. A small variable flow (2 – 20 sccm) of the dilute glyoxal mixture was passed into the main air flow (10 slm) during the calibration procedure for 3 – 5 minute periods at each concentration, achieving a range of mixing ratios between 12 – 124 ppbv, suitable for concentrations observed during chamber studies. The sensitivity determined for the GLYOX-LIP was C_{GLY} = (3.14 ± 0.12) × 10^{-10} counts cm^3 $molecule^{-1}$ s^{-1} mW^{-1} (Figure 5.3). All errors, unless stated otherwise, were determined as statistical at the 1σ level.

5.2.3 The Master Chemical Mechanism Version 3.3.1

All model simulations in this study were performed with the organic chemistry oxidation scheme detailed by the MCMv3.3.1 (Saunders et al., 2003; Jenkin et al., 2003). The MCMv3.3.1 includes the near-explicit oxidation schemes of 143 primary emissions species, including the biogenic species isoprene, α- and β-pinene, limonene, and β-caryophyllene. The resultant mechanism contains ~17,000 distinct reactions between

6,700 species consisting of both stable primary and secondary VOCs and radical intermediates. For model simulations in this work, acetaldehyde was treated as the sole primary VOC, and a subset of the MCMv3.3.1 involving only the initial oxidation of acetaldehyde and its subsequent reactions was used, using a total of 45 species and 136 reactions, including 10 inorganic species and 48 inorganic reactions.

The chemical mechanism was inputted into a zero-dimensional box model using the Kintecus software (Ianni, 2019), which allowed control of parameters such as temperature, pressure, and starting conditions including VOC precursor and NO_x concentrations, as well as the length of simulation time to match HIRAC experiment times. Concentration time profiles of OH, Cl and NO_x, where relevant, were constrained from experimental data in the box model simulations in order to provide the most accurate representation of VOC oxidation schemes. First order loss processes of stable species were incorporated using experimentally determined rate coefficients, and constituted the depletion of the relevant species concentration without a reaction step to form another molecule, imitating dilution and surface adsorption processes within HIRAC. Photolysis rates were separately characterised from experimental data where photolysis reactions have already been included within the MCMv3.3.1.

5.3 OH-Initiated Oxidation

5.3.1 Kinetics Analysis

The OH-initiated oxidation of acetaldehyde was investigated over several iterations of photolytically induced reactions at 293 K. Whilst the production of glyoxal through oxidation is the primary focus of this study, determination of competing losses for acetaldehyde is important for the accurate analysis of measured glyoxal yields from acetaldehyde decomposition. Acetaldehyde is known to readily photolyse in air at wavelengths below 337 nm (Moortgat et al., 2010), primarily producing formaldehyde, methane, CO and CO_2 through reactions R5.1-9:

$$CH_3CHO + h\nu \xrightarrow{\lambda \leq 337\ nm} CH_3 + HCO \quad \text{(R5.1)}$$

$$CH_3CHO + h\nu \xrightarrow{\lambda < 320\ nm} CH_3CO + H \quad \text{(R5.2)}$$

$$CH_3CHO + h\nu \xrightarrow{\lambda < 1027\ nm} \mathbf{CH_4} + \mathbf{CO} \quad \text{(R5.3)}$$

$$CH_3 + O_2\ (+M) \longrightarrow CH_3O_2\ (+M) \quad \text{(R5.4)}$$

$$CH_3O_2 + HO_2/RO_2 \longrightarrow \mathbf{HCHO} + H_2O + O_2 \quad \text{(R5.5)}$$

$$HCO + O_2 \longrightarrow \mathbf{CO} + HO_2 \quad \text{(R5.6)}$$

$$CH_3CO + O_2\ (+M) \longrightarrow CH_3C(O)O_2\ (+M) \quad \text{(R5.7)}$$

$$CH_3C(O)O_2 + HO_2/RO_2 \longrightarrow CH_3C(O)O + OH + O_2 \quad \text{(R5.8)}$$

$$CH_3C(O)O \xrightarrow{k_d} CH_3 + \mathbf{CO_2} \quad \text{(R5.9)}$$

The photolysis rate of acetaldehyde in HIRAC was therefore tested under emissions from the 254 nm lamps in the absence of any OH precursor compounds. The loss of acetaldehyde due to all unimolecular processes, including photolysis, sampling dilution, chamber surface adsorption and heterogeneous uptake, can be characterised by equation E5.3:

$$\frac{-d[CH_3CHO]}{dt} = (k_d + j_\lambda)[CH_3CHO] \quad \text{(E5.3)}$$

where $-d[CH_3CHO]/dt$ is the loss of acetaldehyde over time, k_d is the overall rate coefficient for all first order loss processes excepting photolysis, and j_λ is the photolysis rate coefficient as a function of wavelength. The integrated rate law for first order acetaldehyde loss is then denoted by equation E5.4:

$$\ln([CH_3CHO]) = \ln([CH_3CHO]_0) - (k_d + j_\lambda)t \quad \text{(E5.4)}$$

where t is time, and $[CH_3CHO]_0$ is the concentration of acetaldehyde at time $t = 0$ s. Plots of $\ln([CH_3CHO])$ against t can then be compared during periods where the lamps are either activated or deactivated, with the latter naturally resulting in $j_\lambda = 0\ s^{-1}$. As all other loss processes are assumed to be constant throughout an experiment, the difference between these two slopes yields the value of j_λ during lamp activation (Figure 5.4), and hence during a proceeding oxidation reaction. The photolysis rate at room temperature

Run	$[CH_3CHO]_0$ /10^{-14} molecule cm^{-3}	k_d /10^4 s^{-1}	$k_d + j_\lambda$ /10^4 s^{-1}	j_λ /10^4 s^{-1}
1	1.06 ± 0.05	0.90 ± 0.06	2.04 ± 0.19	**1.14 ± 0.20**
2 [a]	1.01 ± 0.05	0.74 ± 0.04	1.32 ± 0.02	**0.58 ± 0.04**
3 [b]	0.94 ± 0.05	1.17 ± 0.10	1.83 ± 0.03	**0.66 ± 0.10**
4	1.15 ± 0.06	0.55 ± 0.05	1.51 ± 0.05	**0.96 ± 0.07**
5	1.09 ± 0.05	1.01 ± 0.04	1.85 ± 0.03	**0.84 ± 0.05**
6	1.35 ± 0.07	0.56 ± 0.34 [c]	1.64 ± 0.10	**1.08 ± 0.37** [c]
Average	-	**0.76 ± 0.18**	**1.76 ± 0.11**	**1.00 ± 0.21**

Table 5.2 Calculated values for the photolysis rate of acetaldehyde in HIRAC under activation of the GE Optica GE55T8/HO 254 nm lamps. Errors include 5 % uncertainty in $[CH_3CHO]_0$ and statistical error at the 1σ level in k_d and ($k_d + j_\lambda$). Photolysis rate errors were propagated out from statistical errors. [a] Experiment performed at 323 K and therefore not included in the average calculation, but included for comparison. [b] Experimented performed at 348 K and therefore not included in the average calculation. [c] Significant error due to unusually poor SNR in the PTR-MS data.

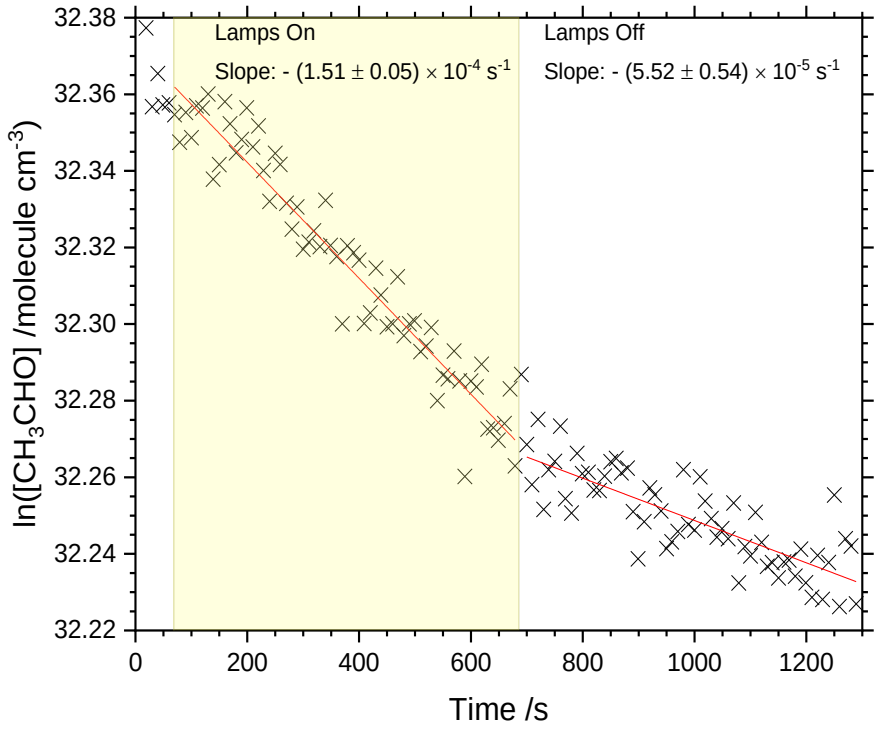

Figure 5.4 Kinetic analysis of the first order loss processes of acetaldehyde in HIRAC through application of the integrated first order rate law. The shaded yellow region indicates activation of 254 nm UV lamps. First order rate coefficients include a collective parameter, k_d, including loss due to sampling dilution, chamber surface adsorption, and heterogeneous uptake, and j_λ, the photolysis rate coefficient as a function of wavelength, where the slope $m = -(k_d + j_\lambda)$. Periods where lamps are deactivated result in $j_\lambda = 0$ s^{-1}, thus the negative difference between these two slopes ($-(m_1 - m_2) = 9.58 \times 10^{-5}$ s^{-1} for this experiment) gives a value for the photolysis rate of acetaldehyde in HIRAC.

was averaged at (1.00 ± 0.21) × 10^{-4} s^{-1} over four repeated experiments, compared with measured k_d values of (7.6 ± 1.8) × 10^{-5} s^{-1} (Table 5.2), and therefore, on average, contributes a little over half of all first order acetaldehyde loss during periods of lamp activation.

5.3.2 Glyoxal Yields

Oxidation of acetaldehyde was initiated through the photolysis of hydrogen peroxide upon lamp activation as a precursor to the OH radical. Several injections of hydrogen peroxide were typically made throughout an experiment in order to maintain OH concentrations in the chamber (see Chapter 3), and as a result, large fluctuations in [OH] are observed during a reaction (as seen in Figure 3.17), atypical of ambient atmospheric conditions. However, an attempt at measuring the glyoxal yield from acetaldehyde oxidation was made nonetheless, calculated simply through a plot of glyoxal production against acetaldehyde loss at each time point, using the reaction initiation time point as reference concentrations for both species.

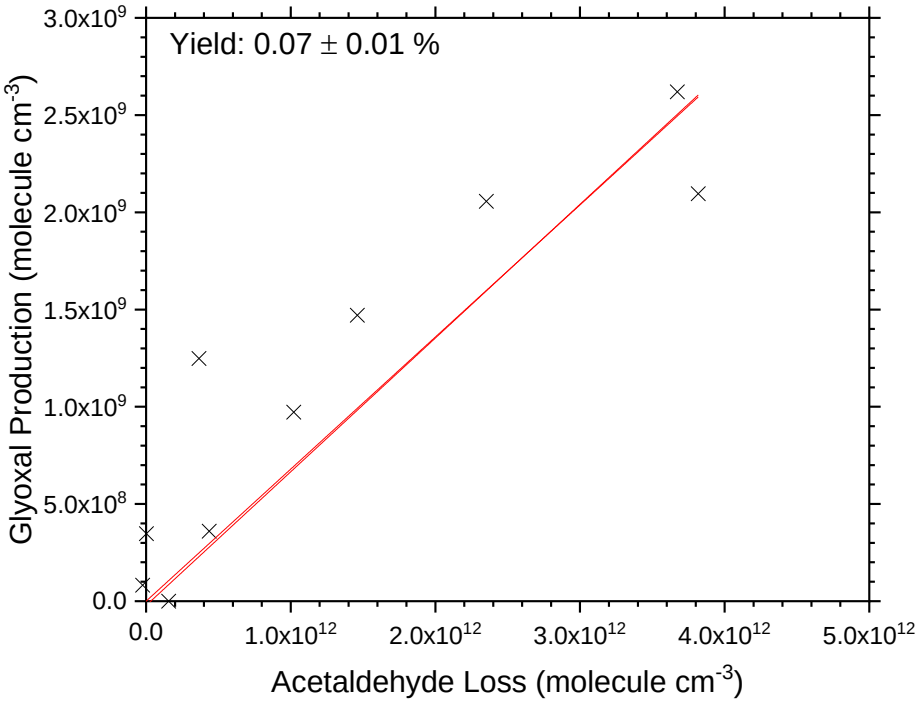

Figure 5.5 Calculated glyoxal yield from the OH-initiated oxidation of acetaldehyde. Data for this yield calculation includes only the initial ~100 s of reaction time. Data complementary to Figures 5.6 & 5.7.

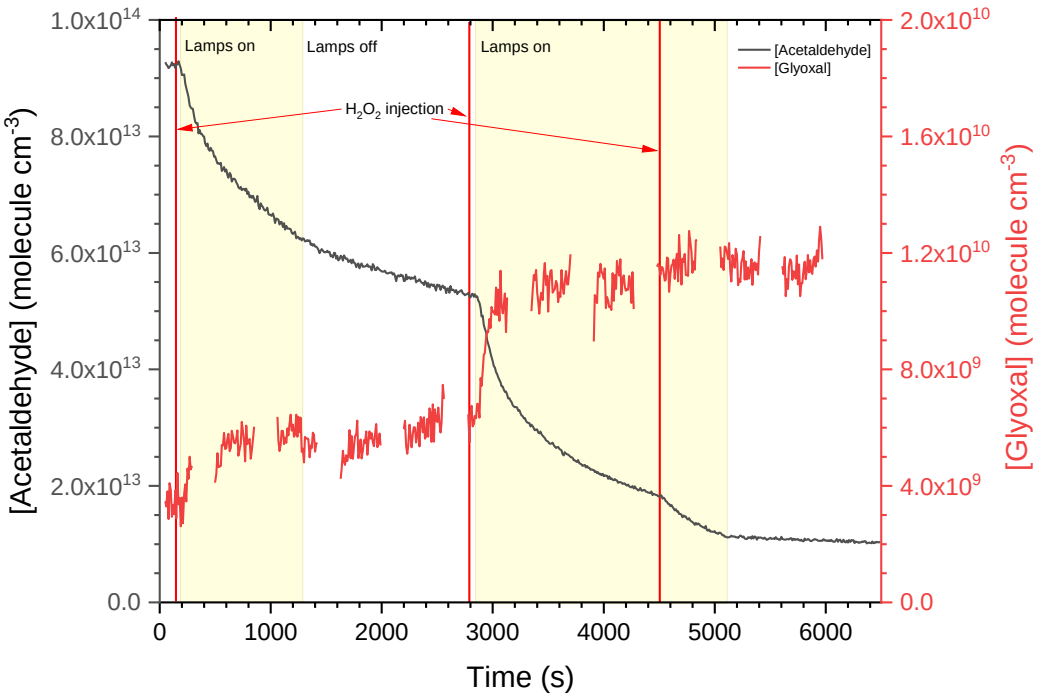

Figure 5.6 Simultaneous concentration time profiles of acetaldehyde (black), measured with PTR-MS, and glyoxal (red), measured with GLYOX-LIP, during OH-initiated oxidation of acetaldehyde in HIRAC. Gaps in glyoxal data correspond to periods of offline wavelength measurement and cycling to online wavelength measurement. Solid red vertical lines indicate points of hydrogen peroxide injection into HIRAC. Shaded yellow regions indicate periods where 254 nm UV lamps are activated. Glyoxal data shows clear increases upon initial oxidation of acetaldehyde, however also demonstrates swift plateauing behaviour due to large loss rates associated with the presence of hydrogen peroxide. Data complementary to Figures 5.5 & 5.7.

An initial yield of 0.07 ± 0.01 % was calculated (Figure 5.5), however increases in measured glyoxal concentration plateaued in under 3 minutes (Figure 5.6) due to rapid losses associated with the presence of hydrogen peroxide (see Chapter 3). Whilst standard glyoxal loss processes and rates can be accounted for in model simulations using measured rate coefficients and experimentally obtained OH constraints, attempts to characterise the accelerated glyoxal loss driven by hydrogen peroxide have proven unsuccessful, producing glyoxal concentration time profiles that do not resemble experimental observation (Figure 5.7). The most probable cause of this is that the parameter used for unimolecular glyoxal loss consists of one fixed rate coefficient, determined experimentally both in the presence and absence of hydrogen peroxide. However, this approach assumes that glyoxal loss is independent of both hydrogen peroxide concentration and any aerosol content produced from the addition of water to the system (see Chapter 3 for earlier discussion). Both of these parameters will vary

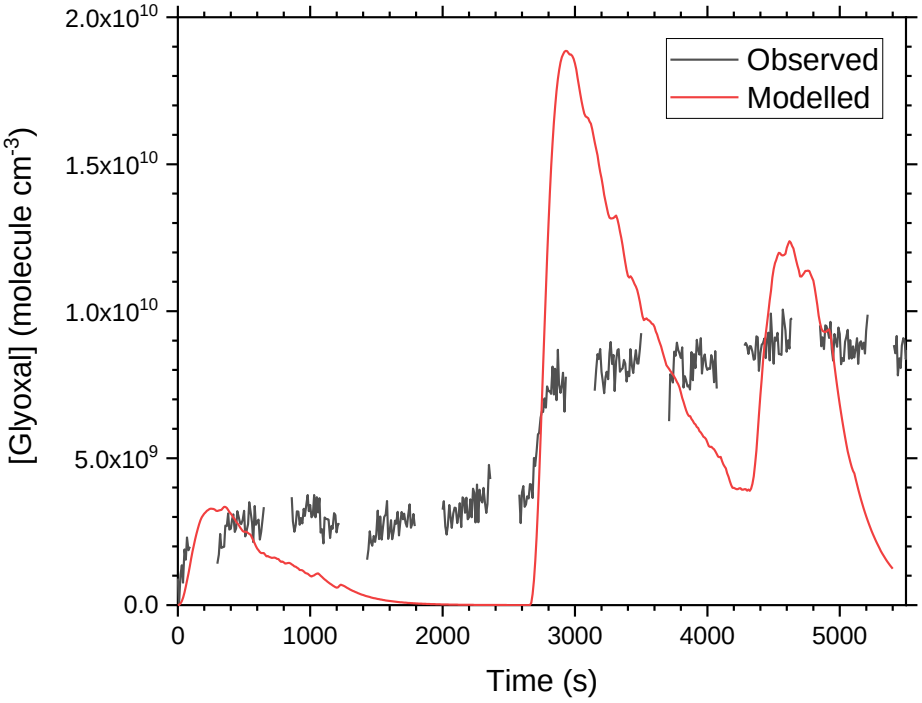

Figure 5.7 Comparison of glyoxal data experimentally observed (black) using GLYOX-LIP in HIRAC and simulated glyoxal data (red) using the acetaldehyde oxidation mechanism provided by the MCMv3.3.1, with the OH concentration constrained by experimental measurements. The initial abstraction site ratio was adjusted from the recommended 5% at the methyl site of acetaldehyde to 0.5%, an order of magnitude lower, in order to attain an initial glyoxal profile that most closely resembled experimental data. Despite this, there remains large discrepancies in the overall profile between measured and modelled data. Data complementary to Figures 5.5 & 5.6.

significantly during the course of a reaction, and are likely to impact glyoxal loss rates, though it is difficult to monitor this through real measurements.

In initial model simulations of glyoxal yields, the OH abstraction branching ratio at the methyl site of acetaldehyde was adjusted from 5 % to 0.5 %, in order to achieve similar quantities of glyoxal throughout the oxidation reaction. However, whilst the initial yield within the first ~5 – 10 minutes demonstrated good agreement, there remained clear discrepancy between modelled and observed glyoxal in both absolute concentrations and the overall time profile (Figure 5.7). It is evident, then, that the balance between glyoxal generation and removal in HIRAC was poorly represented by the MCMv3.3.1 mechanism constrained by experimental OH concentrations. Upon formation of the $HC(O)CH_2OO$ peroxy species, the key branching points affecting the rate of glyoxal formation involve the fate of the $HC(O)CH_2OO$ radical. In the MCMv3.3.1, the primary route to glyoxal in

NO_x-free conditions (see Figure 5.2) is the reaction of $HC(O)CH_2OO$ with HO_2 (R5.10), with subsequent reaction of the organic peroxide with OH (R5.11):

$$HC(O)CH_2OO + HO_2 \longrightarrow HC(O)CH_2OOH + O_2 \quad \text{(R5.10)}$$

$$HC(O)CH_2OOH + OH \longrightarrow CHOCHO + OH + H_2O \quad \text{(R5.11)}$$

Neither of these reactions appear to have been directly studied previously, and the rate coefficients represent estimates based on similar categories of RO_2 + HO_2 or ROOH + OH reactions. One method to experimentally determine the significance of this route to glyoxal could involve the quantification of OH recycling present in R5.11. This would be difficult to achieve in HIRAC, however may be of benefit in future work to establish rate coefficients and glyoxal yields through this mechanistic route.

An alternative route to glyoxal involves the reaction of $HC(O)CH_2OO$ with another peroxy species, producing glyoxal either directly (R5.12) or *via* glycolaldehyde (R5.13), a direct glyoxal precursor.

$$HC(O)CH_2OO + RO_2 \longrightarrow CHOCHO + ROH + O_2 \quad \text{(R5.12)}$$

$$HC(O)CH_2OO + CH_3O_2 \longrightarrow HC(O)CH_2OH + HCHO + O_2 \quad \text{(R5.13)}$$

Similarly, these reactions have not been directly studied, however comprise minor branching fractions for the removal of $HC(O)CH_2OO$ in the MVMv3.3.1. Significantly, the accumulation of glyocolaldehyde in model simulations was too low to account for more than ~0.2 % of glyoxal production. This was supported by a lack of evidence for glycolaldehyde build-up in the analysis of PTR-MS data. However, in the presence of NO_x, reaction of $HC(O)CH_2OO$ with NO constitutes a significant competitor for removal of the peroxy species, and it was hypothesised that this would impact measured glyoxal yields through a significant change in the dominant mechanistic route. Glyoxal yields from the OH-initiated oxidation of acetaldehyde were therefore studied under high NO_x (>5 ppbv) conditions.

5.3.3 NO_x Dependence

Although the investigation of glyoxal sources in the MBL is less relevant to conditions with high NO_x mixing ratios (>5 ppbv), the oxidation of acetaldehyde is not limited to the MBL, and other sources of acetaldehyde include biomass burning and anthropogenic emissions as well as emissions from decaying biomass (Millet et al., 2010), which all occur in urban regions where NO_x mixing ratios are high enough to impact the chemistry further. Studying the oxidation reaction in conditions with NO_x present can also provide insight into branching points in the mechanism through promoting particular channels through formation of alkoxy radicals that lead to an altered ratio of the observable products. It is therefore expected that the peroxy radical formed upon initial hydrogen abstraction from the methyl site will be rapidly converted to its subsequent alkoxy species (R5.14):

$$HC(O)CH_2OO + NO \longrightarrow HC(O)CH_2O + NO_2 \quad \text{(R5.14)}$$

Whilst most alkoxy species are known to either reaction with molecular oxygen, typically with a rate coefficient of ~1×10^{-14} cm^3 $molecule^{-1}$ s^{-1}, or decompose typically into alkyl and carbonyl substituents (Orlando et al., 2003), as discussed in Chapter 1, neither of these processes have been directly studied for $HC(O)CH_2O$ previously. However, the reaction of the $HC(O)CH_2O$ alkoxy species with O_2 is not listed in the MCMv3.3.1, despite being a potential source of glyoxal within the acetaldehyde oxidation mechanism (R5.15). The only loss of $HC(O)CH_2O$ in the MCMv3.3.1 is therefore unimolecular decomposition, which provides another source of formaldehyde instead (R5.16).

$$HC(O)CH_2O + O_2 \longrightarrow CHOCHO + HO_2 \quad \text{(R5.15)}$$

$$HC(O)CH_2O \xrightarrow{k_d} HCHO + HCO \quad \text{(R5.16)}$$

The estimated loss rate for unimolecular decomposition of $HC(O)CH_2O$ in the MCMv3.3.1 is rapid (1×10^6 s^{-1}), and considering oxygen concentrations at standard atmospheric pressure ($[O_2] \approx 5 \times 10^{18}$ molecule cm^{-3}), removal of $HC(O)CH_2O$ *via* reaction with O_2 to produce glyoxal should constitute a mere ~5 % of total $HC(O)CH_2O$

removal. It is therefore anticipated that the addition of NO_x as the primary competitor to HO_2 for $HC(O)CH_2OO$ removal should reduce the measured glyoxal yield from acetaldehyde oxidation. The significance of reaction R5.11 in the overall formation of glyoxal was investigated through comparison of the acetaldehyde oxidation mechanism in both low- and high-NO_x conditions.

Methyl nitrite was chosen as the preferred OH source for these experiments, simultaneously providing a source of NO_x and OH through photolysis (see Chapter 3 for details) with the UV blacklamps, which have a wavelength output centred around 300 – 450 nm. An advantage of using a longer wavelength photolysis source is the reduced photolysis rate of glyoxal. Tadić et al. (2006) note a rapid decrease in absolute quantum yield of glyoxal photolysis in 700 Torr air at wavelengths above 335 nm, based on measurements in that work using three UV sources at 275-380 nm, 390-470 nm and 254 nm, as well as data from previously reported measurements (Calvert and Layne, 1953; Langford and Moore, 1984; Zhu, L. et al., 1996; Chen and Zhu, 2003). These observations were supported more recently by Salter et al. (2013), however also included an additional quenching mechanism for all photolysis channels that lowered the overall glyoxal photolysis rate at wavelengths between 300 – 350 nm, yet slightly elevated the photolysis rate from previous measurements at longer wavelengths (>350 nm). Nevertheless, even with this inclusion, the rate of glyoxal photolysis was still reduced to ~ 0 s^{-1} at wavelengths above ~420 nm. Although photolysis likely remains a contributing factor to the overall loss of glyoxal with activation of the blacklamps, it was assumed that this loss rate was minimal compared with that of dilution, heterogeneous uptake and surface adsorption. The first order glyoxal loss rate, for modelling purposes, was therefore regarded as that measured after deactivation of the lamps and termination of OH-initiated oxidation.

Use of the blacklamps likewise saw a reduction in acetaldehyde photolysis during experimental procedures. The overall first order loss rate of acetaldehyde was measured during periods where the UV blacklamps in HIRAC were activated and deactivated to determine a photolysis rate prior to the addition of any radical precursors. As denoted in equation E5.4 from first order rate law, the loss rate was calculated through the negative slope of the natural logarithm of acetaldehyde concentration, measured with the PTR-MS, over time. The first order loss rate coefficient, both in the dark and under the UV blacklamps, was measured at $k' = (4.34 \pm 0.62) \times 10^{-5}$ s^{-1} and $(4.11 \pm 0.23) \times 10^{-5}$ s^{-1} respectively, falling within error of each other (Figure 5.8). This strongly suggests that

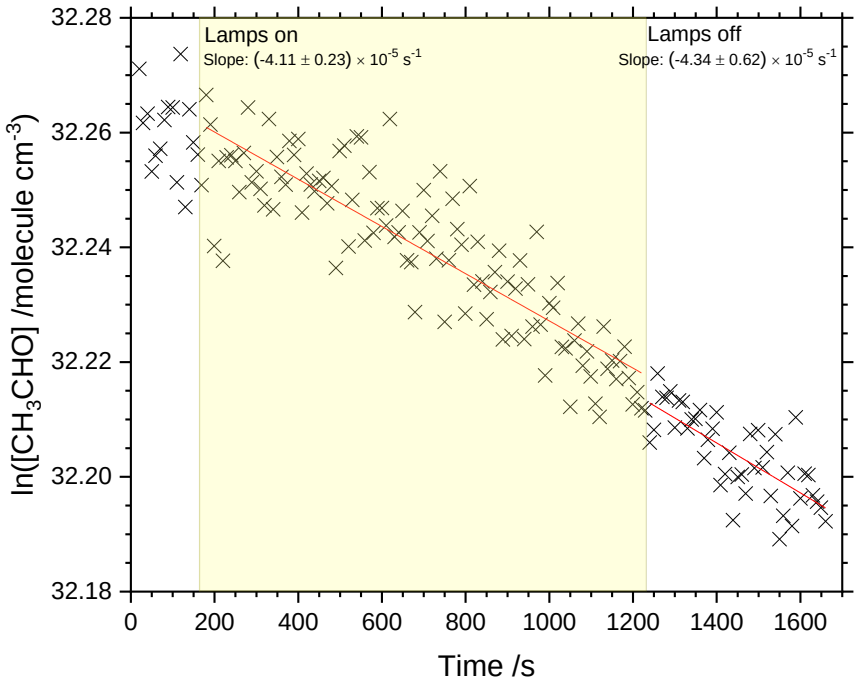

Figure 5.8 Analysis of the photolysis rate of acetaldehyde in HIRAC under the UV blacklamps. First order rate coefficients were determined through the negative slopes of the natural logarithm of acetaldehyde concentration over time. Measured rate coefficients both in the dark and under activation of the blacklamps fall within error of one another, indicating that photolysis of acetaldehyde at the longer wavelengths is negligible compared with other loss processes in HIRAC.

any photolysis of acetaldehyde due to activation of the blacklamps is negligible compared with other loss rates such as sampling dilution and surface wall adsorption. These observations are likewise supported by the continued decrease of the acetaldehyde absorption cross-section below 1×10^{-20} cm^2 molecule^{-1} at longer wavelengths ($\lambda > 326$ nm) determinedly previously (Martinez et al., 1992). Lack of photolysis here assists in simplifying model simulations of acetaldehyde oxidation, where the removal of acetaldehyde constitutes the bimolecular reaction with OH at the two abstraction sites and a dilution parameter throughout the simulation.

A further simplification of model simulations comes from the ability to produce consistent OH concentrations through the photolysis of methyl nitrite compared with that of hydrogen peroxide (see Chapter 3 for details). As aforementioned, due to the requirement of several injections of hydrogen peroxide solution over the course of a reaction, large variations in OH concentration as a result can be detrimental in reproducing yields observed in experiment, previously seen in Figure 5.7. However, a single delivery of methyl nitrite prior to reaction initiation is sufficient for the consistent

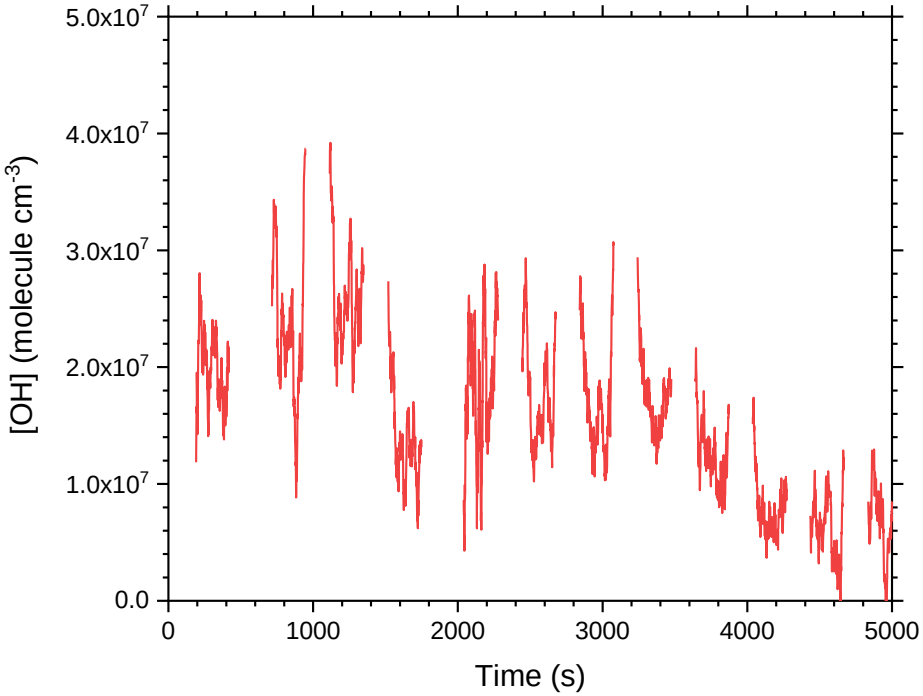

Figure 5.9 FAGE measurements of OH concentration in HIRAC generated through the photolysis of methyl nitrite in the presence of ppmv levels of acetaldehyde. Concentrations produced are consistent over a long period of time (~60 minutes), with a steady decline as methyl nitrite in HIRAC is depleted. Gaps in the data occur as a result of the FAGE instrument cycling 'offline' every few minutes to measure the baseline fluorescence signal. Data complementary to Figures 5.10 & 5.11.

generation of OH throughout a 60 – 90 minute reaction, as observed through FAGE measurements (Figure 5.9). Although the OH concentration undergoes a steady decline as methyl nitrite in the chamber is depleted, the change in concentration is much smaller, and therefore easier to reproduce in models, obtaining glyoxal yields that are more consistent with experimental measurements.

Oxidation of acetaldehyde in air using methyl nitrite as an OH precursor produced detectable concentrations of glyoxal (ppbv mixing ratios), showing a steady increase over time as acetaldehyde was depleted (Figure 5.10). A much clearer alignment of glyoxal production with acetaldehyde removal was achieved through this method, and the measured glyoxal yield from this reaction was indeed smaller than that determined under NO_x-free conditions. A simple plot of glyoxal production against acetaldehyde removal revealed a glyoxal yield of ~0.06 %, calculated over a wider range of concentrations than previously shown (Figure 5.11). Three glyoxal yields measured from the OH-initiated oxidation of acetaldehyde in high-NO_x conditions demonstrated an average yield of 0.06

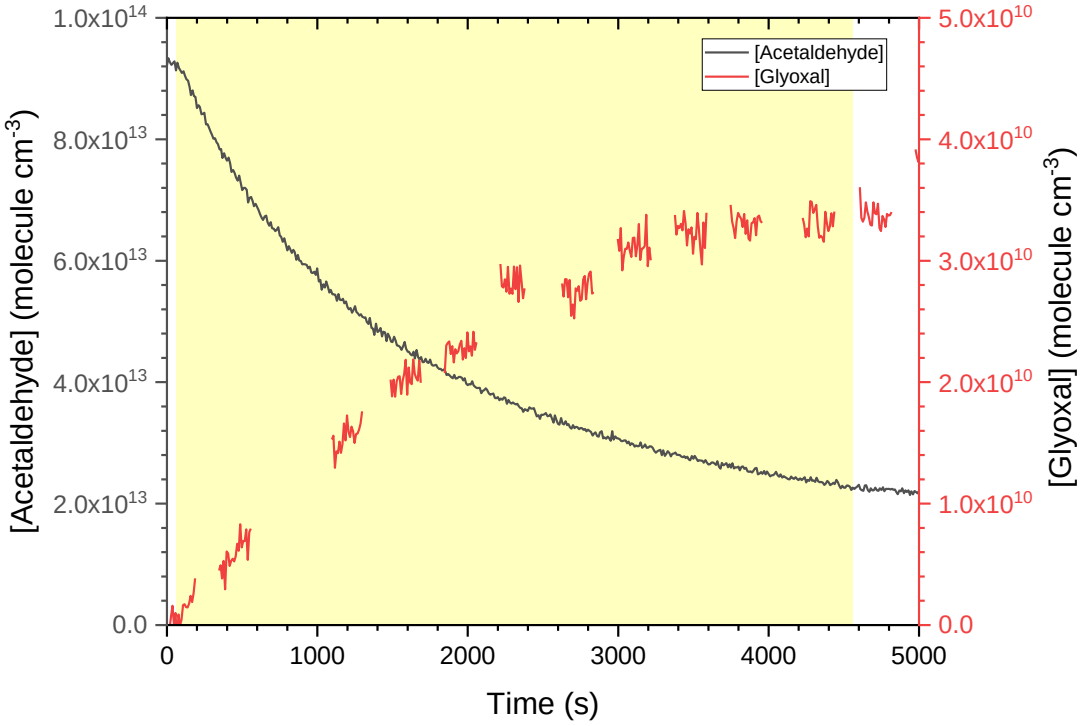

Figure 5.10 Measured production of glyoxal (red) concurrent with the removal of acetaldehyde (black) through OH-initiated oxidation following the photolysis of methylnitrite. The yellow shaded region indicates activation of the UV blacklamps in HIRAC, triggering methylnitrite photolysis. Data complementary to Figures 5.9 & 5.11.

± 0.01 %, where the error was calculated as the standard deviation of the yield values to the 2σ level.

Direct model comparisons with the experimental yield in the presence of NO_x cannot be guaranteed due to a lack of detectable NO concentrations in HIRAC during the oxidation reaction for model constraints. However, estimating steady state conditions of NO and NO_2 at a fixed 5 ppbv mixing ratio in model runs indicates the potential importance of the alkoxy reaction (R5.16). Inclusion of this reaction in the mechanism, in addition to the reaction scheme already listed by the MCMv3.3.1, increased glyoxal production by ~25 %, bringing glyoxal concentrations closer to observed values from experiment under the 0.5 % initial branching abstraction at the methyl site used in the NO_x-free model. It should be noted, however, that this inclusion resulted in an initial yield of ~0.25 % followed by a steady decline in glyoxal concentration, unlike the time profile observed in experiment. Nevertheless, the lower glyoxal yield measured in high-NO_x conditions indicate that production of glyoxal through $HC(O)CH_2OO + HO_2$ (R5.10 & R5.11) is significantly inhibited where conversion to the alkoxy radical through reaction with NO

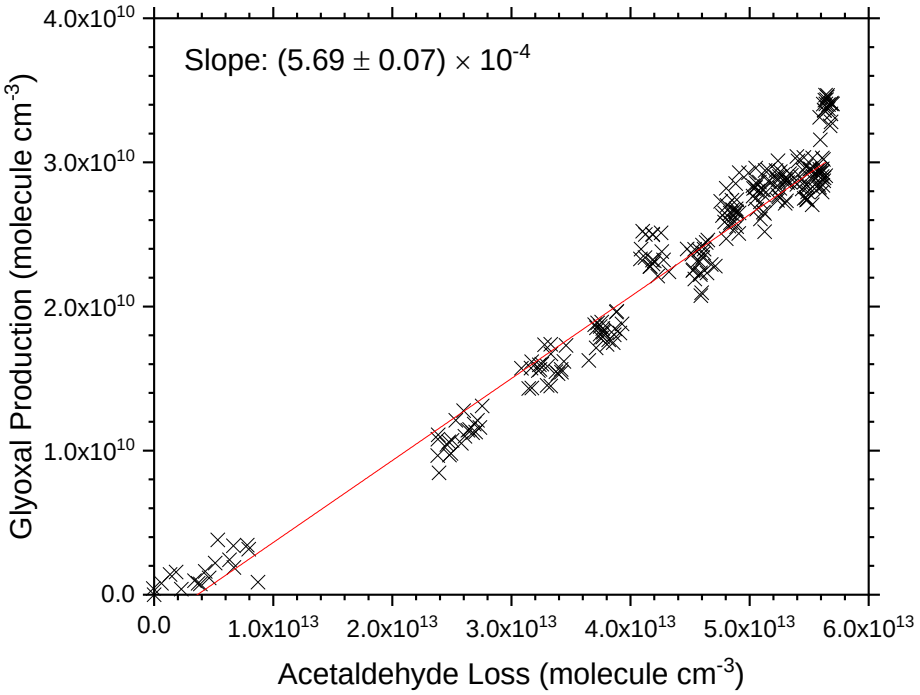

Figure 5.11 The glyoxal yield from the OH-initiated oxidation of acetaldehyde in the presence of NO_x. The yield was measured at ~0.06 % over a wide range of concentrations, demonstrating consistency in glyoxal yield over time. Data complementary to Figures 5.9 & 5.10. Dataset forms one of three glyoxal yields measured through methylnitrite photolysis, averaged at 0.06 ± 0.01 %, where the error is taken as the standard deviation of the three values to the 2σ level.

is instead favoured. The significance of glyoxal production through reaction R5.16 has been further investigated in section 5.4.2.

Whilst these preliminary findings have limitations in attempts to compare glyoxal yields both with and without NO_x present due to both a lack of model constraints and a change in multiple conditions, they do provide an incentive for further investigation. The oxidation of acetaldehyde by Cl atoms was therefore undertaken instead, allowing a more direct comparison of glyoxal yields under the two mechanisms to analyse the impact of key branching points in the absence and presence of NO_x.

5.4 Cl-Initiated Oxidation

The Cl-initiated oxidation of acetaldehyde has been investigated in a number of previous studies, using several techniques including relative rate studies (Niki et al., 1985b; Scollard et al., 1993), discharge flow with mass spectrometric detection (Bartels et al., 1989), flash photolysis-resonance fluorescence (Payne et al., 1990; Tyndall et al., 1999),

and tunable diode laser absorption spectroscopy (Kegley-Owen et al., 1999; Seakins, P. W. et al., 2004). Measurement of the bimolecular rate coefficient for the oxidation of acetaldehyde *via* chlorine atoms (R5.17a, b), $k_{5.17}$, shows good agreement across these studies, with Tyndall et al. (1999) presenting a recommended value with a 95 % confidence limit of $k_{Cl} = (7.8 \pm 1.3) \times 10^{-11}$ cm^3 molecule^{-1} s^{-1}, derived from a combination of findings in both that work and an evaluation of the literature available.

$$CH_3CHO + Cl \longrightarrow CH_3CO + HCl \quad \text{(R5.17a)}$$

$$CH_3CHO + Cl \longrightarrow CH_2CHO + HCl \quad \text{(R5.17b)}$$

Whilst most of these studies do not address the abstraction of a hydrogen at the methyl site, focusing primarily on the overall rate coefficient and the yield of vibrationally excited HCl, Bartels et al. (1989) indicate a branching ratio of at least 93 % at the aldehydic site, although a more exact quantity was not determined. An abstraction ratio of <7 % at the methyl site is therefore reasonably consistent with the purported 5 % ratio from OH-initiated oxidation, and provides a good substitute for measurement of glyoxal yields from acetaldehyde oxidation.

Chlorine atoms were generated through the photolysis of molecular chlorine in HIRAC (see Section 5.2.1 for further experimental details). Due to the broad peak in the absorption cross-section of Cl_2 ranging between 275 – 400 nm, as demonstrated by Maric et al. (1993) alongside several other studies (Gibson and Bayliss, 1933; Seery and Britton, 1964; Burkholder and Bair, 1983), the blacklamps were again chosen as the photolysis source. Similarly to methylnitrite photolysis, use of the blacklamps, rather than the shorter wavelength GE Optica 254 nm lamps, is advantageous in the minimisation of acetaldehyde and glyoxal photolysis, reducing mechanism complexity and glyoxal loss in the system. However, glyoxal removal *via* bimolecular reaction with Cl atoms must also be characterised in order to accurately determine glyoxal yields through Cl-initiated oxidation. The bimolecular rate coefficient for reaction of glyoxal with Cl was therefore investigated prior to study of acetaldehyde oxidation.

5.4.1 Bimolecular Reaction of Glyoxal with Atomic Chlorine

The bimolecular rate coefficient, $k_{5.18}$, for the reaction of glyoxal with atomic chlorine (R5.18) has not received any appreciable attention in previous studies.

$$CHOCHO + Cl \longrightarrow CHOCO + HCl \qquad (R5.18)$$

Although the work of Niki et al. (1985a) reports a value of $k_{5.18} = (3.8 \pm 0.3) \times 10^{-11}$ cm^3 molecule^{-1} s^{-1}, there are no other literature values to compare agreement or discrepancy, and the reliability of a single measurement ought to be reinforced. It seemed therefore prudent to undertake a measurement in this work as a comparison against the literature and a value for use in model simulations of Cl-initiated oxidation. However, due to the HIRAC facility lacking the instrumentation for detection of Cl atoms (see Chapter 2 for details on instrumentation), a relative rate method was chosen for the quantification the bimolecular rate coefficient $k_{5.18}$.

Despite previous extensive study, acetaldehyde could not be used as a reference compound for a relative rate study with glyoxal due to production of glyoxal through acetaldehyde oxidation, therefore methanol was chosen instead. The oxidation of methanol *via* Cl has received some attention in past works (Table 5.3), with an overall bimolecular rate coefficient, $k_{5.19}$, for channels R5.19a and R5.19b measured to a good agreement at 298 K through methods of flash photolysis-resonance fluorescence (Michael et al., 1979); relative rate with cyclohexane (Nelson et al., 1990); fast flow Laser

Detection Technique	$k_{5.19}$ **/10^{11} cm^3 molecule^{-1} s^{-1}**	**Literature**
FP-RF [a]	6.33 ± 0.70	Michael *et al*. (1979)
RR [b]	4.79 ± 0.36	Nelson *et al*. (1990)
Fast Flow LMR-EPR [c]	6.14 ± 0.66	Dóbé *et al*. (1993)
IR DLAS [d]	5.83 ± 0.77	Seakins *et al*. (2004)
IR Chemiluminescence	5.38 ± 0.25	Seakins *et al*. (2004)
	5.69 ± 0.59 [e]	

Table 5.3 Previous literature values on the measured rate coefficient for the reaction of CH_3OH with Cl ($k_{5.19}$), and their associated detection techniques. [a] Flash Photolysis-Resonance Fluorescence. [b] Relative Rate. [c] Fast Flow Laser Magnetic Resonance-Electron Paramagnetic Resonance. [d] Infrared Diode Laser Absorption Spectroscopy. [e] Averaged $k_{5.19}$ with an associated error propagated from previous experimental errors.

Magnetic Resonance-Electron Paramagnetic Resonance detection (Dóbé et al., 1993); and both IR diode laser absorption spectroscopy and IR chemiluminescence (Seakins, P. W. et al., 2004).

$$CH_3OH + Cl \longrightarrow CH_3O + HCl \quad \text{(R5.19a)}$$

$$CH_3OH + Cl \longrightarrow CH_2OH + HCl \quad \text{(R5.19b)}$$

An average rate coefficient, $k_{5.19} = (5.69 \pm 0.59) \times 10^{-11}$ cm^3 molecule^{-1} s^{-1}, was calculated from these studies for use as a reference rate (Table 5.3), in agreement with the value recommended by (Tyndall et al., 1999), based on a similar evaluation of the literature, of $k_{5.19} = (5.4 \pm 0.9) \times 10^{-11}$ cm^3 molecule^{-1} s^{-1}. Oxidation of methanol has been demonstrated as selectively proceeding through channel R5.19b (Dóbé et al., 1994), with near unity yield of hydroxymethyl (CH_2OH) radicals, primarily producing formaldehyde through reaction R5.20, with no possible mechanistic routes to the formation of glyoxal.

$$CH_2OH + O_2 \longrightarrow HCHO + HO_2 \quad \text{(R5.20)}$$

The relative rate between methanol and acetaldehyde in HIRAC was determined to compare with previously attained literature values as a measure of data quality prior to a relative rate with glyoxal. Methanol and acetaldehyde were delivered into HIRAC in similar quantities (~1 – 5 ppm) in 1000 mbar air mixture, attempting to avoid the issue of rapid depletion of one species over the other. Assuming that reaction with Cl atoms is the dominant source of removal for both acetaldehyde and methanol and any dilution term is negligible, integrated rate law can be formulated as in equation E5.5, the derivation of which is detailed by Atkinson (1986):

$$\ln\left(\frac{[CH_3CHO]_0}{[CH_3CHO]_t}\right) = \frac{k_{5.17}}{k_{5.19}} \ln\left(\frac{[CH_3OH]_0}{[CH_3OH]_t}\right) \quad \text{(E5.5)}$$

where $[CH_3CHO]_0$ and $[CH_3OH]_0$ are the concentrations of acetaldehyde and methanol respectively at time $t = 0$, and $[CH_3CHO]_t$ and $[CH_3OH]_t$ denote the concentrations of

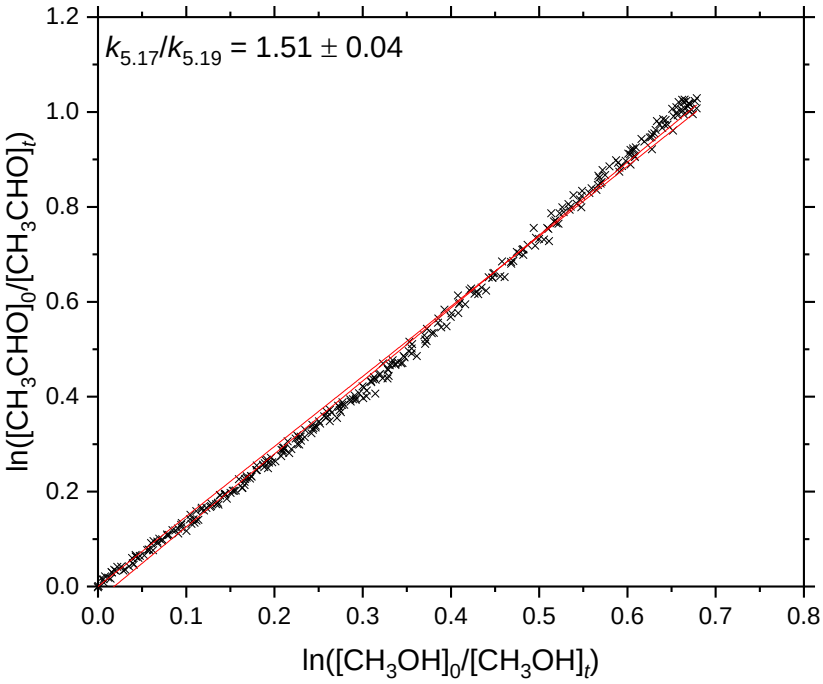

Figure 5.12 A relative rate plot for the Cl-initiated oxidation of methanol and acetaldehyde detected using PTR-MS. The slope of the plot is equal to the ratio of bimolecular rate coefficients $k_{5.17}/k_{5.19}$, with $k_{5.17}$ representing the rate coefficient for reaction of Cl with acetaldehyde and $k_{5.19}$ representing the rate coefficient for reaction of Cl with methanol.

acetaldehyde and methanol at time *t*. Time $t = 0$ was chosen as the point at which oxidation of both species was initiated through the generation of Cl atoms upon activation of the blacklamps. From equation E5.5, a plot of $\ln([CH_3CHO]_0/[CH_3CHO]_t)$ against $\ln([CH_3OH]_0/[CH_3OH]_t)$ therefore yields a slope with the ratio $k_{5.17}/k_{5.19}$. With this method, a ratio of $k_{5.17}/k_{5.19} = 1.51 \pm 0.04$ was found using PTR-MS measurements of both acetaldehyde and methanol at m/z = 45.05 and 33.04 respectively (Figure 5.12). This value is in excellent agreement with those reported by (Tyndall et al., 1997), undertaking a brief pressure-dependent relative rate study between acetaldehyde and ^{13}C-methanol, stating $k_{5.17}/k_{5.19}$ = 1.5 and 1.6 in 700 Torr N_2 and O_2 respectively. Based on the averaged $k_{5.19} = (5.69 \pm 0.34) \times 10^{-11}$ cm^3 molecule^{-1} s^{-1} stated previously, the recommended bimolecular rate coefficient for oxidation of acetaldehyde *via* Cl in this study is $k_{5.17} = (8.74 \pm 0.52) \times 10^{-11}$ cm^3 molecule^{-1} s^{-1}, in reasonable agreement with the value recommended by Tyndall et al. (1999) of $k_{5.17} = (7.8 \pm 1.3) \times 10^{-11}$ cm^3 molecule^{-1} s^{-1}.

Upon establishing the bimolecular rate coefficient for acetaldehyde, a relative rate with methanol and glyoxal was performed in HIRAC. The relative rate was conducted in 1000 mbar air mixture as before. Glyoxal was synthesised as described in Section 5.2.2 and

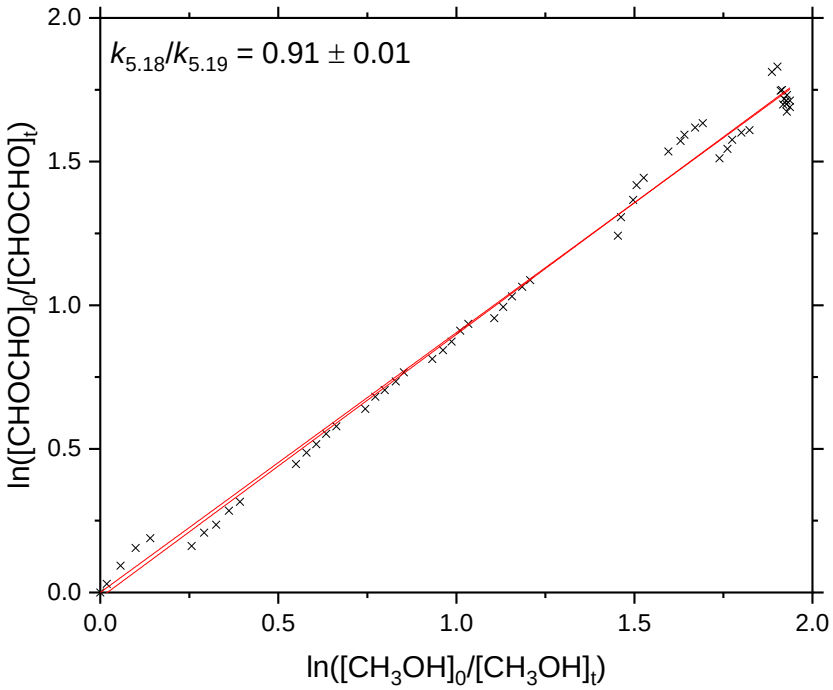

Figure 5.13 A relative rate plot for the Cl-initiated oxidation of methanol and glyoxal, detected using FTIR spectroscopy and GLYOX-LIP respectively. The slope of the plot is equal to the ratio of bimolecular rate coefficients $k_{5.18}/k_{5.19}$, with $k_{5.18}$ representing the rate coefficient for reaction of Cl with glyoxal and $k_{5.19}$ representing the rate coefficient for reaction of Cl with methanol.

diluted to ~30 % in nitrogen prior to delivery into HIRAC. In this instance, methanol was detected using FTIR spectroscopy, and was monitored through the intensity of the peak centred at 1033 cm^{-1}, where there was no overlap with the absorption spectra of glyoxal or any reaction products. Glyoxal was detected using the GLYOX-LIP instrument, and the phosphorescence data, collected every 1 s, was averaged out over 42 s to match the temporal resolution of the FTIR spectra. The relative rate ratio, $k_{5.18}/k_{5.19}$, was determined through equation E5.6:

$$\ln\left(\frac{[\mathrm{CHOCHO}]_0}{[\mathrm{CHOCHO}]_t}\right) = \frac{k_{5.18}}{k_{5.19}} \ln\left(\frac{[\mathrm{CH_3OH}]_0}{[\mathrm{CH_3OH}]_t}\right) \qquad \text{(E5.6)}$$

where $[\mathrm{CHOCHO}]_0$ and $[\mathrm{CHOCHO}]_t$ are the concentrations of glyoxal at time $t = 0$ and time t, respectively. As before, time $t = 0$ was taken as the point at which the reaction was initiated through the generation of Cl atoms upon activation of the blacklamps. Relative first-order loss rates for methanol and glyoxal were determined prior to lamp activation

to determine whether corrections were needed for the bimolecular relative rate calculation due to significantly higher glyoxal loss. However, first-order losses were determined to be within 10 % of one another, and were therefore treated as equivalent for the purposes of bimolecular relative rate calculations. The relative rate ratio was then calculated from the slope of a plot of $\ln([CHOCHO]_0/[CHOCHO]_t)$ against $\ln([CH_3OH]_0/[CH_3OH]_t)$, showing $k_{5.18}/k_{5.19} = 0.91 \pm 0.01$ (Figure 5.13). The bimolecular rate coefficient for reaction of glyoxal with Cl from the relative rate in this study is therefore determined as $k_{5.18} = (5.21 \pm 0.36) \times 10^{-11}$ cm^3 molecule^{-1} s^{-1}. This relative rate value is significantly higher than the value previously determined by Niki et al. (1985a) of $k_{5.18} = (3.8 \pm 0.3) \times 10^{-11}$ cm^3 molecule^{-1} s^{-1} through FTIR detection of a relative rate study with formaldehyde as a reference compound. The impact on modelled simulations of Cl-initiated acetaldehyde oxidation will therefore result in a much slower growth of glyoxal due to faster removal rates.

5.4.2 Glyoxal Yield Comparison

The glyoxal yield from the Cl-initiated oxidation of acetaldehyde was measured in HIRAC at room temperature (293 K) across four data sets (Table 5.4) to examine the consistency of results. In all experiments, initial acetaldehyde mixing ratios were kept within the range of 2 – 4 ppmv, and chlorine gas was delivered in approximately equal proportions to acetaldehyde to ensure sufficient removal of acetaldehyde in yield measurements. As before, acetaldehyde concentrations were monitored through PTR-MS

Run	$[CH_3CHO]_0$ /10^{-13} molecule cm^{-3}	$[Cl_2]_0$ /10^{-13} molecule cm^{-3}	$[Cl]_{av}$ /10^{-6} atom cm^{-3}	Y_{GLY}
1	8.68 ± 0.43	7.31 ± 0.37	9.7 ± 1.7	0.14 ± 0.01 %
2	11.43 ± 0.57	35.27 ± 1.76	45.5 ± 0.8	0.12 ± 0.01 %
3	8.65 ± 0.43	4.61 ± 0.23	4.2 ± 0.6	0.13 ± 0.01 %
4	6.16 ± 0.31	6.15 ± 0.31	6.6 ± 1.5	0.13 ± 0.01 %
Average				**0.13 ± 0.02 %**

Table 5.4 The set of experimental conditions used for the Cl-initiated oxidation of acetaldehyde in HIRAC, alongside the measured glyoxal yield for each run, showing little difference in yield with the variation in initial conditions. Errors for initial acetaldehyde and Cl_2 concentrations were given as 5 %. Averaged Cl atom concentrations were calculated from the acetaldehyde decay observed through PTR-MS detection, with errors calculated as the standard deviation to 2σ of the Cl data.

detection, whilst glyoxal was detected with the GLYOX-LIP instrument, with resulting

data represented in Figure 5.14. The glyoxal yields, calculated from the slope of glyoxal production against acetaldehyde removal (Figure 5.15), showed excellent reproducibility, with an average yield of 0.13 ± 0.02 %, where the error was propagated from all yield measurement errors.

Whilst the glyoxal yield determined through Cl-initiated oxidation is similar to that of OH-initiated oxidation (see Figure 5.5), the data are much more consistent over a wider concentration range throughout Cl-initiated reactions. However, loss rates for glyoxal during Cl-initiated reactions are smaller, and a higher yield might therefore be expected. From the relative rate studies in this work, the ratio for removal of acetaldehyde and glyoxal *via* Cl was indirectly determined to be $k_{5.17}/k_{5.18}$ = 1.68, similar to the ratio of removal *via* OH, however the first order loss of glyoxal through dilution, photolysis and heterogeneous uptake was measured as $k_d = (1.98 \pm 0.28) \times 10^{-4}$ s^{-1}, as much as an order of magnitude lower than measured when using hydrogen peroxide as a precursor to OH molecules. The lower glyoxal loss rate was therefore included in model simulations of glyoxal yields from Cl-initiated acetaldehyde oxidation.

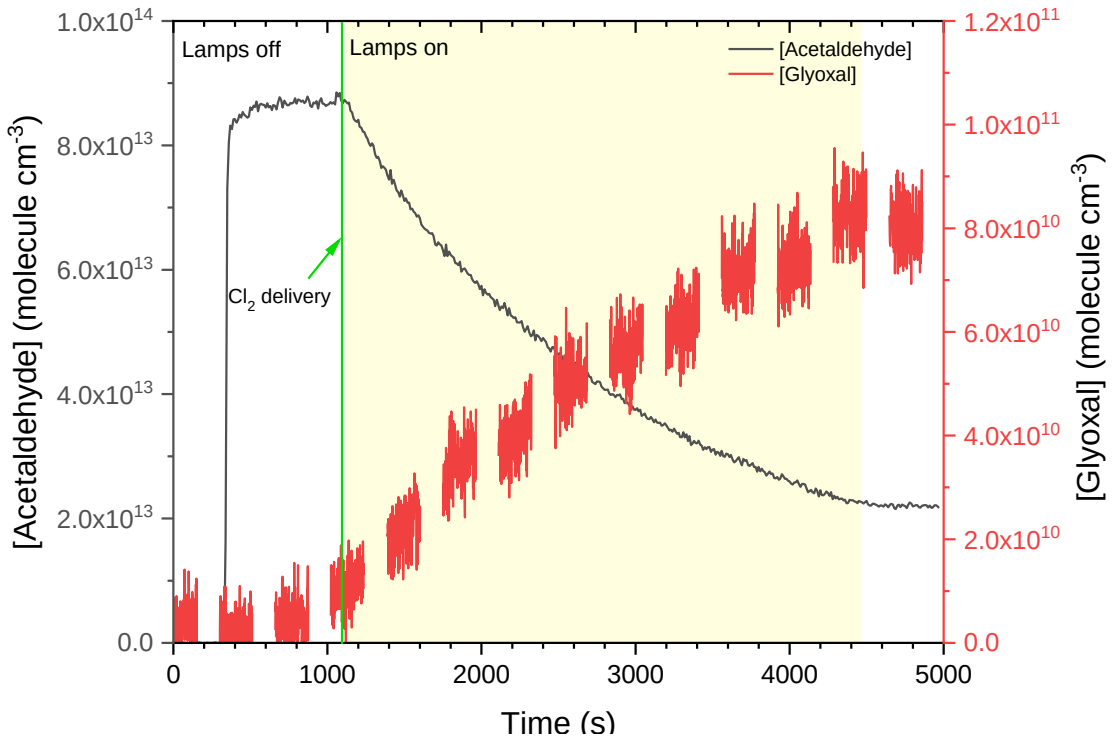

Figure 5.14 Detection of acetaldehyde and glyoxal through PTR-MS and GLYOX-LIP respectively during the Cl-initiated oxidation of acetaldehyde in HIRAC. Scales for concentrations of acetaldehyde and glyoxal differ. The bold green line represents the introduction of gaseous chlorine into the chamber, and the yellow shaded region indicates activation of the UV blacklamps, generating Cl atoms through the photolysis of Cl_2 to initiate the reaction. Data complementary to Figures 5.15 & 5.16.

Model simulations of the Cl-initiated oxidation of acetaldehyde were undertaken using constrained Cl atom concentrations calculated through employing the VOC decay method (see Chapter 4) on measured acetaldehyde data (Figure 5.14) with equation E5.7:

$$[\mathrm{Cl}]_t = \left(\frac{-\frac{\mathrm{d}[\mathrm{CH_3CHO}]}{\mathrm{d}t}}{[\mathrm{CH_3CHO}]_t} - k_\mathrm{d} \right) \Big/ k_{5.17} \qquad \text{(E5.7)}$$

where $[\mathrm{Cl}]_t$ is the concentration of chlorine atoms at time t, $-\mathrm{d}[\mathrm{CH_3CHO}]/\mathrm{d}t$ is the negative slope of acetaldehyde concentration against time, calculated using a window of 10 data points around time t, $[\mathrm{CH_3CHO}]_t$ is the concentration of acetaldehyde at time t, k_d is the rate coefficient for all unimolecular loss processes of acetaldehyde, including sampling dilution, heterogeneous surface adsorption and photolysis, and $k_{5.17}$ is the bimolecular rate coefficient for removal of acetaldehyde *via* reaction with Cl, as detailed above. Average Cl concentrations during each experiment are reported in Table 5.4 above, and remain proportionally consistent to the initial concentration of Cl_2 gas delivered into HIRAC.

It should be noted that calculation of Cl concentrations using this method assumes that removal of acetaldehyde *via* reaction with OH is negligible. However, small quantities of OH (~10^6 molecule cm^{-3}) were accumulated during model simulations of Cl-initiated acetaldehyde oxidation, primarily through RO_2 + HO_2 reactions (R5.21) and the generation of glyoxal through oxidation of the organic hydroperoxide species $HC(O)CH_2OOH$ (R5.22):

$$\mathrm{RO_2 + HO_2 \longrightarrow RO + OH + O_2} \qquad \text{(R5.21)}$$

$$\mathrm{HC(O)CH_2OOH + Cl \longrightarrow CHOCHO + HCl + OH} \qquad \text{(R5.22)}$$

However, as no OH signal was observed through FAGE measurements to be used in model constraints and Cl concentration calculations, OH concentrations were fixed to 0 throughout model simulations in order to simplify accurate replication of acetaldehyde removal, justified on the basis that little difference was observed in modelled product formation ratios between OH- and Cl-initiated oxidation.

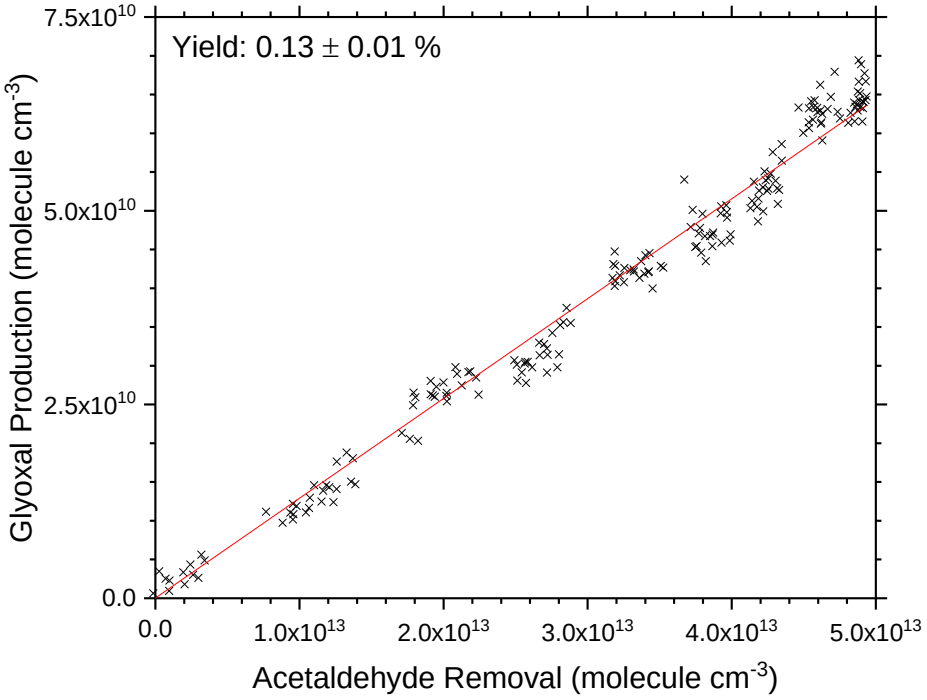

Figure 5.15 The glyoxal yield from the Cl-initiated oxidation of acetaldehyde corresponding to the data shown in Figures 5.14 & 5.16. The GLYOX-LIP data were averaged over 10 s to match the temporal resolution of the PTR-MS detection of acetaldehyde concentrations. The yield shown is calculated merely from the slope of glyoxal production against acetaldehyde removal.

Through the constraint of calculated experimental Cl concentrations and the previously determined bimolecular rate coefficients, $k_{5.17}$ and $k_{5.18}$, the modelled glyoxal yield was compared with experimental observations to examine the mechanism for glyoxal formation. In a simplified analysis, an initial branching ratio for H-abstraction at the methyl site of 0.5 % was used, and a remarkably close agreement was found between measured and modelled glyoxal production (Figure 5.16). It therefore appears increasingly evident that the production of glyoxal through acetaldehyde oxidation, despite accounting for typically higher glyoxal loss rates, is significantly smaller than the current MCMv3.3.1 mechanism suggests. However, further mechanistic tests were undertaken to examine the effects of varying the concentrations of O_2 and NO_x, in order to analyse the potential impact of alkoxy chemistry through the hypothesised reaction R5.15 (see Section 5.3.3).

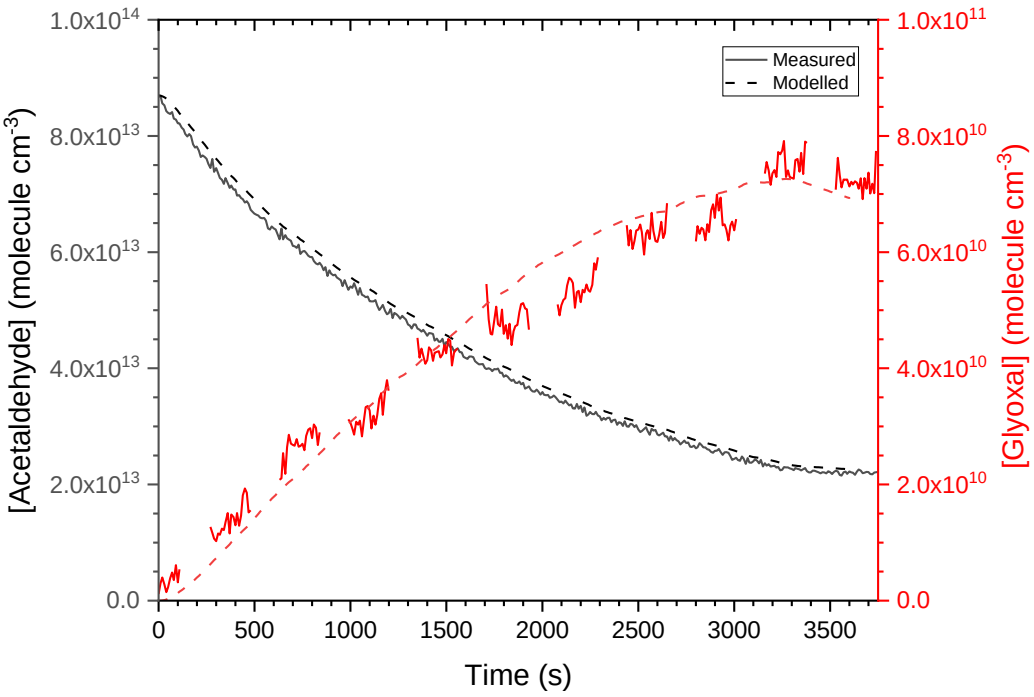

Figure 5.16 Comparison of measured (solid line) and modelled (dashed line) acetaldehyde (black) and glyoxal (red) observations from the Cl-initiated oxidation of acetaldehyde in HIRAC. Model Cl concentrations were constrained from experiment, calculated through the VOC decay method, to replicate the removal of acetaldehyde. The initial branching ratio for abstraction at the methyl site was set to 0.5 %, producing a modelled glyoxal yield with excellent agreement to GLYOX-LIP measurements from experiment. Data complementary to Figures 5.14 & 5.15.

5.4.2.1 O_2 Dependence

As previously stated, the reaction of the alkoxy species, $HC(O)CH_2O$, generated through initial abstraction at the methyl site of acetaldehyde, with O_2 (R5.15) is not included within the MCMv3.3.1 mechanism for acetaldehyde oxidation, instead favouring rapid unimolecular dissocation to produce formaldehyde (R5.16):

$$HC(O)CH_2O + O_2 \longrightarrow CHOCHO + HO_2 \qquad \text{(R5.15)}$$

$$HC(O)CH_2O \xrightarrow{k_d} HCHO + HCO \qquad \text{(R5.16)}$$

As a potentially significant source of glyoxal in the acetaldehyde oxidation mechanism, the exclusion of reaction R5.15 deserves further investigation. Experiments were

therefore conducted to observe the effect on glyoxal yield of varying the O_2 content in the HIRAC bath gas mixture to 50 % and 5 %. It was hypothesised that, should reaction R5.15 prove sufficiently competitive with reaction R5.16, an order of magnitude increase in oxygen concentration would noticeably increase the glyoxal yield observed from acetaldehyde oxidation.

It must here be noted that the method of detection used for observations of glyoxal in HIRAC, namely laser-induced phosphorescence, relies on a calibration performed at a particular ratio of N_2:O_2 to account for the subtraction of background signal in the phosphorescence decay profile for each data point (see Section 5.2.2 & Chapter 2). Altering this ratio results in an altered quenching rate coefficient, k_q, for glyoxal phosphorescence in the triplet state (^3A_u), which subsequently affects the phosphorescence lifetime and hence the background signal to be subtracted. The GLYOX-LIP calibration performed under standard air mixture conditions, and the attained phosphorescence calibration factor, C_{GLY}, therefore become invalid at altered bath gas ratios. However, whilst additional calibrations were not undertaken at the altered bath gas ratios used in acetaldehyde oxidation studies, the quenching effect of oxygen on glyoxal phosphorescence has been previously measured (Yardley, 1972), stating a quenching rate coefficient of $k_{q,O2}$ = (3.0 ± 0.1) × 10^3 s^{-1} $Torr^{-1}$. A corrected phosphorescence decay rate, k_{GLY}, can therefore be calculated at various bath gas ratios using equation E5.8:

$$k_{\mathrm{GLY}} = k_{\mathrm{rad}} + k_{\mathrm{q,O_2}}\, p_{\mathrm{O_2}} + k_{\mathrm{q,GLY}}\, p_{\mathrm{GLY}} \qquad \text{(E5.8)}$$

where k_{rad} is the collision-free phosphorescence decay rate, $k_{q,GLY}$ is the phosphorescence quenching rate coefficient due to self-collision, and p_{O2} and p_{GLY} are the pressures of O_2 and glyoxal respectively inside the detection cell, calculated as a percentage of the total cell pressure (typically ~100 Torr). Both k_{rad} = (3.04 ± 0.10) × 10^2 s^{-1} and $k_{q,GLY}$ = (1.16 ± 0.10) × 10^4 s^{-1} $Torr^{-1}$ were likewise taken from the work of Yardley (1972). The phosphorescence decay curve can then be calculated through an exponential fit (Figure 5.17) using the decay rate at various oxygen ratios through equation E5.9:

$$S_t = S_0\, \mathrm{e}^{-k_{\mathrm{GLY}}\, t} \qquad \text{(E5.9)}$$

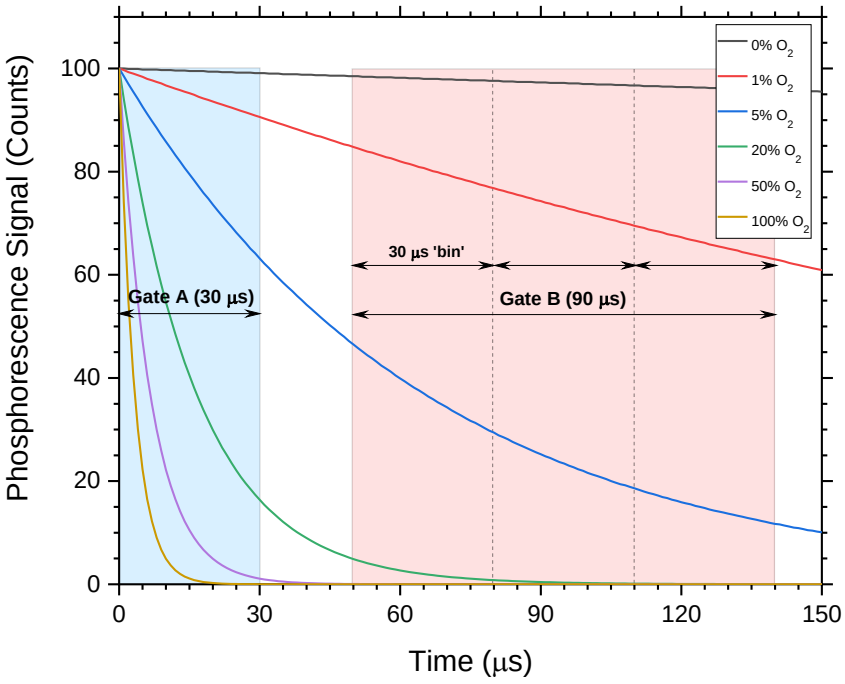

Figure 5.17 The calculated phosphorescence decays of the glyoxal triplet ^3A_u state at various proportions of oxygen within an O_2:N_2 bath gas mixture in a 100 Torr detection cell. Depicted are the decays at O_2 pressures of 0 Torr (black), 1 Torr (red), 5 Torr (blue), 20 Torr (green [standard]), 50 Torr (purple), and 100 Torr (gold). Glyoxal pressure was maintained at 20 μTorr in all calculations for self-collisional quenching correction. An arbitrary signal of S_0 = 100 counts was chosen for ease of interpretation and analysis. Displayed are the A (blue shaded region) and B (red shaded region) gates that would be measured by the GLYOX-LIP instrument in determining the background subtracted counts, calculated cumulatively by counts in A – B/*n*, where *n* is the number of 30 μs 'bins' in the B gate.

where S_t is the phosphorescence signal at time t and S_0 is an arbitrary phosphorescence signal at time t = 0. The number of background subtracted counts must first be calculated through integration of the resulting phosphorescence decay within the A gate (0 – 30 μs) and B gate (50 – 140 μs) (see Figure 5.17) using equation E5.10:

$$\text{Background subtracted counts} = \text{A} - \frac{\text{B}}{n} \qquad \text{(E5.10)}$$

where A and B are the cumulative number of counts in the A and B gates respectively, and n is the number of 30 μs 'bins' within the B gate. The proportional change in background subtracted signal from a standard 20 % O_2 air mixture was then calculated

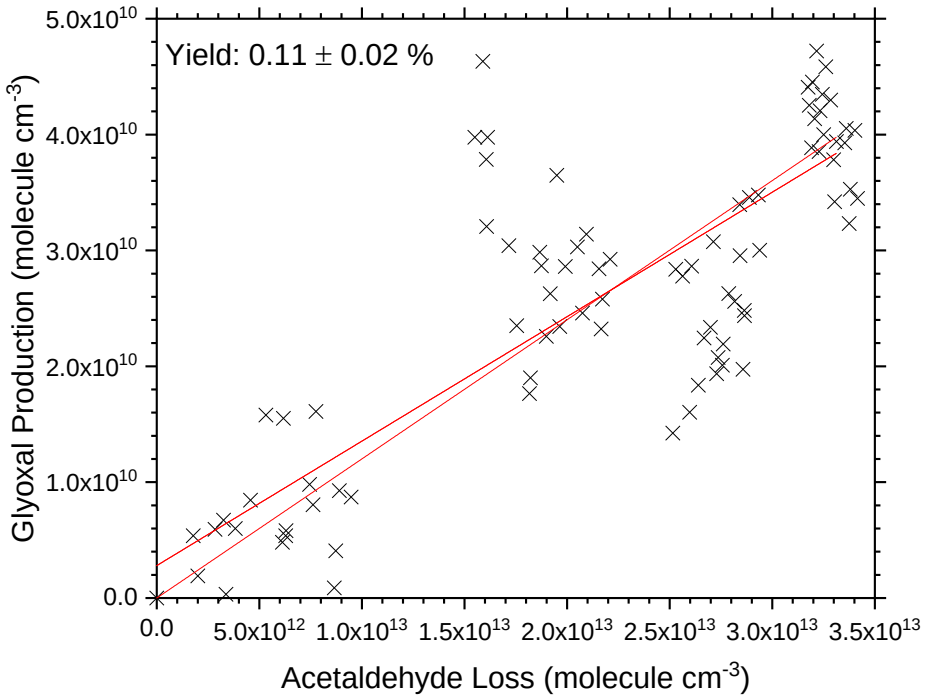

Figure 5.18 The glyoxal yield from the Cl-initiated oxidation of acetaldehyde in a 50:50 mixture of O_2:N_2. Glyoxal concentrations were determined through an applied correction factor to C_{GLY}, measured at a standard air mixture of 20:80 O_2:N_2, based on calculations from the difference in integrated phosphorescence decays under both sets of conditions.

and applied as a correction factor for C_{GLY} in calculation of glyoxal concentrations from normalised phosphorescence signal.

With the appropriately applied correction factors, glyoxal yields were measured from Cl-initiated acetaldehyde oxidation in both 5:95 and 50:50 ratios of O_2:N_2 bath gas. The glyoxal yield at a 50 % oxygen ratio was measured at 0.11 ± 0.02 % (Figure 5.18), and indeed falls within error of the measured yield in a standard air mixture. The lack of increase in yield at a much greater O_2 concentration strongly suggests that reaction of $HCOCH_2O$ with O_2 (R5.15) either does not occur or is negligible at room temperature compared with the unimolecular dissociation of the alkoxy species. In support of this conclusion, the yield at a lower O_2 ratio of 5 % was measured at 0.16 ± 0.02 %, again within the margin of error for the yield in a standard air mixture, and greater than the yield at 50 % O_2. Although any trend in O_2 dependence of glyoxal yield is relatively small, it appears clear that any increase in O_2 concentration does not impact the glyoxal yield positively, and thus suggests that the formation of glyoxal from the oxidation of the alkoxy species, $HCOCH_2O$, is insignificant. The rate coefficient for unimolecular

dissociation in the MCMv3.3.1 is estimated at $k_{5.16} = 1 \times 10^6$ s^{-1}, and RO + O_2 bimolecular rate coefficients are typically consistent at 1×10^{-14} cm^3 $molecule^{-1}$ s^{-1}. Therefore an increase in O_2 content from 5 % to 50 % under these estimations would increase the fraction of alkoxy removal *via* reaction with O_2 from 1.25 % to 12.5 %. This should result in a significant increase in glyoxal yield which is not evidenced by experimental observation, even with the slower conversion of $HC(O)CH_2OO$ to $HC(O)CH_2O$ in the absence of NO_x. However, whilst the evidence shown is seemingly in support of the assumption in the MCMv3.3.1 that reaction R5.15 is negligible, further evidence was sought in the addition of NO_x to the chamber under Cl-initiated oxidation conditions, promoting the conversion of the peroxy $HCOCH_2OO$ species into its subsequent alkoxy species, as in reaction R5.14 (see Section 5.3.3).

5.4.2.2 NO_x Dependence

An increased reaction rate for the bimolecular reaction between $HCOCH_2O$ and O_2 (R5.15) at a constant temperature can be achieved by increasing the concentration of either of the substituents. Whilst an increase in O_2 was specifically designed to increase the reaction rate of R5.15, an increase in $HCOCH_2O$ concentration will accelerate the rates for both R5.15 and the unimolecular dissociation of $HCOCH_2O$ (R5.16). However, it may still be expected that if R5.15 is competitive enough with R5.16 in the oxidation mechanism, an increase in reaction rate for R5.15 will regardless result in an increased glyoxal yield. This would only be the case in the event that an increase in glyoxal production *via* reaction R5.15 is not overly to the detriment of glyoxal production through alternative routes involving HO_2 and RO_2 reactions, which would simultaneously be inhibited by the introduction of NO_x to the system.

Model predictions for the production of glyoxal from a set acetaldehyde concentration and constrained Cl and NO_x concentration profiles at varying ratios of $k_{5.15}[O_2]$:$k_{5.16}$ between 1:1 and 1:20 were simulated, where $k_{5.15}$ is the bimolecular rate coefficient for reaction R5.15, and $k_{5.16}$ is the unimolecular rate coefficient for decomposition reaction R5.16 (Figure 5.19). A significant difference in the glyoxal production profile is the initial growth within the first ~20 minutes. At smaller ratios of $k_{5.15}[O_2]$:$k_{5.16}$, where bimolecular removal of $HCOCH_2O$ *via* O_2 is far less significant, the production of glyoxal observes an apparent delay before the yield increases. It is therefore postulated that in order for the presence of NO_x to increase the yield of glyoxal through acetaldehyde oxidation, the

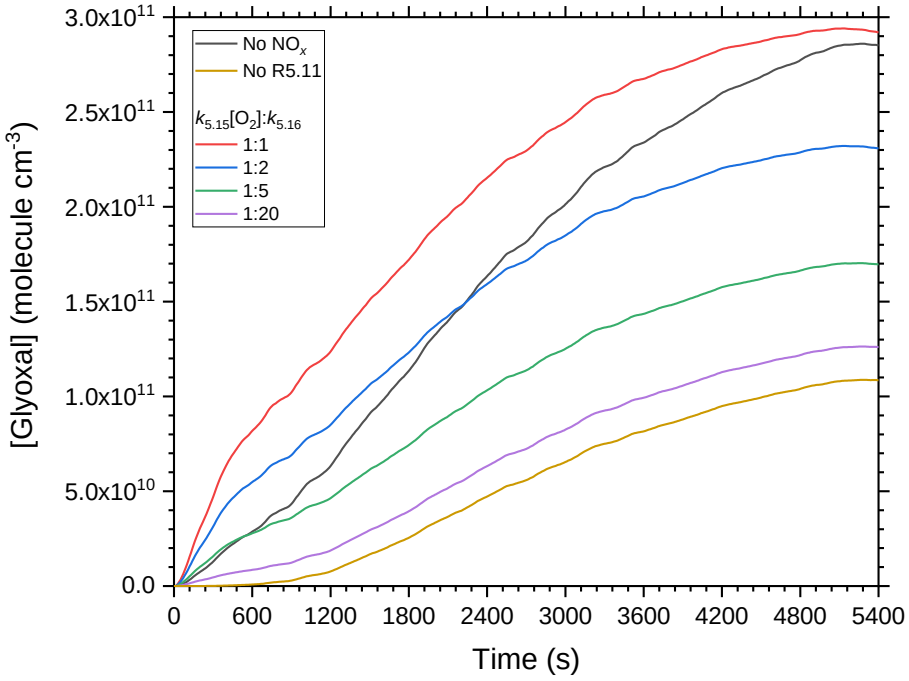

Figure 5.19 Predictions of glyoxal production from the Cl-initiated oxidation of acetaldehyde ($[CH_3CHO]_0 = 7.75 \times 10^{13}$ molecule cm^{-3}) under constrained Cl and NO_x concentration profiles. Model standards were achieved under NO_x-free conditions (black) and inclusion of NO_x without activation of the bimolecular reaction (R5.11) of $HCOCH_2O$ with O_2 (gold). The remaining glyoxal profiles depict the predicted production under differing ratios of $k_{5.11}[O_2]$:$k_{5.12}$ where $k_{5.11}$ is the bimolecular rate coefficient for reaction R5.11 and $k_{5.12}$ is the unimolecular rate coefficient for dissociation of $HCOCH_2O$ (R5.12). The ratios used in model simulations are 1:1 (red), 1:2 (blue), 1:5 (green), and 1:20 (purple). Decreasing ratios, indicating a smaller significance of bimolecular reaction R5.11, are increasingly detrimental to the observed glyoxal yield.

bimolecular reaction R5.15 ought to be significant enough that the ratio of $k_{5.15}[O_2]$:$k_{5.16}$ is at least as great as 1:2. This would seem to require either a significantly increased rate for $k_{5.15}$ or conversely, a significantly decreased rate for $k_{5.16}$, than currently included in the MCMv3.3.1.

The introduction of NO_x to Cl-initiated acetaldehyde oxidation in HIRAC was achieved merely through the addition of nitric oxide (BOC, N2.8 Grade NO) dilute in nitrogen (N_2, BOC, O.F.N., 99.998%). Initial mixing ratios of NO ranged between ~100 – 150 ppbv, and very swiftly reached a steady state during ongoing reaction at ~0.5 ppbv, being rapidly converted into NO_2 through reaction with RO_2 and HO_2 radicals. Experiments were conducted as before, with the generation of Cl atoms through UV photolysis of molecular chlorine gas upon activation of the blacklamps, and the generation of glyoxal was observed through GLYOX-LIP measurements alongside the removal of acetaldehyde through PTR-MS detection. Throughout these experiments, both NO and NO_2

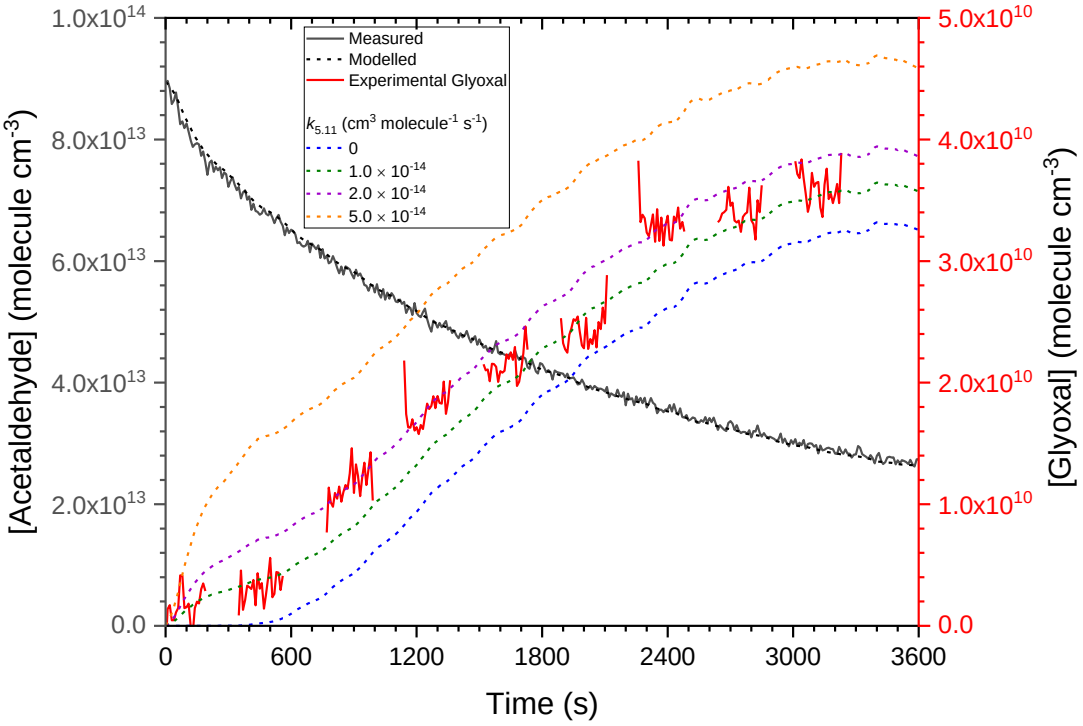

Figure 5.20 A comparison of modelled predictions (dashed line) with direct experimental observations (solid line) for glyoxal (coloured) generation from the Cl-initiated oxidation of acetaldehyde (black). Model simulations are constrained through experimental measurements of NO and NO_2 *via* a commercial NO_x analyser, and calculated Cl atom concentrations obtained through PTR-MS detection of acetaldehyde. Comparisons were made by altering the bimolecular rate coefficient, $k_{5.15}$, for reaction of $HCOCH_2O$ with O_2, ranging between 0 (blue) and 5.0 × 10^{-14} cm^3 molecule^{-1} s^{-1} (orange). A best fit was found with $k_{5.15}$ set to 1.0 × 10^{-14} cm^3 molecule^{-1} s^{-1} (green), closely following the inhibited glyoxal production within the first ~10 minutes prior to reaching a NO_x steady state, as well as the increased yield for the remainder of the reaction.

concentrations were monitored through the use of a commercial NO_x analyser (Thermo Environmental Instruments Model 42C Chemiluminescence NO-NO_2-NO_x Analyser, see Chapter 2 for further details), and the recorded data were used in model constraints for simulating acetaldehyde oxidation. Concentrations of Cl atoms were calculated as before (E5.7), and likewise used to constrain model simulations.

Predicted glyoxal generation from acetaldehyde oxidation was compared with measured GLYOX-LIP data through the alteration of the bimolecular rate coefficient, $k_{5.15}$, for reaction of $HCOCH_2O$ with O_2 (Figure 5.20). Due to the exclusion of this reaction in the MCMv3.3.1, a scenario where $k_{5.15}$ = 0 cm^3 molecule^{-1} s^{-1} was included in comparisons. The model was then tested through varying the rate coefficient in the range of $k_{5.15}$ = (1 – 5) × 10^{-14} cm^3 molecule^{-1} s^{-1}. It was found that the most accurate glyoxal concentration

profile was obtained through inclusion of the reaction at $k_{5.15}$ = 1.0 × 10^{-14} cm^3 $molecule^{-1}$ s^{-1}, following both the inhibition of glyoxal growth within the first ~10 minutes, prior to reaching steady state conditions with NO and NO_2, as well as the subsequent increase in yield for the remainder of the reaction.

Complete exclusion of reaction R5.15 from the mechanism underestimated glyoxal production primarily due to the lack of increase in glyoxal during the period before a NO_x steady state was reached, highlighting a slight inaccuracy in the mechanism. However, with the assumption made in the MCMv3.3.1 for the rate of unimolecular decomposition of $HCOCH_2O$, $k_{5.16}$ = 1.0 × 10^6 s^{-1}, a value of $k_{5.15}$ = 1.0 × 10^{-14} cm^3 $molecule^{-1}$ s^{-1}, consistent with earlier predictions and other RO + O_2 rate coefficients, determines the ratio of $k_{5.15}[O_2]$:$k_{5.16}$ at 1:20, where, at a standard pressure of 1000 mbar, $[O_2] \approx 5.0 \times 10^{18}$ molecule cm^{-3}. The difference in glyoxal yield at atmospherically relevant concentrations, particularly in the absence of NO_x where glyoxal production is dominated by HO_2 and RO_2 reaction routes, is therefore negligible. Indeed, the glyoxal yield measured under high-NO_x conditions in this work, averaged across three datasets, was Y_{GLY} = 0.10 ± 0.03 %, where the error given is the standard deviation of the three yield values to the 2σ level. This is a slight decrease from the observed Y_{GLY} under NO_x-free conditions (0.13 ± 0.02 %, see Table 5.4), further supporting the dominant route of decomposition from the $HCOCH_2O$ alkoxy species by the inhibition of glyoxal generation in the presence of NO_x.

5.5 Conclusions and Future Work

Glyoxal yields have been investigated following both the OH- and Cl-initiated oxidation of acetaldehyde in an attempt to account for the discrepancy observed between glyoxal observations in the MBL and model predictions through constrained data (Walker et al., 2022). It is unclear whether previous recommended branching fractions for H-abstraction at the methyl site of acetaldehyde, 5 % from OH-initiated oxidation (Butkovskaya et al., 2004) and <7 % from Cl-initiated oxidation (Bartels et al., 1989; Cameron et al., 2002), are supported by glyoxal yield observations in this work, due to no direct measurements of the peroxy species $CH_3C(O)OO$ or $HC(O)CH_2OO$. However, low yield measurements of Y_{GLY} = 0.12 ± 0.03 %, in combination with model simulations predicting glyoxal production using species constraints, do indicate uncertainties in the fate of $HC(O)CH_2OO$, both in the case of OH- and Cl- initiated oxidation. Direct RO_2

measurements may assist in distinguishing the initial branching fraction of $HC(O)CH_2OO$ generated. Further, an investigation into OH recycling could be beneficial in determining the significance of glyoxal generated through reaction of $HC(O)CH_2OO$ with HO_2. Required revisions to the MCMv3.3.1 for accurate simulation of glyoxal yields through acetaldehyde oxidation therefore indicates an unrealistic ambient concentration of acetaldehyde (~3 – 5 ppbv) in the MBL to account for daytime glyoxal mixing ratios, and it is therefore highly unlikely that acetaldehyde constitutes the missing source of glyoxal.

Further investigation into the current acetaldehyde oxidation mechanism in the MCMv3.3.1 revealed the exclusion of the reaction of the alkoxy species, $HCOCH_2O$, with O_2 (R5.15), which is a potential route to glyoxal in the mechanism. Experimental studies altering both the concentration of O_2 directly and $HCOCH_2O$ indirectly through the addition of NO_x demonstrated that an inclusion of reaction R5.15 in the mechanism is appropriate with a reaction rate coefficient of $k_{5.15} \approx 1.0 \times 10^{-14}$ cm^3 $molecule^{-1}$ s^{-1}. However, the rate of unimolecular dissociation of $HCOCH_2O$ (R5.16), assumed in the MCMv3.3.1 to be $k_{5.16} = 1.0 \times 10^6$ s^{-1}, is 20 times faster than reaction R5.15 at standard oxygen levels, and inclusion of reaction R5.15 in the mechanism therefore has a negligible impact on the yield of glyoxal from acetaldehyde oxidation, especially in the absence of NO_x, where HO_2 and RO_2 reaction routes dominate.

Whilst the glyoxal yield is much lower than previously thought, determination of R_{GF} from acetaldehyde oxidation remains an important aspect of the UNFOGS campaign. Although accurate formaldehyde yields were not measured in this study, future experiments may focus on a more direct approach to determining the branching fraction of abstraction at the aldehydic site, which is the dominant source of formaldehyde production in the oxidation mechanism. This could be achieved through observation of the acetyl peroxy radical ($CH_3C(O)OO$) in a flash photolysis RO_x-LIF system designed for specific RO_2 detection, in combination with the detection of formaldehyde, to fully establish this reaction in global networks for use with satellite data.

Chapter 6 Glyoxal Yields from the Oxidation of Isoprene

6.1 The Importance of Isoprene Chemistry

Biogenic volatile organic compounds (BVOCs) form an important aspect of atmospheric chemistry through their emission and subsequently rapid oxidation in the troposphere (Atkinson and Arey, 2003), constituting 90 % of all non-methane volatile organic compound (NMVOC) emissions globally (Guenther et al., 1995). BVOCs have very short lifetimes in the atmosphere ranging between 30 minutes to 3 hours due to rapid reaction with OH in the troposphere. The OH-initiated oxidation leads to significant formation of localised oxygenated VOCs (OVOCs), and can consequently lead to the formation of secondary organic aerosol (SOA), particularly in regions where relative humidity is high. The atmospheric lifetime of many BVOCs is reduced further by competing removal *via* ozonolysis, further contributing to the rapid oxidation chemistry of these compounds, as well as the formation of OVOCs and SOA.

Biogenic terpenoids in particular, containing unsaturated double bonds, will undergo ozonolysis *via* formation of an ozonide intermediate (see Chapter 3 for brief discussion on ozonolysis reactions). Ozonolysis is an important sink for regional tropospheric ozone which can be transported vertically from the stratosphere by eddy diffusion due to higher stratospheric mixing ratios (Logan, 1985; Roelofs and Lelieveld, 1997), consequently also forming an important source of OH during daytime and night-time hours (Paulson and Orlando, 1996). However, globally this O_3 sink appears to be offset by an increase in urban tropospheric O_3 (Pfister et al., 2008) through photochemical production in high-NO_x environments (Atkinson, 2000) as a result of increased NMVOC oxidation (see Chapter 1). The chemistry of BVOC emissions is therefore clearly a complex yet important topic to understand in the approach to addressing air quality issues.

Of all BVOC emissions, isoprene (C_5H_8, 2-methyl-1,3-butadiene) is by far the most abundant, individually comprising 80 % of annual terpenoid emissions, including α- and β-pinene, other monoterpenes ($C_{10}H_{16}$ isomers), and sesquiterpenes ($C_{15}H_{24}$ isomers), and represents 64 % of total annual BVOC emissions globally (Sindelarova et al., 2022). Despite this, there remains large uncertainty in the global atmospheric budget of isoprene, with estimates ranging between ~300 – 650 Tg a^{-1} (Guenther et al., 2012; Sindelarova et al., 2014; Sindelarova et al., 2022), and consequently its impact on tropospheric O_3 and SOA levels. Whilst isoprene emissions are predominantly biogenic in origin, there are also anthropogenic sources from biomass burning (Sinha et al., 2014; Andreae, 2019; Bryant et al., 2023), vehicle exhausts (Christensen et al., 1999; Reimann et al., 2000; Borbon et al., 2001; Sahu and Saxena, 2015; Kashyap et al., 2019) and human exhalation

(Ann et al., 2003; Kinoyama et al., 2008; Kushch et al., 2008; Veres et al., 2013) which become important during night-time hours year-round as well as having greater seasonal impact during winter months in urban environments. Studies in the last fifteen years also attribute the impact of urban stressors, such as increased temperatures and ozone concentrations, to triggering an increase in biogenic isoprene emissions within an urban setting where there is no apparently significant change in anthropogenic isoprene emissions or urban vegetative biomass (Pinho et al., 2009; Fu, T.-M. et al., 2015; Khan et al., 2018).

With a focus on the determination of glyoxal to formaldehyde ratios (R_{GF}) from the oxidation of VOCs in order to characterise satellite measurements of emissions (see Chapter 1), an improved understanding of glyoxal yields from isoprene oxidation chemistry is critical. According to Fu, T.-M. et al. (2008), estimated biogenic isoprene emissions (Guenther et al., 2006) contribute nearly half (~47 %) of the combined global sources of glyoxal, calculated through molar yields derived from the GEOS-Chem model version 7.3.6 (Bey et al., 2001), in combination with glyoxal precursors established from the VOC chemistry contained within the Master Chemical Mechanism (MCM) version 3.1 (Saunders et al., 2003; Bloss, C. et al., 2005). With such a large influence on global glyoxal concentrations, it is therefore crucial that the product yields and mechanistic routes to glyoxal from isoprene oxidation are well understood for comparing global chemical transport models such as GEOS-Chem with satellite measurements of R_{GF}.

Advantageously for R_{GF} measurement attribution, isoprene has a very short atmospheric lifetime (~0.5 – 2 hours) due to its rapid oxidation primarily by OH molecules (Medeiros et al., 2018). Glyoxal concentrations monitored using instruments such as the TROPOspheric Monitoring Instrument (TROPOMI) on board the Copernicus Sentinel-5 Precursor satellite (Alvarado et al., 2020; Chen et al., 2022) therefore indicate relatively local sources of glyoxal as a result, as indicated by glyoxal hotspots prevalent over heavily forested regions as well as, in part, more locally confined within large urban areas (Figure 6.1). The dominant anthropogenic source of glyoxal is acetylene emitted predominantly from vehicle exhausts through fuel combustion (Xiao et al., 2007; Fu, T.-M. et al., 2008), and will likely have a larger impact on overall glyoxal concentrations in urban environments than isoprene. However the oxidation of acetylene *via* reaction with OH is approximately 150 times slower than isoprene oxidation, with McKee et al. (2007) measuring a rate coefficient of $k_{OH+C2H2} = 7.1 \times 10^{-13}$ cm^3 molecule^{-1} s^{-1} in 1 bar of N_2 at room temperature. The significantly longer lifetime of acetylene (~3 – 5 days) should

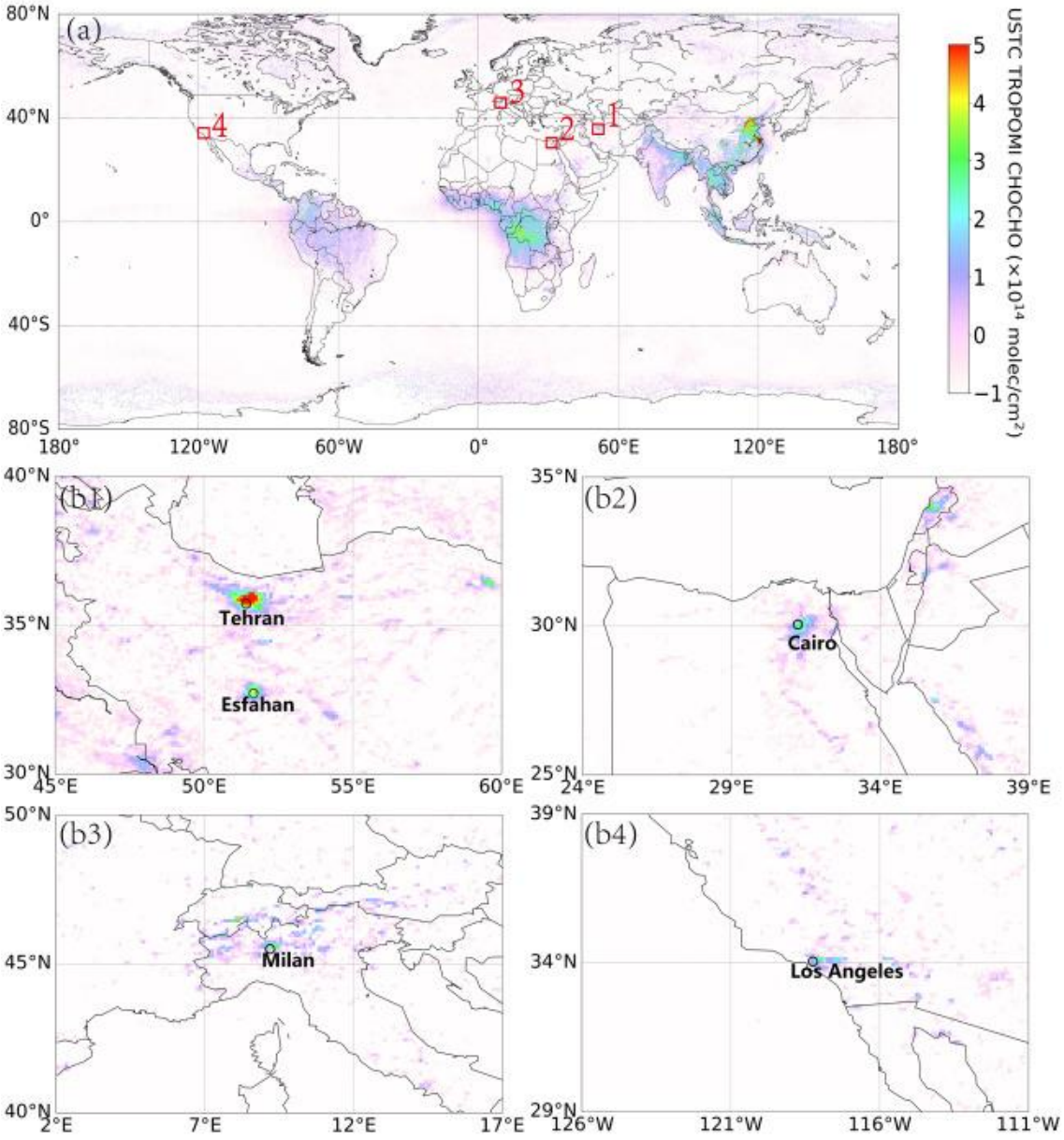

Figure 6.1 The global spatial distribution of glyoxal vertical column densities averaged across January to December of 2019, measured with the TROPOspheric Monitoring Instrument (TROPOMI) on board the Copernicus Sentinel-5 Precursor satellite. The glyoxal distribution highlights hotspots over heavily forested regions where isoprene is prevalent, as well as taking four examples of large urban areas where anthropogenic production of glyoxal is accentuated, both through isoprene emissions and other glyoxal precursors. Taken from Chen *et al*. (2022).

assist in distinguishing urban glyoxal sources and identifying the impact of isoprene on urban glyoxal concentrations, the associated formation of SOA, and the assessment of air quality.

The complete oxidation mechanism for isoprene, whereby the eventual final products consist of CO and CO_2, is highly complex. The MCMv3.3.1 (see Chapter 5) contains a total of 1926 reactions between 602 individual species within the isoprene oxidation scheme, excluding the addition of inorganic reactions, upon relatively recent subjectivity

to major refinement from previous versions of the MCM (Jenkin et al., 2015), as displayed in Figures 6.2 & 6.3. It is therefore not straightforward in distinguishing specific glyoxal routes within the isoprene oxidation mechanism, a complication in the analysis of glyoxal yield measurements. This is apparent in the discrepancies observed by Li et al. (2016) between the AM3ST, AM3B and MCMv3.3.1 models in the simulated reproduction of R_{GF} values measured during the summer 2013 Southeast Nexus (SENEX) campaign (see Chapter 1). Some uncertainties in the mechanism leading to glyoxal can be partially addressed through the investigation of isolated secondary chemistry *via* the reactions of major first-generation oxidation products of isoprene such as methyl vinyl ketone (MVK, 1-buten-3-one) and methacrolein (MACR, 2-methyl-2-propenal), as discussed later (see sections 6.3.4 & 6.3.5). The majority of remaining glyoxal routes appear to originate through the varying fates of the CISOPCO2 peroxy species (see Figure 6.3), either directly as a primary product, or through subsequent oxidation of species such as the hydroxyaldehyde, HC4ACHO, and the hydroperoxyaldehyde, C5HPALD2, formed through 1,6-H isomerisation of the CISOPCO2 species. Comparison of glyoxal yields from isoprene oxidation with those of MVK and MACR oxidation should therefore narrow mechanistic studies of isoprene to the key routes through that one peroxy species.

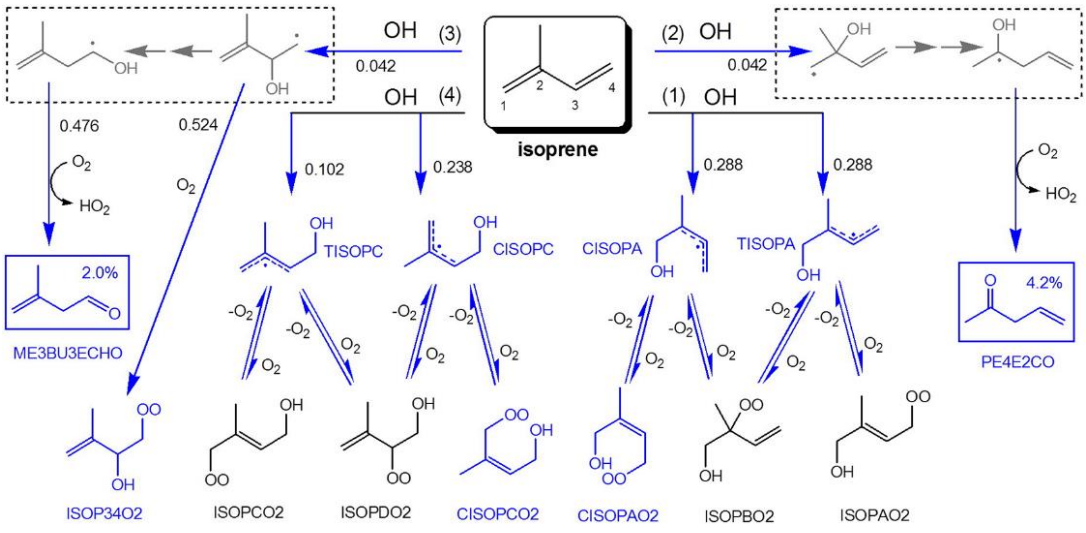

Figure 6.2 A partial schematic of the refined isoprene oxidation mechanism represented within the MCMv3.3.1 through OH addition at each respective numbered site. Displayed are two updated first-generation products in solid boxes alongside their molar yields at 298 K. All species and routes highlighted in blue constitute new mechanistic additions included since previous versions of the MCM. Taken from Jenkin *et al*. (2015).

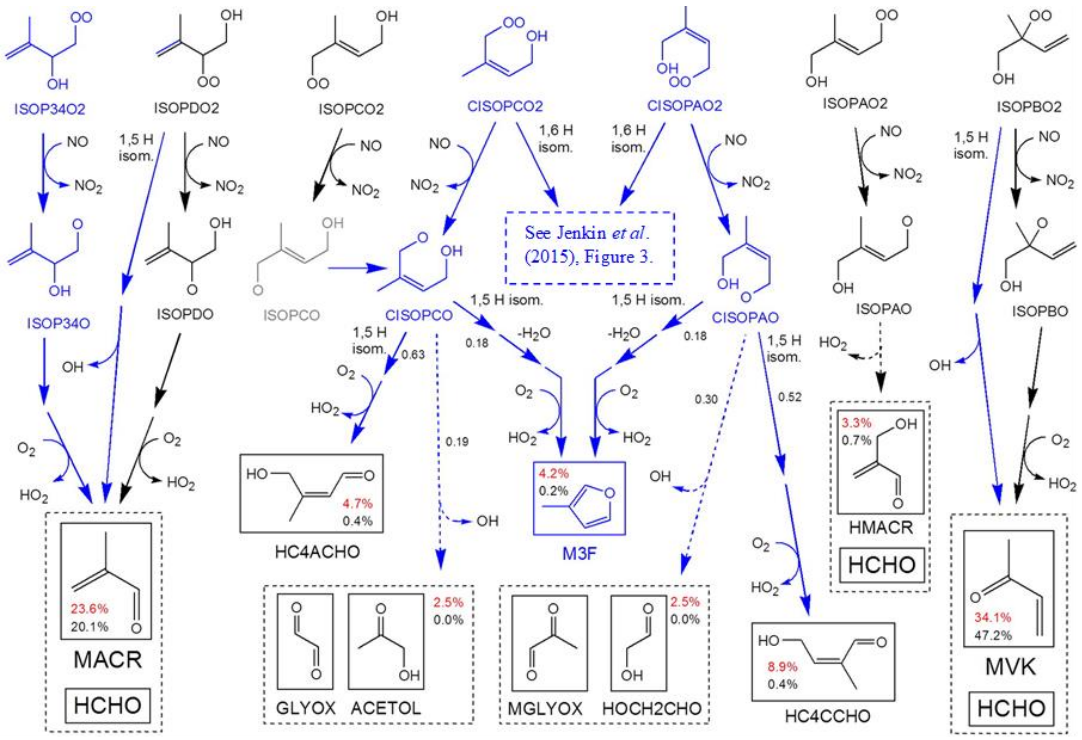

Figure 6.3 A continued schematic of the isoprene oxidation mechanism in the MCMv3.3.1 following the formation of peroxy species shown in Figure 6.2. First-generation products are shown displayed in solid boxes with their respective molar yields under conditions of 1 ppbv NO (red) and 100 pptv NO (black) at 298 K. All species and routes highlighted in blue constitute new mechanistic additions included since previous versions of the MCM. Dashed arrows indicate multiple reaction steps not explicitly outlined in this schematic. Adapted from Jenkin *et al.* (2015).

To that end, this chapter undertakes the investigation of glyoxal yields from isoprene oxidation through chamber experiments in HIRAC. The competing removal rates of isoprene during oxidation are characterised for yield analysis (section 6.3.1), and significant oxidation products are identified for comparison with modelled concentration profiles (section 6.3.2). The oxidation reactions of MACR (section 6.3.4) and MVK (section 6.3.5) are investigated to explore reduced sections of the isoprene mechanism and consequently distinguish glyoxal and methylglyoxal as simultaneous oxidation products. The overall glyoxal yield from isoprene oxidation is determined through observations of glyoxal and methylglyoxal, and the mechanism in the MCMv3.3.1 is explored through comparison of experimental data with model simulations, as described in Chapter 5, to ascertain consistent reproducibility of observed glyoxal yields in HIRAC (section 6.3.6).

6.2 Experimental Methods

The OH-initiated oxidation of isoprene (Sigma-Aldrich, 99%, contains <1000 ppm *p-tert*-butylcatechol as inhibitor) was conducted in the HIRAC facility similarly to the methods described in Chapter 5. In all experiments, isoprene was admitted into HIRAC *via* gaseous delivery under low pressure into a 1 L stainless steel vessel, previously evacuated, and connected to two pressure gauges to generate a known quantity to be flushed through into HIRAC in a flow of nitrogen gas kept at ~2.5 bar pressure. HIRAC was filled prior to isoprene delivery with a 1:4 mixture of oxygen (O_2, BOC, Industrial Grade, 99.5%) and nitrogen (N_2, BOC, O.F.N., 99.998%) to 1000 ± 3 mbar. All experiments were conducted at room temperature (293 ± 2 K). Throughout experimental procedures, HIRAC was maintained at 1000 ± 3 mbar under an adjusted delivery of oxygen and nitrogen in 1:4 mixture through two mass flow controllers (MFC, Brooks) to account for gradual removal of gas over time due to instrumental sampling.

In proceeding with reaction initiation, OH molecules were generated *via* the photolysis of ozone at 254 nm (see sections 6.3 & 6.3.1 for discussion on considerations of isoprene ozonolysis) through activation of the GE Optica GE55T8/HO lamps. Ozone was therefore generated in the flow of oxygen successive to passing through the MFC *via* activation of a mercury pen-ray lamp at 184.9 nm inserted into the oxygen flow. The oxygen atoms produced in the photolysis of oxygen (R6.1) recombine with molecular oxygen to generate ozone (R6.2), which was subsequently delivered into HIRAC in the gas flow.

$$O_2 + h\nu \xrightarrow{\lambda = 184.9\ nm} O + O \qquad \text{(R6.1)}$$

$$O + O_2\ (+M) \longrightarrow O_3\ (+M) \qquad \text{(R6.2)}$$

The delivery rate of ozone into HIRAC may therefore be controlled using two methods. The flow of oxygen through the MFC can be altered to change the amount of oxygen that can be converted into ozone, or the power output of the mercury lamp may be varied by adjusting the lamp current on the power supply, impacting the rate of oxygen photolysis. As gas flow was typically kept constant throughout an experiment to maintain chamber pressure, the variation of lamp current was favoured as the means of controlling ozone delivery. This method allowed consistent delivery of ozone throughout a reaction, with sensitive enough control over delivery rate to maintain constant ozone concentrations for

the duration of the proceedings. Maintaining a constant ozone concentration was considered advantageous for monitoring ozonolysis and generating consistent quantities of OH over the course of a reaction (see section 6.3 for discussion).

The generation of OH *via* ozone photolysis requires the presence of water (see Chapter 3). Ozone is photolysed (R6.3) to produce an excited state singlet atomic oxygen, $O(^1D)$, which may then undergo reaction with a water molecule to produce two OH molecules (R6.4).

$$O_3 + h\nu \xrightarrow{\lambda = 254\ nm} O_2 + O(^1D) \quad \text{(R6.3)}$$

$$O(^1D) + H_2O \longrightarrow OH + OH \quad \text{(R6.4)}$$

To avoid variations in experimental parameters, deionised water (~20 mL) was injected slowly into HIRAC through a rubber vacuum seal with a 2 mL syringe prior to reaction initiation. The injections were performed during the chamber filling stage to encourage vaporisation of the water droplets at lower pressure and prevent excess adsorption onto the chamber surfaces. The fans were switched on as early as possible during the chamber fill to accelerate mixing of the water vapour between injections.

The instrumentation (see Chapter 2) involved in the monitoring of isoprene oxidation reactions included the Proton Transfer Reaction-Mass Spectrometer (PTR-MS) for observation of isoprene and several of its oxidation products; the laser-induced phosphorescence instrument (GLYOX-LIP) for observation of glyoxal (see section 6.3.3 on methylglyoxal interference); the commercial ozone analyser; and the Fluorescence Assay by Gas Expansion (FAGE) instrument for OH and HO_2 observations (see Chapter 4 on issues of OH measurement in the presence of isoprene). Data from all instruments were recorded and analysed for the retrieval of glyoxal yields from isoprene oxidation in HIRAC.

6.3 OH-Initiated Oxidation of Isoprene

The artificial generation of OH in chamber studies may be conducted through several means including ozonolysis, alkyl nitrite (RONO) photolysis, and hydrogen peroxide photolysis (see Chapter 3). Due to the nature of isoprene as a BVOC predominantly

present in rural environments under low NO_x conditions, a method of generating OH without the introduction of NO_x to HIRAC was desired. Alkyl nitrite photolysis was therefore discounted as a viable source for OH generation. Whilst hydrogen peroxide is ordinarily chosen as a convenient NO_x-free OH precursor, it was avoided under present circumstances following evidence observing accelerated glyoxal loss in the presence of hydrogen peroxide, detailed in Chapter 3. Ozonolysis reactions were likewise avoided due in part to limited OH production that would be a poor competitor for isoprene removal with the concurrent ozonolysis of isoprene. Ozonolysis of alkenes would additionally and unnecessarily complicate the chemistry occurring inside HIRAC, creating difficulty in distinguishing between reaction products, in particular resulting in signal observed on GLYOX-LIP instrument, associated with interference from methylglyoxal production (see Chapter 3 or section 6.3.3 for discussion). Ozone photolysis was therefore chosen as a cleaner approach to OH generation without introducing any further VOCs, where the elevated levels of OH produced ($>10^7$ molecule cm^{-3}) should prove an adequate competitor to ozonolysis for removal of isoprene (see section 6.3.1).

With the need for shorter wavelength (254 nm) lamps for ozone photolysis, the photolysis rate of isoprene was investigated prior to the addition of ozone to characterise any input into model simulations if required. However, it should be noted that there is no photolysis process for isoprene listed in the MCMv3.3.1, in considering that OH addition is expected to be a much more significant sink within the troposphere than VUV photolysis *via* sunlight (Campuzano-Jost et al., 2004). More specifically for artificially produced UV wavelength outputs, Martins et al. (2009) state that within the lowest photon energies of their study, 4.6 – 5.0 eV (248 – 269.5 nm wavelength), there is no evidence for any photoabsorption in isoprene. Indeed, measurements performed in HIRAC through PTR-MS detection of isoprene (m/z = 69.12) show negligible difference in isoprene loss before and during activation of the UV lamps prior to the addition of any radical precursors (Figure 6.4). No photolysis processes were therefore added to the MCMv3.3.1 mechanism for isoprene degradation in model simulations, and all products generated throughout isoprene experiments were assumed to be produced from either ozonolysis or OH-initiated oxidation.

In being concerned with the glyoxal yield through the OH-initiated oxidation of isoprene, it is imperative to distinguish between removal of isoprene *via* OH and removal *via* ozonolysis. However, due to a combination of the generation of OH through isoprene ozonolysis (Biesenthal et al., 1998) and issues with elevated FAGE detection of OH in

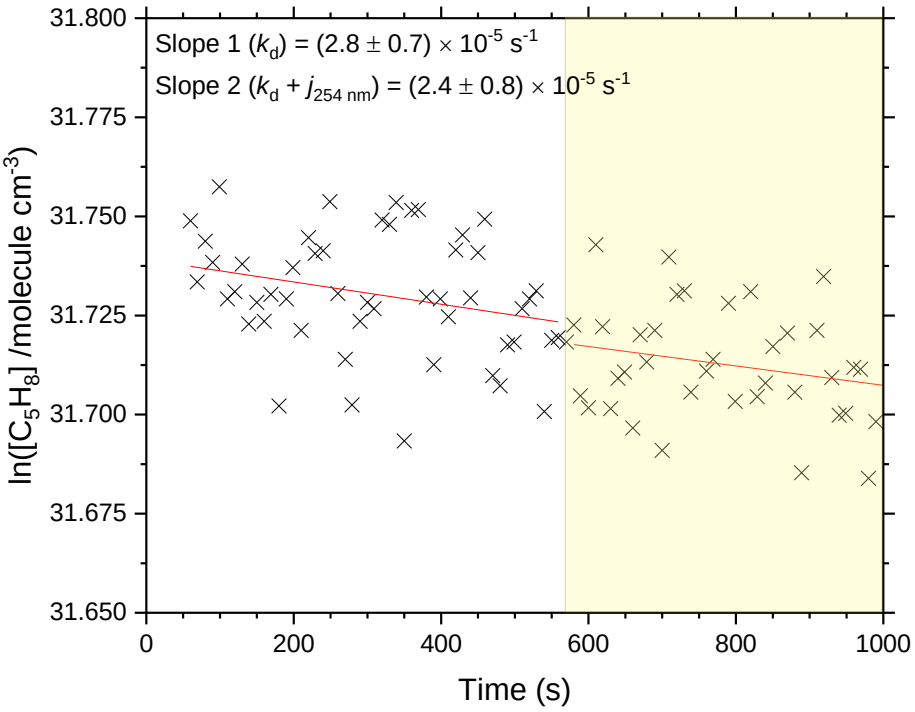

Figure 6.4 Measurement of the first order loss rate for isoprene in HIRAC through PTR-MS detection (m/z = 69.12) prior to the addition of any radical precursors. The yellow shaded region indicates activation of the 254 nm UV lamps within HIRAC. The negligible difference between slopes indicates little evidence for any photolysis of isoprene at this wavelength.

the presence of isoprene (see Chapter 4), this analysis is not straightforward. A discussion is therefore included on the distinction of contributions to isoprene removal and their respective impacts on glyoxal generation.

6.3.1 OH Generation and Ozonolysis

The reaction rate for the ozonolysis of isoprene has been widely studied previously, either through monitoring the pseudo-first-order rate of ozone depletion in a large excess of isoprene (Adeniji et al., 1981; Atkinson et al., 1982b; Treacy et al., 1992; Grosjean, E. and Grosjean, 1996), or by monitoring the isoprene decay in the presence of an OH scavenger, both as a relative rate experiment (Greene and Atkinson, 1992; Khamaganov and Hites, 2001) and through the direct UV photometric detection of ozone alongside isoprene (Grosjean, D. et al., 1993; Neeb and Moortgat, 1999; Klawatsch-Carrasco et al., 2004). The recommended rate coefficient for isoprene ozonolysis (R6.5), established from several of these studies, has been given as $k_{6.5}$ = 1.28 × 10^{-17} cm^3 $molecule^{-1}$ s^{-1} at

298 K (Cox et al., 2020), and is the value used for all calculations of the OH removal of isoprene (R6.6) in accounting for ozonolysis in this study.

$$CH_2{=}C(CH_3)CH{=}CH_2 + O_3 \longrightarrow \text{Products} + OH \quad \text{(R6.5)}$$

$$CH_2{=}C(CH_3)CH{=}CH_2 + OH \longrightarrow \text{Products} \quad \text{(R6.6)}$$

The rate coefficient for the reaction of isoprene with OH has been similarly well studied, and the value obtained by Medeiros et al. (2018) will be used here, where $k_{6.6}$ = (1.04 ± 0.04) × 10^{-10} cm^3 $molecule^{-1}$ s^{-1} at 298 K, in excellent agreement with several previous works (Atkinson et al., 1982a; Atkinson and Aschmann, 1984; Edney et al., 1986; Gill and Hites, 2002; Yumi et al., 2002; Karl et al., 2004; Poppe et al., 2007). All errors calculated for this work are statistical to the 1σ level unless stated otherwise.

6.3.1.1 OH Yield from Isoprene Ozonolysis

As a result of the method of ozone delivery into HIRAC (see section 6.2), the ozone concentration was able to be kept constant during ozonolysis measurement by adjusting the delivery rate to match the rate of ozone depletion in the chamber. This allowed easier analysis of the OH yield (Y_{OH}) from ozonolysis under steady-state conditions in characterising the competing removal rates for isoprene, outlined by equation E6.1:

$$\frac{-\mathrm{d}[C_5H_8]}{\mathrm{d}t} = k_{6.5}[O_3][C_5H_8] + k_{6.6}[OH][C_5H_8] + k_{\mathrm{d}}[C_5H_8] \quad \text{(E6.1)}$$

where $-\mathrm{d}[C_5H_8]/\mathrm{d}t$ is the total removal rate of isoprene and k_{d} is the overall rate coefficient for all first-order loss processes of isoprene including dilution, chamber wall surface adsorption and any heterogeneous uptake. No lamps were activated during ozonolysis measurements, however based on measurements in this work (see section 6.3), it is assumed that no isoprene photolysis occurs throughout experiments regardless. The OH concentration cannot be directly measured during ozonolysis, both due to the detection limit of the FAGE apparatus (~2 – 5 × 10^6 molecule cm^{-3} in HIRAC) and in consideration of the disparity between FAGE and VOC decay measurements of OH in the presence of isoprene (see Chapter 4). However, if the OH produced through ozonolysis is assumed to

be in steady-state conditions, where OH removal is predominantly through reaction with isoprene, OH concentration may therefore be approximated independently of the isoprene concentration by equation E6.2:

$$[\mathrm{OH}]_{\mathrm{SS}} = \frac{k_{6.5} Y_{\mathrm{OH}} [\mathrm{O_3}]}{k_{6.6}} \quad \text{(E6.2)}$$

where $[\mathrm{OH}]_{\mathrm{SS}}$ is the steady-state concentration of OH and Y_{OH} is the yield of OH molecules from isoprene ozonolysis. Substituting E6.2 into E6.1 gives the relationship between total isoprene removal rate and OH yield in equation E6.3:

$$\frac{-\mathrm{d}[\mathrm{C_5H_8}]}{\mathrm{d}t} = (1 + Y_{\mathrm{OH}}) k_{6.5} [\mathrm{O_3}][\mathrm{C_5H_8}] + k_{\mathrm{d}} [\mathrm{C_5H_8}] \quad \text{(E6.3)}$$

This can then be rearranged to calculate Y_{OH} from ozonolysis without the need to measure OH concentrations (E6.4):

$$Y_{\mathrm{OH}} = \frac{\frac{-\mathrm{d}[\mathrm{C_5H_8}]}{\mathrm{d}t} - k_{\mathrm{d}} [\mathrm{C_5H_8}]}{k_{6.5} [\mathrm{O_3}][\mathrm{C_5H_8}]} - 1 \quad \text{(E6.4)}$$

The concentration of ozone is kept constant, and an average of experimental data was therefore used in calculations. Both k_{d} and $-\mathrm{d}[\mathrm{C_5H_8}]/\mathrm{d}t$ were determined as constants, the former through a linear regression of $\ln([\mathrm{C_5H_8}])$ over time prior to ozone addition, according to first-order rate law, and the latter through a linear regression of $[\mathrm{C_5H_8}]$ over time due to the relatively small fraction of total isoprene depleted (~10 %), and therefore displaying only very minor exponential behaviour. The isoprene concentration was taken from experimental data taken every 10 seconds through PTR-MS detection. The OH yield was calculated typically throughout a ~10 – 15 minute period of ozonolysis (Figure 6.5), showing consistent results with an average of $Y_{\mathrm{OH}} = 0.37 \pm 0.09$. This calculation is in good agreement with several previous works (Atkinson et al., 1992; Paulson et al., 1998; Neeb and Moortgat, 1999; Malkin et al., 2010), affirming the validity of both the bimolecular rate coefficients and the experimentally determined ozone concentrations in HIRAC.

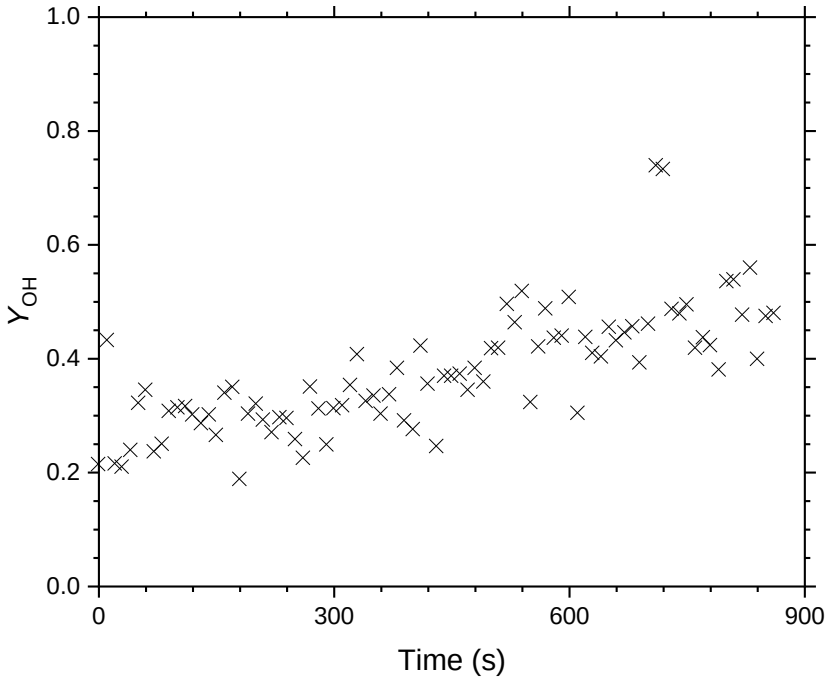

Figure 6.5 Calculations of the OH yield from the ozonolysis of isoprene prior to activation of the UV lamps. The average yield was calculated as $Y_{OH} = 0.37 \pm 0.09$.

Calculation of Y_{OH} also allows an estimation of $[OH]_{SS}$ during ozonolysis, through equation E6.2, for constraint in model simulations to compare the production of glyoxal prior to activation of the UV lamps. Typical steady-state concentrations produced are on the order of 10^5 molecule cm^{-3} – approximately seven orders of magnitude lower than that of ozone – and consequently represents ~30 % of isoprene oxidation during ozonolysis. This is a significant fraction of isoprene removal, and should result in a small yield of glyoxal that would not be observed from ozonolysis alone.

6.3.1.2 Ozone Photolysis

Subsequently to the ozonolysis measurement period, the 254 nm UV lamps were activated to generate OH radicals directly through the photolysis of ozone (R6.3, 6.4, see section 6.2 and Chapter 3). As during ozonolysis, of paramount importance to this study is the distinction between sources of isoprene removal, with the aim of ensuring that the dominant sink is *via* reaction with OH. Critical to this distinction is the characterisation of glyoxal yields from the degradation of isoprene specifically through OH-initiated oxidation, however, to some extent, the empirical yield is inseparable from the contributions of both OH- and O_3-initiated reactions due to the presence of both species

at all times during isoprene oxidation. Comparison with modelled yields is therefore needed, where both [OH] and [O_3] are constrained through empirically obtained data to account for their contributions towards isoprene removal and glyoxal production.

Due to the unreliability of FAGE measurements during isoprene oxidation (see Chapter 4), the OH concentration during lamp activation must instead be calculated through an analysis of the isoprene decay. This can be achieved through a rearrangement of equation E6.1, as follows:

$$[\mathrm{OH}]_t = \left(\frac{\frac{-\mathrm{d}[\mathrm{C_5H_8}]}{\mathrm{d}t}}{[\mathrm{C_5H_8}]_t} - k_{6.5}[\mathrm{O_3}]_t - k_{\mathrm{d}} \right) \Big/ k_{6.6} \qquad \text{(E6.5)}$$

where $[\mathrm{OH}]_t$, $[\mathrm{O_3}]_t$, and $[\mathrm{C_5H_8}]_t$ are the concentrations of OH, ozone and isoprene respectively at time *t*. The concentration of ozone was kept constant through the addition of ozone into the chamber at an equivalent rate to that of its removal *via* ozonolysis and

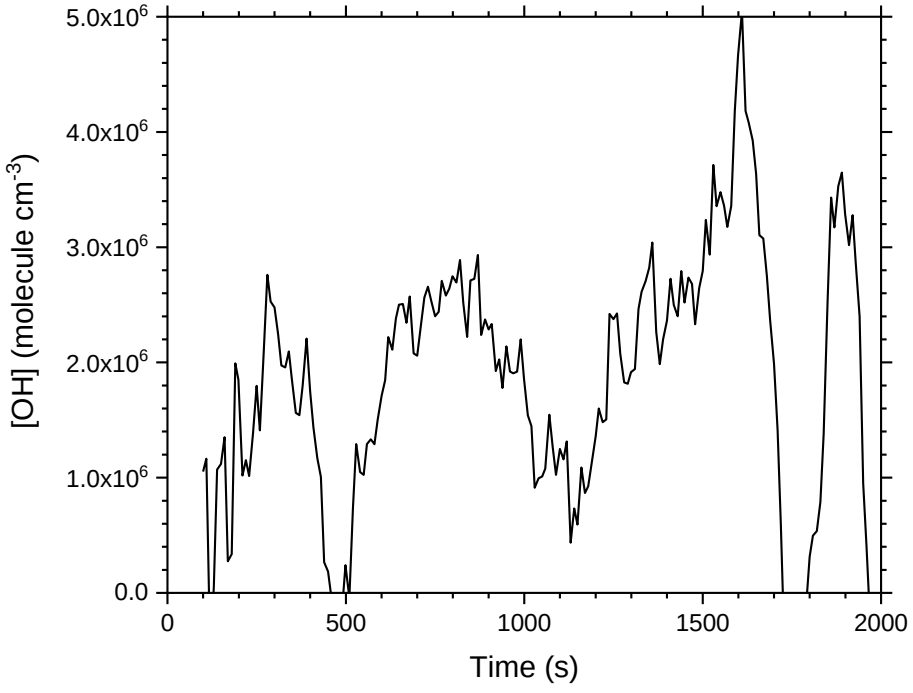

Figure 6.6 Concentrations of OH generated through the photolysis of ozone at 254 nm in the presence of water vapour during the OH-initiated oxidation of isoprene. Concentrations are calculated through differentiation of the isoprene decay detected with the PTR-MS, accounting for alternative sources of isoprene removal including ozonolysis and first-order loss processes such as dilution and surface adsorption. Data complementary to Figure 6.7.

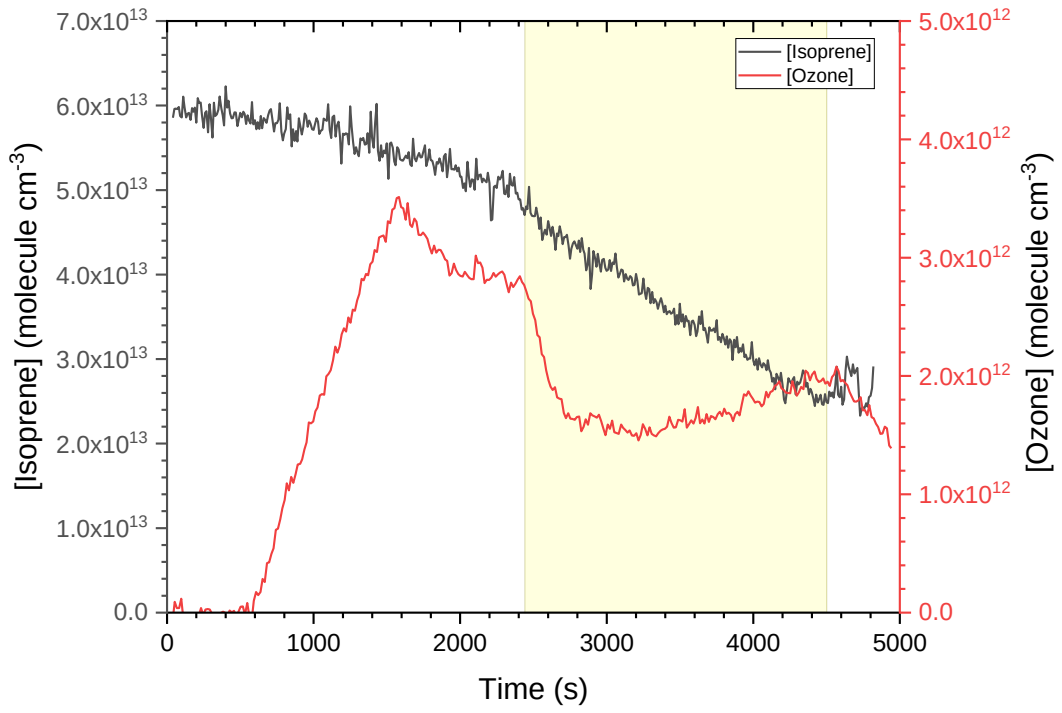

Figure 6.7 The concentration of isoprene (black) shown alongside concurrent ozone concentrations (red) in HIRAC during isoprene oxidation. The yellow shaded region indicates activation of the 254 nm UV lamps, triggering ozone photolysis to generate OH radicals. Prior to lamp activation, OH radicals generated through isoprene ozonolysis contribute to ~30 % of isoprene oxidation. Upon photolysis of ozone, OH radicals contribute ~90 % of isoprene oxidation, indicating glyoxal generation is primarily a result of the OH-initiated oxidation of isoprene. Data complementary to Figure 6.6.

photolysis, and a fixed concentration was therefore used in the calculation of $[OH]_t$. The removal of isoprene over time, $-d[C_5H_8]/dt$, was calculated as described previously (see Chapter 4), obtained through the first differential of $[C_5H_8]$ against time and smoothed over a window of ~10 – 15 points using the Savitzky-Golay method (Savitzky and Golay, 1964). The first-order rate coefficient, k_d, was experimentally obtained as described above (see section 6.3.1.1), and $[C_5H_8]_t$ was taken from empirical PTR-MS detection of isoprene throughout the reaction. The bimolecular rate coefficients, $k_{6.5}$ and $k_{6.6}$, remained the recommended literature values stated above (see section 6.3.1). The calculation was performed for the duration of lamp activation during isoprene oxidation, typically over a period of ~30 – 60 minutes, resulting in OH concentrations on the order of $1 – 5 \times 10^6$ molecule cm^{-3} (Figure 6.6). In comparing with the decreased ozone concentration observed during periods of photolysis (Figure 6.7), accounting also for additional first-order loss rates present throughout experiments, removal of isoprene *via* reaction with OH typically represents ~90 % of isoprene oxidation, contributing the high majority of isoprene removal, and importantly, the generation of glyoxal observed in this study is

therefore predominantly a product of the OH-initiated oxidation of isoprene rather than the ozonolysis of isoprene.

6.3.2 Isoprene Oxidation Products

Through initial measurements from the OH-initiated oxidation of isoprene in HIRAC, some key products were identified through analysis of selected *m*/*z* peaks from PTR-MS detection throughout experimental proceedings. Mass spectra were recorded every 10 seconds, using a cumulative integrated signal count accrued over 9 seconds of data collection. The largest peak growth observed following isoprene oxidation was at *m*/*z* = 71.10, corresponding to species with molecular formula $C_4H_7O^+$, the protonated forms of both methyl vinyl ketone (MVK) and methacrolein (MACR). Both MVK and MACR are major oxidation products of isoprene, with first-generation yields previously reported at 30.4 ± 1.3 % and 22.01 ± 0.62 % respectively under high-NO_x conditions (Galloway et al., 2011) Meanwhile, in low-NO_x (<70 pptv) conditions, Liu et al. (2013) report significantly lower MVK and MACR yields of 4.6 ± 0.7 % and 3.2 ± 0.6 % respectively. These yields remain high enough that detection of MVK and MACR in HIRAC should be possible at typical chamber concentrations (~10^{11} – 10^{12} molecule cm^{-3}), however, due

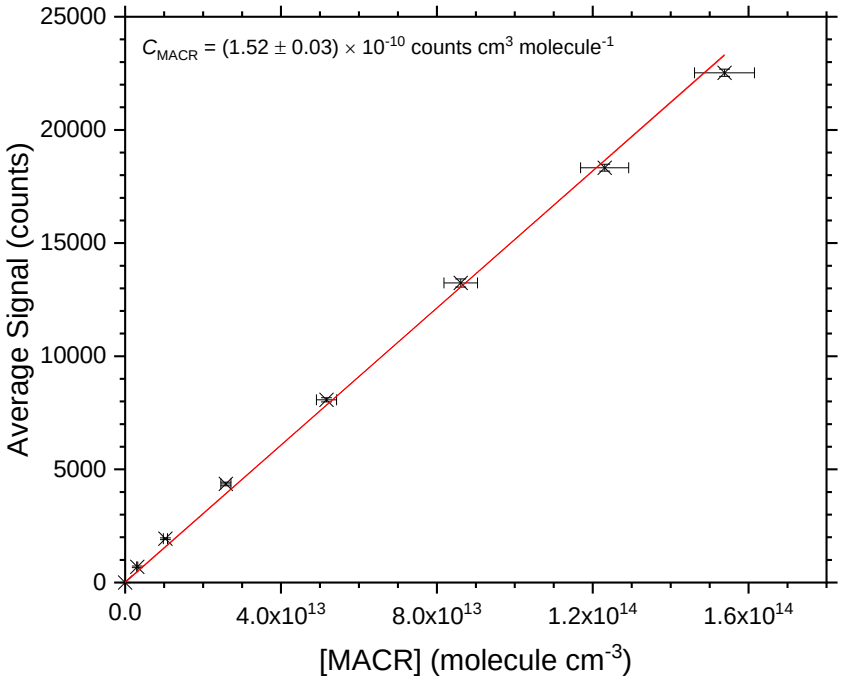

Figure 6.8 The calibration of methacrolein for PTR-MS detection in HIRAC over a range of concentrations appropriate for chamber oxidation studies.

to the isobaric nature of MVK and MACR, their mass spectrometric signal is inseparable, and they cannot therefore be distinguished without the use of additional instrumental detection such as spectroscopic techniques.

Despite this inseparability during isoprene oxidation, individual calibrations of MVK and MACR were performed in HIRAC over a range of concentrations between ~3.0×10^{12} – 1.5×10^{14} to observe the linearity and assess the calibration factor for conversion of *m*/*z* counts to concentration (Figure 6.8). The desired linearity was observed in both calibrations beyond concentrations typically present during oxidation reactions, and the calibration factors were almost identical, to within a small error of one another, where $C_{MVK} = (1.51 \pm 0.02) \times 10^{-10}$ counts cm^3 molecule^{-1} and $C_{MACR} = (1.52 \pm 0.03) \times 10^{-10}$ counts cm^3 molecule^{-1}. In effect, a combined concentration of MVK and MACR may therefore be obtained through PTR-MS data, which can be compared with a similarly combined concentration from model simulations to analyse the product yields to a lesser extent.

A significantly smaller peak at *m*/*z* 61.06, indicative of a species with molecular formula $C_2H_5O_2^+$, was also observed. Similarly, this peak is also thought to correspond to two distinct yet isobaric species; namely glycolaldehyde and acetic acid. Glycolaldehyde is a

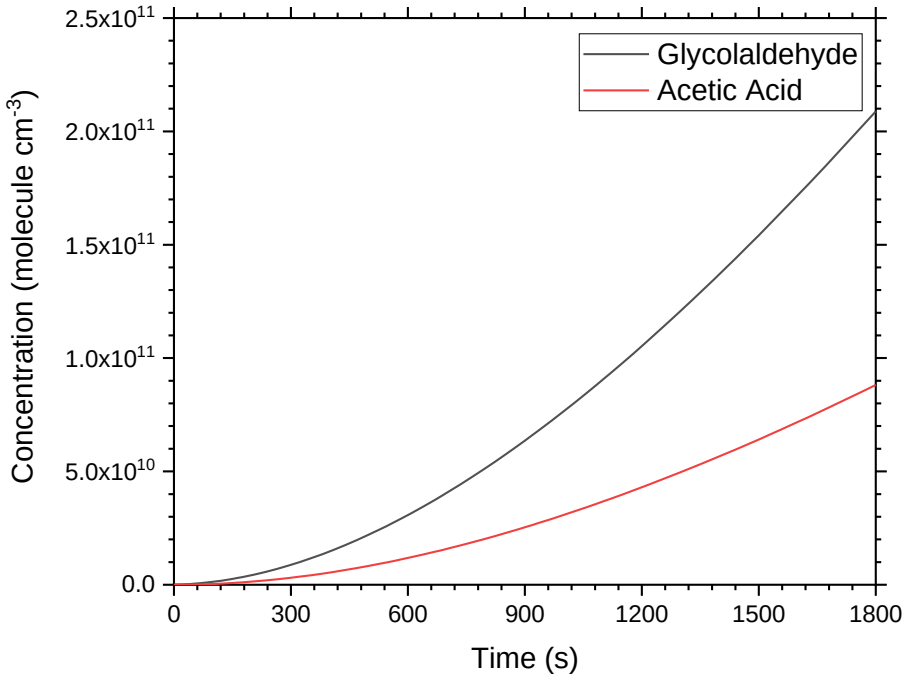

Figure 6.9 Modelled production of glycolaldehyde and acetic acid from the OH-initiated oxidation of isoprene with the MCMv3.3.1 degradation mechanism. Modelled yields over a 30 minute period suggest that distinction of either product through PTR-MS detection is not possible due to their isobaric nature.

direct oxidative precursor to glyoxal, and may therefore form an important aspect of the isoprene oxidation mechanism. Measurement of glycolaldehyde yields would assist in quantifying the proportion of glyoxal produced through glycolaldehyde rather than other mechanistic routes. However, model simulations of isoprene oxidation using the MCMv3.3.1 mechanism suggest that acetic acid is present with a yield approximately half that of glycolaldehyde (Figure 6.9), and therefore not an insignificant product. It was concluded that glycolaldehyde yields could not be determined in this study, and it may be beneficial to include more selective detection between acetic acid and glycolaldehyde in future works.

Arguably most significantly, methylglyoxal was observed through a peak at m/z = 73.07, corresponding to molecular formula $C_3H_5O_2^+$. Whilst methylglyoxal is isobaric with acrylic acid (propenoic acid, CH_2=CHC(O)OH), which is present in the isoprene oxidation mechanism, no significant build-up of acrylic acid was observed in model simulations, and the yield was therefore assumed to be negligible with respect to PTR-MS detection, and all signal at m/z = 73.07 representing detection of methylglyoxal. However, the simultaneous production of both glyoxal and methylglyoxal through isoprene oxidation causes difficulties in the selective detection of glyoxal through the laser-induced phosphorescence technique (see Chapter 3 on earlier discussion of methylglyoxal interference). A discussion is therefore included on the nature of phosphorescence signal interference and the techniques involved in separating methylglyoxal phosphorescence detection from that of glyoxal detection in establishing the glyoxal yield from isoprene oxidation.

6.3.3 Methylglyoxal Interference

Both glyoxal and methylglyoxal can be detected through laser-induced phosphorescence at a probe excitation wavelength of 440.141 nm, as demonstrated previously by a similar instrumental setup (Henry et al., 2012). The sensitivity of phosphorescence detection observed in methylglyoxal is approximately an order of magnitude lower than the sensitivity for glyoxal, owing to differences in the structure and size of their absorption cross-sections around 440.14 nm, their phosphorescence decay lifetimes, and the efficiency of the intersystem crossing from the singlet into the triplet state required to induce phosphorescence in each molecule. As a consequence of these differences, the

contribution of both species to a total phosphorescence signal can be determined through an analysis of the phosphorescence decay to determine the individual concentrations.

However, separation of the phosphorescence decays would first require the calibration of methylglyoxal with the GLYOX-LIP instrument, and hence induce additional uncertainty through methylglyoxal synthesis and surface losses during calibration. Additionally, analysis of each phosphorescence decay over the longer time periods involved in chamber oxidation experiments would inevitably become very time-consuming. Therefore, an alternative approach was sought to calibrate the methylglyoxal phosphorescence signal with the signal observed through PTR-MS detection at *m*/*z* 73.07. In order to achieve this, the OH-initiated oxidation of hydroxyacetone ($CH_3C(O)CH_2OH$) was investigated in HIRAC.

Methylglyoxal is a direct first-generation product from hydroxyacetone oxidation, and is listed as the major component of all products observed, notably without any observations of glyoxal (Grosjean, D. et al., 1993; Jenkin et al., 1993; Butkovskaya et al., 2006; Orlando and Tyndall, 2020). The oxidation of hydroxyacetone proceeds predominantly through abstraction at the hydroxy-substituted methyl site (R6.7).

$$CH_3C(O)CH_2OH + OH \longrightarrow CH_3C(O)CHOH + H_2O \qquad \text{(R6.7)}$$

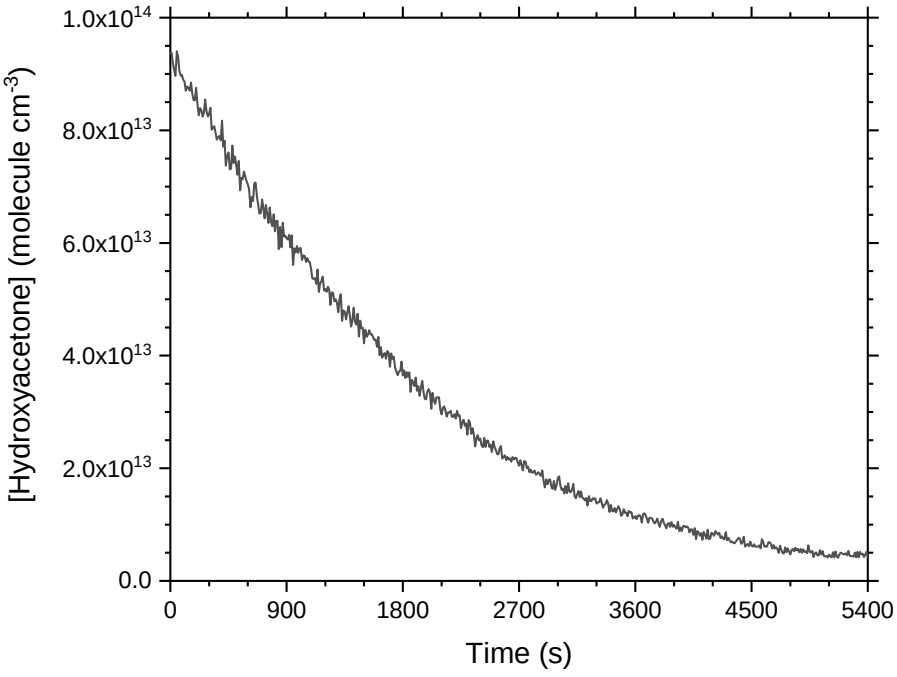

Figure 6.10 The decay of hydroxyacetone due to reaction with OH radicals in HIRAC, monitored via PTR-MS detection with the peak at *m*/*z* = 75.09.

Reaction at the other two available sites is possible, however, the recommended rate coefficient for the OH-initiated oxidation of acetone (Atkinson et al., 1997) is at least an order of magnitude lower than for hydroxyacetone, suggesting that reaction at the alternative methyl site is a very minor route in hydroxyacetone oxidation. Similarly, abstraction at an alcohol site is typically considered a minor route, with Butkovskaya et al. (2006) assigning a branching fraction of ~3 % to both channels from an analysis of acetylperoxy radical and formaldehyde yield measurements. It is therefore assumed that >90 % of hydroxyacetone oxidation proceeds *via* reaction R6.7, and the radical species formed subsequently reacts with O_2 to produce methylglyoxal as the major product (R6.8):

$$CH_3C(O)CHOH + O_2 \longrightarrow CH_3C(O)CHO + HO_2 \qquad \text{(R6.8)}$$

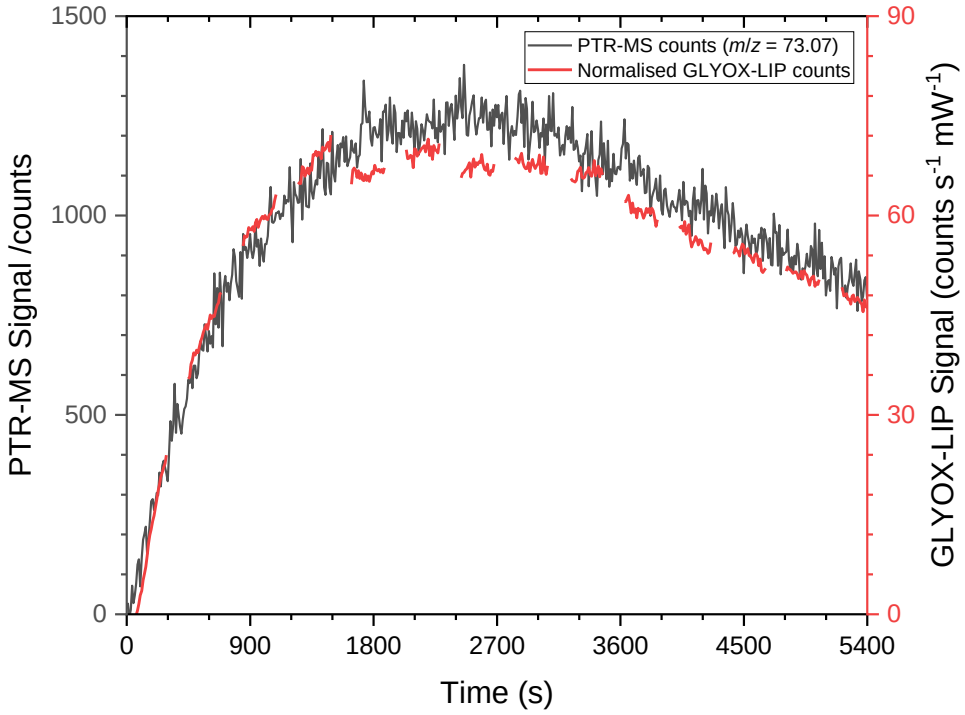

Figure 6.11 Comparisons of methylglyoxal detection from hydroxyacetone oxidation using both PTR-MS monitoring the peak at *m*/*z* = 73.07 and GLYOX-LIP in the absence of any glyoxal. Signal from both methods of detection shows very good overlap, confirming the observations of methylglyoxal phosphorescence.

A known quantity of hydroxyacetone (Sigma-Aldrich, contains ≤500 ppm Na_2CO_3 as stabiliser, technical grade, 90 %) was delivered into HIRAC *via* liquid injection. OH radicals were generated through the photolysis of ozone as described previously (section 6.2). A combination of PTR-MS and GLYOX-LIP detection were employed to establish a relationship between the signal corresponding to methylglyoxal observed using both methods. Hydroxyacetone was detected through PTR-MS monitoring the peak at *m*/*z* = 75.09 to ensure an appropriate quantity of hydroxyacetone removal for production of methylglyoxal (Figure 6.10).

The subsequent methylglyoxal production was monitored, and the observed signals through PTR-MS and GLYOX-LIP detection compared (Figure 6.11). The shape of the signal-time profiles display a large amount of overlap, affirming observations of methylglyoxal phosphorescence with the GLYOX-LIP setup for HIRAC oxidation experiments. Whilst an exact concentration for methylglyoxal cannot be extracted without calibrating either instrument for methylglyoxal, these measurements do provide a metric for the specific detection of methylglyoxal which can then be subtracted from total phosphorescence signal observed where both glyoxal and methylglyoxal are

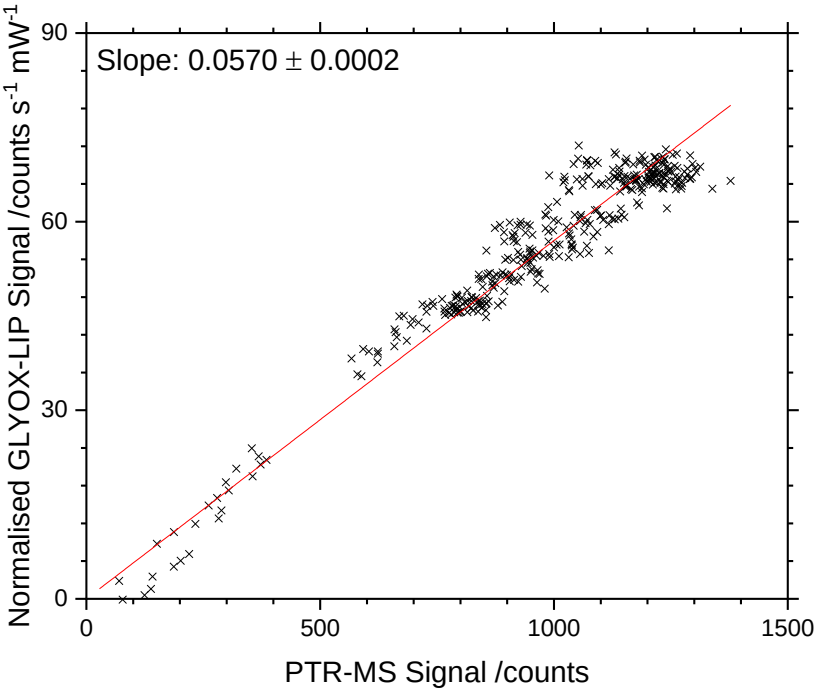

Figure 6.12 A calibration for the phosphorescence signal produced by methylglyoxal with a conversion factor from the integrated peak counts monitored through PTR-MS detection at *m*/*z* = 73.07, attributable to methylglyoxal.

produced simultaneously. The normalised GLYOX-LIP phosphorescence signal was plotted against PTR-MS signal for *m*/*z* = 73.07 to acquire a conversion factor for extracting phosphorescence signal from PTR-MS detection of methylglyoxal (Figure 6.12). The linearity of the data producing this conversion factor demonstrates the feasibility of this method for separating phosphorescence contributions from glyoxal and methylglyoxal during isoprene oxidation. However, it was deemed appropriate to evaluate the reliability of this method by investigating methylglyoxal comparisons under a more complex chemistry regime. Therefore the oxidation of methacrolein was studied with the aim of detecting methylglyoxal production and comparing the resulting conversion factor with that obtained through hydroxyacetone oxidation.

6.3.4 Methacrolein Oxidation

The OH-initiated oxidation of MACR can proceed *via* four distinct pathways. The first two pathways involve the addition of OH onto either end of the C=C double bond, at both the terminal carbon (R6.9a) and the tertiary methyl-substituted carbon (R6.9b). The second two involve abstraction at either the aldehydic site (R6.9c) or the methyl site (R6.9d).

$$CH_2{=}C(CH_3)CHO + OH\,(+M) \longrightarrow HOCH_2C^{\cdot}(CH_3)CHO\,(+M) \quad \text{(R6.9a)}$$

$$CH_2{=}C(CH_3)CHO + OH\,(+M) \longrightarrow {}^{\cdot}CH_2C(CH_3)(OH)CHO\,(+M) \quad \text{(R6.9b)}$$

$$CH_2{=}C(CH_3)CHO + OH \longrightarrow CH_2{=}C(CH_3)C^{\cdot}{=}O + H_2O \quad \text{(R6.9c)}$$

$$CH_2{=}C(CH_3)CHO + OH \longrightarrow CH_2{=}C({}^{\cdot}CH_2)CHO + H_2O \quad \text{(R6.9d)}$$

It is generally considered that OH-initiated MACR oxidation predominantly proceeds through reactions R6.9a and R6.9c in approximately equal proportion, whilst R6.9b forms a minor channel and R6.9d is negligible (Tuazon and Atkinson, 1990; Orlando et al., 1999; Crounse et al., 2012). The major products from MACR oxidation have been well established to be formaldehyde, hydroxyacetone, and methylglyoxal, specifically with no glyoxal generation observed (Tuazon and Atkinson, 1990; Orlando et al., 1999; Galloway et al., 2011; Brégonzio-Rozier et al., 2015; Xing et al., 2018). Methylglyoxal is generated as a second-generation product from MACR, with the primary precursor being either

hydroxyacetone or, in some minor routes, 2-hydroxy-2-methylpropanedial ($HCOC(OH)(CH_3)CHO$). Observations of methylglyoxal yields from MACR oxidation should therefore be similar to those of hydroxyacetone. A comparison of the conversion factor for the PTR-MS signal at *m*/*z* 73.07 to phosphorescence signal from methylglyoxal produced during both MACR and hydroxyacetone oxidation will demonstrate the reliability of this method for extracting and separating methylglyoxal and glyoxal phosphorescence signals.

It is worth noting that methylglyoxal can also be generated through the ozonolysis of MACR (Deng et al., 2012), either directly (R6.10a) or *via* a stabilised Criegee intermediate, CI_{MGLY} (R6.10b).

$$CH_2{=}C(CH_3)CHO + O_3 \longrightarrow CH_3C(O)CHO + H_2C{=}O^+O^- \quad \text{(R6.10a)}$$

$$CH_2{=}C(CH_3)CHO + O_3 \longrightarrow CI_{MGLY} + HCHO \quad \text{(R6.10b)}$$

However, on the basis of previously measured rate coefficients for reaction of MACR with OH (average $k_{6.9} = (2.88 \pm 0.42) \times 10^{-11}$ cm^3 molecule^{-1} s^{-1}) (Kleindienst et al., 1982; Atkinson et al., 1983; Chuong and Stevens, 2004; Peirone et al., 2014) and O_3 (average $k_{6.10} = (1.08 \pm 0.32) \times 10^{-18}$ cm^3 molecule^{-1} s^{-1}) (Atkinson et al., 1981a; Treacy et al., 1992; Grosjean, D. et al., 1993; Grosjean, E. and Grosjean, 1998), and the ratio of [OH]:[O_3] (~1:4 × 10^5 molecule cm^{-3}) produced in HIRAC through ozone photolysis during MACR oxidation, it was calculated that ozonolysis constitutes <2 % removal of MACR during reaction. Nevertheless, any occurring ozonolysis will have no impact on the comparison of signals observed between PTR-MS and GLYOX-LIP detection, as methylglyoxal and formaldehyde remain the primary products and no glyoxal is produced.

Two MACR oxidation experiments were conducted in HIRAC to analyse the reliability of methylglyoxal detection techniques compared with the instrument intercomparison undertaken through hydroxyacetone oxidation. Known quantities (~5 × 10^{13} molecule cm^{-3}) of MACR (Sigma-Aldrich, 95 %) were delivered into HIRAC and detected *via* PTR-MS (*m*/*z* 71.10) to monitor the amount of total MACR decay and ensure sufficient production of methylglyoxal for detection *via* PTR-MS and GLYOX-LIP. OH radicals were generated through the photolysis of ozone as described previously (see section 6.2). Upon reaction initiation through activation of the UV lamps, MACR decay and product generation was observed over ~90 – 120 minutes to acquire as much data as possible for

the intercomparison. Excellent correlation was observed between the growths in phosphorescence signal and *m*/*z* 73.07 signal attributed to methylglyoxal (Figure 6.13), as well as their subsequent decay due to removal primarily *via* reaction with OH. The continued correlation of data reinforced the assignment of methylglyoxal to the observed phosphorescence signal in the absence of glyoxal.

The normalised GLYOX-LIP signal was plotted against the PTR-MS signal at *m*/*z* 73.07 (Figure 6.14), combining the data sets from both experiments, to produce a linear calibration factor, C_{MGLY}, for calculating methylglyoxal contributions to phosphorescence signal. The resultant calibration factor from MACR oxidation (C_{MGLY} = 0.0569 ± 0.0003) was within error of the calibration factor obtained through hydroxyacetone oxidation (C_{MGLY} = 0.0570 ± 0.0002), further demonstrating the reliability of this technique for extracting methylglyoxal phosphorescence data. Advantageously, the data for C_{MGLY} calculations through MACR oxidation spanned the quantities (~50 – 300 counts at *m*/*z* 73.07) typically observed during isoprene oxidation, where the majority of the data fell within this range. This was included in the hydroxyacetone C_{MGLY} calculation, however formed the lower end of the data range, with

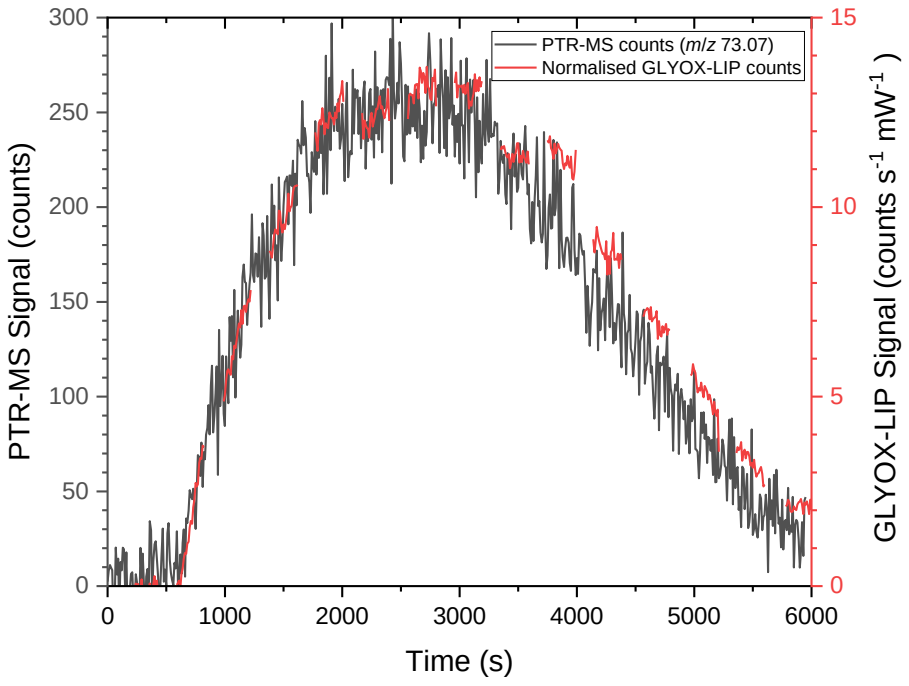

Figure 6.13 An instrument intercomparison of the PTR-MS (black) and GLYOX-LIP (red) detection of methylglyoxal through the OH-initiated oxidation of MACR in HIRAC. 90 % of [MACR] depleted by *t* = 3000 s, resulting in overall of depletion of methylglyoxal due to faster loss rates than production rates.

very few data points to establish a linear correlation. The MACR C_{MGLY} data therefore

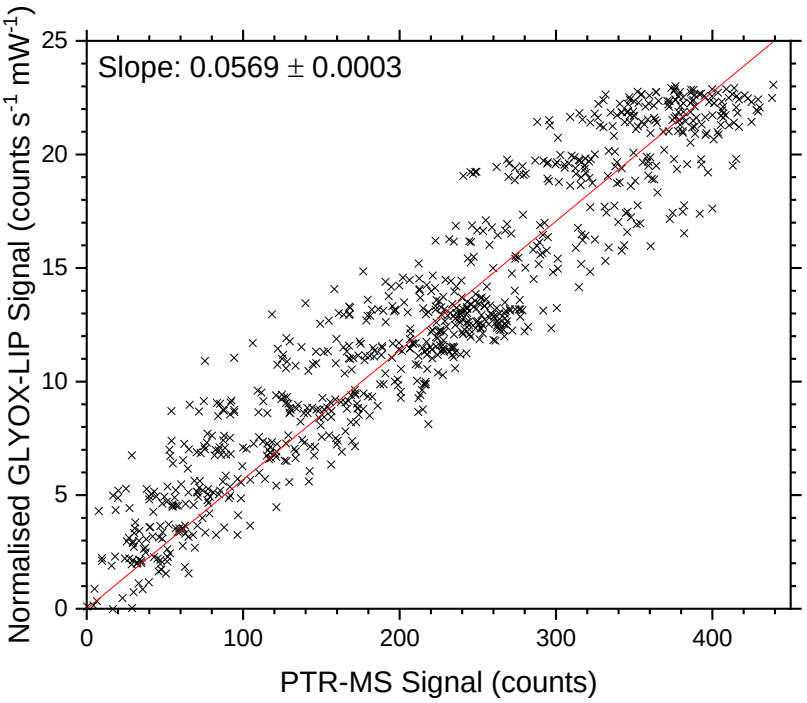

Figure 6.14 Calculation of a calibration factor, C_{MGLY}, for conversion of PTR-MS signal at *m/z* 73.07 to normalised phosphorescence signal attributable to methylglyoxal. Displayed are the combined data generated from two OH-initiated MACR oxidation experiments in HIRAC.

served to demonstrate the reproducibility of accurate signal conversion for methylglyoxal phosphorescence at quantities relevant for isoprene oxidation.

6.3.5 Methyl Vinyl Ketone Oxidation

The ability to extract methylglyoxal phosphorescence from the overall signal observed *via* the GLYOX-LIP instrument was tested through the oxidation of MVK. MVK was chosen as the test experiment for two reasons. Firstly, MVK is a major product of isoprene oxidation, and quantification of oxidation products will therefore shape part of the isoprene oxidation mechanism used in simulations. Secondly, both glycolaldehyde and methylglyoxal are produced as first-generation oxidation products from the reaction of OH with MVK (Tuazon and Atkinson, 1989; Grosjean, D. et al., 1993; Galloway et al., 2011; Praske et al., 2015; Fuchs et al., 2018), and as glycolaldehyde is a direct precursor to glyoxal, both glyoxal and methylglyoxal are produced simultaneously. The OH-initiated oxidation of MVK proceeds *via* addition of OH to the C=C double bond site (Tuazon and Atkinson, 1989), either at the carbon adjacent to the carbonyl group

(R6.11a), forming the minor channel (~30 %, Atkinson et al. (2006)), or at the terminal carbon (R6.11b), forming the major channel (~70 %, Atkinson et al. (2006)).

$$CH_3C(O)CH{=}CH_2 + OH\,(+M) \longrightarrow CH_3C(O)CH(OH)^{\cdot}CH_2\,(+M) \qquad \text{(R6.11a)}$$

$$CH_3C(O)CH{=}CH_2 + OH\,(+M) \longrightarrow CH_3C(O)^{\cdot}CHCH_2OH\,(+M) \qquad \text{(R6.11b)}$$

The resultant peroxy species formed through subsequent reaction of radicals from R6.11a and R6.11b with O_2 will be termed $HMVKAO_2$ and $HMVKBO_2$ respectively, as denoted in the MCMv3.3.1. The minor peroxy radical, $HMVKAO_2$, forms the primary route to methylglyoxal, whilst $HMVKBO_2$ conversely dictates the route to glycolaldehyde, and subsequently glyoxal (Figure 6.15). Knowledge of the branching fraction for $HMVKAO_2$ and $HMVKBO_2$ is therefore highly useful for predicting yields of glyoxal and methylglyoxal from MVK oxidation. Historically, a branching fraction of 0.3:0.7 for $HMVKAO_2$:$HMVKBO_2$ has been recommended (Atkinson et al., 2006) for use in model

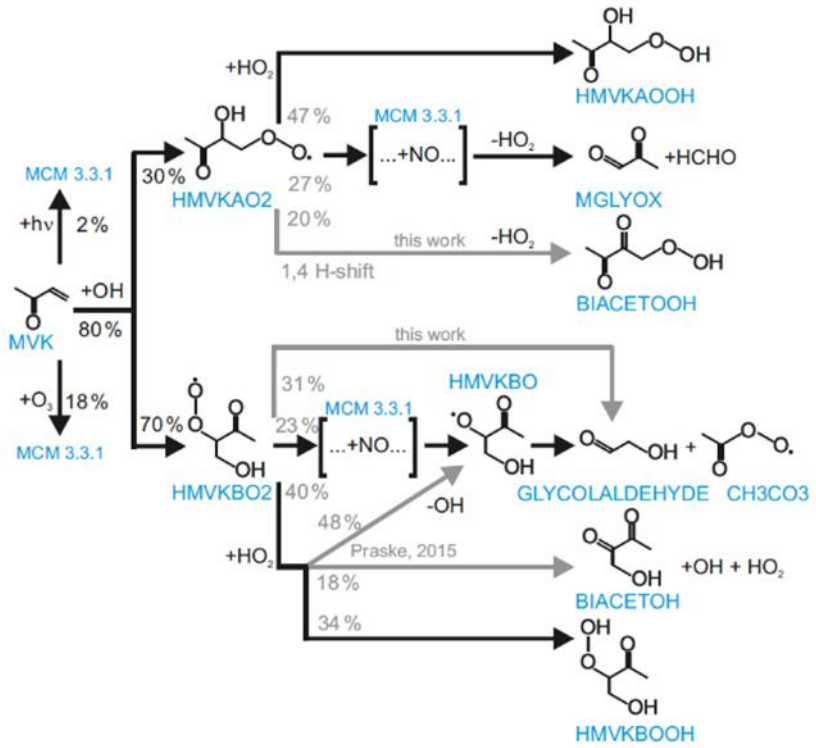

Figure 6.15 A simplified diagram of the oxidation mechanism for MVK. Species, reaction arrows, and branching fractions in black are currently employed by the MCMv3.3.1, with the associated species notation in blue. Reaction arrows and branching fractions in grey indicate suggested updates by either Praske *et al.* (2015) or Fuchs *et al.* (2018). Figure taken from Fuchs *et al.*, (2018).

simulations. However, a product yield analysis following the possible reactions of both peroxy species undertaken by Praske et al. (2015) has led to the suggestion of slightly altered peroxy yields, listed as 24 ± 14 % and 76 ± 14 % for $HMVKAO_2$ and $HMVKBO_2$ respectively. A more recent chamber study (Fuchs et al., 2018) of product yields from MVK oxidation in SAPHIR (Simulation of Atmospheric Photochemistry In a Large Reaction Chamber) has recommended the inclusion of these new branching fractions, as well as other reactions relating to the fate of both peroxy species, in the MCMv3.3.1. These recommended additions were therefore included in model simulations of MVK oxidation, and consequently isoprene oxidation, in this work.

Whilst methylglyoxal is a minor product of OH-initiated MVK oxidation, it is also produced through ozonolysis, either directly (R6.12a) or through CI_{MGLY} (R6.12b), in a similar fashion to MACR ozonolysis (see section 6.3.4).

$$CH_3C(O)CH{=}CH_2 + O_3 \longrightarrow CH_3C(O)CHO + H_2C{=}O^+O^- \quad \text{(R6.12a)}$$

$$CH_3C(O)CH{=}CH_2 + O_3 \longrightarrow CI_{MGLY} + HCHO \quad \text{(R6.12b)}$$

Due to ozone photolysis being used as the method of OH generation, it was anticipated that a fraction of the methylglyoxal produced would originate from ozonolysis. The bimolecular rate coefficients for both OH addition ($k_{6.11}$) and ozonolysis ($k_{6.12}$) have been well studied in the literature. Therefore, averaged values from previous measurements were taken, using $k_{6.11} = (1.94 \pm 0.38) \times 10^{-11}$ cm^3 molecule^{-1} s^{-1} (Kleindienst et al., 1982; Atkinson et al., 1983; Gierczak et al., 1997; Aschmann and Atkinson, 1998; Chuong and Stevens, 2004) and $k_{6.12} = (4.99 \pm 1.01) \times 10^{-18}$ cm^3 molecule^{-1} s^{-1} (Atkinson et al., 1981a; Treacy et al., 1992; Grosjean, D. et al., 1993; Grosjean, E. and Grosjean, 1998; Neeb et al., 1998), and paired with averaged [O_3] (~2×10^{12} molecule cm^{-3}) measurements, to calculate concentrations of OH in HIRAC during MVK oxidation through equation E6.6:

$$[OH]_t = \left(\frac{\frac{-d[MVK]}{dt}}{[MVK]_t} - k_{6.12}[O_3]_t - k_d \right) \Big/ k_{6.11} \quad \text{(E6.6)}$$

The average [OH] was found to be ~2 × 10^7 molecule cm^{-3}, and accounting for first-order loss rates of MVK, it was calculated that ~2.5 % of MVK oxidation could be attributed to ozonolysis. It is therefore likely that only a small portion of total methylglyoxal production originated from ozonolysis despite the high yield, however the ozone concentrations were measured throughout the oxidation reaction and constrained in model simulations for more accurate reproduction of methylglyoxal concentrations over time.

MVK (Sigma-Aldrich, stabilised, ≥93.5 %) was delivered (~5 × 10^{13} molecule cm^{-3}) into HIRAC and oxidation was initiated through photolysis of ozone to generate OH. Both MVK and methylglyoxal were monitored through PTR-MS detection at *m*/*z* 71.10 and 73.07 respectively, with simultaneous detection of glyoxal and methylglyoxal phosphorescence using the GLYOX-LIP instrument. The phosphorescence signal attributable to glyoxal, PS_{GLY}, was calculated by subtracting the methylglyoxal phosphorescence signal, PS_{MGLY}, from the total observed signal, PS_{tot}, at time *t* (E6.7)

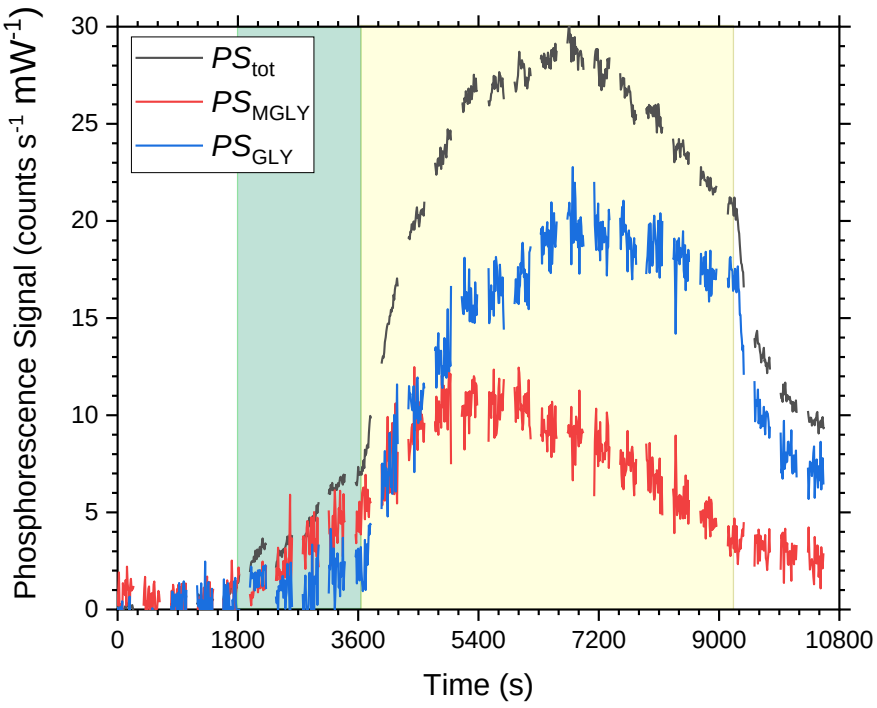

Figure 6.16 The glyoxal phosphorescence signal (blue) calculated from MVK oxidation through subtracting the calibrated PTR-MS methylglyoxal signal (red) from the total observed phosphorescence signal (black). The green shaded region indicates a dark period of MVK ozonolysis, highlighting the generation of methylglyoxal whilst glyoxal signal remains relatively stable. The yellow shaded region indicates activation of the UV lamps, inducing ozone photolysis to generate OH radicals, producing both glyoxal and methylglyoxal through OH-initiated MVK oxidation.

through substituting in equation E6.8:

$$PS_{\mathrm{GLY}} = PS_{\mathrm{tot}} - PS_{\mathrm{MGLY}} \quad \text{(E6.7)}$$

$$PS_{\mathrm{MGLY}} = MS_{73.07} C_{\mathrm{MGLY}} \quad \text{(E6.8)}$$

where $MS_{73.07}$ is the PTR-MS signal observed at m/z 73.07 and time t, and C_{MGLY} is the calibration factor established previously. The methylglyoxal subtraction was performed over the entire data set to produce a glyoxal signal profile (Figure 6.16) which could then be converted into glyoxal concentration. Upon examination of the subtracted phosphorescence signal, an increase in methylglyoxal was observed during the ozonolysis phase whilst glyoxal signal remained relatively stable. This was supportive of the MVK ozonolysis mechanism, whereby methylglyoxal and formaldehyde are dominant products, with no generation of glyoxal, and therefore provided confidence in the phosphorescence signal subtraction method used in determining glyoxal concentrations.

Whilst the GLYOX-LIP instrument was not calibrated for methylglyoxal, the signal time

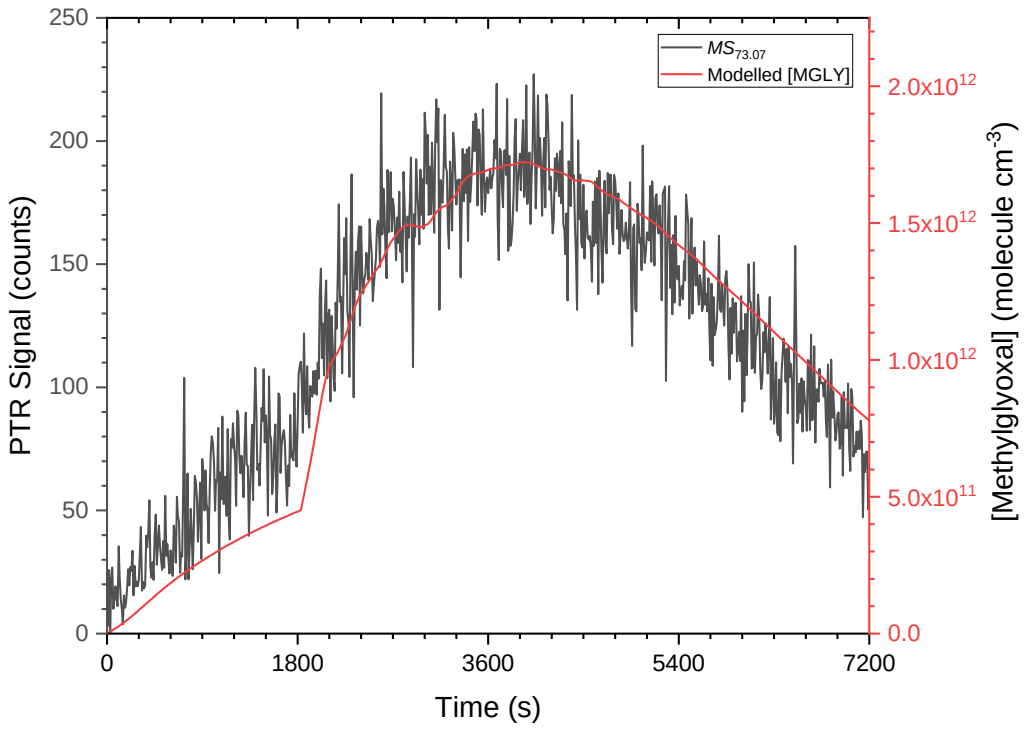

Figure 6.17 A time profile comparison of the measured PTR-MS signal at m/z 73.07 (black) with modelled methylglyoxal concentration (red) from MVK oxidation, using experimental OH and O_3 concentration data constraints in the model run.

profile was compared with model simulations of methylglyoxal concentrations to determine the suitability of the calculated glyoxal concentrations (Figure 6.17). Using

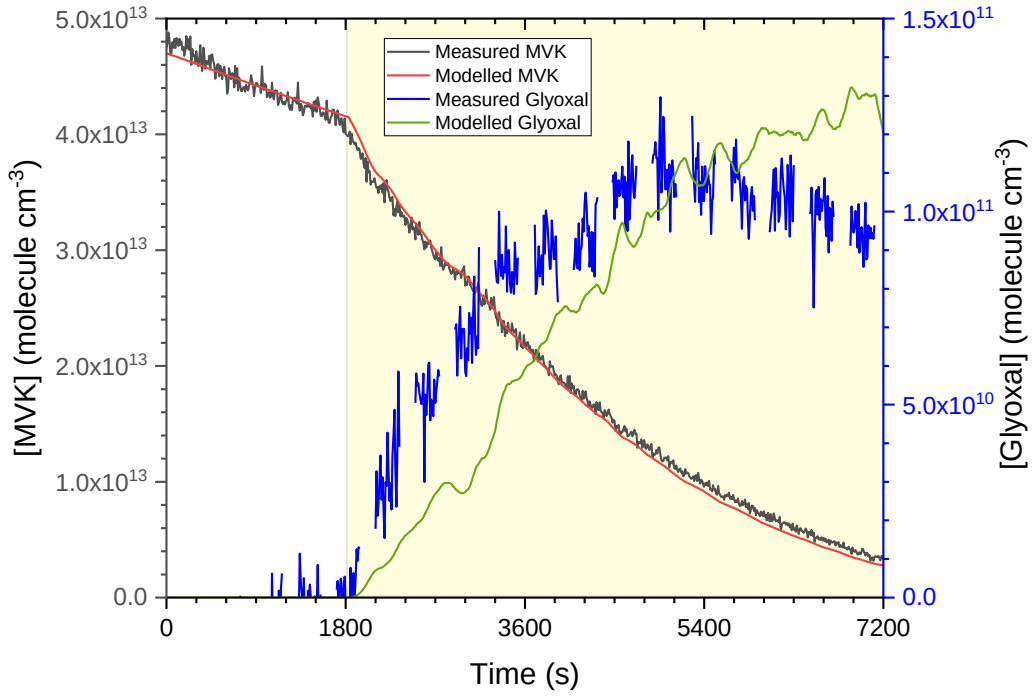

Figure 6.18 Comparisons of experimental data for MVK oxidation (black) and glyoxal production (blue) alongside the corresponding modelled concentrations of MVK (red) and glyoxal (green). The yellow shaded region indicates the period where the UV lamps were activated to initiate OH generation. O_3 and OH concentrations were constrained in the model from experimental data. Loss rates prior to lamp activation include a period of first-order loss (typically measured at ~$0.8 – 1.0 \times 10^{-4}$ s^{-1}) combined with ozonolysis. Any glyoxal signal build-up prior to lamp activation during ozonolysis was subtracted to a baseline in order to examine the glyoxal specifically from OH-initiated oxidation.

experimentally derived [OH] and [O_3] data to constrain concentrations in the model, the methylglyoxal concentration output demonstrated a close match with the observed $MS_{73.07}$. It was therefore considered that the calculated glyoxal phosphorescence data was a good representation of the experimental glyoxal yield from MVK oxidation. The accuracy of the modelled glyoxal yield was then assessed through a comparison with the subtracted glyoxal phosphorescence data (Figure 6.18). The modelled rate of glyoxal growth was slightly underestimated toward the beginning of the reaction, however overall glyoxal concentration increase was similar, suggesting a reasonable understanding of glyoxal generation in the model, and an appropriate order of magnitude for glyoxal phosphorescence measurements in oxidation reactions where methylglyoxal is simultaneously generated. Glycolaldehyde production was not analysed in this study, however future work may benefit from glycolaldehyde measurement data as a direct and primary precursor to glyoxal in MVK oxidation, assisting in further improving the

mechanism for glyoxal production both in the isolated study of MVK and in the isoprene oxidation mechanism as a whole.

6.3.6 Glyoxal Yields from Isoprene Oxidation

The distinction of phosphorescence signal attributable to methylglyoxal has been established through analysis of MACR and MVK oxidation. During isoprene oxidation, PS_{MGLY} consisted of approximately half the total normalised LIP signal, using the same method of methylglyoxal subtraction described in section 6.3.5 (Figure 6.19), and the production of glyoxal from the OH-initiated isoprene oxidation through ozone photolysis was subsequently monitored and analysed. The observed glyoxal production from phosphorescence data was compared against model simulations of glyoxal production using the isoprene oxidation mechanism outlined in the MCMv3.3.1 (Figure 6.20). The

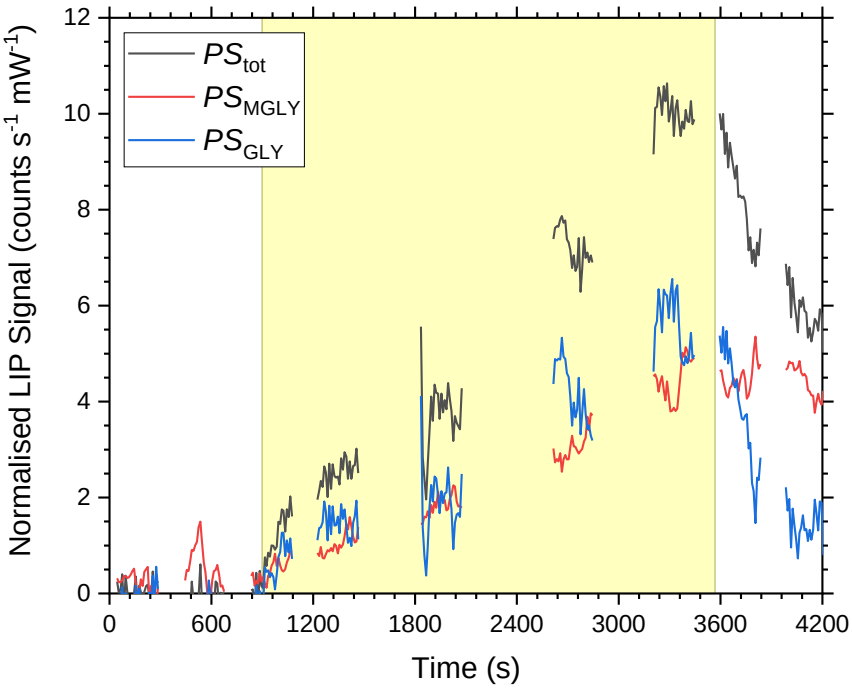

Figure 6.19 An example of the subtraction of calibrated methylglyoxal LIP signal (red) from the total LIP signal (black) to calculate the contribution of glyoxal (blue) to the observed phosphorescence during the OH-initiated oxidation of isoprene. Yellow shaded region indicates activation of the UV lamps in HIRAC to generate OH through ozone photolysis. Data complementary to Figure 6.20a.

model mechanism was updated to include the adjusted branching fractions for $HMVKAO_2$ and $HMVKBO_2$ generation suggested by Praske et al. (2015) (see section 6.3.5). Praske et al. (2015) and Fuchs et al. (2018) also suggested additional fates for the

reactions of the two peroxy species not currently included in the MCMv3.3.1 (R6.13 – 6.15), which were likewise added to the isoprene mechanism in this study.

$$HMVKBO_2 + HO_2 \longrightarrow HMVKBO + OH \quad \text{(R6.13)}$$

$$HMVKBO_2 + HO_2 \longrightarrow BIACETOH + OH + HO_2 \quad \text{(R6.14)}$$

$$HMVKAO_2 \longrightarrow HO_2 + BIACETOOH \quad \text{(R6.15)}$$

Notation for these reactions is as displayed in the MCMv3.3.1, where HMVKBO denotes the corresponding alkoxy species to $HMVKBO_2$, BIACETOH denotes 1-hydroxy-2,3-butanedione ($CH_3C(O)C(O)CH_2OH$), and BIACETOOH denotes 1-hydroperoxy-2,3-butanedione ($CH_3C(O)C(O)CH_2OOH$). The model discrepancies observed by Li et al. (2016), along with the resulting mechanism updates suggested, were largely derived from a NO_x-dependent reaction scheme, and were therefore deemed irrelevant for this study, performed in a NO_x-free environment. However, future investigation may warrant the inclusion of the updated NO_x chemistry in the MCMv3.3.1.

Model simulations were constrained by experimentally derived OH and O_3 concentrations characterised separately for each individual experiment. Ozone was monitored directly by the commercial analyser (see Chapter 2), and OH concentrations were calculated from the isoprene decay as described by E6.5 (see section 6.3.1). Loss rates for key stable products as a result of sampling dilution, chamber wall surface adsorption, heterogeneous uptake, and photolysis were estimated based upon previous work done in this study, including those for methylglyoxal, MACR, MVK, hydroxyacetone, and glycolaldehyde.

Glyoxal loss rates were specifically characterised for each experiment through phosphorescence measurements following lamp deactivation and reaction termination. The first order loss rates for glyoxal were rapid, ranging between $k' = 2.5 – 5.0 \times 10^{-3}$ s^{-1}, and prevented any significant accumulation of glyoxal beyond 1 – 2 ppbv. The most likely cause of this was the high water content introduced into HIRAC to accommodate OH generation through ozone photolysis (see Chapter 3). Glyoxal is known to undergo rapid uptake by water and aerosol content (Liggio et al., 2005b; Liggio et al., 2005a; Corrigan et al., 2008; Ip et al., 2009), and therefore suffers much faster removal rates than many VOCs in chamber experiments where the relative humidity is high. The dependence on

relative humidity also renders a consistent loss rate difficult to characterise across

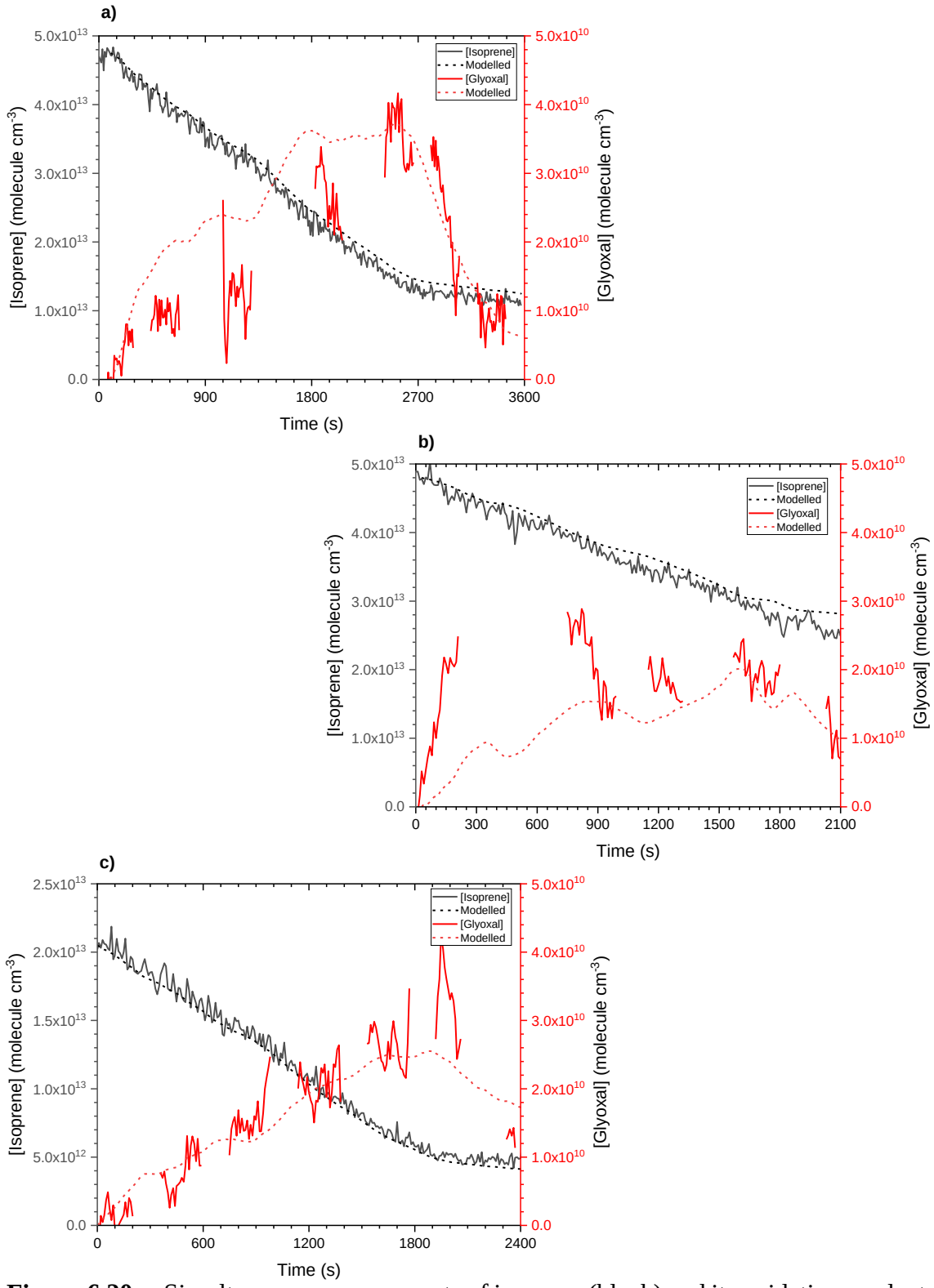

Figure 6.20 Simultaneous measurements of isoprene (black) and its oxidation product, glyoxal (red), across three separate OH-initiated oxidation experiments in HIRAC. Experimental observations (solid lines) were compared with model simulations (dashed lines) using an adjusted version of the MCMv3.3.1, updated to include suggestions made by Praske *et al*. (2015) and Fuchs *et al*. (2018) through the oxidation of MVK. Ozone was delivered into HIRAC and each reaction initiated through lamp activation at 0 s. Lamps were subsequently deactivated to terminate OH production at (a) 2700 s; (b) 1800 s; and (c) 1900 s.

experiments, which subsequently has a high impact on model outputs. Therefore the first order loss was adjusted and tailored for each model simulation to entail the most accurate representation of the experimental conditions.

Modelled glyoxal concentrations generally overlapped the order of magnitude observed from phosphorescence detection during experiments, however there were discrepancies observed in the concentration time profile for all model runs, seemingly without pattern. Figure 6.20a presents an overestimation of glyoxal build-up towards the start of the oxidation process, however model concentrations then begin to align with the phosphorescence data after ~30 – 40 minutes. The glyoxal decay observed at the end suggests that glyoxal loss was reasonably included, however there is no easy method to measure and include a variable loss factor throughout the reaction, which may have impacted glyoxal accumulation towards the beginning. Another possibility is that first-generation product chemistry, which would have more impact towards the start of the oxidation process, was less well modelled by the MCMv3.3.1, however the good agreement observed in Figure 6.20c does not seem to support this theory. Similarly, the underestimation of glyoxal accumulation towards the beginning of the reaction observed in the model run for Figure 6.20b indicates that there may have been variability in the glyoxal loss rate during the experiment, which was then more reasonably represented by the similar decay rates observed in the latter half.

The initial glyoxal increase experimentally observed in Figure 6.20b is particularly striking in comparison to those observed in Figures 6.20a & c, however, it should be noted that, in Figure 6.20a, only half the UV lamps were initially activated, resulting in a slower increase in oxidation products. It is not therefore unreasonable on such a basis to observe a faster increase in glyoxal as that observed in Figure 6.20b. The removal of isoprene in Figure 6.20c was also slower due to a reduced concentration of isoprene delivered into HIRAC, resulting in a slower production of glyoxal compared with observations in Figures 6.20a & b. The phosphorescence data therefore represents sensible glyoxal concentrations produced from the oxidation of isoprene, and inconsistencies with the model suggest either a gap in the understanding of the oxidation mechanism leading to glyoxal or a lack of knowledge regarding the heterogeneous uptake of glyoxal leading to rapid but variable loss throughout oxidation experiments. Further investigations of the mechanism should be undertaken to determine the source of any mechanistic gaps or misrepresented branching fractions, and future work, particularly in chamber studies,

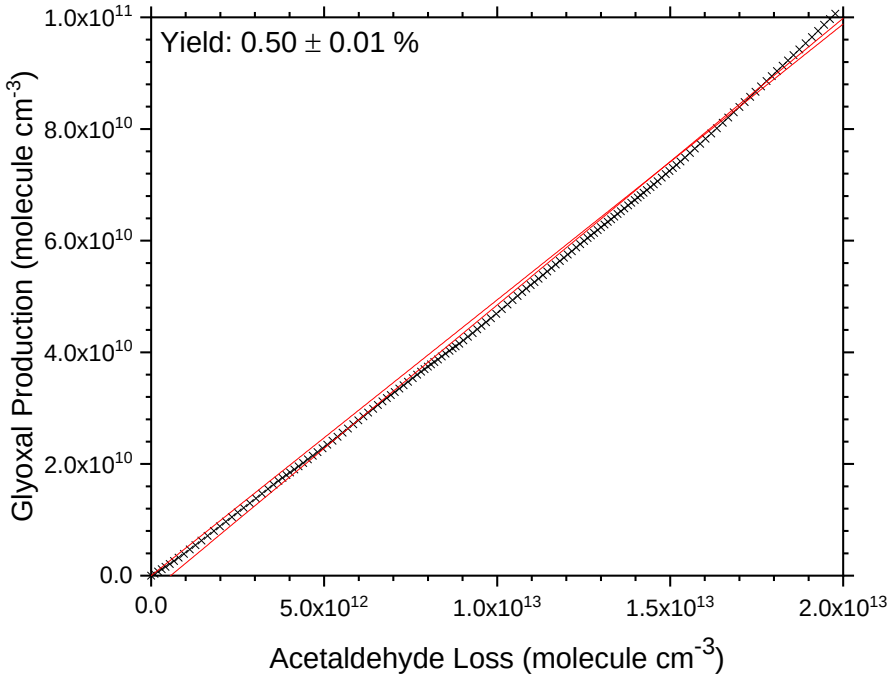

Figure 6.21 An estimated glyoxal yield calculation through the simulation of glyoxal production from isoprene oxidation in a low-NO_x regime, excluding all glyoxal loss processes and constraining ozone concentration to 0.

should incorporate relative humidity measurements in an attempt to better characterise glyoxal loss rates throughout reaction procedures.

Glyoxal yields were initially calculated in a similar manner to those from acetaldehyde oxidation (see Chapter 5), through glyoxal production plotted against isoprene removal. The three experiments displayed in Figure 6.20 were analysed to produce individual glyoxal yields, which were then averaged to calculate a value for Y_{GLY} = 0.32 ± 0.16 %, where the error is the standard deviation of individual yield values at the 2σ level. However, as indicated by the significant error, the glyoxal yield was highly dependent on concentrations of O_3 present, which impacted alternative mechanistic routes to glyoxal through various ozonolysis reactions from isoprene oxidation. Therefore, an attempt to simplify the mechanism was made by modelling glyoxal production solely due to OH-initiated oxidation. Experimental OH concentrations were used in model constraints, and the O_3 concentration was fixed to 0 to achieve an approximate glyoxal yield calculated through simulation of glyoxal production with both the exclusion of glyoxal loss processes and ozonolysis reactions (Figure 6.21). Modelled glyoxal production was plotted against isoprene removal solely due to reaction with OH across the three datasets, and an average yield was calculated of Y_{GLY} = 0.52 ± 0.06 %, where the error again

represents the standard deviation of individual Y_{GLY} values at the 2σ level. To the author's knowledge, this represents the first direct glyoxal yield measurement through LIP detection from OH-initiated isoprene oxidation in low-NO_x conditions. Similar chamber studies incorporating a high-NO_x environment ranging between 10ppbv to as much as 1 ppmv average NO_x mixing ratios in previous works (Volkamer et al., 2006; Galloway et al., 2011) exhibit a far greater yield of 2 – 3 %.

MVK yields from isoprene oxidation appear to be much smaller in low-NO_x environments, averaging a ~10 % yield in the absence of NO_x compared with ~40 % at higher NO_x mixing ratios (Liu et al., 2013) (see section 6.3.2). As a key intermediate species in the formation of glyoxal from isoprene oxidation mechanism, MVK yields a factor of 4 lower in the present NO_x-free study are consistent with the lower glyoxal yields observed in this work, which have been determined as between 4 and 6 times smaller than under a high-NO_x chemistry regime. However, due to the isobaric nature of MVK and MACR, it has not been possible in this study to measure their specific yields from isoprene oxidation through PTR-MS detection, and it is unclear from experimental data in this work to what extent other mechanistic routes may impact glyoxal yields under a NO_x-free regime.

Although formaldehyde yields were not measured in this study, the glyoxal yields calculated here indicate that R_{GF} from OH-initiated isoprene oxidation is low (<0.02), assuming a substantial formaldehyde yield of ~30 – 40 %. In contrast, the R_{GF} measurement indicated by (Chan Miller et al., 2016) over the Pearl River Delta (PRD) appears to be ~0.05. However, retrieval of the NO_2 vertical column density revealed significant quantities of NO_2 over the PRD, and it therefore seems appropriate to treat the tropospheric chemistry as being under a high-NO_x regime. It might therefore be expected that the estimated R_{GF} given from this work, despite the lack of formaldehyde yield measurements, would be reduced from any R_{GF} measurements where NO_x mixing ratios are much higher. Consequently, this has implications for R_{GF} detection from isoprene oxidation on a global scale, where large areas of significant isoprene emission, such as heavily forested regions, will have very low quantities of NO_x, impacting the observed R_{GF}.

The oxidation of isoprene in the troposphere is rapid, with an atmospheric lifetime due to reaction with OH on the order of 1 – 2 hours, assuming ambient [OH] ≈ 2×10^6 molecule cm^{-3} (Atkinson and Arey, 2003). Chemical transport of isoprene is therefore relatively minimal, and R_{GF} measurements as a result of isoprene oxidation should be considerably

localised. Remote regions where isoprene emissions are high, such as heavily forested areas, should dominate low R_{GF} calculations from satellite measurements. However, it is anticipated that R_{GF} measurements in urban regions with significant areas of vegetative mass may be impacted by higher R_{GF} values due to isoprene oxidation as a result of the increased MVK and glyoxal yields observed in high-NO_x environments. Additional studies measuring the NO_x dependence of R_{GF} from the oxidation of isoprene would be beneficial in assessing the impact of isoprene on local tropospheric chemistry through satellite measurements of R_{GF} with complementary measurements of geographically dependent ambient NO_x mixing ratios.

6.4 Conclusion and Future Work

Glyoxal yields from the OH-initiated oxidation of isoprene have been investigated in this study (Y_{GLY} = 0.52 ± 0.06 %). Methylglyoxal phosphorescence was characterised and calibrated with respect to the observed $MS_{73.07}$ through PTR-MS detection, so that glyoxal phosphorescence could be distinguished during isoprene oxidation. Suggested mechanism updates regarding the oxidation of MVK were added to the MVMv3.3.1 mechanism for isoprene oxidation to examine the model representation of glyoxal generation from isoprene and MVK. Ozone concentrations were measured throughout experimental procedures to characterise ozonolysis rates for data analysis and model simulations, allowing the calculation of OH concentration from isoprene decays simultaneously to ozonolysis removal of isoprene. The modelled glyoxal yields for MVK and isoprene oxidation demonstrated a reasonable mechanistic understanding, producing some overlap in the glyoxal concentration. However, discrepancies remained, warranting further investigation into the mechanistic routes to glyoxal and better characterising loss rates of glyoxal during experiment, utilising relative humidity measurements to determine the quantity of heterogeneous uptake by water and aerosol content.

Further studies in the presence of NO_x would be of benefit in narrowing sources of gaps in the isoprene oxidation mechanism. Suggested mechanism updates to the MCMv3.3.1 (Li et al., 2016; Praske et al., 2015; Fuchs et al., 2018) include several NO_x-dependent reactions, and inclusion of these alongside experimental data may highlight the impacts of HO_2 or RO_2 reactions at varying concentrations of NO_x. NO_x studies would also be of benefit in more accurately determining the impact of isoprene emissions within urban

environments, which may be crucial in heavily populated cities where there is a large surface area of vegetative biomass.

An analysis of additional product yields complementary to glyoxal and methylglyoxal would be of benefit in future work. Concentrations of glyoxal and methylglyoxal are dependent on their direct precursors, glycolaldehyde and hydroxyacetone respectively, and monitoring these concentrations in tandem would prove advantageous, however calibration is not straightforward due to the highly adsorbing nature of these compounds. Calibration of the GLYOX-LIP instrument for methylglyoxal concentration would likewise be appropriate in further studies to establish a yield of methylglyoxal alongside that of glyoxal to enhance model simulation comparison. Additionally, formaldehyde yield measurements are crucial to the determination of R_{GF} values and the model assessment of isoprene on global R_{GF}. Future work should incorporate the detection of formaldehyde from oxidation of isoprene and its first-generation oxidation products, however formaldehyde is also a common product of ozonolysis reactions, and an alternative OH source, such as hydrogen peroxide or methyl nitrite, may therefore be more appropriate for this analysis.

Finally, large discrepancies observed between OH measurements through both FAGE detection and VOC decay in the presence of significant quantities of isoprene (see Chapter 4) were not fully investigated in this work. Establishing and accounting for the source of this interference would be beneficial both to chamber and field studies where there is an abundance of isoprene. A dependence on VOC decay calculations in chamber studies is acceptable, however the analysis process is more time-consuming, especially when accounting for the ozonolysis of isoprene simultaneously. Further, it is unknown whether this phenomenon applies singularly to chamber studies, where typical VOC concentrations are much higher than in ambient air, or to OH measurements in the presence of isoprene in general. An investigation into correlations between magnitudes of OH interference and the concentration of isoprene, as well as the concentrations of its oxidation products, may provide a solution in both calibrating for the interference and determining a lower concentration limit in which interference comes into effect.

Chapter 7 Summary of Conclusions and Future Work

7.1 Thesis Conclusions

This thesis has aimed to characterise glyoxal yields from the OH-initiated oxidation of acetaldehyde (see Chapter 5) and isoprene (see Chapter 6), both of which were considered atmospherically relevant BVOCs for study. As part of the UNFOGS project (see Chapter 1), a key goal in both quantitatively and qualitatively identifying the global distribution of VOC emissions is understanding the ratio of glyoxal to formaldehyde (R_{GF}) produced through varying categories of primary emissions. Glyoxal and formaldehyde may be used as chemical tracers through satellite detection of R_{GF} to determine primary or secondary VOC precursors that are emitted and subsequently transported within the troposphere. However, whilst the chemistry occurring in the troposphere is inherently non-trivial to characterise, individual reactions have been examined here in chamber studies designed to improve existing knowledge of oxidation mechanisms for use in global chemical reaction and transport models.

The Leeds HIRAC facility is well suited to performing an analysis of isolated reaction systems, and has been characterised, along with its instrumentation, in Chapter 2. Of particular note is the ability to control parameters such as temperature and pressure, as well as inducing low- or high-NO_x conditions, in order to produce a range of artificial environments that are both stable and relevant to the troposphere. A selective glyoxal phosphorescence instrument (GLYOX-LIP) has also been employed in HIRAC for the first time to achieve the direct detection of glyoxal generation from BVOC oxidation. This has been coupled with other instrumentation, including the FAGE instrument for direct selective detection of OH radicals, and the PTR-MS, which can detect a variety of both unsaturated and oxygenated VOCs with a high degree of selectivity at an appropriate temporal resolution (10 s) between recorded mass spectra.

In order to analyse the rate of glyoxal production through OH-initiated VOC oxidation, knowledge of both VOC and OH concentrations is a requirement. Two calibration techniques for the FAGE instrument have therefore been investigated and compared in HIRAC, considering both the water vapour photolysis method and the VOC decay method (see Chapter 4). Initial comparisons highlighted a minor discrepancy between calibration factors (C_{OH}) determined using either method, which was of particular importance for the generation of OH through hydrogen peroxide photolysis. Questions raised regarding the homogeneity of OH concentrations throughout HIRAC have been addressed through the repositioning of instrument sampling lines and regular cleaning of the inside surfaces of the chamber.

Further investigations involved the temperature-dependent calibration of FAGE, detailed more fully elsewhere (Winiberg et al., 2023), with observed fluorescence signal displaying a minor positive temperature dependence. Whilst each FAGE instrument is unique, this has implications particularly for aircraft instruments with longer sampling inlets that operate at high altitudes where ambient temperatures are much cooler, as well as more specific implications for the detection of OH in HIRAC where internal chamber temperatures are altered.

With an interest in glyoxal yields from isoprene oxidation as the most abundant BVOC emission (Guenther et al., 2006; Guenther et al., 2012; Sindelarova et al., 2014; Sindelarova et al., 2022) and the largest global source of glyoxal (Fu, T.-M. et al., 2008), an investigation was also developed into an observed OH signal interference during isoprene oxidation in chamber experiments. As the source of this interference was not characterised in this work, the investigation highlighted a necessity for use of the VOC decay method in determining OH concentrations for isoprene experiments.

Various methods of OH generation were also examined (see Chapter 3) to determine the most effective methods for the purpose of measuring glyoxal yields in HIRAC. Whilst several methods exist for producing OH radicals in atmospheric simulation chambers – including photolysis of alkyl nitrites and peroxide species, as well as the ozonolysis of unsaturated hydrocarbons – not all were deemed appropriate for the effective determination of glyoxal yields from BVOC oxidation. Ozonolysis reactions were thought to be of merit due to no requirements of photolysis, which subsequently reduces complexity in the photo-oxidation scheme. However, of the two alkenes investigated, namely ethylene and tetramethylethlyene (TME), neither could be labelled as suitable due to increases in GLYOX-LIP signal as a direct result of the ozonolysis reaction. In the case of ethylene, this was attributed to glyoxal generated from the OH-initiated oxidation of ethylene, whilst TME ozonolysis was thought to generate excessive quantities of methylglyoxal, which in turn produced a phosphorescence signal that interfered with measurements of glyoxal (see Chapter 6 for discussion on methylglyoxal interference).

The OH precursors chosen for this study in NO_x-free conditions were hydrogen peroxide and ozone, each producing OH as the singular product through photolysis, and were similarly advantageous in reducing chemical complexity within the chamber. However, a significant increase in glyoxal loss in HIRAC, at least an order of magnitude higher than with glyoxal as the sole species present, was observed particularly in the presence of hydrogen peroxide. This was attributed primarily to higher relative humidity levels in

consideration of glyoxal having a very high water solubility, with an effective Henry's law constant reported as $K_H = 4.2 \times 10^5$ mol dm^{-3} atm^{-1} (Matsumoto et al., 2005; Coburn et al., 2014), although it remains unclear to what extent hydrogen peroxide itself may act as an additional solvent for the heterogeneous uptake of glyoxal. Attempts were made to characterise glyoxal first-order loss rates on a case-by-case basis, treating glyoxal losses as distinct for each individual experiment performed, however this could not be monitored throughout specified reaction periods, and may therefore have had some impact on measured yields.

In experiments that involved reaction studies under high-NO_x conditions, methylnitrite was chosen as an appropriate precursor for OH, and additional NO was supplied at the beginning of these experiments as a supplement for total NO_x mixing ratios as well as for the generation of OH. However, in continuations of this work where high-NO_x reaction schemes are studied, formaldehyde produced through the photolysis of methylnitrite will affect the determination of R_{GF} from the OH-initiated oxidation of VOCs. The formaldehyde yield from methylnitrite photolysis in HIRAC should therefore be well characterised in order to be separated from the formaldehyde yield generated through OH-initiated VOC oxidation. Alternatively, NO_x may be delivered independently of the OH precursor with hydrogen peroxide employed as the preferred OH source.

Upon establishing the appropriate OH precursors for this study, the OH- and Cl-initiated oxidation of acetaldehyde was investigated (see Chapter 5) to determine whether acetaldehyde oxidation may constitute the missing source of glyoxal within the MBL (Walker et al., 2022). Glyoxal is produced from the photo-oxidation of acetaldehyde selectively through the initial abstraction of a hydrogen atom at the methyl site. This initial branching fraction is thought to be (and included in the MCMv3.3.1 as) 5 %, based on yield measurements of the CH_3CO and CH_2CHO radicals (Cameron et al., 2002; Butkovskaya et al., 2004), and the subsequent IUPAC recommendation (Atkinson et al., 2006).

However, under the current mechanistic regime in the MCMv3.3.1, observed glyoxal yields (Y_{GLY}) from experiment were an order of magnitude lower than those simulated in model runs, being measured as low as $Y_{GLY} = 0.07 \pm 0.01$ % from OH-initiated oxidation and 0.13 ± 0.02 % from Cl-initiated oxidation in NO_x-free conditions. These results have highlighted a discrepancy between the measured and modelled data that implies either a largely overestimated initial branching fraction at the methyl site or a misrepresentation of branching points within the mechanism leading to glyoxal formation. It is therefore

unlikely that the photo-oxidation of acetaldehyde constitutes the missing source of glyoxal in the MBL, and further studies will be needed to narrow the gap between field glyoxal measurements and base model outputs observed by Walker et al. (2022).

Further investigations attempted to evaluate the potentially erroneous exclusion of the reaction between O_2 and the alkoxy radical, $HCOCH_2O$, in the MCMv3.3.1, which could serve as a route to glyoxal formation in competition with the alkoxy decomposition to formaldehyde and HCO. However, studies analysing the NO_x- and O_2-dependence of the acetaldehyde oxidation mechanism concluded that reaction with O_2 forms only a minor channel for the fate of $HCOCH_2O$, estimated at ~5 %, and therefore produces very little glyoxal. Generation of glyoxal seems instead to be dominated by various reactions of the peroxy species, $HCOCH_2OO$, with HO_2 and RO_2 radicals, and these ought to be examined and, where possible, better characterised, in order to determine the exact cause of the discrepancy between Y_{GLY} measurements and the current mechanistic understanding of acetaldehyde oxidation.

Lastly, direct glyoxal yields were determined from the OH-initiated oxidation of isoprene in NO_x-free conditions for the first time to the author's knowledge. Although previous chamber studies of isoprene have involved glyoxal yield measurements (Volkamer et al., 2006; Galloway et al., 2011), these involved high-NO_x chemistry, with initial NO_x mixing ratios ranging between ~10 ppbv to as high as ~1 ppmv. Whilst previous glyoxal yield measurements were determined between 2 – 3 % under a high-NO_x regime, the current study in the absence of NO_x has reported an average yield of 0.52 ± 0.06 %, significantly a factor of ~5 lower. With MVK considered to be a key intermediate species in the formation of glyoxal from isoprene, this appears to be in keeping with the reduced MVK yield previously observed through the oxidation of isoprene in low-NO_x (~10 %) compared with high-NO_x conditions (~40 %) (Liu et al., 2013).

Although a significant quantity of O_3 (~100 ppbv) was present in the system due to O_3 photolysis being used as a method of OH generation, contributions of ozone to the removal of isoprene through ozonolysis were characterised prior to glyoxal yield determinations. However, because isoprene ozonolysis generates OH, it was deemed non-trivial to attribute a glyoxal yield purely to ozonolysis reactions alone, made more difficult by the observed OH interference during isoprene oxidation described previously (see Chapter 4). Therefore OH concentrations were calculated from the measured isoprene decays to be used in model constraints, and O_3 concentrations were fixed to 0 to determine a modelled yield in the absence of O_3. Observed glyoxal concentration profiles

were compared with modelled glyoxal constraining both O_3 and OH in order to validate the oxidation mechanism used, demonstrating reasonable agreement across three experiments. Any contributions of methylglyoxal to the phosphorescence signal detected was subtracted using a calibrated signal from simultaneous PTR-MS measurements. The modelled glyoxal yield of 0.52 ± 0.06 % was therefore concluded to be a reasonable figure to use in the determination of R_{GF} from isoprene oxidation in NO_x-free conditions.

7.2 Future Directions

The direct measurement of glyoxal yields from the oxidation of acetaldehyde and isoprene as biogenic precursors within the present work has provided some foundations for the aims of the UNFOGS project in the determination of R_{GF} values to accurately establish global emissions inventories and ambient tropospheric VOC concentrations. However, a key element to UNFOGS is the simultaneous detection of both glyoxal and formaldehyde. Whilst this work has not focused on formaldehyde yield measurements, there is potential for the selective detection of formaldehyde in future HIRAC experiments through the use of a laser-induced fluorescence instrument operating in a similar fashion to the FAGE instrument (see Chapter 2), and described in detail previously (Cryer, 2016). Ideally, formaldehyde should be measured in tandem with glyoxal in order to provide R_{GF} values. However, where formaldehyde or glyoxal yields can be determined consistently across repeat experiments, they can be analysed separately and compared to retrieve R_{GF} values instead, providing experimental conditions (e.g. relative humidity, NO_x concentrations, temperature, pressure, chamber surfaces, OH precursors, and artificial light sources) are kept reasonably consistent. Glyoxal yields measured here may therefore provide half of the study required for determination of R_{GF} from both acetaldehyde and isoprene oxidation.

Glyoxal yield measurements performed in this work were subject to characterisation of first order loss rates of glyoxal in HIRAC, particularly regarding surface adsorption and heterogeneous uptake into aerosol matter. Further studies involving glyoxal yield measurements could attempt to clarify a dependency of glyoxal loss rates on factors such as relative humidity, using a RH probe, and hydrogen peroxide concentration, which may be determined through FTIR spectroscopy. This would be of particular benefit for quantifying low glyoxal yields through minor channels of VOC oxidation mechanisms,

however also has wider applications for the analysis of mechanistic routes leading to glyoxal formation more generally.

There remains discrepancies between measured and modelled glyoxal concentration profiles from isoprene oxidation. It is unclear to what extent this discrepancy has been impacted by varying glyoxal loss rates throughout a given experiment. However, the direct detection of OH during isoprene chamber experiments would be advantageous in determining any sources of misrepresentation in current the oxidation mechanism, particularly where ozone photolysis is used as the source of OH. To that end, future studies could attempt to further investigate the source of interference observed in FAGE detection of OH during isoprene studies conducted in this work. There does not seem to be cause to suspect an alternative source of fluorescence at 308 nm, therefore it seems likely that an excess of OH is being produced within the fluorescence detection cell, possibly as a result of flash photolysis or through chemical reaction. Interference may then be dependent on the concentration of a known, detectable species arising through isoprene oxidation, and establishing that link could allow for correction of the observed fluorescence signal.

A final consideration from the work of this thesis is the missing source of glyoxal in the MBL. Glyoxal yields detected directly from both the OH- and Cl-initiated oxidation of acetaldehyde in HIRAC suggest that acetaldehyde present in the ambient MBL does not provide an adequate source of glyoxal alone to bridge the discrepancy observed between measurements and model predictions of average glyoxal mixing ratios. An alternative source of glyoxal, other than the sources already identified by Walker et al. (2022) including glycolaldehyde and acetylene, is not immediately obvious, particularly with the significant glyoxal sink associated with high solubility and the potential for rapid removal *via* ocean surface interactions (Volkamer et al., 2009; Ervens and Volkamer, 2010). One possible source is the emission of isoprene from marine phytoplankton, which has shown increasing interest over the last 15 years, summarised by Conte et al. (2020) and references therein. However, there are still significant uncertainties around the ocean-air flux of isoprene, therefore further investigations may still be needed both to quantify marine sources of isoprene as well as determine whether this may be a viable source of glyoxal to explain the discrepancy previously observed through the comparison of field measurements and model simulations. Glyoxal yields from isoprene oxidation under NO_x-free conditions obtained in this work may be of use in pursuing this avenue of

interest and analysing the potential impact of marine isoprene emissions on ambient glyoxal mixing ratios.

References

Adeniji, S.A., Kerr, J.A. and Williams, M.R. 1981. Rate constants for ozone–alkene reactions under atmospheric conditions. *International Journal of Chemical Kinetics.* **13**(2), pp.209-217.

Ahlm, L., Liu, S., Day, D.A., Russell, L.M., Weber, R., Gentner, D.R., Goldstein, A.H., DiGangi, J.P., Henry, S.B., Keutsch, F.N., VandenBoer, T.C., Markovic, M.Z., Murphy, J.G., Ren, X. and Scheller, S. 2012. Formation and growth of ultrafine particles from secondary sources in Bakersfield, California. *Journal of Geophysical Research.* **117**(D21).

Alam, M.S., Camredon, M., Rickard, A.R., Carr, T., Wyche, K.P., Hornsby, K.E., Monks, P.S. and Bloss, W.J. 2011. Total radical yields from tropospheric ethene ozonolysis. *Physical Chemistry Chemical Physics.* **13**(23), pp.11002-11015.

Alvarado, L.M.A., Richter, A., Vrekoussis, M., Hilboll, A., Kalisz Hedegaard, A.B., Schneising, O. and Burrows, J.P. 2020. Unexpected long-range transport of glyoxal and formaldehyde observed from the Copernicus Sentinel-5 Precursor satellite during the 2018 Canadian wildfires. *Atmospheric Chemistry and Physics.* **20**(4), pp.2057-2072.

Anderson, L.G., Parmenter, C.S. and Poland, H.M. 1973. Collision induced intersystem crossing the photophysics of glyoxal vapor excited at 4358 Å. *Chemical Physics.* **1**(5), pp.401-417.

Andreae, M.O. 2019. Emission of trace gases and aerosols from biomass burning – an updated assessment. *Atmospheric Chemistry and Physics.* **19**(13), pp.8523-8546.

Ann, M.D., Patrik, Š. and David, S. 2003. Time variation of ammonia, acetone, isoprene and ethanol in breath: a quantitative SIFT-MS study over 30 days. *Physiological Measurement.* **24**(1), p107.

Aschmann, S.M. and Atkinson, R. 1998. Kinetics of the gas-phase reactions of the oh radical with selected glycol ethers, glycols, and alcohols. *International Journal of Chemical Kinetics.* **30**(8), pp.533-540.

Aschmutat, U., Hessling, M., Holland, F. and Hofzumahaus, A. 1994. A tunable source of hydroxyl (OH) and hydroperoxy (HO_2) radicals: in the range between 106 and 109 cm^{-3}. *Physico-Chemical Behaviour of Atmospheric Pollutants.* (European Commission, Brussels).

Atkinson, R. 1986. Kinetics and mechanisms of the gas-phase reactions of the hydroxyl radical with organic compounds under atmospheric conditions. *Chemical Reviews.* **86**(1), pp.69-201.

Atkinson, R. 1990. Gas-phase tropospheric chemistry of organic compounds: A review. *Atmospheric Environment. Part A. General Topics.* **24**(1), pp.1-41.

Atkinson, R. 1994. Gas-phase tropospheric chemistry of organic compounds. *Journal of Physical and Chemical Reference Data.* **2**, pp.1-216.

Atkinson, R. 1997. Gas-Phase Tropospheric Chemistry of Volatile Organic Compounds: 1. Alkanes and Alkenes. *Journal of Physical and Chemical Reference Data.* **26**(2), pp.215-290.

Atkinson, R. 2000. Atmospheric chemistry of VOCs and NO_x. *Atmospheric Environment.* **34**(12), pp.2063-2101.

Atkinson, R. 2003. Kinetics of the gas-phase reactions of OH radicals with alkanes and cycloalkanes. *Atmospheric Chemistry and Physics.* **3**(6), pp.2233-2307.

Atkinson, R. and Arey, J. 2003. Gas-phase tropospheric chemistry of biogenic volatile organic compounds: a review. *Atmospheric Environment.* **37**, pp.197-219.

Atkinson, R. and Aschmann, S.M. 1984. Rate constants for the reaction of OH radicals with a series of alkenes and dialkenes at 295 ± 1 K. *International Journal of Chemical Kinetics.* **16**(10), pp.1175-1186.

Atkinson, R., Aschmann, S.M., Arey, J. and Shorees, B. 1992. Formation of OH radicals in the gas phase reactions of O_3 with a series of terpenes. *Journal of Geophysical Research.* **97**(D5), pp.6065-6073.

Atkinson, R., Aschmann, S.M. and Pitts Jr., J.N. 1983. Kinetics of the gas-phase reactions of OH radicals with a series of α,β-unsaturated carbonyls at 299 ± 2 K. *International Journal of Chemical Kinetics.* **15**(1), pp.75-81.

Atkinson, R., Aschmann, S.M., Winer, A.M. and Pitts Jr., J.N. 1981a. Rate constants for the gas-phase reactions of O_3 with a series of carbonyls at 296 K. *International Journal of Chemical Kinetics.* **13**(11), pp.1133-1142.

Atkinson, R., Aschmann, S.M., Winer, A.M. and Pitts Jr., J.N. 1982a. Rate constants for the reaction of OH radicals with a series of alkanes and alkenes at 299 ± 2 K. *International Journal of Chemical Kinetics.* **14**(5), pp.507-516.

Atkinson, R., Baulch, D., Cox, R., Crowley, J., Hampson, R., Hynes, R., Jenkin, M., Rossi, M. and Troe, J. 2006. Evaluated kinetic and photochemical data for atmospheric chemistry: Volume II–gas phase reactions of organic species. *Atmospheric Chemistry and Physics.* **6**(11), pp.3625-4055.

Atkinson, R., Baulch, D.L., Cox, R.A., Crowley, J.N., Hampson, R.F., Hynes, R.G., Jenkin, M.E., Rossi, M.J. and Troe, J. 2004. Evaluated kinetic and photochemical data for atmospheric chemistry: Volume I - gas phase reactions of O_x, HO_x, NO_x and SO_x species. *Atmospheric Chemistry and Physics.* **4**(6), pp.1461-1738.

Atkinson, R., Baulch, D.L., Cox, R.A., Hampson, R.F., Jr., Kerr, J.A., Rossi, M.J. and Troe, J. 1997. Evaluated Kinetic, Photochemical and Heterogeneous Data for Atmospheric Chemistry: Supplement V. IUPAC Subcommittee on Gas Kinetic Data Evaluation for Atmospheric Chemistry. *Journal of Physical and Chemical Reference Data.* **26**(3), pp.521-1011.

Atkinson, R., Baulch, D.L., Cox, R.A., Hampson, R.F., Jr., Kerr , J.A. and Troe, J. 1989. Evaluated Kinetic and Photochemical Data for Atmospheric Chemistry: Supplement III. IUPAC Subcommittee on Gas Kinetic Data Evaluation for Atmospheric Chemistry. *Journal of Physical and Chemical Reference Data.* **18**(2), pp.881-1097.

Atkinson, R., Carter, W.P., Winer, A.M. and Pitts Jr, J.N. 1981b. An experimental protocol for the determination of OH radical rate constants with organics using methyl nitrite photolysis as an OH radical source. *Journal of the Air Pollution Control Association.* **31**(10), pp.1090-1092.

Atkinson, R. and Carter, W.P.L. 1991. Reactions of alkoxy radicals under atmospheric conditions: The relative importance of decomposition versus reaction with O_2. *Journal of Atmospheric Chemistry.* **13**(2), pp.195-210.

Atkinson, R. and Pitts Jr., J.N. 1978. Kinetics of the reactions of the OH radical with HCHO and CH_3CHO over the temperature range 299–426°K. **68**(8), pp.3581-3584.

Atkinson, R., Winer, A.M. and Pitts, J.N. 1982b. Rate constants for the gas phase reactions of O_3 with the natural hydrocarbons isoprene and α- and β-pinene. *Atmospheric Environment (1967).* **16**(5), pp.1017-1020.

Bailey, A.E., Heard, D.E., Paul, P.H. and Pilling, M.J. 1997. Collisional quenching of OH ($A_2\Sigma^+$, $v'= 0$) by N_2, O_2 and CO_2 between 204 and 294 K. Implications for atmospheric measurements of OH by laser-induced fluorescence. *Journal of the Chemical Society, Faraday Transactions.* **93**(16), pp.2915-2920.

Bardwell, M.W., Bacak, A., Teresa Raventos, M., Percival, C.J., Sanchez-Reyna, G. and Shallcross, D.E. 2003. Kinetics of the $HO_2 + NO$ reaction: A temperature and pressure dependence study using chemical ionisation mass spectrometry. *Physical Chemistry Chemical Physics.* **5**(11), pp.2381-2385.

Bartels, M., Hoyermann, K. and Lange, U. 1989. An Experimental Study of the Reactions $CH_3CHO + Cl$, $C_2H_4O + Cl$, and $C_2H_4O + F$ in the Gas-Phase. *Berichte der Bunsengesellschaft für physikalische Chemie.* **93**(4), pp.423-427.

Bauer, D., Ingham, T., Carl, S.A., Moortgat, G.K. and Crowley, J.N. 1998. Ultraviolet−Visible Absorption Cross Sections of Gaseous HOI and Its Photolysis at 355 nm. *The Journal of Physical Chemistry A.* **102**(17), pp.2857-2864.

Baxendale, J.H. and Wilson, J.A. 1957. The photolysis of hydrogen peroxide at high light intensities. *Transactions of the Faraday Society.* **53**(0), pp.344-356.

Bell, M.L., Dominici, F. and Samet, J.M. 2005. A meta-analysis of time-series studies of ozone and mortality with comparison to the national morbidity, mortality, and air pollution study. *Epidemiology (Cambridge, Mass.).* **16**(4), pp.436-445.

Benjamin, M.T. and Winer, A.M. 1998. Estimating the ozone-forming potential of urban trees and shrubs. *Atmospheric Environment.* **32**(1), pp.53-68.

Berndt, T. 2021. Peroxy Radical Processes and Product Formation in the OH Radical-Initiated Oxidation of α-Pinene for Near-Atmospheric Conditions. *The Journal of Physical Chemistry A.* **125**(41), pp.9151-9160.

Berndt, T., Hyttinen, N., Herrmann, H. and Hansel, A. 2019. First oxidation products from the reaction of hydroxyl radicals with isoprene for pristine environmental conditions. *Communications Chemistry.* **2**(1), p21.

Berndt, T., Kaethner, R., Voigtländer, J., Stratmann, F., Pfeifle, M., Reichle, P., Sipilä, M., Kulmala, M. and Olzmann, M. 2015. Kinetics of the unimolecular reaction of CH_2OO and the bimolecular reactions with the water monomer, acetaldehyde and acetone under atmospheric conditions. *Physical Chemistry Chemical Physics.* **17**(30), pp.19862-19873.

Bey, I., Jacob, D.J., Yantosca, R.M., Logan, J.A., Field, B.D., Fiore, A.M., Li, Q., Liu, H.Y., Mickley, L.J. and Schultz, M.G. 2001. Global modeling of tropospheric chemistry with assimilated meteorology: Model description and evaluation. *Journal of Geophysical Research: Atmospheres.* **106**(D19), pp.23073-23095.

Biesenthal, T.A., Bottenheim, J.W., Shepson, P.B., Li, S.M. and Brickell, P.C. 1998. The chemistry of biogenic hydrocarbons at a rural site in eastern Canada. *Journal of Geophysical Research.* **103**(D19), pp.25487-25498.

Bloss, C., Wagner, V., Bonzanini, A., Jenkin, M.E., Wirtz, K., Martin-Reviejo, M. and Pilling, M.J. 2005. Evaluation of detailed aromatic mechanisms (MCMv3 and MCMv3.1) against environmental chamber data. *Atmospheric Chemistry and Physics.* **5**(3), pp.623-639.

Bloss, W.J., Lee, J.D., Bloss, C., Heard, D.E., Pilling, M.J., Wirtz, K., Martin-Reviejo, M. and Siese, M. 2004. Validation of the calibration of a laser-induced fluorescence instrument for the measurement of OH radicals in the atmosphere. *Atmospheric Chemistry and Physics.* **4**(2), pp.571-583.

Bogumil, K., Orphal, J., Homann, T., Voigt, S., Spietz, P., Fleischmann, O.C., Vogel, A., Hartmann, M., Kromminga, H., Bovensmann, H., Frerick, J. and Burrows, J.P. 2003. Measurements of molecular absorption spectra with the SCIAMACHY pre-flight model: instrument characterization and reference data for atmospheric remote-sensing in the 230–2380 nm region. *Journal of Photochemistry and Photobiology A: Chemistry.* **157**(2), pp.167-184.

Bohn, B., Rohrer, F., Brauers, T. and Wahner, A. 2005. Actinometric measurements of NO_2 photolysis frequencies in the atmosphere simulation chamber SAPHIR. *Atmospheric Chemistry and Physics.* **5**(2), pp.493-503.

Bohn, B., Siese, M. and Zetzschn, C. 1996. Kinetics of the OH + C_2H_2 reaction in the presence of O_2. *Journal of the Chemical Society, Faraday Transactions.* **92**(9), pp.1459-1466.

Bohn, B. and Zetzsch, C. 1997. Rate Constants of HO_2 + NO Covering Atmospheric Conditions. 1. HO_2 Formed by OH + H_2O_2. *Journal of Physical Chemistry A.* **101**(8), pp.1488-1493.

Bohn, B. and Zetzsch, C. 1998. Formation of HO_2 from OH and C_2H_2 in the presence of O_2. *Journal of the Chemical Society, Faraday Transactions.* **94**(9), pp.1203-1210.

Borbon, A., Fontaine, H., Veillerot, M., Locoge, N., Galloo, J.C. and Guillermo, R. 2001. An investigation into the traffic-related fraction of isoprene at an urban location. *Atmospheric Environment.* **35**(22), pp.3749-3760.

Brégonzio-Rozier, L., Siekmann, F., Giorio, C., Pangui, E., Morales, S.B., Temime-Roussel, B., Gratien, A., Michoud, V., Ravier, S., Cazaunau, M., Tapparo, A., Monod, A. and Doussin, J.F. 2015. Gaseous products and secondary organic aerosol formation during long term oxidation of isoprene and methacrolein. *Atmospheric Chemistry and Physics.* **15**(6), pp.2953-2968.

Brion, J., Chakir, A., Daumont, D., Malicet, J. and Parisse, C. 1993. High-resolution laboratory absorption cross section of O_3. Temperature effect. *Chemical Physics Letters.* **213**(5), pp.610-612.

Bryant, D.J., Nelson, B.S., Swift, S.J., Budisulistiorini, S.H., Drysdale, W.S., Vaughan, A.R., Newland, M.J., Hopkins, J.R., Cash, J.M., Langford, B., Nemitz, E., Acton, W.J.F., Hewitt, C.N., Mandal, T., Gurjar, B.R., Shivani, Gadi, R., Lee, J.D., Rickard, A.R. and Hamilton, J.F. 2023. Biogenic and anthropogenic sources of isoprene and monoterpenes and their secondary organic aerosol in Delhi, India. *Atmospheric Chemistry and Physics.* **23**(1), pp.61-83.

Bucsela, E., Krotkov, N., Celarier, E., Lamsal, L., Swartz, W., Bhartia, P., Boersma, K., Veefkind, J., Gleason, J. and Pickering, K. 2013. A new

stratospheric and tropospheric NO_2 retrieval algorithm for nadir-viewing satellite instruments: applications to OMI. *Atmospheric Measurement Techniques.* **6**(1).

Burkholder, J. and Bair, E. 1983. Potential energy parameters and shapes of the vibrational components of the 345-nm system of chlorine. *Journal of Physical Chemistry.* **87**(11), pp.1859-1863.

Burkholder, J., Sander, S., Abbatt, J., Barker, J., Cappa, C., Crounse, J., Dibble, T., Huie, R., Kolb, C. and Kurylo, M. 2020. *Chemical kinetics and photochemical data for use in atmospheric studies; Evaluation Number 19.* Pasadena, CA: Jet Propulsion Laboratory, National Aeronautics and Space Administration.

Butkovskaya, N., Kukui, A. and Le Bras, G. 2004. Branching Fractions for H_2O Forming Channels of the Reaction of OH Radicals with Acetaldehyde. *The Journal of Physical Chemistry A.* **108**(7), pp.1160-1168.

Butkovskaya, N., Pouvesle, N., Kukui, A., Mu, Y. and Le Bras, G. 2006. Mechanism of the OH-Initiated Oxidation of Hydroxyacetone over the Temperature Range 236−298 K. *The Journal of Physical Chemistry A.* **110**(21), pp.6833-6843.

Calvert, J.G. and Layne, G.S. 1953. The Photolysis of Glyoxal Vapor at Wavelength 3130 Å.1. *Journal of the American Chemical Society.* **75**(4), pp.856-859.

Cameron, M., Sivakumaran, V., Dillon, T.J. and Crowley, J.N. 2002. Reaction between OH and CH_3CHO Part 1. Primary product yields of CH_3 (296 K), CH_3CO (296 K), and H (237–296 K). *Physical Chemistry Chemical Physics.* **4**(15), pp.3628-3638.

Campuzano-Jost, P., Williams, M.B., D'Otton, L. and Hynes, A.J. 2004. Kinetics and Mechanism of the Reaction of the Hydroxyl Radical with h_8-Isoprene and d_8-Isoprene: Isoprene Absorption Cross Sections, Rate Coefficients, and the Mechanism of Hydroperoxyl Radical Production. *The Journal of Physical Chemistry A.* **108**(9), pp.1537-1551.

Campuzano-Jost, P., Williams, M.B., O'Ottone, L. and Hynes, A.J. 2000. Kinetics of the OH-initiated oxidation of isoprene. *Geophysical Research Letters.* **27**(5), pp.693-696.

Cantrell, C.A., Zimmer, A. and Tyndall, G.S. 1997. Absorption cross sections for water vapor from 183 to 193 nm. *Geophysical Research Letters.* **24**(17), pp.2195-2198.

Carpenter, L.J. and Nightingale, P.D. 2015. Chemistry and Release of Gases from the Surface Ocean. *Chemical Reviews.* **115**(10), pp.4015-4034.

Carter, W.P.L., Lloyd, A.C., Sprung, J.L. and Pitts Jr., J.N. 1979. Computer modeling of smog chamber data: Progress in validation of a detailed

mechanism for the photooxidation of propene and n-butane in photochemical smog. *International Journal of Chemical Kinetics.* **11**(1), pp.45-101.

Chan Miller, C., Gonzalez Abad, G., Wang, H., Liu, X., Kurosu, T., Jacob, D.J. and Chance, K. 2014. Glyoxal retrieval from the Ozone Monitoring Instrument. *Atmospheric Measurement Techniques.* **7**(11), pp.3891-3907.

Chan Miller, C., Jacob, D.J., González Abad, G. and Chance, K. 2016. Hotspot of glyoxal over the Pearl River delta seen from the OMI satellite instrument: implications for emissions of aromatic hydrocarbons. *Atmospheric Chemistry and Physics.* **16**(7), pp.4631-4639.

Chan Miller, C., Jacob, D.J., Marais, E.A., Yu, K., Travis, K.R., Kim, P.S., Fisher, J.A., Zhu, L., Wolfe, G.M., Hanisco, T.F., Keutsch, F.N., Kaiser, J., Min, K.E., Brown, S.S., Washenfelder, R.A., González Abad, G. and Chance, K. 2017. Glyoxal yield from isoprene oxidation and relation to formaldehyde: chemical mechanism, constraints from SENEX aircraft observations, and interpretation of OMI satellite data. *Atmospheric Chemistry and Physics.* **17**(14), pp.8725-8738.

Chen, Y., Su, W., Xing, C., Yin, H., Lin, H., Zhang, C., Liu, H., Hu, Q. and Liu, C. 2022. Kilometer-level glyoxal retrieval via satellite for anthropogenic volatile organic compound emission source and secondary organic aerosol formation identification. *Remote Sensing of Environment.* **270**, p112852.

Chen, Y. and Zhu, L. 2003. Wavelength-dependent photolysis of glyoxal in the 290-420 nm region. *Journal of Physical Chemistry A.* **107**(23), pp.4643-4651.

Cheng, H.-P. 1998. Water Clusters: Fascinating Hydrogen-Bonding Networks, Solvation Shell Structures, and Proton Motion. *The Journal of Physical Chemistry A.* **102**(31), pp.6201-6204.

Cheng, X., Li, H., Zhang, Y., Li, Y., Zhang, W., Wang, X., Bi, F., Zhang, H., Gao, J., Chai, F., Lun, X., Chen, Y., Gao, J. and Lv, J. 2018. Atmospheric isoprene and monoterpenes in a typical urban area of Beijing: Pollution characterization, chemical reactivity and source identification. *Journal of Environmental Sciences.* **71**, pp.150-167.

Christensen, C.S., Skov, H. and Palmgren, F. 1999. C_5–C_8 non-methane hydrocarbon measurements in Copenhagen: concentrations, sources and emission estimates. *Science of The Total Environment.* **236**(1), pp.163-171.

Chuong, B. and Stevens, P.S. 2004. Measurements of the kinetics of the OH-initiated oxidation of methyl vinyl ketone and methacrolein. *International Journal of Chemical Kinetics.* **36**(1), pp.12-25.

Cleary, P.A., Romero, M.T.B., Blitz, M.A., Heard, D.E., Pilling, M.J., Seakins, P.W. and Wang, L. 2006. Determination of the temperature and pressure dependence of the reaction OH + C_2H_4 from 200–400 K using

experimental and master equation analyses. *Physical Chemistry Chemical Physics.* **8**(48), pp.5633-5642.

Coburn, S., Ortega, I., Thalman, R., Blomquist, B., Fairall, C. and Volkamer, R. 2014. Measurements of diurnal variations and eddy covariance (EC) fluxes of glyoxal in the tropical marine boundary layer: description of the Fast LED-CE-DOAS instrument. *Atmospheric Measurement Techniques.* **7**(10), p3579.

Conte, L., Szopa, S., Aumont, O., Gros, V. and Bopp, L. 2020. Sources and Sinks of Isoprene in the Global Open Ocean: Simulated Patterns and Emissions to the Atmosphere. *Journal of Geophysical Research: Oceans.* **125**(9), pe2019JC015946.

Copeland, R.A. and Crosley, D.R. 1986. Temperature dependent electronic quenching of OH($A_2\Sigma^+$, v'=0) between 230 and 310 K. *The Journal of Chemical Physics.* **84**(6), pp.3099-3105.

Corrigan, A.L., Hanley, S.W. and De Haan, D.O. 2008. Uptake of Glyoxal by Organic and Inorganic Aerosol. *Environmental Science & Technology.* **42**(12), pp.4428-4433.

Cox, R.A., Ammann, M., Crowley, J.N., Herrmann, H., Jenkin, M.E., McNeill, V.F., Mellouki, A., Troe, J. and Wallington, T.J. 2020. Evaluated kinetic and photochemical data for atmospheric chemistry: Volume VII – Criegee intermediates. *Atmospheric Chemistry and Physics.* **20**(21), pp.13497-13519.

Creasey, D.J., Halford-Maw, P.A., Heard, D.E., Pilling, M.J. and Whitaker, B.J. 1997a. Implementation and initial deployment of a field instrument for measurement of OH and HO_2 in the troposphere by laser-induced fluorescence. *Journal of the Chemical Society, Faraday Transactions.* **93**(16), pp.2907-2913.

Creasey, D.J., Heard, D.E. and Lee, J.D. 2000. Absorption cross-section measurements of water vapour and oxygen at 185 nm. Implications for the calibration of field instruments to measure OH, HO_2 and RO_2 radicals. *Geophysical Research Letters.* **27**(11), pp.1651-1654.

Creasey, D.J., Heard, D.E., Pilling, M.J., Whitaker, B.J., Berzins, M. and Fairlie, R. 1997b. Visualisation of a supersonic free-jet expansion using laser-induced fluorescence spectroscopy: Application to the measurement of rate constants at ultralow temperatures. *Applied Physics B.* **65**(3), pp.375-391.

Criegee, R. and Wenner, G. 1949. Die Ozonisierung des 9,10-Oktalins. **564**(1), pp.9-15.

Crounse, J.D., Knap, H.C., Ørnsø, K.B., Jørgensen, S., Paulot, F., Kjaergaard, H.G. and Wennberg, P.O. 2012. Atmospheric Fate of

Methacrolein. 1. Peroxy Radical Isomerization Following Addition of OH and O_2. *The Journal of Physical Chemistry A.* **116**(24), pp.5756-5762.

Cryer, D.R. 2016. *Measurements of hydroxyl radical reactivity and formaldehyde in the atmosphere*. thesis, University of Leeds.

D'Anna, B., Andresen, Ø., Gefen, Z. and Nielsen, C.J. 2001. Kinetic study of OH and NO_3 radical reactions with 14 aliphatic aldehydes. *Physical Chemistry Chemical Physics.* **3**(15), pp.3057-3063.

Davis, D.D., Heaps, W. and McGee, T. 1976. Direct measurements of natural tropospheric levels of OH via an aircraft borne tunable dye laser. *Geophysical Research Letters.* **3**(6), pp.331-333.

Deng, J.-g., Chen, J.-h., Geng, C.-m., Liu, H.-j., Wang, W., Bai, Z.-p. and Xu, Y.-S. 2012. The Overall Reaction Process of Ozone with Methacrolein and Isoprene in the Condensed Phase. *The Journal of Physical Chemistry A.* **116**(7), pp.1710-1716.

Devolder, P., Fittschen, C., Frenzel, A., Hippler, H., Poskrebyshev, G., Striebel, F. and Viskolcz. 1999. Complete falloff curves for the unimolecular decomposition of i-propoxy radicals between 330 and 408 K. *Physical Chemistry Chemical Physics.* **1**(4), pp.675-681.

DiGangi, J.P., Henry, S.B., Kammrath, A., Boyle, E.S., Kaser, L., Schnitzhofer, R., Graus, M., Turnipseed, A., Park, J.H., Weber, R.J., Hornbrook, R.S., Cantrell, C.A., Maudlin Iii, R.L., Kim, S., Nakashima, Y., Wolfe, G.M., Kajii, Y., Apel, E.C., Goldstein, A.H., Guenther, A., Karl, T., Hansel, A. and Keutsch, F.N. 2012. Observations of glyoxal and formaldehyde as metrics for the anthropogenic impact on rural photochemistry. *Atmospheric Chemistry and Physics.* **12**(20), pp.9529-9543.

Dillon, T.J., Dulitz, K., Groß, C.B.M. and Crowley, J.N. 2017. Temperature-dependent rate coefficients for the reactions of the hydroxyl radical with the atmospheric biogenics isoprene, alpha-pinene and delta-3-carene. *Atmospheric Chemistry and Physics.* **17**(24), pp.15137-15150.

Dóbé, S., Bérces, T., Temps, F., Wagner, H.G. and Ziemer, H. 1994. Formation of methoxy and hydroxymethyl free radicals in selected elementary reactions. *Symposium (International) on Combustion.* **25**(1), pp.775-781.

Dóbé, S., Otting, M., Temps, F., Wagner, H.G. and Ziemer, H. 1993. Fast Flow Kinetic Studies of the Reaction $CH_2OH + HCl \leftrightharpoons CH_3OH + Cl$. The Heat of Formation of Hydroxymethyl. *Berichte der Bunsengesellschaft für physikalische Chemie.* **97**(7), pp.877-883.

Doussin, J.-F., Ritz, D., Durand-Jolibois, R., Monod, A. and Carlier, P. 1997. Design of an environmental chamber for the study of atmospheric chemistry: New developments in the analytical device. *Analusis.* **25**(7), pp.236-242.

Drozd, G.T., Kurtén, T., Donahue, N.M. and Lester, M.I. 2017. Unimolecular Decay of the Dimethyl-Substituted Criegee Intermediate in Alkene Ozonolysis: Decay Time Scales and the Importance of Tunneling. *The Journal of Physical Chemistry A.* **121**(32), pp.6036-6045.

Dusanter, S., Vimal, D. and Stevens, P.S. 2008. Technical note: Measuring tropospheric OH and HO_2- by laser-induced fluorescence at low pressure. A comparison of calibration techniques. *Atmospheric Chemistry and Physics.* **8**(2), pp.321-340.

Edney, E.O., Kleindienst, T.E. and Corse, E.W. 1986. Room temperature rate constants for the reaction of OH with selected chlorinated and oxygenated hydrocarbons. *International Journal of Chemical Kinetics.* **18**(12), pp.1355-1371.

Edwards, G.D., Cantrell, C.A., Stephens, S., Hill, B., Goyea, O., Shetter, R.E., Mauldin, R.L., Kosciuch, E., Tanner, D.J. and Eisele, F.L. 2003. Chemical Ionization Mass Spectrometer Instrument for the Measurement of Tropospheric HO_2 and RO_2. *Analytical Chemistry.* **75**(20), pp.5317-5327.

Emmerson, K.M. and Evans, M.J. 2009. Comparison of tropospheric gas-phase chemistry schemes for use within global models. *Atmospheric Chemistry and Physics.* **9**(5), pp.1831-1845.

Ervens, B. and Volkamer, R. 2010. Glyoxal processing by aerosol multiphase chemistry: towards a kinetic modeling framework of secondary organic aerosol formation in aqueous particles. *Atmospheric Chemistry and Physics.* **10**(17), pp.8219-8244.

Faloona, I.C., Tan, D., Lesher, R.L., Hazen, N.L., Frame, C.L., Simpas, J.B., Harder, H., Martinez, M., Di Carlo, P., Ren, X. and Brune, W.H. 2004. A Laser-induced Fluorescence Instrument for Detecting Tropospheric OH and HO_2: Characteristics and Calibration. *Journal of Atmospheric Chemistry.* **47**(2), pp.139-167.

Feierabend, K.J., Zhu, L., Talukdar, R.K. and Burkholder, J.B. 2008. Rate Coefficients for the OH + HC(O)C(O)H (Glyoxal) Reaction between 210 and 390 K. *The Journal of Physical Chemistry A.* **112**(1), pp.73-82.

Fenske, J.D., Hasson, A.S., Paulson, S.E., Kuwata, K.T., Ho, A. and Houk, K.N. 2000. The Pressure Dependence of the OH Radical Yield from Ozone−Alkene Reactions. *The Journal of Physical Chemistry A.* **104**(33), pp.7821-7833.

Fittschen, C., Whalley, L.K. and Heard, D.E. 2014. The Reaction of CH_3O_2 Radicals with OH Radicals: A Neglected Sink for CH_3O_2 in the Remote Atmosphere. *Environmental Science & Technology.* **48**(14), pp.7700-7701.

Fu, D., Millet, D.B., Wells, K.C., Payne, V.H., Yu, S., Guenther, A. and Eldering, A. 2019. Direct retrieval of isoprene from satellite-based infrared measurements. *Nature Communications.* **10**(1), p3811.

Fu, T.-M., Jacob, D.J., Wittrock, F., Burrows, J.P., Vrekoussis, M. and Henze, D.K. 2008. Global budgets of atmospheric glyoxal and methylglyoxal, and implications for formation of secondary organic aerosols. *Journal of Geophysical Research: Atmospheres.* **113**(D15303).

Fu, T.-M., Zheng, Y., Paulot, F., Mao, J. and Yantosca, R.M. 2015. Positive but variable sensitivity of August surface ozone to large-scale warming in the southeast United States. *Nature Climate Change.* **5**(5), pp.454-458.

Fuchs, H., Albrecht, S., Acir, I., Bohn, B., Breitenlechner, M., Dorn, H.P., Gkatzelis, G.I., Hofzumahaus, A., Holland, F., Kaminski, M., Keutsch, F.N., Novelli, A., Reimer, D., Rohrer, F., Tillmann, R., Vereecken, L., Wegener, R., Zaytsev, A., Kiendler-Scharr, A. and Wahner, A. 2018. Investigation of the oxidation of methyl vinyl ketone (MVK) by OH radicals in the atmospheric simulation chamber SAPHIR. *Atmospheric Chemistry and Physics.* **18**(11), pp.8001-8016.

Fuchs, H., Bohn, B., Hofzumahaus, A., Holland, F., Lu, K.D., Nehr, S., Rohrer, F. and Wahner, A. 2011. Detection of HO-$_2$ by laser-induced fluorescence: calibration and interferences from RO_2 radicals. *Atmospheric Measurement Techniques.* **4**(6), pp.1209-1225.

Galano, A., Ruiz-Suárez, L.G. and Vivier-Bunge, A. 2008. On the mechanism of the OH initiated oxidation of acetylene in the presence of O_2 and NO_x. *Theoretical Chemistry Accounts.* **121**(5), pp.219-225.

Galloway, M.M., Huisman, A.J., Yee, L.D., Chan, A.W.H., Loza, C.L., Seinfeld, J.H. and Keutsch, F.N. 2011. Yields of oxidized volatile organic compounds during the OH radical initiated oxidation of isoprene, methyl vinyl ketone, and methacrolein under high-NO_x conditions. *Atmospheric Chemistry and Physics.* **11**(21), pp.10779-10790.

Gibson, G.E. and Bayliss, N.S. 1933. Variation with Temperature of the Continuous Absorption Spectrum of Diatomic Molecules: Part I. Experimental, The Absorption Spectrum of Chlorine. *Physical Review.* **44**(3), pp.188-192.

Gierczak, T., Burkholder, J.B., Talukdar, R.K., Mellouki, A., Barone, S.B. and Ravishankara, A.R. 1997. Atmospheric fate of methyl vinyl ketone and methacrolein. *Journal of Photochemistry and Photobiology A: Chemistry.* **110**(1), pp.1-10.

Giguère, P.A. and Maass, O. 1940. Vapour pressures and boiling points of binary mixtures of hydrogen peroxide and water. **18b**(7), pp.181-193.

Gill, K.J. and Hites, R.A. 2002. Rate Constants for the Gas-Phase Reactions of the Hydroxyl Radical with Isoprene, α- and β-Pinene, and Limonene as a Function of Temperature. *The Journal of Physical Chemistry A.* **106**(11), pp.2538-2544.

Glowacki, D., Goddard, A., Hemavibool, K., Malkin, T., Commane, R., Anderson, F., Bloss, W., Heard, D., Ingham, T., Pilling, M. and Seakins, P. 2007a. Design of and initial results from a Highly Instrumented Reactor for Atmospheric Chemistry (HIRAC). *Atmospheric Chemistry and Physics.* **7**(20), pp.5371-5390.

Glowacki, D., Goddard, A. and Seakins, P. 2007b. Design and performance of a throughput-matched, zero-geometric-loss, modified three objective multipass matrix system for FTIR spectrometry. *Applied Optics.* **46**(32), pp.7872-7883.

Glowacki, D., Liang, C.-H., Morley, C., Pilling, M. and Robertson, S. 2012. MESMER: An Open-Source Master Equation Solver for Multi-Energy Well Reactions. *The Journal of Physical Chemistry A.* **116**(38), pp.9545-9560.

Goebbert, D.J. and Wenthold, P.G. 2004. Water Dimer Proton Affinity from the Kinetic Method: Dissociation Energy of the Water Dimer. *European Journal of Mass Spectrometry.* **10**(6), pp.837-845.

González Abad, G., Liu, X., Chance, K., Wang, H., Kurosu, T.P. and Suleiman, R. 2015. Updated Smithsonian Astrophysical Observatory Ozone Monitoring Instrument (SAO OMI) formaldehyde retrieval. *Atmospheric Measurement Techniques.* **8**(1), pp.19-32.

Greene, C.R. and Atkinson, R. 1992. Rate constants for the gas-phase reactions of O_3 with a series of alkenes at 296 ± 2 K. *International Journal of Chemical Kinetics.* **24**(9), pp.803-811.

Grosjean, D., Williams, E.L. and Grosjean, E. 1993. Atmospheric chemistry of isoprene and of its carbonyl products. *Envionmental Science & Technology.* **27**(5), pp.830-840.

Grosjean, E. and Grosjean, D. 1996. Rate constants for the gas-phase reaction of ozone with 1,1-disubstituted alkenes. *International Journal of Chemical Kinetics.* **28**(12), pp.911-918.

Grosjean, E. and Grosjean, D. 1998. Rate constants for the gas-phase reaction of ozone with unsaturated oxygenates. *International Journal of Chemical Kinetics.* **30**(1), pp.21-29.

Guenther, A., Hewitt, C., Erickson, D., Fall, R., Geron, C., Graedel, T., Harley, P., Klinger, L., Lerdau, M., Mckay, W., Pierce, T., Scholes, B., Steinbrecher, R., Tallamraju, R., Taylor, J. and Zimmerman, P. 1995. A global model of natural volatile organic compound emissions. *Journal of Geophysical Research: Atmospheres.* **100**(D5), pp.8873-8892.

Guenther, A., Jiang, X., Heald, C., Sakulyanontvittaya, T., Duhl, T., Emmons, L. and Wang, X. 2012. The Model of Emissions of Gases and Aerosols from Nature version 2.1 (MEGAN2.1): an extended and updated framework for modeling biogenic emissions. *Geoscientific Model Development.* **5**(6), pp.1471-1492.

Guenther, A., Karl, T., Harley, P., Wiedinmyer, C., Palmer, P. and Geron, C. 2006. Estimates of global terrestrial isoprene emissions using MEGAN (Model of Emissions of Gases and Aerosols from Nature). *Atmospheric Chemistry and Physics.* **6**(11), pp.3181-3210.

Guenther, A., Monson, R. and Fall, R. 1991. Isoprene and monoterpene emission rate variability: Observations with eucalyptus and emission rate algorithm development. *Journal of Geophysical Research: Atmospheres.* **96**(D6), pp.10799-10808.

Guenther, A., Zimmerman, P., Harley, P., Monson, R. and Fall, R. 1993. Isoprene and monoterpene emission rate variability: Model evaluations and sensitivity analyses. *Journal of Geophysical Research: Atmospheres.* **98**(D7), pp.12609-12617.

Haagen-Smit, A.J. 1952. Chemistry and Physiology of Los Angeles Smog. *Industrial & Engineering Chemistry.* **44**(6), pp.1342-1346.

Haagen-Smit, A.J. and Fox, M.M. 1954. Photochemical ozone formation with hydrocarbons and automobile exhaust. *Air Repair.* **4**(3), pp.105-136.

Hard, T.M., George, L.A. and O'Brien, R.J. 1995. FAGE Determination of Tropospheric OH and HO_2. *Journal of Atmospheric Sciences.* **52**(19), pp.3354-3372.

Hard, T.M., O'Brien, R.J., Cook, T.B. and Tsongas, G.A. 1979. Interference suppression in OH fluorescence detection. *Applied Optics.* **18**(19), pp.3216-3217.

Harrison, J.J., Allen, N.D.C. and Bernath, P.F. 2011a. Infrared absorption cross sections for acetone (propanone) in the 3μm region. *Journal of Quantitative Spectroscopy and Radiative Transfer.* **112**(1), pp.53-58.

Harrison, J.J., Humpage, N., Allen, N.D.C., Waterfall, A.M., Bernath, P.F. and Remedios, J.J. 2011b. Mid-infrared absorption cross sections for acetone (propanone). *Journal of Quantitative Spectroscopy and Radiative Transfer.* **112**(3), pp.457-464.

Hatakeyama, S., Washida, N. and Akimoto, H. 1986. Rate constants and mechanisms for the reaction of hydroxyl (OD) radicals with acetylene, propyne, and 2-butyne in air at 297 ± 2 K. *The Journal of Physical Chemistry.* **90**(1), pp.173-178.

Hays, M.D., Geron, C.D., Linna, K.J., Smith, N.D. and Schauer, J.J. 2002. Speciation of Gas-Phase and Fine Particle Emissions from Burning of Foliar Fuels. *Environmental Science & Technology.* **36**(11), pp.2281-2295.

Heard, D.E. and Pilling, M.J. 2003. Measurement of OH and HO_2 in the Troposphere. *Chemical Reviews.* **103**(12), pp.5163-5198.

Hellén, H., Tykkä, T. and Hakola, H. 2012. Importance of monoterpenes and isoprene in urban air in northern Europe. *Atmospheric Environment.* **59**, pp.59-66.

Henry, S.B., Kammrath, A. and Keutsch, F.N. 2012. Quantification of gas-phase glyoxal and methylglyoxal via the Laser-Induced Phosphorescence of (methyl)GLyOxal Spectrometry (LIPGLOS) Method. *Atmospheric Measurement Techniques.* **5**(1), pp.181-192.

Hofzumahaus, A., Kraus, A. and Muller, M. 1999. Solar actinic flux spectroradiometry: a technique for measuring photolysis frequencies in the atmosphere. *Applied Optics.* **38**(21), pp.4443-4460.

Holzer, W. and Ramsay, D.A. 1970. Laser-induced emission from glyoxal. *Canadian Journal of Physics.* **48**(15), pp.1759-1765.

Howes, N.U.M., Mir, Z.S., Blitz, M.A., Hardman, S., Lewis, T.R., Stone, D. and Seakins, P.W. 2018. Kinetic studies of C_1 and C_2 Criegee intermediates with SO_2 using laser flash photolysis coupled with photoionization mass spectrometry and time resolved UV absorption spectroscopy. *Physical Chemistry Chemical Physics.* **20**(34), pp.22218-22227.

Hsieh, H.-C., Ou-Yang, C.-F. and Wang, J.-L. 2017. Revelation of Coupling Biogenic with Anthropogenic Isoprene by Highly Time-Resolved Observations. *Aerosol and Air Quality Research.* **17**(3), pp.721-729.

Huisman, A.J., Hottle, J.R., Coens, K.L., DiGangi, J.P., Galloway, M.M., Kammrath, A. and Keutsch, F.N. 2008. Laser-Induced Phosphorescence for the in Situ Detection of Glyoxal at Part per Trillion Mixing Ratios. *Analytical Chemistry.* **80**(15), pp.5884-5891.

Huisman, A.J., Hottle, J.R., Galloway, M.M., DiGangi, J.P., Coens, K.L., Choi, W., Faloona, I.C., Gilman, J.B., Kuster, W.C., de Gouw, J., Bouvier-Brown, N.C., Goldstein, A.H., LaFranchi, B.W., Cohen, R.C., Wolfe, G.M., Thornton, J.A., Docherty, K.S., Farmer, D.K., Cubison, M.J., Jimenez, J.L., Mao, J., Brune, W.H. and Keutsch, F.N. 2011. Photochemical modeling of glyoxal at a rural site: observations and analysis from BEARPEX 2007. *Atmospheric Chemistry and Physics.* **11**(17), pp.8883-8897.

Hynes, R.G., Angove, D.E., Saunders, S.M., Haverd, V. and Azzi, M. 2005. Evaluation of two MCM v3.1 alkene mechanisms using indoor environmental chamber data. *Atmospheric Environment.* **39**(38), pp.7251-7262.

Ianni, J.C. 2019. *Kintecus Version 6.80.* [Online]. [Accessed 17th December]. Available from: http://www.kintecus.com/

Ip, H.S.S., Huang, X.H.H. and Yu, J.Z. 2009. Effective Henry's law constants of glyoxal, glyoxylic acid, and glycolic acid. *Geophysical Research Letters.* **36**(L01802).

Ito, K., De Leon, S.F. and Lippmann, M. 2005. Associations between Ozone and Daily Mortality: Analysis and Meta-Analysis. *Epidemiology.* **16**(4), pp.446-457.

Jaeglé, L., Jacob, D.J., Brune, W.H. and Wennberg, P.O. 2001. Chemistry of HO_x radicals in the upper troposphere. *Atmospheric Environment.* **35**(3), pp.469-489.

Jenkin, M., Cox, R., Emrich, M. and Moortgat, G. 1993. Mechanisms of the Cl-atom-initiated oxidation of acetone and hydroxyacetone in air. *Journal of the Chemical Society, Faraday Transactions.* **89**(16), pp.2983-2991.

Jenkin, M., Saunders, S. and Pilling, M. 1997. The tropospheric degradation of volatile organic compounds: a protocol for mechanism development. *Atmospheric Environment.* **31**(1), pp.81-104.

Jenkin, M., Saunders, S., Wagner, V. and Pilling, M. 2003. Protocol for the development of the Master Chemical Mechanism, MCM v3 (Part B): tropospheric degradation of aromatic volatile organic compounds. *Atmospheric Chemistry and Physics.* **3**(1), pp.181-193.

Jenkin, M., Young, J. and Rickard, A. 2015. The MCM v3.3.1 degradation scheme for isoprene. *Atmospheric Chemistry and Physics.* **15**(20), pp.11433-11459.

Jerrett, M., Burnett, R.T., Pope, C.A., Ito, K., Thurston, G., Krewski, D., Shi, Y., Calle, E. and Thun, M. 2009. Long-Term Ozone Exposure and Mortality. *The New England Journal of Medicine.* **360**(11), pp.1085-1095.

Junkermann, W., Platt, U. and Volz-Thomas, A. 1989. A photoelectric detector for the measurement of photolysis frequencies of ozone and other atmospheric molecules. *Journal of Atmospheric Chemistry.* **8**(3), pp.203-227.

Karl, M., Brauers, T., Dorn, H.-P., Holland, F., Komenda, M., Poppe, D., Rohrer, F., Rupp, L., Schaub, A. and Wahner, A. 2004. Kinetic Study of the OH-isoprene and O_3-isoprene reaction in the atmosphere simulation chamber, SAPHIR. *Geophysical Research Letters.* **31**(L05117).

Kashyap, P., Kumar, A., Kumar, R.P. and Kumar, K. 2019. Biogenic and anthropogenic isoprene emissions in the subtropical urban atmosphere of Delhi. *Atmospheric Pollution Research.* **10**(5), pp.1691-1698.

Kawai, Y., Yamaguchi, S., Okada, Y., Takeuchi, K., Yamauchi, Y., Ozawa, S. and Nakai, H. 2003. Reactions of protonated water clusters $H^+(H_2O)_n$ (n=1–6) with dimethylsulfoxide in a guided ion beam apparatus. *Chemical Physics Letters.* **377**(1), pp.69-73.

Kegley-Owen, C.S., Tyndall, G.S., Orlando, J.J. and Fried, A. 1999. Tunable diode laser studies of the reaction of Cl atoms with CH_3CHO. *International Journal of Chemical Kinetics.* **31**(11), pp.766-775.

Khamaganov, V.G. and Hites, R.A. 2001. Rate Constants for the Gas-Phase Reactions of Ozone with Isoprene, α- and β-Pinene, and Limonene as a Function of Temperature. *The Journal of Physical Chemistry A.* **105**(5), pp.815-822.

Khan, M.A.H., Schlich, B.-L., Jenkin, M.E., Shallcross, B.M.A., Moseley, K., Walker, C., Morris, W.C., Derwent, R.G., Percival, C.J. and Shallcross, D.E. 2018. A Two-Decade Anthropogenic and Biogenic Isoprene Emissions Study in a London Urban Background and a London Urban Traffic Site. *Atmosphere.* **9**(10), p387.

Kinoyama, M., Nitta, H., Watanabe, A. and Ueda, H. 2008. Acetone and Isoprene Concentrations in Exhaled Breath in Healthy Subjects. *Journal of Health Science.* **54**(4), pp.471-477.

Klawatsch-Carrasco, N., Doussin, J.F. and Carlier, P. 2004. Absolute rate constants for the gas-phase ozonolysis of isoprene and methylbutenol. *International Journal of Chemical Kinetics.* **36**(3), pp.152-156.

Kleindienst, T.E., Harris, G.W. and Pitts, J.N. 1982. Rates and temperature dependences of the reaction of hydroxyl radical with isoprene, its oxidation products, and selected terpenes. *Environmental Science & Technology.* **16**(12), pp.844-846.

KoreTechnology. 2015. Hardware Reference. Unipolar Horizontal PTR-TOF Mass Spectrometer. *Unpublished.*

Kroll, J.H., Donahue, N.M., Cee, V.J., Demerjian, K.L. and Anderson, J.G. 2002. Gas-Phase Ozonolysis of Alkenes: Formation of OH from Anti Carbonyl Oxides. *Journal of the American Chemical Society.* **124**(29), pp.8518-8519.

Kroll, J.H., Hanisco, T.F., Donahue, N.M., Demerjian, K.L. and Anderson, J.G. 2001. Accurate, direct measurements of OH yields from gas-phase ozone-alkene reactions using an in situ LIF Instrument. *Geophysical Research Letters.* **28**(20), pp.3863-3866.

Kushch, I., Arendacká, B., Štolc, S., Mochalski, P., Filipiak, W., Schwarz, K., Schwentner, L., Schmid, A., Dzien, A., Lechleitner, M., Witkovský, V., Miekisch, W., Schubert, J., Unterkofler, K. and Amann, A. 2008. Breath isoprene – aspects of normal physiology related to age, gender and cholesterol profile as determined in a proton transfer reaction mass spectrometry study. **46**(7), pp.1011-1018.

Langford, A.O. and Moore, C.B. 1984. Collision complex formation in the reactions of formyl radicals with nitric oxide and oxygen. *The Journal of Chemical Physics.* **80**(9), pp.4211-4221.

Lary, D.J. and Shallcross, D.E. 2000. Central role of carbonyl compounds in atmospheric chemistry. *Journal of Geophysical Research.* **105**(D15), pp.19771-19778.

Lawson, S., Selleck, P., Galbally, I., Keywood, M., Harvey, M., Lerot, C., Helmig, D. and Ristovski, Z. 2015. Seasonal in situ observations of glyoxal and methylglyoxal over the temperate oceans of the Southern Hemisphere. *Atmospheric Chemistry and Physics.* **15**, pp.223-240.

Lelieveld, J., Evans, J.S., Fnais, M., Giannadaki, D. and Pozzer, A. 2015. The contribution of outdoor air pollution sources to premature mortality on a global scale. *Nature.* **525**(7569), pp.367-371.

Lerot, C., Stavrakou, T., De Smedt, I., Müller, J. and Van Roozendael, M. 2010. Glyoxal vertical columns from GOME-2 backscattered light measurements and comparisons with a global model. *Atmospheric Chemistry and Physics.* **10**(24), pp.12,059-012,072.

Lewis, T.R., Blitz, M.A., Heard, D.E. and Seakins, P.W. 2015. Direct evidence for a substantive reaction between the Criegee intermediate, CH_2OO, and the water vapour dimer. *Physical Chemistry Chemical Physics.* **17**(7), pp.4859-4863.

Li, J., Mao, J., Min, K.-E., Washenfelder, R.A., Brown, S.S., Kaiser, J., Keutsch, F.N., Volkamer, R., Wolfe, G.M., Hanisco, T.F., Pollack, I.B., Ryerson, T.B., Graus, M., Gilman, J.B., Lerner, B.M., Warneke, C., de Gouw, J.A., Middlebrook, A.M., Liao, J., Welti, A., Henderson, B.H., McNeill, V.F., Hall, S.R., Ullmann, K., Donner, L.J., Paulot, F. and Horowitz, L.W. 2016. Observational constraints on glyoxal production from isoprene oxidation and its contribution to organic aerosol over the Southeast United States. *Journal of Geophysical Research: Atmospheres.* **121**(16), pp.9849-9861.

Liggio, J., Li, S.-M. and McLaren, R. 2005a. Heterogeneous Reactions of Glyoxal on Particulate Matter: Identification of Acetals and Sulfate Esters. *Environmental Science & Technology.* **39**(6), pp.1532-1541.

Liggio, J., Li, S.-M. and McLaren, R. 2005b. Reactive uptake of glyoxal by particulate matter. *Journal of Geophysical Research: Atmospheres.* **110**(D10).

Lim, S.S., Vos, T., Flaxman, A.D., Danaei, G., Shibuya, K., Adair-Rohani, H., AlMazroa, M.A., Amann, M., Anderson, H.R., Andrews, K.G., Aryee, M., Atkinson, C., Bacchus, L.J., Bahalim, A.N., Balakrishnan, K., Balmes, J., Barker-Collo, S., Baxter, A., Bell, M.L., Blore, J.D., Blyth, F., Bonner, C., Borges, G., Bourne, R., Boussinesq, M., Brauer, M., Brooks, P., Bruce, N.G., Brunekreef, B., Bryan-Hancock, C., Bucello, C., Buchbinder, R., Bull, F., Burnett, R.T., Byers, T.E., Calabria, B., Carapetis, J., Carnahan, E., Chafe, Z., Charlson, F., Chen, H., Chen, J.S., Cheng, A.T.-A., Child, J.C., Cohen, A., Colson, K.E., Cowie, B.C., Darby, S., Darling, S., Davis, A., Degenhardt, L., Dentener, F., Des Jarlais, D.C., Devries, K., Dherani, M., Ding, E.L., Dorsey, E.R., Driscoll, T., Edmond, K., Ali, S.E., Engell, R.E., Erwin, P.J., Fahimi, S., Falder, G., Farzadfar, F., Ferrari, A., Finucane,

M.M., Flaxman, S., Fowkes, F.G.R., Freedman, G., Freeman, M.K., Gakidou, E., Ghosh, S., Giovannucci, E., Gmel, G., Graham, K., Grainger, R., Grant, B., Gunnell, D., Gutierrez, H.R., Hall, W., Hoek, H.W., Hogan, A., Hosgood, H.D., Hoy, D., Hu, H., Hubbell, B.J., Hutchings, S.J., Ibeanusi, S.E., Jacklyn, G.L., Jasrasaria, R., Jonas, J.B., Kan, H., Kanis, J.A., Kassebaum, N., Kawakami, N., Khang, Y.-H., Khatibzadeh, S., Khoo, J.-P., Kok, C., Laden, F., Lalloo, R., Lan, Q., Lathlean, T., Leasher, J.L., Leigh, J., Li, Y., Lin, J.K., Lipshultz, S.E., London, S., Lozano, R., Lu, Y., Mak, J., Malekzadeh, R., Mallinger, L., Marcenes, W., March, L., Marks, R., Martin, R., McGale, P., McGrath, J., Mehta, S., Memish, Z.A., Mensah, G.A., Merriman, T.R., Micha, R., Michaud, C., Mishra, V., Hanafiah, K.M., Mokdad, A.A., Morawska, L., Mozaffarian, D., Murphy, T., Naghavi, M., Neal, B., Nelson, P.K., Nolla, J.M., Norman, R., Olives, C., Omer, S.B., Orchard, J., Osborne, R., Ostro, B., Page, A., Pandey, K.D., Parry, C.D.H., Passmore, E., Patra, J., Pearce, N., Pelizzari, P.M., Petzold, M., Phillips, M.R., Pope, D., Pope, C.A., Powles, J., Rao, M., Razavi, H., Rehfuess, E.A., Rehm, J.T., Ritz, B., Rivara, F.P., Roberts, T., Robinson, C., Rodriguez-Portales, J.A., Romieu, I., Room, R., Rosenfeld, L.C., Roy, A., Rushton, L., Salomon, J.A., Sampson, U., Sanchez-Riera, L., Sanman, E., Sapkota, A., Seedat, S., Shi, P., Shield, K., Shivakoti, R., Singh, G.M., Sleet, D.A., Smith, E., Smith, K.R., Stapelberg, N.J.C., Steenland, K., Stöckl, H., Stovner, L.J., Straif, K., Straney, L., Thurston, G.D., Tran, J.H., Van Dingenen, R., van Donkelaar, A., Veerman, J.L., Vijayakumar, L., Weintraub, R., Weissman, M.M., White, R.A., Whiteford, H., Wiersma, S.T., Wilkinson, J.D., Williams, H.C., Williams, W., Wilson, N., Woolf, A.D., Yip, P., Zielinski, J.M., Lopez, A.D., Murray, C.J.L. and Ezzati, M. 2012. A comparative risk assessment of burden of disease and injury attributable to 67 risk factors and risk factor clusters in 21 regions, 1990–2010: a systematic analysis for the Global Burden of Disease Study 2010. *The Lancet.* **380**(9859), pp.2224-2260.

Lin, C.L., Rohatgi, N.K. and DeMore, W.B. 1978. Ultraviolet absorption cross sections of hydrogen peroxide. *Geophysical Research Letters.* **5**(2), pp.113-115.

Liu, Y.J., Herdlinger-Blatt, I., McKinney, K.A. and Martin, S.T. 2013. Production of methyl vinyl ketone and methacrolein via the hydroperoxyl pathway of isoprene oxidation. *Atmospheric Chemistry and Physics.* **13**(11), pp.5715-5730.

Lockhart, J., Blitz, M.A., Heard, D.E., Seakins, P.W. and Shannon, R.J. 2013. Mechanism of the Reaction of OH with Alkynes in the Presence of Oxygen. *The Journal of Physical Chemistry A.* **117**(26), pp.5407-5418.

Logan, J.A. 1985. Tropospheric ozone: Seasonal behavior, trends, and anthropogenic influence. *Journal of Geophysical Research: Atmospheres.* **90**(D6), pp.10463-10482.

Long, J. and Munson, B. 1970. On the Proton Affinity of Water. *The Journal of Chemical Physics.* **53**(4), pp.1356-1359.

Malicet, J., Daumont, D., Charbonnier, J., Parisse, C., Chakir, A. and Brion, J. 1995. Ozone UV spectroscopy. II. Absorption cross-sections and temperature dependence. *Journal of Atmospheric Chemistry.* **21**(3), pp.263-273.

Malkin, T.L. 2010. *Detection of free-radicals and other species to investigate atmospheric chemistry in the HIRAC chamber*. thesis, University of Leeds.

Malkin, T.L., Goddard, A., Heard, D.E. and Seakins, P.W. 2010. Measurements of OH and HO_2 yields from the gas phase ozonolysis of isoprene. *Atmospheric Chemistry and Physics.* **10**(3), pp.1441-1459.

Maric, D., Burrows, J.P., Meller, R. and Moortgat, G.K. 1993. A study of the UV—visible absorption spectrum of molecular chlorine. *Journal of Photochemistry and Photobiology A: Chemistry.* **70**(3), pp.205-214.

Maricq, M.M. and Wallington, T.J. 1992. Absolute UV cross sections of methyl and ethyl peroxy radicals. *The Journal of Physical Chemistry.* **96**(2), pp.986-992.

Martinez, R.D., Buitrago, A.A., Howell, N.W., Hearn, C.H. and Joens, J.A. 1992. The near U.V. absorption spectra of several aliphatic aldehydes and ketones at 300 K. *Atmospheric Environment. Part A. General Topics.* **26**(5), pp.785-792.

Martins, G., Ferreira-Rodrigues, A.M., Rodrigues, F.N., de Souza, G.G.B., Mason, N.J., Eden, S., Duflot, D., Flament, J.P., Hoffmann, S.V., Delwiche, J., Hubin-Franskin, M.J. and Limão-Vieira, P. 2009. Valence shell electronic spectroscopy of isoprene studied by theoretical calculations and by electron scattering, photoelectron, and absolute photoabsorption measurements. *Physical Chemistry Chemical Physics.* **11**(47), pp.11219-11231.

Matsumi, Y. and Kawasaki, M. 2003. Photolysis of Atmospheric Ozone in the Ultraviolet Region. *Chemical Reviews.* **103**(12), pp.4767-4782.

Matsumoto, K., Kawai, S. and Igawa, M. 2005. Dominant factors controlling concentrations of aldehydes in rain, fog, dew water, and in the gas phase. *Atmospheric Environment.* **39**(38), pp.7321-7329.

McDonald, J.D., Zielinska, B., Fujita, E.M., Sagebiel, J.C., Chow, J.C. and Watson, J.G. 2000. Fine Particle and Gaseous Emission Rates from Residential Wood Combustion. *Environmental Science & Technology.* **34**(11), pp.2080-2091.

McKee, K.W., Blitz, M.A., Cleary, P.A., Glowacki, D.R., Pilling, M.J., Seakins, P.W. and Wang, L. 2007. Experimental and Master Equation Study of the Kinetics of OH + C2H2: Temperature Dependence of the Limiting

High Pressure and Pressure Dependent Rate Coefficients. *The Journal of Physical Chemistry A.* **111**(19), pp.4043-4055.

McKeen, S.A., Gierczak, T., Burkholder, J.B., Wennberg, P.O., Hanisco, T.F., Keim, E.R., Gao, R.-S., Liu, S.C., Ravishankara, A.R. and Fahey, D.W. 1997. The photochemistry of acetone in the upper troposphere: A source of odd-hydrogen radicals. *Geophysical Research Letters.* **24**(24), pp.3177-3180.

Medeiros, D.J., Blitz, M.A., James, L., Speak, T.H. and Seakins, P.W. 2018. Kinetics of the Reaction of OH with Isoprene over a Wide Range of Temperature and Pressure Including Direct Observation of Equilibrium with the OH Adducts. *The Journal of Physical Chemistry A.* **122**(37), pp.7239-7255.

Meller, R., Raber, W., Crowley, J.N., Jenkin, M.E. and Moortgat, G.K. 1991. The UV-visible absorption spectrum of methylglyoxal. *Journal of Photochemistry and Photobiology A: Chemistry.* **62**(2), pp.163-171.

Mérienne, M.F., Jenouvrier, A. and Coquart, B. 1995. The NO_2 absorption spectrum. I: Absorption cross-sections at ambient temperature in the 300–500 nm region. *Journal of Atmospheric Chemistry.* **20**(3), pp.281-297.

Metzger, A., Dommen, J., Gaeggeler, K., Duplissy, J., Prevot, A.S.H., Kleffmann, J., Elshorbany, Y., Wisthaler, A. and Baltensperger, U. 2008. Evaluation of 1,3,5-trimethylbenzene degradation in the detailed tropospheric chemistry mechanism, MCMv3.1, using environmental chamber data. *Atmospheric Chemistry and Physics.* **8**(21), pp.6453-6468.

Michael, J.V., Nava, D.F., Payne, W.A. and Stief, L.J. 1979. Rate constants for the reaction of atomic chlorine with methanol and dimethyl ether from 200 to 500 K. *The Journal of Chemical Physics.* **70**(8), pp.3652-3656.

Mihelcic, D., Heitlinger, M., Kley, D., Müsgen, P. and Volz-Thomas, A. 1999. Formation of hydroxyl and hydroperoxy radicals in the gas-phase ozonolysis of ethene. *Chemical Physics Letters.* **301**(5), pp.559-564.

Millet, D.B., Guenther, A., Siegel, D.A., Nelson, N.B., Singh, H.B., de Gouw, J.A., Warneke, C., Williams, J., Eerdekens, G., Sinha, V., Karl, T., Flocke, F., Apel, E., Riemer, D.D., Palmer, P.I. and Barkley, M. 2010. Global atmospheric budget of acetaldehyde: 3-D model analysis and constraints from in-situ and satellite observations. *Atmospheric Chemistry and Physics.* **10**(7), pp.3405-3425.

Mishra, A.K. and Sinha, V. 2020. Emission drivers and variability of ambient isoprene, formaldehyde and acetaldehyde in north-west India during monsoon season. *Environmental Pollution.* **267**(115538).

Molina, L.T. and Molina, M.J. 1981. UV absorption cross sections of HO_2NO_2 vapor. *Journal of Photochemistry.* **15**(2), pp.97-108.

Molina, L.T. and Molina, M.J. 1986. Absolute absorption cross sections of ozone in the 185- to 350-nm wavelength range. *Journal of Geophysical Research.* **91**(D13), pp.14501-14508.

Molina, L.T., Schinke, S.D. and Molina, M.J. 1977. Ultraviolet absorption spectrum of hydrogen peroxide vapor. *Geophysical Research Letters.* **4**(12), pp.580-582.

Moortgat, G.K., Meyrahn, H. and Warneck, P. 2010. Photolysis of Acetaldehyde in Air: CH_4, CO and CO_2 Quantum Yields. **11**(18), pp.3896-3908.

Myriokefalitakis, S., Vrekoussis, M., Tsigaridis, K., Wittrock, F., Richter, A., Bruhl, C., Volkamer, R., Burrows, J.P. and Kanakidou, M. 2008. The influence of natural and anthropogenic secondary sources on the glyoxal global distribution. *Atmospheric Chemistry and Physics.* **8**, pp.4965-4981.

Neeb, P., Kolloff, A., Koch, S. and Moortgat, G.K. 1998. Rate constants for the reactions of methylvinyl ketone, methacrolein, methacrylic acid, and acrylic acid with ozone. *International Journal of Chemical Kinetics.* **30**(10), pp.769-776.

Neeb, P. and Moortgat, G.K. 1999. Formation of OH Radicals in the Gas-Phase Reaction of Propene, Isobutene, and Isoprene with O_3: Yields and Mechanistic Implications. *The Journal of Physical Chemistry A.* **103**(45), pp.9003-9012.

Nelson, L., Rattigan, O., Neavyn, R., Sidebottom, H., Treacy, J. and Nielsen, O.J. 1990. Absolute and relative rate constants for the reactions of hydroxyl radicals and chlorine atoms with a series of aliphatic alcohols and ethers at 298 K. *International Journal of Chemical Kinetics.* **22**(11), pp.1111-1126.

Nguyen, T.B., Bates, K.H., Crounse, J.D., Schwantes, R.H., Zhang, X., Kjaergaard, H.G., Surratt, J.D., Lin, P., Laskin, A., Seinfeld, J.H. and Wennberg, P.O. 2015. Mechanism of the hydroxyl radical oxidation of methacryloyl peroxynitrate (MPAN) and its pathway toward secondary organic aerosol formation in the atmosphere. *Physical Chemistry Chemical Physics.* **17**(27), pp.17914-17926.

Nicovich, J.M. and Wine, P.H. 1988. Temperature-dependent absorption cross sections for hydrogen peroxide vapor. **93**(D3), pp.2417-2421.

Niki, H., Maker, P.D., Savage, C.M. and Breitenbach, L.P. 1978. Relative rate constants for the reaction of hydroxyl radical with aldehydes. *The Journal of Physical Chemistry.* **82**(2), pp.132-134.

Niki, H., Maker, P.D., Savage, C.M. and Breitenbach, L.P. 1985a. An FTIR study of the Cl-atom-initiated reaction of glyoxal. *International Journal of Chemical Kinetics.* **17**(5), pp.547-558.

Niki, H., Maker, P.D., Savage, C.M. and Breitenbach, L.P. 1985b. FTIR study of the kinetics and mechanism for chlorine-atom-initiated reactions of acetaldehyde. *Journal of Physical Chemistry.* **89**(4), pp.588-591.

Nishida, S., Takahashi, K., Matsumi, Y., Taniguchi, N. and Hayashida, S. 2004. Formation of $O(^3P)$ Atoms in the Photolysis of N_2O at 193 nm and $O(^3P) + N_2O$ Product Channel in the Reaction of $O(^1D) + N_2O$. *The Journal of Physical Chemistry A.* **108**(13), pp.2451-2456.

Novelli, A., Hens, K., Tatum Ernest, C., Kubistin, D., Regelin, E., Elste, T., Plass-Dülmer, C., Martinez, M., Lelieveld, J. and Harder, H. 2014. Characterisation of an inlet pre-injector laser-induced fluorescence instrument for the measurement of atmospheric hydroxyl radicals. *Atmospheric Measurement Techniques.* **7**(10), pp.3413-3430.

O'Brien, J.M., Czuba, E., Hastie, D.R., Francisco, J.S. and Shepson, P.B. 1998. Determination of the Hydroxy Nitrate Yields from the Reaction of C_2-C_6 Alkenes with OH in the Presence of NO. *The Journal of Physical Chemistry A.* **102**(45), pp.8903-8908.

O'Brien, R.J. 1974. Photostationary state in photochemical smog studies. *Environmental Science & Technology.* **8**(6), pp.579-583.

Okabe, H. 1978. *Photochemistry of small molecules.* Wiley New York.

Onel, L., Blitz, M., Seakins, P., Heard, D. and Stone, D. 2020. Kinetics of the Gas Phase Reactions of the Criegee Intermediate CH_2OO with O_3 and IO. *The Journal of Physical Chemistry A.* **124**(31), pp.6287-6293.

Orlando, J.J. and Tyndall, G.S. 2001. The atmospheric chemistry of the HC(O)CO radical. *International Journal of Chemical Kinetics.* **33**(3), pp.149-156.

Orlando, J.J. and Tyndall, G.S. 2020. The atmospheric oxidation of hydroxyacetone: Chemistry of activated and stabilized $CH_3C(O)CH(OH)OO•$ radicals between 252 and 298 K. *International Journal of Chemical Kinetics.* **52**(4), pp.236-250.

Orlando, J.J., Tyndall, G.S. and Paulson, S.E. 1999. Mechanism of the OH-initiated oxidation of methacrolein. *Geophysical Research Letters.* **26**(14), pp.2191-2194.

Orlando, J.J., Tyndall, G.S. and Wallington, T.J. 2003. The Atmospheric Chemistry of Alkoxy Radicals. *Chemical Reviews.* **103**(12), pp.4657-4690.

Panopoulou, A., Liakakou, E., Sauvage, S., Gros, V., Locoge, N., Stavroulas, I., Bonsang, B., Gerasopoulos, E. and Mihalopoulos, N. 2020. Yearlong measurements of monoterpenes and isoprene in a Mediterranean city (Athens): Natural vs anthropogenic origin. *Atmospheric Environment.* **243**(117803).

Paulson, S.E., Chung, M., Sen, A.D. and Orzechowska, G. 1998. Measurement of OH radical formation from the reaction of ozone with several biogenic alkenes. *Journal of Geophysical Research.* **103**(D19), pp.25533-25539.

Paulson, S.E., Fenske, J.D., Sen, A.D. and Callahan, T.W. 1999. A Novel Small-Ratio Relative-Rate Technique for Measuring OH Formation Yields from the Reactions of O_3 with Alkenes in the Gas Phase, and Its Application to the Reactions of Ethene and Propene. *The Journal of Physical Chemistry A.* **103**(13), pp.2050-2059.

Paulson, S.E., Flagan, R.C. and Seinfeld, J.H. 1992. Atmospheric photooxidation of isoprene part I: The hydroxyl radical and ground state atomic oxygen reactions. *International Journal of Chemical Kinetics.* **24**(1), pp.79-101.

Paulson, S.E. and Orlando, J.J. 1996. The reactions of ozone with alkenes: An important source of HO_x in the boundary layer. *Geophysical Research Letters.* **23**(25), pp.3727-3730.

Paulson, S.E. and Seinfeld, J.H. 1992. Development and evaluation of a photooxidation mechanism for isoprene. *Journal of Geophysical Research: Atmospheres.* **97**(D18), pp.20703-20715.

Payne, W., Nava, D., Nesbitt, F. and Stief, L. 1990. Rate Constant for the Reaction of Atomic Chlorine with Acetaldehyde from 210 to 343 K. *Journal of Physical Chemistry.* **94**(18), pp.7190-7193.

Peeters, J., Müller, J.-F., Stavrakou, T. and Nguyen, V.S. 2014. Hydroxyl Radical Recycling in Isoprene Oxidation Driven by Hydrogen Bonding and Hydrogen Tunneling: The Upgraded LIM1 Mechanism. *The Journal of Physical Chemistry A.* **118**(38), pp.8625-8643.

Peirone, S.A., Cometto, P.M. and Lane, S.I. 2014. OH-Initiated Photooxidations of 1-Pentene and 2-Methyl-2-propen-1-ol: Mechanism and Yields of the Primary Carbonyl Products. *ChemPhysChem.* **15**(17), pp.3848-3854.

Pfister, G.G., Emmons, L.K., Hess, P.G., Lamarque, J.-F., Orlando, J.J., Walters, S., Guenther, A., Palmer, P.I. and Lawrence, P.J. 2008. Contribution of isoprene to chemical budgets: A model tracer study with the NCAR CTM MOZART-4. *Journal of Geophysical Research: Atmospheres.* **113**(D05308).

Picquet, B., Heroux, S., Chebbi, A., Doussin, J.-F., Durand-Jolibois, R., Monod, A., Loirat, H. and Carlier, P. 1998. Kinetics of the reactions of OH radicals with some oxygenated volatile organic compounds under simulated atmospheric conditions. **30**(11), pp.839-847.

Pinho, P.G., Lemos, L.T., Pio, C.A., Evtyugina, M.G., Nunes, T.V. and Jenkin, M.E. 2009. Detailed chemical analysis of regional-scale air pollution

in western Portugal using an adapted version of MCM v3.1. *Science of The Total Environment.* **407**(6), pp.2024-2038.

Plum, C.N., Sanhueza, E., Atkinson, R., Carter, W.P.L. and Pitts, J.N. 1983. Hydroxyl radical rate constants and photolysis rates of α-dicarbonyls. *Environmental Science & Technology.* **17**(8), pp.479-484.

Poppe, D., Brauers, T., Dorn, H.P., Karl, M., Mentel, T., Schlosser, E., Tillmann, R., Wegener, R. and Wahner, A. 2007. OH-initiated degradation of several hydrocarbons in the atmosphere simulation chamber SAPHIR. *Journal of Atmospheric Chemistry.* **57**(3), pp.203-214.

Praske, E., Crounse, J.D., Bates, K.H., Kurtén, T., Kjaergaard, H.G. and Wennberg, P.O. 2015. Atmospheric Fate of Methyl Vinyl Ketone: Peroxy Radical Reactions with NO and HO_2. *The Journal of Physical Chemistry A.* **119**(19), pp.4562-4572.

Pusede, S.E., Gentner, D.R., Wooldridge, P.J., Browne, E.C., Rollins, A.W., Min, K.E., Russell, A.R., Thomas, J., Zhang, L., Brune, W.H., Henry, S.B., DiGangi, J.P., Keutsch, F.N., Harrold, S.A., Thornton, J.A., Beaver, M.R., St. Clair, J.M., Wennberg, P.O., Sanders, J., Ren, X., VandenBoer, T.C., Markovic, M.Z., Guha, A., Weber, R., Goldstein, A.H. and Cohen, R.C. 2014. On the temperature dependence of organic reactivity, nitrogen oxides, ozone production, and the impact of emission controls in San Joaquin Valley, California. *Atmospheric Chemistry and Physics.* **14**(7), pp.3373-3395.

Raff, J.D. and Finlayson-Pitts, B.J. 2010. Hydroxyl Radical Quantum Yields from Isopropyl Nitrite Photolysis in Air. *Environmental Science & Technology.* **44**(21), pp.8150-8155.

Regelin, E., Harder, H., Martinez, M., Kubistin, D., Tatum Ernest, C., Bozem, H., Klippel, T., Hosaynali-Beygi, Z., Fischer, H., Sander, R., Jöckel, P., Königstedt, R. and Lelieveld, J. 2013. HO_x measurements in the summertime upper troposphere over Europe: a comparison of observations to a box model and a 3-D model. *Atmospheric Chemistry and Physics.* **13**(21), pp.10703-10720.

Reimann, S., Calanca, P. and Hofer, P. 2000. The anthropogenic contribution to isoprene concentrations in a rural atmosphere. *Atmospheric Environment.* **34**(1), pp.109-115.

Ren, X., Harder, H., Martinez, M., Lesher, R.L., Oliger, A., Simpas, J.B., Brune, W.H., Schwab, J.J., Demerjian, K.L., He, Y., Zhou, X. and Gao, H. 2003. OH and HO_2 Chemistry in the urban atmosphere of New York City. *Atmospheric Environment.* **37**(26), pp.3639-3651.

Rickard, A.R., Johnson, D., McGill, C.D. and Marston, G. 1999. OH Yields in the Gas-Phase Reactions of Ozone with Alkenes. *The Journal of Physical Chemistry A.* **103**(38), pp.7656-7664.

Roelofs, G.-J. and Lelieveld, J. 1997. Model study of the influence of cross-tropopause O_3 transports on tropospheric O_3 levels. *Tellus B: Chemical and Physical Meteorology.* **49**(1), pp.38-55.

Rohrer, F., Bohn, B., Brauers, T., Brüning, D., Johnen, F.J., Wahner, A. and Kleffmann, J. 2005. Characterisation of the photolytic HONO-source in the atmosphere simulation chamber SAPHIR. *Atmospheric Chemistry and Physics.* **5**(8), pp.2189-2201.

Rosado-Reyes, C.M. and Francisco, J.S. 2007. Atmospheric oxidation pathways of propane and its by-products: Acetone, acetaldehyde, and propionaldehyde. **112**(D14310).

Roselle, S.J. and Schere, K.L. 1995. Modeled response of photochemical oxidants to systematic reductions in anthropogenic volatile organic compound and NO_x emissions. *Journal of Geophysical Research: Atmospheres.* **100**(D11), pp.22929-22941.

Sahu, L.K. and Saxena, P. 2015. High time and mass resolved PTR-TOF-MS measurements of VOCs at an urban site of India during winter: Role of anthropogenic, biomass burning, biogenic and photochemical sources. *Atmospheric Research.* **164-165**, pp.84-94.

Salter, R.J., Blitz, M.A., Heard, D.E., Kovacs, T., Pilling, M.J., Rickard, A.R. and Seakins, P.W. 2013. Quantum yields for the photolysis of glyoxal below 350 nm and parameterisations for its photolysis rate in the troposphere. *Physical Chemistry Chemical Physics.* **15**(14), pp.4984-4994.

Sander, S., Friedl, R., Abbatt, J., Barker, J., Burkholder, J., Golden, D., Kolb, C., Kurylo, M., Moortgat, G. and Wine, P. 2011. Chemical kinetics and photochemical data for use in atmospheric studies, evaluation number 14. *JPL publication.* **10**.

Sander, S., Friedl, R., DeMore, W., Golden, D., Kurylo, M., Hampson, R., Huie, R., Moortgat, G., Ravishankara, A. and Kolb, C. 2000. Chemical kinetics and photochemical data for use in stratospheric modeling. Evaluation Number 13. *JPL Publication.*

Sandu, A. and Sander, R. 2006. Technical note: Simulating chemical systems in Fortran90 and Matlab with the Kinetic PreProcessor KPP-2.1. *Atmospheric Chemistry and Physics.* **6**(1), pp.187-195.

Saunders, S.M., Jenkin, M.E., Derwent, R.G. and Pilling, M.J. 2003. Protocol for the development of the Master Chemical Mechanism, MCM v3 (Part A): tropospheric degradation of non-aromatic volatile organic compounds. *Atmospheric Chemistry and Physics.* **3**(1), pp.161-180.

Savitzky, A. and Golay, M.J.E. 1964. Smoothing and Differentiation of Data by Simplified Least Squares Procedures. *Analytical Chemistry.* **36**(8), pp.1627-1639.

Schultz, M., Heitlinger, M., Mihelcic, D. and Volz-Thomas, A. 1995. Calibration source for peroxy radicals with built-in actinometry using H_2O and O_2 photolysis at 185 nm. *Journal of Geophysical Research: Atmospheres.* **100**(D9), pp.18811-18816.

Schweitzer, F., Magi, L., Mirabel, P. and George, C. 1998. Uptake Rate Measurements of Methanesulfonic Acid and Glyoxal by Aqueous Droplets. *The Journal of Physical Chemistry A.* **102**(3), pp.593-600.

Scollard, D., Treacy, J., Sidebottom, H., Balestra-Garcia, C., Laverdet, G., LeBras, G., MacLeod, H. and Teton, S. 1993. Rate constants for the reactions of hydroxyl radicals and chlorine atoms with halogenated aldehydes. *Journal of Physical Chemistry.* **97**(18), pp.4683-4688.

Seakins, P.W. 2010. A brief review of the use of environmental chambers for gas phase studies of kinetics, chemical mechanisms and characterisation of field instruments. *EPJ Web of Conferences.* **9**, pp.143-163.

Seakins, P.W., Orlando, J.J. and Tyndall, G.S. 2004. Rate coefficients and production of vibrationally excited HCl from the reactions of chlorine atoms with methanol, ethanol, acetaldehyde and formaldehyde. *Physical Chemistry Chemical Physics.* **6**(9), pp.2224-2229.

Seery, D.J. and Britton, D. 1964. The continuous absorption spectra of chlorine, bromine, bromine chloride, iodine chloride, and iodine bromide. *Journal of Physical Chemistry.* **68**(8), pp.2263-2266.

Sharpe, S.W., Johnson, T.J., Sams, R.L., Chu, P.M., Rhoderick, G.C. and Johnson, P.A. 2004. Gas-Phase Databases for Quantitative Infrared Spectroscopy. *Applied Spectroscopy.* **58**(12), pp.1452-1461.

Sillman, S. 1999. The relation between ozone, NO_x and hydrocarbons in urban and polluted rural environments. *Atmospheric Environment.* **33**(12), pp.1821-1845.

Sindelarova, K., Granier, C., Bouarar, I., Guenther, A., Tilmes, S., Stavrakou, T., Müller, J.F., Kuhn, U., Stefani, P. and Knorr, W. 2014. Global data set of biogenic VOC emissions calculated by the MEGAN model over the last 30 years. *Atmospheric Chemistry and Physics.* **14**(17), pp.9317-9341.

Sindelarova, K., Markova, J., Simpson, D., Huszar, P., Karlicky, J., Darras, S. and Granier, C. 2022. High-resolution biogenic global emission inventory for the time period 2000–2019 for air quality modelling. *Earth System Science Data.* **14**(1), pp.251-270.

Sinha, V., Kumar, V. and Sarkar, C. 2014. Chemical composition of pre-monsoon air in the Indo-Gangetic Plain measured using a new air quality facility and PTR-MS: high surface ozone and strong influence of biomass burning. *Atmospheric Chemistry and Physics.* **14**(12), pp.5921-5941.

Sinreich, R., Coburn, S., Dix, B. and Volkamer, R. 2010. Ship-based detection of glyoxal over the remote tropical Pacific Ocean. *Atmospheric Chemistry and Physics.* **10**(6), pp.11359-11371.

Speak, T.H. 2019. *Development of an apparatus for time resolved measurement of OH and HO_2, with application to atmospherically relevant reactions*. thesis, University of Leeds.

Sprengnether, M., Demerjian, K.L., Donahue, N.M. and Anderson, J.G. 2002. Product analysis of the OH oxidation of isoprene and 1,3-butadiene in the presence of NO. *Journal of Geophysical Research.* **107**(D15), pp.ACH 8-1-ACH 8-13.

Stief, L.J., Nava, D.F., Payne, W.A. and Michael, J.V. 1980. Rate constant for the reaction of hydroxyl radical with formaldehyde over the temperature range 228–362 K. *The Journal of Chemical Physics.* **73**(5), pp.2254-2258.

Stone, D., Blitz, M., Daubney, L., Howes, N.U.M. and Seakins, P. 2014. Kinetics of CH_2OO reactions with SO_2, NO_2, NO, H_2O and CH_3CHO as a function of pressure. *Physical Chemistry Chemical Physics.* **16**(3), pp.1139-1149.

Stone, D., Whalley, L.K. and Heard, D.E. 2012. Tropospheric OH and HO_2 radicals: field measurements and model comparisons. *Chemical Society Reviews.* **41**(19), pp.6348-6404.

Taatjes, C.A., Welz, O., Eskola, A.J., Savee, J.D., Osborn, D.L., Lee, E.P.F., Dyke, J.M., Mok, D.W.K., Shallcross, D.E. and Percival, C.J. 2012. Direct measurement of Criegee intermediate (CH_2OO) reactions with acetone, acetaldehyde, and hexafluoroacetone. *Physical Chemistry Chemical Physics.* **14**(30), pp.10391-10400.

Taatjes, C.A., Welz, O., Eskola, A.J., Savee, J.D., Scheer, A.M., Shallcross, D.E., Rotavera, B., Lee, E.P.F., Dyke, J.M., Mok, D.K.W., Osborn, D.L. and Percival, C.J. 2013. Direct Measurements of Conformer-Dependent Reactivity of the Criegee Intermediate CH_3CHOO. *Science.* **340**(6129), pp.177-180.

Tadić, J., Moortgat, G.K. and Wirtz, K. 2006. Photolysis of glyoxal in air. *Journal of Photochemistry and Photobiology A: Chemistry.* **177**(2), pp.116-124.

Taha, H. 1996. Modeling impacts of increased urban vegetation on ozone air quality in the South Coast Air Basin. *Atmospheric Environment.* **30**(20), pp.3423-3430.

Takahashi, K., Hayashi, S., Matsumi, Y., Taniguchi, N. and Hayashida, S. 2002. Quantum yields of $O(^1D)$ formation in the photolysis of ozone between 230 and 308 nm. *Journal of Geophysical Research: Atmospheres.* **107**(D20), pp.ACH 11-11-ACH 11-18.

Takeda, K., Katoh, S., Mitsui, Y., Nakano, S., Nakatani, N. and Sakugawa, H. 2014. Spatial distributions of and diurnal variations in low molecular weight carbonyl compounds in coastal seawater, and the controlling factors. *Science of The Total Environment.* **493**, pp.454-462.

Tan, Z., Fuchs, H., Lu, K., Hofzumahaus, A., Bohn, B., Broch, S., Dong, H., Gomm, S., Häseler, R., He, L., Holland, F., Li, X., Liu, Y., Lu, S., Rohrer, F., Shao, M., Wang, B., Wang, M., Wu, Y., Zeng, L., Zhang, Y., Wahner, A. and Zhang, Y. 2017. Radical chemistry at a rural site (Wangdu) in the North China Plain: observation and model calculations of OH, HO_2 and RO_2 radicals. *Atmospheric Chemistry and Physics.* **17**(1), pp.663-690.

Taucher, J., Hansel, A., Jordan, A., Fall, R., Futrell, J.H. and Lindinger, W. 1997. Detection of isoprene in expired air from human subjects using proton-transfer-reaction mass spectrometry. *Rapid Communications in Mass Spectrometry.* **11**(11), pp.1230-1234.

Taylor, W.D., Allston, T.D., Moscato, M.J., Fazekas, G.B., Kozlowski, R. and Takacs, G.A. 1980. Atmospheric photodissociation lifetimes for nitromethane, methyl nitrite, and methyl nitrate. *International Journal of Chemical Kinetics.* **12**(4), pp.231-240.

Treacy, J., Hag, M.E., O'Farrell, D. and Sidebottom, H. 1992. Reactions of Ozone with Unsaturated Organic Compounds. *Berichte der Bunsengesellschaft für physikalische Chemie.* **96**(3), pp.422-427.

Troe, J. 2000. Are Primary Quantum Yields of NO_2 Photolysis at $\lambda \leq 398$ nm Smaller than Unity? *Zeitschrift für Physikalische Chemie.* **214**(5), p573.

Tuazon, E.C. and Atkinson, R. 1989. A product study of the gas-phase reaction of methyl vinyl ketone with the OH radical in the presence of NO_x. *International Journal of Chemical Kinetics.* **21**(12), pp.1141-1152.

Tuazon, E.C. and Atkinson, R. 1990. A product study of the gas-phase reaction of Methacrolein with the OH radical in the presence of NO_x. *International Journal of Chemical Kinetics.* **22**(6), pp.591-602.

Tyndall, G.S., Orlando, J.J., Kegley-Owen, C., Wallington, T. and Hurley, M. 1999. Rate coefficients for the reactions of chlorine atoms with methanol and acetaldehyde. *International Journal of Chemical Kinetics.* **31**(11), pp.776-784.

Tyndall, G.S., Orlando, J.J., Wallington, T. and Hurley, M. 1997. Pressure dependence of the rate coefficients and product yields for the reaction of CH_3CO radicals with O_2. *International Journal of Chemical Kinetics.* **29**(9), pp.655-663.

Tyndall, G.S., Staffelbach, T.A., Orlando, J.J. and Calvert, J.G. 1995. Rate coefficients for the reactions of OH radicals with methylglyoxal and acetaldehyde. *International Journal of Chemical Kinetics.* **27**(10), pp.1009-1020.

Vaghjiani, G.L. and Ravishankara, A.R. 1989. Absorption cross sections of CH_3OOH, H_2O_2, and D_2O_2 vapors between 210 and 365 nm at 297 K. *Journal of Geophysical Research: Atmospheres.* **94**(D3), pp.3487-3492.

Vereecken, L. 2013. Lifting the Veil on an Old Mystery. *Science.* **340**(6129), pp.154-155.

Veres, P.R., Faber, P., Drewnick, F., Lelieveld, J. and Williams, J. 2013. Anthropogenic sources of VOC in a football stadium: Assessing human emissions in the atmosphere. *Atmospheric Environment.* **77**, pp.1052-1059.

Volkamer, R., Barnes, I., Platt, U., Molina, L.T. and Molina, M.J. 2006. Remote Sensing of Glyoxal by Differential Optical Absorption Spectroscopy (DOAS): Advancements in Simulation Chamber and Field Experiments. In: *Dordrecht*. Springer Netherlands, pp.129-141.

Volkamer, R., Molina, L.T., Molina, M.J., Shirley, T. and Brune, W.H. 2005a. DOAS measurement of glyoxal as an indicator for fast VOC chemistry in urban air. *Geophysical Research Letters.* **32**(L08806).

Volkamer, R., Platt, U. and Wirtz, K. 2001. Primary and Secondary Glyoxal Formation from Aromatics: Experimental Evidence for the Bicycloalkyl−Radical Pathway from Benzene, Toluene, and p-Xylene. *The Journal of Physical Chemistry A.* **105**(33), pp.7865-7874.

Volkamer, R., San Martini, F., Molina, L.T., Salcedo, D., Jimenez, J.L. and Molina, M.J. 2007. A missing sink for gas-phase glyoxal in Mexico City: Formation of secondary organic aerosol. *Geophysical Research Letters.* **34**(L19807).

Volkamer, R., Spietz, P., Burrows, J. and Platt, U. 2005b. High-resolution absorption cross-section of glyoxal in the UV–vis and IR spectral ranges. *Journal of Photochemistry and Photobiology A: Chemistry.* **172**(1), pp.35-46.

Volkamer, R., Ziemann, P.J. and Molina, M.J. 2009. Secondary Organic Aerosol Formation from Acetylene (C_2H_2): seed effect on SOA yields due to organic photochemistry in the aerosol aqueous phase. *Atmospheric Chemistry and Physics.* **9**(6), pp.1907-1928.

Volz-Thomas, A., Lerner, A., Pätz, H.-W., Schultz, M., McKenna, D.S., Schmitt, R., Madronich, S. and Röth, E.P. 1996. Airborne measurements of the photolysis frequency of NO_2. *Journal of Geophysical Research: Atmospheres.* **101**(D13), pp.18613-18627.

Vrekoussis, M., Wittrock, F., Richter, A. and Burrows, J.P. 2009. Temporal and spatial variability of glyoxal as observed from space. *Atmospheric Chemistry and Physics.* **9**(13), pp.4485-4504.

Vrekoussis, M., Wittrock, F., Richter, A. and Burrows, J.P. 2010. GOME-2 observations of oxygenated VOCs: what can we learn from the ratio glyoxal

to formaldehyde on a global scale? *Atmospheric Chemistry and Physics.* **10**(21), pp.10145-10160.

Walker, H., Stone, D., Ingham, T., Hackenberg, S., Cryer, D., Punjabi, S., Read, K., Lee, J., Whalley, L., Spracklen, D.V., Carpenter, L.J., Arnold, S.R. and Heard, D.E. 2022. Observations and modelling of glyoxal in the tropical Atlantic marine boundary layer. *Atmospheric Chemistry and Physics.* **22**(8), pp.5535-5557.

Wang, J., Doussin, J., Perrier, S., Perraudin, E., Katrib, Y., Pangui, E. and Picquet-Varrault, B. 2011. Design of a new multi-phase experimental simulation chamber for atmospheric photosmog, aerosol and cloud chemistry research. *Atmospheric Measurement Techniques.* **4**(11), p2465.

Warneke, C., Trainer, M., de Gouw, J.A., Parrish, D.D., Fahey, D.W., Ravishankara, A.R., Middlebrook, A.M., Brock, C.A., Roberts, J.M., Brown, S.S., Neuman, J.A., Lerner, B.M., Lack, D., Law, D., Hübler, G., Pollack, I., Sjostedt, S., Ryerson, T.B., Gilman, J.B., Liao, J., Holloway, J., Peischl, J., Nowak, J.B., Aikin, K.C., Min, K.E., Washenfelder, R.A., Graus, M.G., Richardson, M., Markovic, M.Z., Wagner, N.L., Welti, A., Veres, P.R., Edwards, P., Schwarz, J.P., Gordon, T., Dube, W.P., McKeen, S.A., Brioude, J., Ahmadov, R., Bougiatioti, A., Lin, J.J., Nenes, A., Wolfe, G.M., Hanisco, T.F., Lee, B.H., Lopez-Hilfiker, F.D., Thornton, J.A., Keutsch, F.N., Kaiser, J., Mao, J. and Hatch, C.D. 2016. Instrumentation and measurement strategy for the NOAA SENEX aircraft campaign as part of the Southeast Atmosphere Study 2013. *Atmospheric Measurement Techniques.* **9**(7), pp.3063-3093.

Washenfelder, R.A., Langford, A.O., Fuchs, H. and Brown, S.S. 2008. Measurement of glyoxal using an incoherent broadband cavity enhanced absorption spectrometer. *Atmospheric Chemistry and Physics.* **8**(24), pp.7779-7793.

Wayne, R.P. 1987. The photochemistry of ozone. *Atmospheric Environment (1967).* **21**(8), pp.1683-1694.

Welz, O., Savee, J.D., Osborn, D.L., Vasu, S.S., Percival, C.J., Shallcross, D.E. and Taatjes, C.A. 2012. Direct Kinetic Measurements of Criegee Intermediate (CH_2OO) Formed by Reaction of CH_2I with O_2. *Science.* **335**(6065), pp.204-207.

Wennberg, P.O., Hanisco, T.F., Jaeglé, L., Jacob, D.J., Hintsa, E.J., Lanzendorf, E.J., Anderson, J.G., Gao, R.-S., Keim, E.R., Donnelly, S.G., Negro, L.A.D., Fahey, D.W., McKeen, S.A., Salawitch, R.J., Webster, C.R., May, R.D., Herman, R.L., Proffitt, M.H., Margitan, J.J., Atlas, E.L., Schauffler, S.M., Flocke, F., McElroy, C.T. and Bui, T.P. 1998. Hydrogen Radicals, Nitrogen Radicals, and the Production of O_3 in the Upper Troposphere. *Science.* **279**(5347), pp.49-53.

Wingenter, O.W., Kubo, M.K., Blake, N.J., Smith Jr., T.W., Blake, D.R. and Rowland, F.S. 1996. Hydrocarbon and halocarbon measurements as photochemical and dynamical indicators of atmospheric hydroxyl, atomic chlorine, and vertical mixing obtained during Lagrangian flights. *Journal of Geophysical Research: Atmospheres.* **101**(D2), pp.4331-4340.

Winiberg, F.A.F. 2014. *Characterisation of FAGE apparatus for HOx detection and application in an environmental chamber*. thesis, University of Leeds.

Winiberg, F.A.F., Smith, S.C., Bejan, I., Brumby, C.A., Ingham, T., Malkin, T.L., Orr, S.C., Heard, D.E. and Seakins, P.W. 2015. Pressure-dependent calibration of the OH and HO_2 channels of a FAGE HO_x instrument using the Highly Instrumented Reactor for Atmospheric Chemistry (HIRAC). *Atmospheric Measurement Techniques.* **8**(2), pp.523-540.

Winiberg, F.A.F., Warman, W.J., Brumby, C.A., Boustead, G., Bejan, I.G., Speak, T.H., Heard, D.E., Stone, D. and Seakins, P.W. 2023. Comparison of temperature-dependent calibration methods of an instrument to measure OH and HO_2 radicals using laser-induced fluorescence spectroscopy. *Atmospheric Measurement Techniques.* **16**(19), pp.4375-4390.

Wittrock, F., Richter, A., Oetjen, H., Burrows, J.P., Kanakidou, M., Myriokefalitakis, S., Volkamer, R., Beirle, S., Platt, U. and Wagner, T. 2006. Simultaneous global observations of glyoxal and formaldehyde from space. *Geophysical Research Letters.* **33**(L16804).

Wood, E.C. and Cohen, R.C. 2006. Fluorescence Methods. In: Heard, D.E. ed. *Analytical Techniques for Atmospheric Measurement.* pp.189-228.

Woodward-Massey, R., Slater, E.J., Alen, J., Ingham, T., Cryer, D.R., Stimpson, L.M., Ye, C., Seakins, P.W., Whalley, L.K. and Heard, D.E. 2020. Implementation of a chemical background method for atmospheric OH measurements by laser-induced fluorescence: characterisation and observations from the UK and China. *Atmospheric Measurement Techniques.* **13**(6), pp.3119-3146.

Wròblewski, T., Ziemczonek, L. and Karwasz, G.P. 2004. Proton transfer reactions for ionized water clusters. *Czechoslovak Journal of Physics.* **54**(3), pC747.

Xiao, Y., Jacob, D.J. and Turquety, S. 2007. Atmospheric acetylene and its relationship with CO as an indicator of air mass age. *Journal of Geophysical Research: Atmospheres.* **112**(D12305).

Xing, Y., Li, H., Huang, L., Wu, H., Shen, H. and Chen, Z. 2018. The production of formaldehyde and hydroxyacetone in methacrolein photooxidation: New insights into mechanism and effects of water vapor. *Journal of Environmental Sciences.* **66**, pp.1-11.

Yan, C., Kocevska, S. and Krasnoperov, L.N. 2016. Kinetics of the Reaction of CH_3O_2 Radicals with OH Studied over the 292–526 K Temperature Range. *Journal of Physical Chemistry A.* **120**(31), pp.6111-6121.

Yan, C. and Krasnoperov, L.N. 2019. Pressure-Dependent Kinetics of the Reaction between CH_3O_2 and OH: TRIOX Formation. *The Journal of Physical Chemistry A.* **123**(39), pp.8349-8357.

Yardley, J.T. 1972. Collisional Quenching and Photochemistry of trans-Glyoxal (^3A_u) Molecules. *The Journal of Chemical Physics.* **56**(12), pp.6192-6197.

Yetter, R.A., Rabitz, H., Dryer, F.L., Maki, R.G. and Klemm, R.B. 1989. Evaluation of the rate constant for the reaction $OH+H_2CO$: Application of modeling and sensitivity analysis techniques for determination of the product branching ratio. *The Journal of Chemical Physics.* **91**(7), pp.4088-4097.

Yeung, L.Y., Pennino, M.J., Miller, A.M. and Elrod, M.J. 2005. Kinetics and Mechanistic Studies of the Atmospheric Oxidation of Alkynes. *The Journal of Physical Chemistry A.* **109**(9), pp.1879-1889.

Yumi, I., Kinichi, O. and Takashi, I. 2002. Rate Constant for the Reaction of OH Radicals with Isoprene at 298 ± 2 K. *Chemistry Letters.* **31**(8), pp.792-793.

Zádor, J., Turányi, T., Wirtz, K. and Pilling, M.J. 2006. Measurement and investigation of chamber radical sources in the European Photoreactor (EUPHORE). *Journal of Atmospheric Chemistry.* **55**(2), pp.147-166.

Zheng, J., Shao, M., Che, W., Zhang, L., Zhong, L., Zhang, Y. and Streets, D. 2009. Speciated VOC Emission Inventory and Spatial Patterns of Ozone Formation Potential in the Pearl River Delta, China. *Environmental Science & Technology.* **43**(22), pp.8580-8586.

Zhong, L., Louie, P.K.K., Zheng, J., Yuan, Z., Yue, D., Ho, J.W.K. and Lau, A.K.H. 2013. Science–policy interplay: Air quality management in the Pearl River Delta region and Hong Kong. *Atmospheric Environment.* **76**, pp.3-10.

Zhu, L., Kellis, D. and Ding, C.-F. 1996. Photolysis of glyoxal at 193, 248, 308 and 351 nm. *Chemical Physics Letters.* **257**(5), pp.487-491.

Zhu, Y. and Kieber, D. 2019. Concentrations and Photochemistry of Acetaldehyde, Glyoxal, and Methylglyoxal in the Northwest Atlantic Ocean. *Environmental Science & Technology.* **53**(16), pp.9512-9521.